Spectroscopic characterisation of TCV divertor towards a detached regime

Lorenzo MARTINELLI

École
polytechnique
fédérale
de Lausanne

2023

The
dedication
of this thesis
is split
seven ways
to Marion,
to my parents,
to Félix,
to my friends
to my sister
to my aunts
and to my
office mates, who
stuck with me
until the
very
end

Abstract

The challenge of power exhaust of the high heat and particle fluxes foreseen for ITER and the forthcoming nuclear fusion reactors can be mitigated by operating in a *detached divertor* regime. This regime has been the object of three decades of studies, as its achievement leads to a simultaneous reduction of target temperature and particle fluxes, relieving the wall's materials from melting and erosion processes. The physical processes leading to divertor detachment involve impurity radiation and plasma-neutral (i.e. atoms and molecules) interactions for momentum, particles (e.g. ions) and energy removal from the flux tubes near the separatrix, where the heat and particle fluxes are concentrated. The effect of these processes can be summed into *loss coefficients* within 0-D models (e.g. the two-point model - 2PM, the power/particle model, or both models combined) describing the heat transport through the divertor region.

In this thesis, we present the hardware upgrade to TCV's Divertor Spectroscopy System (DSS), which consisted in the installation of a mirror-based collection optics coupled to a new triple fibre bundle, conveying the light emitted by the same plasma volume to three independent spectrometers. This upgrade included the installation of two high-resolution spectrometers (i.e. $\Delta\lambda_{FWHM} \approx 0.2$ Å), capable of resolving line-shape broadening contributions of several spectral lines. This enabled a new estimation of ion and neutral species temperatures in the divertor region, based on the measurement of the Doppler broadening contribution to the observed spectral line-shapes.

This thesis presents detachment-relevant experiments, based on deuterium density ramps, in which three spatially resolved diagnostics came together for a detailed characterisation of the divertor leg during its evolution from an attached towards a detached regime. These diagnostics are the DSS, the Multispectral Advanced Narrowband Tokamak Imaging System (MANTIS), which provides 2-D emissivity maps of spectral lines of interest across the whole divertor region, and the Thomson Scattering system (TS), which provides T_e and n_e measurements along the path length of three vertical laser beams. Exploiting TCV's shaping capabilities over several repeat discharges, we were able to reconstruct radial profiles of n_e, T_e and p_e along the divertor leg and across the density ramps using TS data, while the DSS provided the ion temperatures associated with C^+, C^{2+}, He^+ impurity ion species and the neutral temperature associated with atomic deuterium. The essential integration of MANTIS data allowed for the comparison of ion temperature with *effective* electron temperatures $T_e^*(\alpha)$ associated with

Abstract

the ion species α, to observe electron-ions thermalisation in the highly collisional plasma characterising the divertor leg in detachment relevant experiments.

One first observation from these experiments regarded the need to consider a cold influx of neutral particles (i.e. D and C) released in the target vicinity in order to match the measured $T_i(\alpha) < T_e^*(\alpha)$. This hypothesis was tested by considering a simple model that included a collisional-radiative model for low temperature and density C and He particles to calculate their charge state distributions, emissivity and thermalisation times with plasma D ions.

A second measurement carried out in this thesis regarded the determination of characteristic temperatures associated with the *C III radiation front*, or - more properly - the C III emission at 465 nm, a proxy for the achievement of *low T_e* in the divertor. Values of peak T_e and average T_e are presented, together with the determination of a lower T_e limit for C III emission.

Lastly, the temperatures predicted by extensions of the 2PM were tested against those reconstructed in the experiments, highlighting the roles of conductive and convective heat transport in the divertor leg. The static pressure, also observed to decrease during the transition towards a detached regime, is indicative of the redistribution of momentum between different flux tubes while volumetric power losses in the divertor increase. These experiments allow for qualitative estimations of the role of the main *loss coefficients* in the 2PM and their contribution to the divertor evolution towards a detached regime.

Keywords: spectroscopy, divertor, tokamak, detachment, nuclear fusion, power exhaust, ion temperature, spectral line-shape, Doppler broadening, Zeeman splitting, high-resolution spectroscopy, density ramp, long-legged divertor.

Sinossi

 La sfida ingengneristica rappresentata dagli elevati flussi di calore e particelle previsti per
ITER ed i prossimi reattori a fusione nucleare, può essere facilitata operando in regime di
divertor detachment, o di divertore distaccato. Questo regime è stato oggetto di molti studi
nell'arco delle ultime tre decadi, poiché il suo conseguimento porta alla riduzione simultanea
del flusso di particelle che raggiungono i punti di contatto con le pareti (chiamati *targets*) e
della loro temperatura. In tal modo, i processi di fusione o erosione che interessano i materiali
che compongono le pareti interne dei reattori vengono alleviati. Il raggiungimento del regime
di detachment implica la radiazione da parte di impurezze e l'interazione del plasma con
particelle neutre, come atomi e molecole. Tali processi sono responsabili per la riduzione di
energia e di quantità di moto dai tubi di flusso vicino alla cosiddetta *separatrice*, dove i flussi
di calore e particelle sono concentrati. Il loro effetto può essere riassunto tramite l'uso di
coefficienti di perdita, parte di un modello 0-D chiamato *Two Point Model* - 2PM, che descrive
il trasporto del calore attraverso il divertore.

Questa tesi presenta un aggiornamento hardware del Sistema di Spettroscopia del Divertore
o *Divertor Spectroscopy System* - DSS. Tale aggiornamento comprende l'installazione di un
sistema di specchi per la raccolta della luce, accoppiato ad un gruppo di fibre ottiche, le quali
trasmettono la luce emessa da uno stesso volume di plasma a tre diversi spettrometri. Grazie
ad un' ulteriore installazione di due spettrometri ad alta risoluzione spettrale ($\Delta\lambda_{FWHM} \approx$
0.2 Å), è possibile risolvere i vari contributi di allargamento di diverse line spettrali. L'alta
risoluzione spettrale rende disponibile una nuova tecnica per stimare la temperatura di speci
ioniche e neutre nel divertore, basata sulla misura del contributo di allargamento Doppler alle
line spettrali osservate.

In questa tesi vengono presentati esperimenti rilevanti per lo studio del regime di detachment,
basati sulle rampe di densità, utilizzando deuterio come gas primario. Negli esperimenti
vengono utilizzate principalmente tre diagnostiche di spettroscopia, i cui dati sono uniti in
un'analisi organica volta alla caratterizzazione della gamba esterna del divertore durante la
sua evoluzione da regime attaccato (*attached*) a regime distaccato (*detached*). Le diagnostiche
utilizzate oltre la DSS, sono MANTIS -acronimo di *Multispectral Advanced Narrowband To-
kamak Imaging System*- che fornisce mappe 2-D nel piano poloidale di TCV dell'emissività
di alcune linee spettrali selezionate, ed il sistema di Thomson Scattering (TS), che fornisce
misure puntuali di densità n_e e temperatura T_e elettroniche lungo il cammino ottico dei suoi

fasci laser. Sfruttando la capacità di TCV di creare equilibri magnetici *ad hoc* e ripetendo le rampe di densità, siamo stati in grado di ricostruire i profili radiali di n_e e T_e lungo la gamba del divertore all'aumentare della densità utilizzando il TS. La DSS, invece, è stata utilizzata principalmente per misure della temperatura di ioni C II, C III e di He II, e della temperatura associata agli atomi di deuterio. La fruttuosa integrazione dei dati forniti da MANTIS, ha permesso il confronto tra le temperature ioniche e una temperatura elettronica *effettiva* $T_e^*(\alpha)$, associata alla specie ionica α, permettendo di osservare la termalizzazione tra elettroni e speci ioniche nel plasma altamente collisionale che caratterizza la gamba del divertore.

Una prima osservazione derivante da questi esperimenti riguarda la differenza tra temperature ioniche ed elettroniche effettive, $T_i(\alpha) < T_e^*(\alpha)$, la quale suggerisce la presenza di un afflusso di particelle neutre fredde (ad esempio D e C) rilasciate in prossimità del target. Questa ipotesi è stata testata considerando un semplice *collisional-radiative model* per C ed He a bassa densità e temperatura, in grado di calcolare la distribuzione dei loro stati ionizzati, la loro emissività e i tempi di termalizzazione con gli ioni di deuterio.

Un secondo tipo di misura effettuata riguarda la caratterizzazione di temperature caratteristiche associate al *fronte di radiazione del C III*, una quantità spesso utilizzata come indicatore di *bassa temperatura elettronica* nel divertore. In questa tesi vengono presentati tre valori di temperatura associata al fronte di radiazione del C III: il picco del profilo di T_e, la sua media, ed un valore minimo di temperatura per cui il C III possa emettere radiazione.

Infine, le temperature previste da estensioni del 2PM vengono testate utilizzando le temperature ricostruite durante gli esperimenti, evidenziando il ruolo del trasporto di calore convettivo e conduttivo nella gamba del divertore. Una riduzione nella pressione statica del plasma è inoltre osservata durante la transizione da regime attached verso il regime detached, indicando la redistribuzione di quantità di moto verso tubi di flusso più lontani dalla separatrice. Un aumento della radiazione, e più in generale di perdite volumetriche di potenza, è osservato nel divertore durante la rampa di densità. Questi esperimenti offrono quindi stime qualitative del ruolo dei principali coefficienti di perdita nel 2PM e del loro contributo durante l'evoluzione da regime attached verso un regime detached.

Parole chiave: spettroscopia, divertore, tokamak, detachment, fusione nucleare, temperatura ionica, allargamento Doppler, Zeeman splitting, spettroscopia ottica ad alta risoluzione, rampa di densità, divertore a gamba lunga, dissipazione di potenza, forma delle linee spettrali.

Contents

Contents

1 Introduction

1.1 Nuclear Fusion as a form of energy

Nuclear fusion holds the promise for a clean and abundant form of energy, with the potential to have a big impact on the fight against climate change. The most promising fusion reaction involves the nuclei of two hydrogen isotopes, deuterium and tritium. Their fusion produces a helium nucleus and a neutron, releasing 17.6 MeV from the mass reduction of the products compared to that of the reactants. Despite the remaining physical and engineering obstacles being challenging to solve, huge progress has been made since the first proposition to exploit this method for energy production, leading to the construction of the largest fusion experiments in the world that aim to demonstrate a 10× energy gain from nuclear fusion reactions.

In November 2022, the global population reached the milestone of 8 billion living individuals, as reported by a United Nations report (2022) [1]. This can be attributed to advancements in public health, nutrition, personal hygiene, and medicine. However, as developing countries strive to improve their human development index [2], there has been a continuous increase in worldwide energy consumption. Correlations between GDP and energy consumption per capita have been observed. Examples of this are given in Faisal et al. (2017) [3] describing the case of Belgium in the period between 1960-2012; or worldwide, as reported in a European Environment Agency document (2015) [4], based on 2011 data.

Since most of the global energy is, as of today, still produced by fossil fuel plants (around 70%, as reported in the International Energy Agency outlook (2022) [5]), it's not a surprise that the global energy-related CO_2 emission grew by 0.9% in 2022, as documented in [6]. The acceleration of these emissions from the 1950s (see, for instance, [7]) contributed to a 1.15 °C global rise in the average temperature of the atmosphere and oceans relative to the 1850-1900 baseline [8]. Despite significant efforts to meet the goals set by the Paris Agreement (2016) [9], which would require a 45% CO_2 emission reduction by 2030 and a net-zero CO_2 emission by 2050, it is *unlikely* that the current rate of progress will be sufficient to limit global warming to 2 °C, as stated in the 2022 IPCC report [10]. This is well above the agreement's limit of 1.5 °C, which will potentially lead to the dire consequences described in that same report.

Introduction

A paradigm shift, rather than a transition towards less carbon-based energy production schemes, is needed to reach the net-zero CO_2 emission goal before 2050. The world must move towards cleaner global energy production, which requires alternative, strongly CO_2-emitting reduced, energy sources. The significant investments foreseen by the world's advanced economies and China before 2030 [11], focusing on increasing the electricity generation derived by renewables (mainly solar photovoltaic and wind) and nuclear fission, represent an essential step towards CO_2-free global energy production. However, renewable energy sources' intermittent nature, i.e. their dependence on weather conditions, complicates their implementation in the electric grids and requires solutions to store the energy surplus to consistently and reliably meet electricity demand. Nuclear fission has also been identified as a viable substitute for fossil fuel-based electricity production. Countries such as China, South Korea, and Japan are planning significant investments in this field to support their green transition, as noted in the 2022 World Energy Outlook report by the International Energy Agency [12]. However, concerns surrounding the handling of long-lived radioactive waste and the gravity of, albeit rare, nuclear accidents have led some countries to phase out this electricity production method. For example, the German Federal Ministry for the Environment, Nature Conservation, Nuclear Safety and Consumer Protection has released a statement on this matter (2023) [13], announcing their withdrawal from their nuclear program, in fact, slowing down the progress towards achieving the net-zero goal. There is a strong element of scientific, ecological and political turmoil in choosing an appropriate energy mix to meet the global energy demand increase and the CO_2 emission reduction.

In this complicated and grim scenario, nuclear fusion incarnates the promise of a clean and abundant form of energy that has the potential to make a significant impact in the fight against climate change. A nuclear fusion power plant would require only approximately 100 kg of deuterium and tritium to produce the equivalent amount of energy generated by a coal power plant in a year without releasing greenhouse gases or generating long-lasting nuclear waste. In contrast, a coal plant would require $3 \cdot 10^{15}$ kg of fuel and release $11 \cdot 10^{15}$ kg of CO_2 to generate the same energy output [14]. Moreover, unlike fission, nuclear fusion power plants would not pose any danger, as no chain reaction is exploited in energy production.

Nuclear fusion is the fundamental process that powers the Sun and the other stars, as discovered about 100 years ago by A. S. Eddington (1920) [15], and thus indirectly represents the primary energy source responsible for *all* energy sources. As the name implies, nuclear fusion is the process by which two atomic nuclei combine to form a single heavier one. When this reaction occurs, the nucleons (protons and neutrons) of the two reactants rearrange, affecting the binding energy of the nucleons and, thus, the mass of the resulting product. If this is lower than that of the reactants, the reaction is exothermic, with the released energy given by the renowned formula $E = mc^2$, where E is the released energy, m the mass difference between reactants and products, and c is the speed of light.

Recently, nuclear fusion has been experiencing an increased interest in its potential, stimulating investments from the private sector to finance new experimental reactors, some of

which are illustrated in this review by Nature [16]. Moreover, twenty-four years after its major experimental record, the Joint European Torus (JET), the largest operative fusion device up to date, produced 59 MJ of fusion energy over 5 s (see the EuroFusion press release [17]) - the highest achieved by an experimental reactor. The number itself is not extraordinarily large - it is equivalent to the energy produced by the combustion of ~2 kg of coal - but was obtained by consuming 0.1 mg of tritium and 0.07 mg of deuterium, the two hydrogen isotopes representing the fuel for nuclear fusion reactions. But this record is foreseen to be surpassed once ITER [18], the international nuclear fusion experimental reactor involving the European Union, U.S.A., China, India, Russia, Japan and South Korea, would demonstrate the feasibility of nuclear fusion as a sustainable and viable form of energy [19]. ITER aims to reach an out-versus-in power amplification ratio of the fusion reaction $Q_{fus} = 10$, meaning that the foreseen thermal power produced by the nuclear fusion reaction, of 500 MW, will be provided by a 50 MW input power heating the deuterium and tritium gas mixture to the temperatures necessary for the reactions to occur.
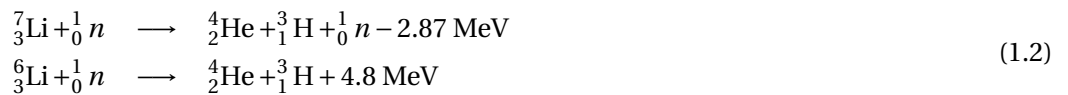
1.1.1 The DT nuclear fusion reaction

The most accessible reaction for nuclear fusion power plants involves the two aforementioned hydrogen isotopes: deuterium (D, or $_1^2$H) and tritium (T, or $_1^3$H). Their nuclei have one and two neutrons more than that of the hydrogen nucleus. The fusion of deuterium and tritium nuclei forms an unstable isotope of helium ($_2^5$H) that almost immediately decays, releasing a stable He nucleus and a neutron n.

$$_1^2\text{H} + _1^3\text{H} \quad \longrightarrow \quad _2^5\text{He} \quad \longrightarrow \quad n + _2^4\text{He} + 17.6\,\text{MeV} \tag{1.1}$$

The reaction decay is highly exothermic, with the released energy distributed between the products, inversely proportional to their mass, from momentum conservation. The $_2^4$He will then carry a kinetic energy of 3.5 MeV[*] and the neutron the remaining 14.1 MeV.

Deuterium is a naturally abundant element with a ratio of 1:6700 for every hydrogen nucleus and can be relatively easily extracted from water [20]. Conversely, tritium is an unstable isotope that undergoes β^- decay with a half-life of $\approx$12 years. Its presence on Earth occurs only in trace form and must be bred by nuclear reactions. Initially provided from neutron irradiation from a fission reactor, the candidate reactions for sustained tritium breeding involve lithium isotopes with the neutron produced by the D-T reaction 1.1:

$$_3^7\text{Li} + _0^1 n \quad \longrightarrow \quad _2^4\text{He} + _1^3\text{H} + _0^1 n - 2.87\,\text{MeV}$$
$$_3^6\text{Li} + _0^1 n \quad \longrightarrow \quad _2^4\text{He} + _1^3\text{H} + 4.8\,\text{MeV} \tag{1.2}$$

Tritium could therefore be produced *in situ*, from the relatively abundant Li resources. Using

---

[*]1 eV indicates the kinetic energy of an electron when accelerated by an electric field of 1 V. It can be used to measure the thermal energy of particles, from which one can derive an equivalent definition of temperature applying the conversion factor 1 eV = 11606 K.

feasible reactions and extraction efficiency, a single neutron will be insufficient to maintain T supplies. The energetic neutron must first be used to generate more, less energetic, neutrons by other nuclear reactions before T breeding. Lithium should therefore be considered as a primary fuel for nuclear fusion reactions. This element is often taken for granted and considered as a *limitless* resource within the fusion community. Its availability on Earth for fusion applications is discussed in [21]. However, concerns exist on the sustainability of Lithium extraction, expressed in [22], and solutions need to be addressed that consider the other application needs for this element (i.e. batteries) together with the need to improve lithium recycling.

It should be noted that the D-T reaction products consist of helium and neutrons only: no greenhouse gases nor long-living radioactive materials are involved in the reaction. The only concerns on radioactive hazards derive from emitted neutrons activating nearby materials that can be designed to decay within only a few decades by selecting the reactor chamber and surrounding materials appropriately [23].

The D-T reaction can occur if the two reacting nuclei collide at sufficient velocity. During the collision, when the nuclei reach a distance of the order of a nuclear diameter (i.e. $\sim 10^{-15}$ m), the short-range, attractive, nuclear force acts between the nucleons, fusing them into the intermediate product. As mentioned in the previous section, for so-called "thermonuclear" fusion where this velocity is provided by thermal energy, the D-T gas mixture needs to be heated, reaching higher temperatures than the core of the Sun. Indeed, the reaction cross-section σ, which reflects the probability of the reaction happening, peaks at around ~60 keV [24]. Fusion reactions can still take place at lower temperatures, e.g. 15 keV, exploiting the high-temperature tail of the plasma Maxwellian distribution. At these temperatures, the fuel gas mixture is in the state of *plasma*, a term first proposed by I. Langmuir in 1927 to refer to totally or partially ionised gases. The plasma heating, moreover, helps the positively charged nuclei overcome the *Coulomb barrier*, given by the electrostatic repulsion dominating the plasma dynamics at a long-range scale and inhibiting the reaction.

A power *break-even* is obtained when the thermal power produced by the reaction equals the power injected in the system ($Q_{fus} = 1$). To reach break-even, fusion devices must achieve plasma conditions for which a high number of reactions, proportional to the product of the reactants' density, is sustained for a relatively long time. J. D. Lawson first proposed this criterion in 1957 [25] to give an order of magnitude of the problems involved in making nuclear fusion a viable form of energy, examining the energy balance for power plants using a hot plasma. The thermal power provided by the fusion reactions is given by:

$$P_{fus} = \frac{1}{4} n_D \cdot n_T \langle \sigma v \rangle \Delta E_{fus} \tag{1.3}$$

where $n_D = n_T$ are the densities of deuterium and tritium nuclei, which for a mixture of hydrogen isotopes is half that of electrons n_e, $\langle \sigma v \rangle$ indicates the average over a Maxwellian distribution function at reactant temperature T of the reactivity σv, and ΔE_{fus} is the energy released by the reaction. This must be greater than that lost by the system -we will see in the

next section how-, which can be expressed using an *energy confinement time* τ_E

$$P_{loss} = \frac{3 n_e T_e V}{\tau_E} \qquad (1.4)$$

which has to be compensated by external heating P_{ext} and/or by the energy provided by the charged fusion reaction products to the plasma volume V, given by $\frac{1}{4} n_e^2 \langle \sigma v \rangle \Delta E_{charged}$.

The $\frac{P_{fus}}{P_{ext}} > 1$ condition can be rewritten highlighting a figure of merit, called the *triple product*, combining n_e, T and τ_E as

$$n_e \cdot T \cdot \tau_E > \frac{12 T^2}{\langle \sigma v \rangle (\Delta E_{fus} + \Delta E_{charged})} \qquad (1.5)$$

with this formula being valid between 10-20 keV. In the parameter space operated by nuclear fusion reactors, the triple product must be greater than

$$n_e \cdot T \cdot \tau_E > 10^{21} \ [\text{m}^{-3} \ \text{keV s}] \qquad (1.6)$$

for T in the range of 10 to 20 keV. Different reactor concepts try to maximise this product in different ways. Stars like our Sun, for example, operate with $n_e \sim 10^{32}$ m^{-3} and $T \sim 1.3$ keV in their core[†]. While in stars plasma confinement is provided by gravity, the same solution clearly cannot be exploited on Earth.

Two main paths have been explored. One aims to achieve a high triple product by operating at high temperatures and high density i.e. $\approx 10^{31}$ m^{-3}, for very short time scales i.e. ≈ 10 ns, controlling *mini-explosions* induced by high-power lasers. This approach is called *inertial confinement*, and, in December 2022, achieved the milestone value of $Q_{fus} = 1.5$, generating 3.15 MJ of fusion energy [27]. This result, achieved at the National Ignition Facility of the Lawrence Livermore National Laboratory, represents a physical breakthrough, but it is far from demonstrating the feasibility of inertial confinement power plants as a viable option in the near future. A different approach aims to harness nuclear fusion by exploiting the electromagnetic properties of plasma, using *magnetic confinement* to keep the fusion fuel together. Here, the plasma is typically less dense than for the inertial confinement case ($n_e \approx 10^{20}$ m^{-3}) but requires temperatures of $T > 5$ keV and an energy confinement time of the order of 1 s. An example of this kind of device is represented by the *tokamak*, described in the next section.

[†]The chain of nuclear reactions occurring in the sun are however different from the D-T fusion, involving in a first step the fusion of two protons [26] as

$$p + p \longrightarrow D + e^+ + \nu_e \qquad (1.7)$$

a process with several orders of magnitude smaller cross-sections than the D-T fusion.
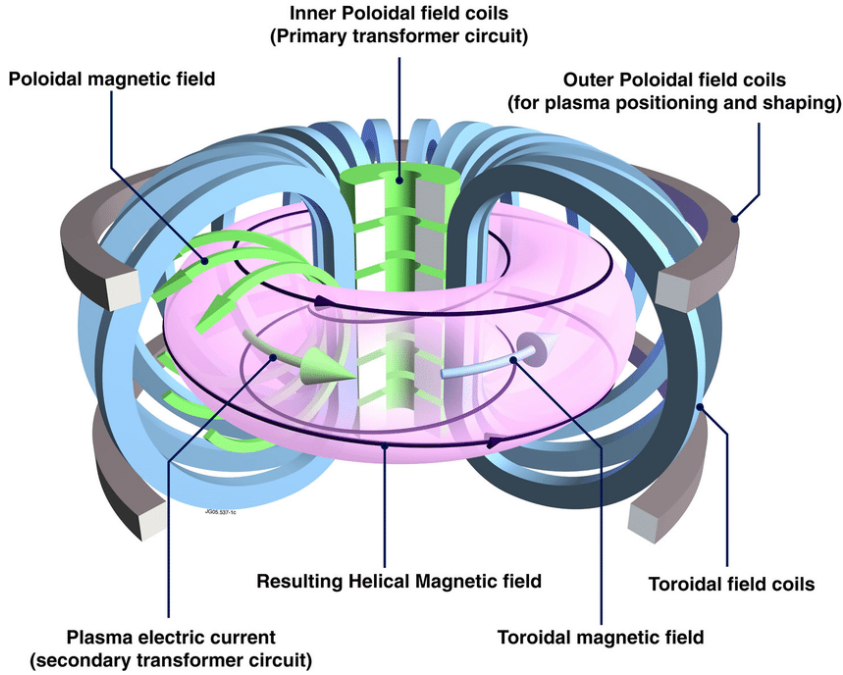
Figure 1.1: Sketch of a tokamak device, image from [14].

.

1.1.2 The tokamak concept

Many magnetic confinement devices have been proposed as experimental fusion reactors, but the most studied and, so far, the most promising solution is the *Tokamak* configuration. The tokamak, from the Russian acronym TOroidal'naya KAmera s MAgnitnymi Katushkami, which means *toroidal chamber with magnetic coils*, uses magnetic fields to confine the plasma within a toroidal vessel [28] and was firstly proposed by the soviet scientists Andrei Sakharov and Igor Tamm in the 1950s.

The essential components of a tokamak are:

- a toroidal *vacuum vessel*, where the plasma - drawn in pink in figure 1.1 - and neutral gases are contained.

- a set of poloidally wounded coils, referred to as *toroidal* field coils, to create a magnetic field in the toroidal direction, $\vec{B}_\phi$. These are drawn in blue in figure 1.1. The toroidal magnetic field, calculated at the axis of medium-to-large machines, can reach a few T.

- a set of toroidally wounded coils located in the centre of the torus, forming the *central solenoid*, drawn in green in figure 1.1. This element constitutes a primary transformer circuit, and the plasma in the torus constitutes the secondary, where a plasma current I_p is induced, flowing in the toroidal direction (see the green conical arrow in figure 1.1). The toroidal plasma current generates a poloidal magnetic field, $\vec{B}_\theta$, indicated by the other green arrows in figure 1.1. In the largest existing devices, I_p is of the order of MA.

- a second set of external toroidally wounded coils, called *vertical field coils*, shown in grey in figure 1.1, generates a vertical contribution to the magnetic field. This is necessary to balance the radial forces given by the plasma toroidal geometry that push it outwards. The vertical field results in a Lorentz force that equilibrate this radial force

$$\vec{F}_L = 2\pi R_p (I_p \hat{e}_\phi \times B_v \hat{e}_z) \tag{1.8}$$

These coils are also often employed to improve the plasma shaping.

The vectorial sum of the $\vec{B}_\phi$ and $\vec{B}_\theta$ magnetic field components gives rise to a helical magnetic field, whose field lines are drawn in figure 1.1 by the black lines. These helical field lines wrap around the torus, describing toroidal *flux surfaces*.

The confinement of plasma within tokamaks can be explained by examining the trajectories of particles with charge q and velocity $\vec{v}$ in the presence of electric and magnetic fields, $\vec{E}$ and $\vec{B}$. They are subjected to a Lorenz force

$$\vec{F} = q(\vec{E} + \vec{v} \times \vec{B}) \tag{1.9}$$

which compels them to describe orbits around the magnetic field lines while, on average, streaming along them.

In the presence of a toroidal field alone, particles moving along the field lines are affected by drifts caused by the intrinsic non-homogeneity of the magnetic field and its curvature. These drifts would cause charge separation, which would, in turn, give rise to $\vec{E} \times \vec{B}$ drifts, driving the plasma particles towards the machine walls. The poloidal field compensates for this separation: making the particles rotate poloidally, they drift up and down half the time, effectively shorting out the charge separation. Faraday's law describes how the central solenoid provides this field component by a constant magnetic flux change due to current ramps in this element. This method of current drive to generate the poloidal field implies a pulsed operation of tokamak devices, with practical plasma discharge durations ranging from seconds to a few minutes. However, non-inductive current drive methods, such as those reviewed in [29], can significantly extend the duration of the pulses.

Despite the poloidal field component, particles still experience some *cross-field* transport, causing the particles to change the field line they were following. This phenomenon can be due to collisions across gradients within the plasma, driving diffusion described by *neoclassical transport*, or by turbulent mechanisms, that reduce the effectiveness of the magnetic confinement.

This thesis presents experiments conducted in a Tokamak device, the Tokamak à Configuration Variable, presented in the next section.

1.2 TCV: The Tokamak à Configuration Variable

TCV is a medium size, highly elongated, carbon-walled tokamak at the Swiss Plasma Center, a research centre of the École Polytechnique Fédérale de Lausanne (EPFL) in Switzerland. The main trademarks of this machine are its high flexibility in creating a wide range of poloidal magnetic configurations and the availability of state-of-the-art, mostly student-powered, plasma diagnostics.
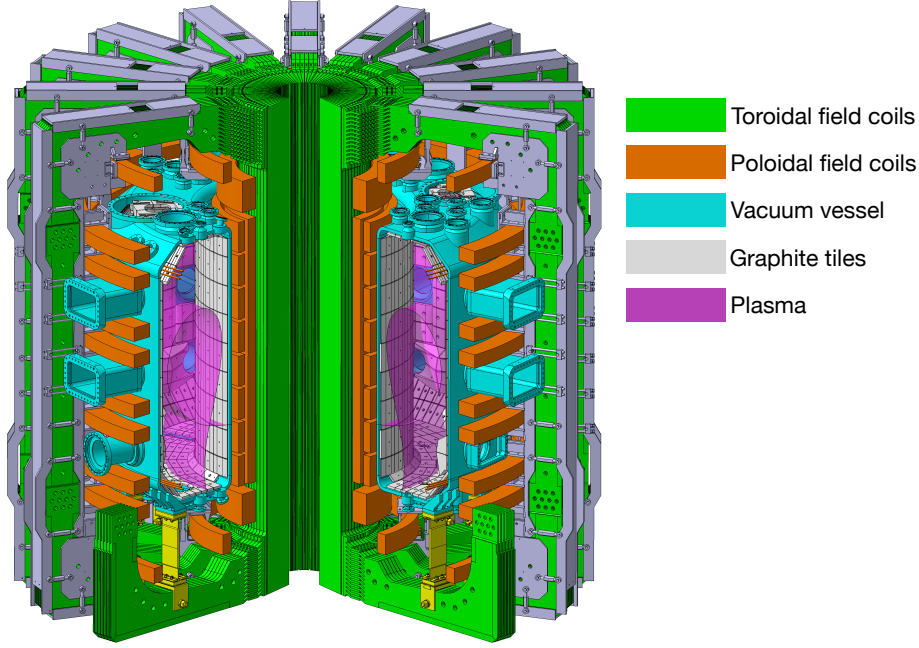

Figure 1.2: Cad drawing illustrating the main components of the TCV tokamak. Courtesy of M. Toussaint.

TCV's major radius is $R_0 = 0.88$ m, with a minor radius of $a = 0.255$ m. The toroidal magnetic field is given by a set of 16 toroidal field coils, together with sixteen poloidal field coils, also called *shaping* coils, that are independently powered, giving TCV its unique capability of strong main plasma and divertor shaping. Some of the geometries achieved in TCV are shown in figure 1.3. The toroidal field coils can generate a maximum toroidal magnetic field that, on axis, is of $B_0 = 1.54$ T. TCV record plasma current I_p is 1 MA, as in figure 1.3e), but it usually operates with plasma currents between 190 and 320 kA. The toroidal magnetic field and the I_p direction can be chosen for each discharge.

For auxiliary heating, TCV is equipped with two main systems that underwent significant upgrades between 2019 and 2022, as described in A. Fasoli et al. (2020) [30]. This concerned the installation of a second neutral beam heating system, NBH, presented in A. Karpushov et al. (2023) [31], capable of injecting up to 1 MW (< 60 keV neutrals), tangentially aligned to the toroidal magnetic field, but in the opposite direction to the first 1 MW (< 27 keV neutrals) NBH

system (described in A. Karpushov et al. (2017) [32]) operational since 2016. The second system employs electron cyclotron resonance heating, ECRH, with up to 5 MW power, exploiting the X2 and X3 harmonic frequencies at full toroidal field.

TCV's typical plasma discharge duration is 2 s. Typical line-averaged electron densities lie in the range $10^{19} \leq n_e \leq 2 \cdot 10^{20}$ m^{-3}, with core electron temperatures reaching up to 15 keV with strong ECRH heating. It operates primarily with deuterium gas, but isotope studies are possible, with a majority of hydrogen or helium plasma, as studied in F. Bagnato et al.(2023) [33]. As part of the recent upgrades, a part of which is presented in N. Offeddu et al.(2022) [34], new gas injection valves were installed. It is, therefore, possible to inject controlled amounts of impurities such as He, N, Ar and Ne and to study their emission properties, as in Février et al. (2020) [35], Decker et al. (2022) [36] and B. Linehan et al. (2023) [37].
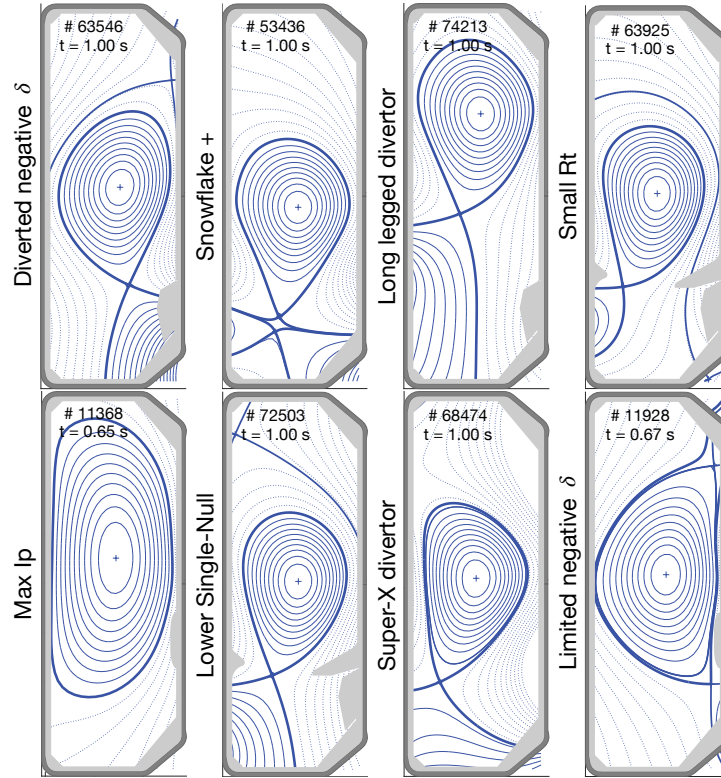
Figure 1.3: Assorted magnetic equilibria achievable in TCV, reconstructed by the LIUQE magnetic reconstruction code [38] and plotted inside TCV poloidal cross-section.

Up to 95% of the 1.54 m high vessel interior is covered by graphite tiles. The carbon sputtered from these tiles is often the strongest plasma impurity, but its presence can be exploited for numerous plasma parameters and regime identification, as in F. Bagnato et al. (2023) [33] for core impurity transport. In this thesis, in chapters 4 and 5, C emission will be exploited for measuring plasma parameters, such as the temperature of the ions, in the frame of power exhaust studies. Graphite was chosen since, when exposed to the plasma heat fluxes within

the tokamak vacuum, it doesn't melt but sublimates so that the high-density carbon-rich cloud's interaction with that plasma radiates profusely, protecting the underlying material surface. Carbon is a low-Z impurity that radiates mostly at low T_e causing little degradation of the core plasma performance compared to higher-Z materials, i.e. tungsten, employed in other machines (i.e. JET-ILW [39], or Asdex-U [40]). On the other hand, solid carbon features high hydrogen isotope retention, making it unsuitable for D-T machines from the nuclear safety viewpoint, where the amount of T stored in the machine is strictly limited. We will see how neutral carbon and deuterium fluxes can explain the observations presented in chapter 4, and discussed in chapter 5.

Figure 1.4: Fisheye view of TCV interior, taken by one of the 169 viewports. The graphite tiles are visible, covering almost all of the TCV's first wall. Image source: *SPC, EPFL.*

The remaining surface of the inner wall is reserved for viewports, in which numerous plasma diagnostics are installed. The plasma diagnostics' variety and quality are another remarkable strength of the TCV facility. They span core turbulence diagnostics, fast ions loss detectors, magnetic flux probes, wall-embedded and reciprocating Langmuir probes, infrared cameras, reflectometry, Thomson scattering, neutral pressure gauges, interferometry, X-ray cameras, spectroscopy and many more. These diagnostics are fundamental to progress in the many research fields active on TCV. Over the years, scientists at TCV focused on the properties of confinement in negative-triangularity, disruption mitigation and avoidance, control optimisation and many other topics, as presented in the recent reviews by S. Coda et al.(2017) [41] and H. Reimerdes et al.(2022) [42].

We will see in section 4.1 how TCV's signature flexibility and the abundance of state-of-the-art diagnostics, some of which are presented in greater detail in chapter 2, are the key to the research presented in this thesis, which is in the framework of power exhaust studies. More insight into the challenges of this research field is presented in the following section.

1.3   Divertor detachment

Divertor detachment is seen as a mandatory solution to mitigate the power directed towards the first wall of forthcoming nuclear fusion power plants. The study of the physical processes leading to this regime is the main theme of this thesis.
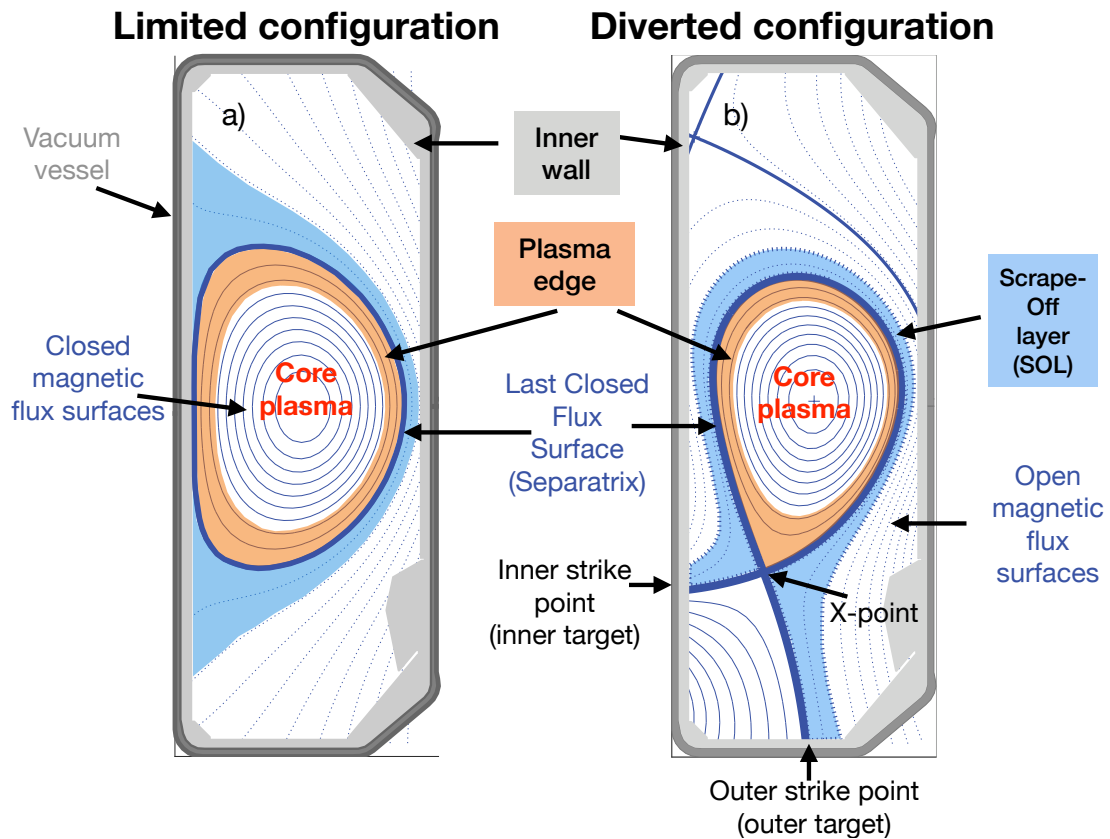
Figure 1.5: a) Limited and b) diverted configurations illustrated in the TCV poloidal cross-section.

In section 1.1.1, we have seen why thermonuclear fusion requires extremely high temperatures. Such temperatures imply that the energy and particle fluxes that inevitably leak from the magnetically confined region are also exceptionally high. If unmitigated, they will mostly follow the field lines that intercept the vessel and damage the fusion power plant. Indeed, the research field of power exhaustion from fusion-relevant tokamaks is very active, studying how to safely deliver -from the machine's point of view- the exhausted heat fluxes to the machine's first wall while minimising erosion and melting events. Over recent decades [43], much of this

effort has been focused on the study of *divertor detachment* as a promising solution to this problem.

To understand what divertor detachment is, it is necessary first to introduce the concept of *divertor*, first proposed by L. Spitzer in 1958 [44] in his research on stellarator devices.

In tokamak machines, it is possible to control the intensity of the poloidal magnetic field to generate a local null point, called *X-point*, of such field in the poloidal plane, see figure 1.5b. The introduction of the X-point creates a dipole-like configuration where the plasma can be confined. At this point, the field lines intersect each other at a 90° angle. These field lines can create two kinds of configurations: if both loops close inside the vessel, we have a *doublet* configuration, but if one of the loops intersects the machine walls before closing, we obtain a *diverted* configuration. Here, the plasma leaving the closed flux surfaces region must follow the perpendicular flux surfaces that branch off the X-point, called divertor legs. The plasma-wall interactions then occur over narrow regions (called inner/outer *targets*, or *strike points*) where the field lines intersect the machine [45]. From this point of view, diverted configurations can be considered as opposed to the *limited* ones, where the Last Closed Flux Surface (LCFS) enclosing the core plasma is directly determined by the outermost closed flux surface that grazes the machine walls. Figure 1.5 illustrates the difference between these configurations representing the main geometric plasma components in the TCV poloidal cross-section. Here are highlighted the *plasma edge* region, where strong perpendicular temperature and density gradients develop between the core and the LCFS, and the scrape-off layer region (SOL), radially outboard of the LCFS, where collisionality is high compared to the core plasma and interaction between plasma and neutral particles becomes significant.

Implementing a divertor in a tokamak often requires the use of dedicated poloidal field coils, increasing the machine's complexity. Moreover, in some cases, of which TCV is an example, it can use up a large part of the chamber's volume that could otherwise be used to increase the plasma volume and the fusion reactions. Despite this, operating a tokamak in a diverted configuration offers many advantages. For instance, the impurities generated at the targets are distant from the plasma core in the topological space, reducing their transport toward the bulk. This is contrary to the limited case, where they are produced at the LCFS. Introducing a divertor region significantly decreases the core's Z_{eff}, thus also diminishing the plasma fuel dilution and increasing the reaction rates. Secondly, a small interaction region facilitates the design of the divertor targets, i.e. by using materials capable of resisting high thermal loads, i.e. tungsten (W), used in JET-ILW [39] and chosen for ITER [46, 47], and/or by optimising neutral compression [48], power exhaust and pumping of He *ashes*. Moreover, if in limited configurations, the machine wall is in direct contact with the LCFS, where the electron temperatures can reach values of $\approx$ 100 eV, a divertor offers the means to dissipate the power fluxes leaking from the plasma edge into the SOL, before they can reach the wall at the divertor targets, by volumetric processes such as radiation and charge-exchange with neutral particles [49]. In present designs, $\approx$ 20% of the fusion power will likely reach the divertor, with the rest, i.e. neutrons and radiation, being distributed on the walls. These properties, in particular, are going to be presented in more detail in the next section, where we describe how energy,

particles and momentum are transported in the tokamak SOL to show how to simultaneously reduce the parameters endangering the target safety, namely the heat and particle fluxes and, finally, reducing the target temperature.

1.3.1 Heat transport in SOL: the two-point model

The two-point model is a simplified description of the SOL, assuming pressure conservation along a flux tube, that we can use to predict target parameters, i.e. T_t and n_t, from upstream values. This section is derived by [49].
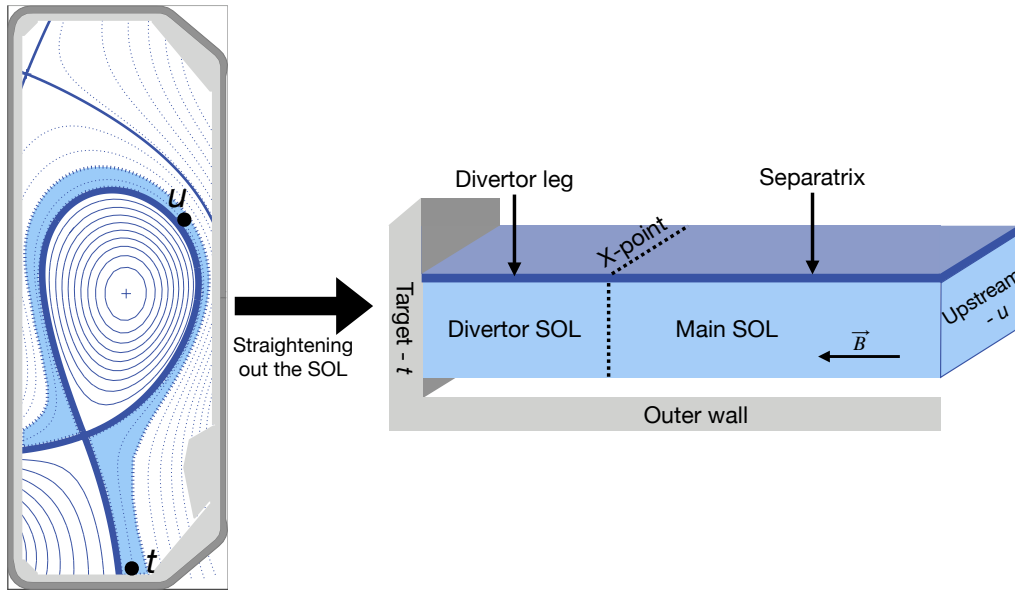

Figure 1.6: Geometry of the two-point model, adapted from [49] to the TCV SOL.

We have discussed how reaching sufficiently low heat fluxes at the divertor strike points is a fundamental requirement for the safe operation of all, including reactor-relevant, regimes. In this context, a simple 0-D model called the Two-Point Model (2PM), can be used to relate plasma parameters evaluated at two characteristic positions in the SOL, namely the target, indicated with subscript t, and an upstream point along the flux tube, indicated with subscript u. The reference geometry is illustrated in the sketch of figure 1.6, where TCV SOL, taken as an example, is drawn straightened out and considered as a plasma 1D slab. The model is based on simple assumptions regarding particle, pressure and power balance, as explained in *The Plasma Boundary of Magnetic Fusion Devices* by P. Stangeby [49], chapter 5.2:

- *particle balance:* The only flow considered in the model, parallel to $\vec{B}$, occurs in a narrow region before the target, in a cycle where the neutral particles, resulting from wall recycling of ions, are re-ionised and accelerated towards the target reaching the ion sound speed. The considered particle balance is one-dimensional and takes place

within a flux tube. A further assumption of the 2PM is that no energy is spent during ionisation.

- *pressure balance:* The model assumes constant pressure along a flux tube. This is given by the sum of a static - $p_{stat} = nkT$ - and dynamic - $p_{dyn} = nmv^2$ - contributions:

$$p = nkT_e + nkT_i + nmv^2 \tag{1.10}$$

where n is the plasma density, k the Boltzmann constant and m the mass of the considered particles. From the considerations expressed in the previous point, the absence of flows implies that $v_u = 0$ while, at the target, particles attain the ion sound speed $v_t = c_s = \sqrt{\frac{2kT_e}{m_i}}$. The model further assumes $T_e = T_i$, so that we can write

$$n_t(2kT_t + mv_t^2) = 2n_u kT_u \qquad \longrightarrow \qquad 2n_t T_t = n_u T_u \tag{1.11}$$

- *power balance:* In the absence of flows and of volumetric power losses, the parallel heat flux density, $q_\parallel$, measured in $[\text{W m}^{-2}]$, is dominated by conduction, making possible a $\nabla_\parallel T$ along the flux tube. Considering a distance L between u and t, the two points characteristic temperatures are related by

$$T_u^{7/2} = T_t^{7/2} + \frac{7}{2}q_\parallel \frac{L}{\kappa_{0e}} \tag{1.12}$$

where κ_{0e} is the electron parallel conductivity coefficient, and we have assumed that the electron conductivity is much higher than that of the ions. In this framework, the parallel kinetic heat flux entering the sheath depends upon the target density and temperature, as

$$q_\parallel = q_{t,kin} = \gamma n_t kT_t c_{st} = \gamma \sqrt{\frac{2}{m_i}} kn_t T_t^{3/2} \tag{1.13}$$

where $\gamma \approx 7$ is called the sheath heat transmission coefficient. It should be noted the total plasma heat flux loaded at the target, q_t, is also composed of a potential energy component linked to the potential energy of the ions, so that

$$q_t = q_{t,kin} + q_{t,pot} \tag{1.14}$$

where

$$q_{t,pot} = \Gamma_t \cdot \varepsilon \tag{1.15}$$

and ε is the ionisation energy. For hydrogen atoms, $\varepsilon = 13.6$ eV.

Equations 1.11, 1.12, and 1.13 provide a system which can be used to solve for the three unknowns, namely T_u, T_t and n_t. The other variables, i.e. $q_\parallel$ and n_u can be seen instead as

control parameters as they are strictly related to the average plasma density and the power input, easily tunable in a tokamak device. In contrast, the other terms are constant, i.e. γ and κ_{0e}, or depend upon the specific geometry, i.e. L. The system can be solved assuming $T_u \gg T_t$, yielding the following solutions [49]

$$T_u \simeq \left(\frac{7}{2} \frac{q_\parallel L}{\kappa_{0e}} \right)^{2/7} \tag{1.16}$$

$$T_t = \frac{m_i}{2e} \frac{4q_\parallel^2}{\gamma^2 e^2 n_u^2 T_u^2} = \frac{m_i}{2e} \frac{4q_\parallel^2 \left(\frac{7}{2} \frac{q_\parallel L}{\kappa_{0e}} \right)^{-4/7}}{\gamma^2 e^2 n_u^2} \tag{1.17}$$

and lastly

$$n_t = \frac{n_u^3}{q_\parallel^2} \left(\frac{7}{2} \frac{q_\parallel L}{\kappa_{0e}} \right)^{4/7} \frac{\gamma^2 e^3}{4m_i} \tag{1.18}$$

From equation 1.17 we see that one of the most effective ways to decrease T_t is to increase n_u, as $T_t \propto n_u^{-2}$. Operating the tokamak at high density benefits the target safety and increases the fusion triple product, see equation 1.5. It, however, increases n_t, as from equation 1.18 $n_t \propto n_u^3$, overall causing an increase of q_t, which ultimately is one of the quantities we seek to minimise.

We note here, and further elaborate in the next section, how the q_t predicted by these equations is derived using the assumption that no power is used in the ionisation processes.

Another quantity we want to act on and that we can derive from the 2PM is the target particle flux Γ_t. This is given by

$$\Gamma_t = \frac{q_\parallel}{\gamma e T_t} \qquad \longrightarrow \qquad \Gamma_t = \frac{n_u^2}{q_\parallel} \left(\frac{7}{2} \frac{q_\parallel L}{\kappa_{0e}} \right)^{4/7} \frac{\gamma e^2}{2m_i} \tag{1.19}$$

It is essential to minimise this quantity because the ions recombining on the wall would release their potential energy at the target, increasing the overall thermal load. Equation 1.19 states that the target particle flux is sensitive to the upstream density and to the parallel heat flux, as $\Gamma_t \propto n_u^2 q_\parallel^{-3/7}$.

The model can be made more realistic by dropping some of the initial hypotheses and introducing volumetric power losses, that the basic 2PM neglected. These, for example, could be due to radiation in the SOL, q_{rad}^{SOL}, or an interaction with neutrals, such as charge exchange, q_{cx}^{SOL}, introducing a *power loss factor* f_{power} in equation 1.13:

$$q_{rad}^{SOL} + q_{cx}^{SOL} = f_{power} q_\parallel \qquad \longrightarrow \qquad (1 - f_{power}) q_\parallel = \gamma k T_t n_t c_{st} \tag{1.20}$$

It is important to note that f_{power} also includes power losses associated with ionisation. In a high-recycling divertor, for which it is possible to use a closed box approximation, a portion of f_{power} is therefore linked to Γ_t, as more ionisation leads to more power losses. The interaction with neutrals can also cause *momentum losses*, via viscous forces and volumetric recombination, introducing a *momentum loss factor* in equation 1.11:

$$2n_t T_t = (1 - f_{mom})n_u T_u \tag{1.21}$$

essentially introducing a pressure gradient along the flux tube (see Labombard et al. (1997) [50]), relaxing the hypothesis of pressure conservation. A third correction factor has to be included in equation 1.12 to account for heat transport through *convection*, which reduces the temperature gradient along the flux tube established by conduction alone:

$$T_u^{7/2} = T_t^{7/2} + \frac{7}{2}f_{cond}q_\parallel \frac{L}{\kappa_{0e}} = T_t^{7/2} + \frac{7}{2}(1 - f_{conv})q_\parallel \frac{L}{\kappa_{0e}} \tag{1.22}$$

The introduction of the loss factors can affect the target parameters, as illustrated in figure 1.7. This figure compares two calculations of the $T(l)$ along the SOL, plotted as a function of *distance from the target*, using the parameter L as a variable in equation 1.22.
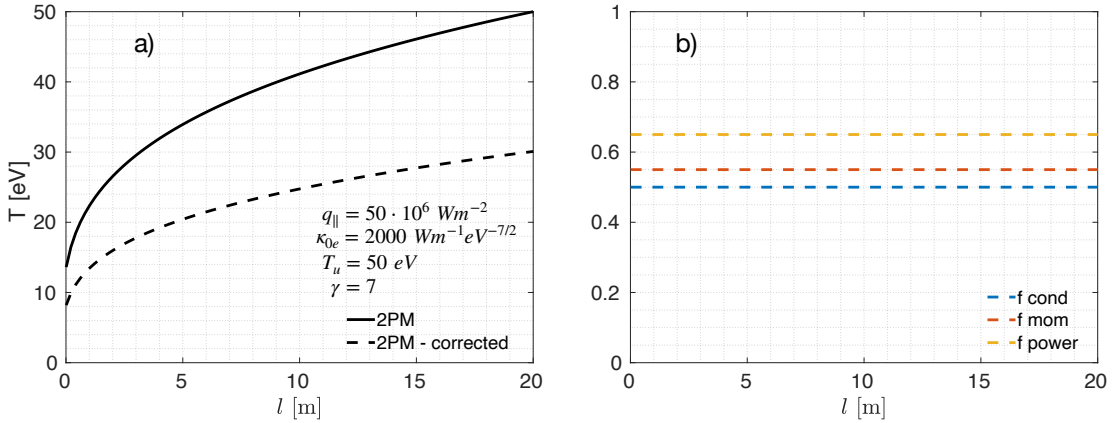
Figure 1.7: Panel a) plots the temperature computed by the 2PM. Here the symbol l indicates the distance from the target, considered as a variable as opposed to the choice of a fixed parameter L in the model. The solid lines are traced using equation 1.12, while the dashed line refers to equation 1.22, using the correction factors as plotted in panel b). It should be noted that the correction factors are *not* necessarily flat, but rather they can have a complex dependency on T_e and n_e, not shown here for simplicity's sake.

These correction factors mostly affect T_t and n_t. By solving the new system of equations, we

find that [49]

$$T_t \propto \frac{(1 - f_{power})^2}{(1 - f_{mom})^2 (1 - f_{conv})^{4/7}} \qquad\qquad n_t \propto \frac{(1 - f_{mom})^3 (1 - f_{conv})^{6/7}}{(1 - f_{power})^2} \qquad (1.23)$$

Volumetric power losses strongly decrease T_t, but both momentum losses and convection counteract this effect (remember that all f_{power}, f_{mom} and $f_{cond} < 1$). The opposite is found for n_t, which is strongly reduced by momentum losses but counteracted by the volumetric power losses. The balance here is made more complicated by the n, T dependence of the momentum and power loss mechanisms driven by the involved atomic/molecular processes, such as excitation, ionisation, recombination and charge exchange. Lastly, also Γ_t is affected by these corrections through the more accurate evaluation of T_t and $q_\parallel$. Equation 1.19 can be rewritten, highlighting the dependence on the loss factors, as [49]

$$\Gamma_t \propto \frac{(1 - f_{mom})^2 (1 - f_{conv})^{4/7}}{1 - f_{power}} \qquad (1.24)$$

In summary, the 2PM indicates two main mechanisms to reduce the target temperature: operating at high density - i.e. high n_u - and introducing significant volumetric power losses - i.e. through radiation - are beneficial in lowering T_t, but lead to an increase of the particle fluxes at the target. This quantity can be reduced by including momentum losses and, with a minor impact, by introducing heat convection in the model. Indeed, a combination of *all* the loss factors is needed to attain the simultaneous decrease of T_t, $q_\parallel$ and Γ_t. When this is reached, the divertor is said to enter the regime of *divertor detachment*, presented in the next paragraph and extensively studied in this thesis. The need for all the loss factors is made explicit in further publications by P. Stangeby (2020) [51, 52], where a *degree of detachment* is defined in terms f_{power} and f_{mom}. Over the years, many extensions to the 2PM have been proposed to describe regimes observed in Tokamaks SOL. These may include geometric considerations, as in Theiler et al. (2017) [53] or in M. Carpita et al. (in preparation) [54], where interactions of parallel flows with geometrical effects are taken into account. One more example of these extensions is presented in Siccinio et al. (2016) [55], where the SOL is split into two regions, one in which heat transport is dominated by conduction and another dominated by convection. In this work, the points used to describe the SOL become three instead of two. We will see in section 5.3.3 an application of this model to the data presented in this thesis.

In section 1.3.2, we will see how to drive a detachment regime and what is needed to act on the loss factors described by the 2PM.

The power/particle model

Two main perspectives can be used for detachment description, depending on the aspects one wants to highlight. The one used by Stangeby ([49, 51, 52]) and summarised in the previous chapter is able to capture many of the physics mechanisms of plasma detachment by

mainly considering momentum and power balance. An alternative point of view, presented by Lipschultz et al. (1999) [56] or by Krasheninnikov, Kukushkin, Pshenov (2022) [57], highlights instead the power and particle balance.

While the first approach leads to an introduction of loss factors introduction and to the notion of a degree of detachment, the second can provide more detailed insight into the particle physics underlying the detachment process. In particular, this interpretation leads to a picture of power limitation (or power *starvation*) illustrated in K. Verhaegh PhD thesis [58], limiting the ion source. One outcome of this approach is the notion that these ion sinks can lead to the Γ_t decrease by neutralising the ions before they reach the target. In this case, the ion target flux model prediction becomes

$$\Gamma_t = \left(\frac{q_{recl}}{E_{ion}} - \Gamma_r\right) \cdot \left(\frac{1}{1 + \gamma T_t / E_{ion}}\right) \tag{1.25}$$

where q_{recl} is the power entering the recycling region, defined as $q_{recl} = q_\parallel - q_{rad,imp}$, with $q_{rad,imp}$ the power radiated by the impurities in the same region; Γ_r is the ion sink given by volumetric recombination processes, such as electron-ion or molecular-activated recombination (see next paragraph for further information); and E_{ion} is the energy cost of ionisation.

In detached conditions, the electron temperature is much lower than the energy required to ionise neutral species ($T_t \ll E_{ion}$), leading to

$$\Gamma_t \approx \frac{q_{recl}}{E_{ion}} - \Gamma_r \tag{1.26}$$

By including power losses in the ionisation process, the model recovers the observations where an increase in upstream density is followed by a decrease in target heat flux.

The main difference between these approaches is that Stangeby's assumes that divertor parameters cannot impact the upstream pressure. This can be seen, for instance, from equation 1.16, where the small T_u exponent makes this quantity rather insensitive to the other parameters. Here, in order to get a reduction of the target pressure, volumetric momentum losses are required. In Krasheninnikov's approach, divertor conditions can impact the upstream pressure. Here, volumetric momentum losses are not a requirement to obtain detachment but, instead, an ingredient to drive pressure gradients from upstream to the target while keeping a high upstream pressure. Indeed, were these not present, a reduction in target pressure could result in an upstream pressure collapse, an undesirable event from the plasma confinement point of view.

Combining the two models within the frame of the 2PM is possible, and was performed by Verhaegh et al. (2019) [59]. Here, it is shown that the two approaches are identical and that target pressure losses are, in both descriptions, a critical requirement for detachment.

1.3.2 On the physics of detachment

Operating a diverted plasma at high density enables running experiments in a *high recycling regime* [60], where the ion target flux is dominated by divertor particle balance, e.g. the ion target flux is approximately given by the balance of divertor sources and sinks, while sources from outside the divertor region are negligible. Here, the divertor plasma is dense enough that the neutral hydrogenic particles resulting from recombination at the divertor plates can undergo several cycles of ionisation and recombination before being pumped away or absorbed at the walls. As equation 1.18 suggests, the target density can be higher than that of the plasma edge, localising the ionisation of the neutrals in this region. This causes a decrease in the plasma temperature but increases the plasma flux at the targets [45]. Diverted configurations in high recycling regimes enhance isotropic power dissipation through radiation, as the neutral particles and light impurities (e.g. C, N, Ar, Ne,...) are highly effective radiators when interacting with these rather cold and dense plasmas, driving the f_{power} factor higher through volumetric power losses. Indeed, recent studies focused on this property of diverted plasma, as in the works of Bernert et al. (2021) [61] and Lunt et al. (2023) [62], where a concentrated radiation region located in the X-point surroundings was capable of dissipating around 95% of the power crossing the separatrix to the SOL by nitrogen divertor injection and was found to be highly beneficial in terms of reducing the power fluxes through the divertor legs to the targets, that reached desired low target temperatures.

More generally, impurity radiation, be it extrinsic or originated by impurities released from the first wall, is a necessary ingredient to reach low temperatures in the target vicinity. Similar results can be obtained by different approaches, i.e. by pushing the core plasma density towards its limit, in experiments called *density ramps* (see [63–67]). By puffing gas into the divertor, the density increases in this region and in the core. By increasing n_u, T_t is decreased (i.e. as in equation 1.17), which in turn facilitates radiation power losses and a further reduced T_t. This thesis will probe the physics of this kind of discharge.

Considering the 2PM equations, the increase in the f_{power} factor alone, characteristic of the high recycling regime, leads to a decrease of the kinetic heat loading to the target $q_\parallel$ but is insufficient to reduce Γ_t (see, for instance, equation 1.24). It is, therefore, necessary to go a step further, introducing other mechanisms of momentum losses, transitioning the divertor into a *detached* regime that, from this point of view, can be considered as an extension of the high recycling regime at higher n_u and lower T_t. Here, the low T_t, driven by volumetric power losses, triggers divertor conditions where power, particle and momentum balance are all affected via inter-dependent loss factors f_{power}, f_{cond} and f_{mom}.

The atomic and molecular processes occurring in a divertor evolving from a high-recycling towards a detached regime are well described in K. Verhaegh et al. (2021, 2023) [68, 69], and illustrated in the cartoon of figure 1.8

In the high-recycling regime, radiation and ionisation of recycled neutrals are the main mechanisms for an increase in f_{power}. We note that ionisation is not sufficient to decrease the power
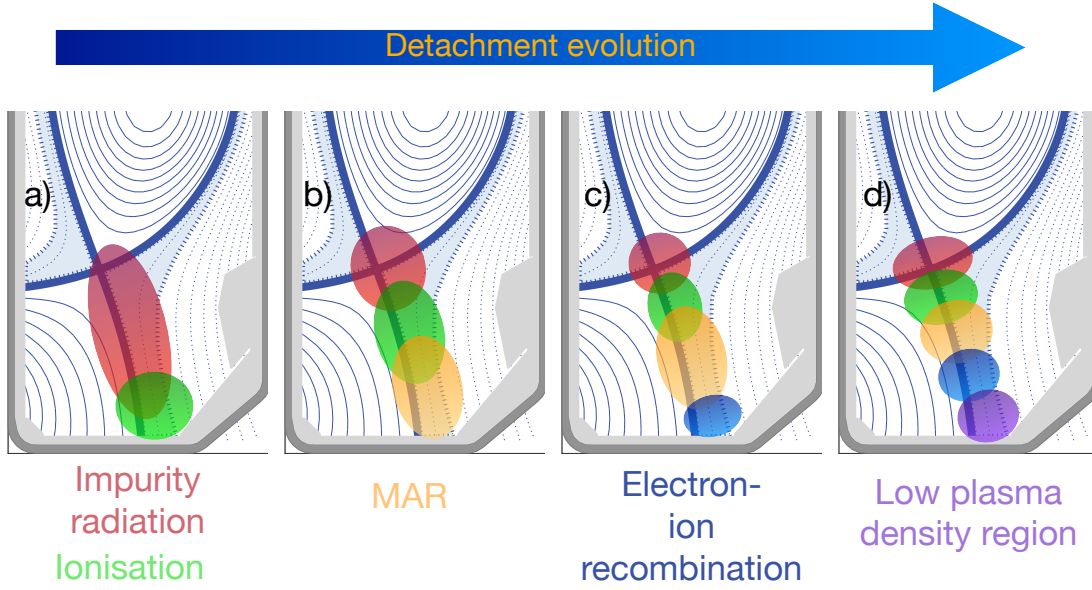
Figure 1.8: Processes involved in divertor detachment evolution, cartoon adapted from [70] to the TCV geometry.

loads at the target *per se*, as the ionisation energy spent by the electrons remains *stored* in the ion as potential energy and is released at the target where the ions recombine. However, as density increases across the discharge, ionisation results in increased electron energy losses with a consequent decrease of T_t, until the electron temperature becomes too low and ionisation can no longer occur. At this stage, the divertor enters a regime of *power limitation*, or *power starvation*, described in K. Verhaegh's PhD thesis [58], where the heat fluxes reaching the recycling region are no longer sufficient for ionisation of the neutral particles. This power reduction leads to a decrease in the particle source, observed by a saturation of the particle flux at the target with the increasing density.

The reduced electron temperature reached at this stage now favours different atomic and molecular reactions affecting f_{mom}. One example is given by charge exchange recombination reactions, where a *hot* ion reacts with a *cold* neutral atom, resulting in a *cold* ion and *hot* atom. This reaction effectively reduces the momentum in the ion's original flux tube, as part of it is carried by the neutral atom away from the strike point.

In Stangeby's description of detachment, another example of reaction contributing to a minor increase of f_{mom} can be represented by the molecular assisted recombination (MAR), whose importance is explained in K. Verhaegh et al. (2021, 2023) [68, 69]. Here, a molecular ion, generated from dissociation of H_2 by interaction with an ion H^+, captures an electron, effectively

removing an ion and an electron from the flux tube:

$$
\begin{aligned}
H_2 + H^+ &\longrightarrow H_2^+ + H \\
H_2^+ + e^- &\longrightarrow H + H
\end{aligned}
\tag{1.27}
$$

This reaction leaves the resulting hydrogen atoms in excited atomic states, causing spectral line radiation. This can be measured by state-of-the-art spectroscopic analysis [71], which found that the MAR reaction becomes significant for $T_e \approx 5$ eV [69], i.e. after power starvation becomes significant but before electron-ion recombination (EIR) becomes important ($T_e < 1$ eV). Finally, across the density ramp, EIR represents the ultimate particle and momentum dissipation mechanism before the target, such that only a low plasma density remains, attaining the deepest stage of detachment, where all the quantities Γ_t, q_t and T_e were successfully reduced (see [70]). We note here that although these reactions do contribute to momentum losses, their principal impact is on the power/particle balance, as they represent ion sinks.

In figure 1.8, the high recycling regime is illustrated by panel a), where the radiation region in the divertor extends from the X-point until the point where T_e becomes insufficient - depending upon the species generating the main radiation losses. Lower target temperatures force this *radiation front* to retreat from the strike point towards the X-point, as illustrated by comparing panels a) and b). This phenomenon will be described in chapter 5. Similarly to the radiation front, the ionisation front is also observed to retreat towards the X-point as the divertor evolves towards a more detached regime (see figures 1.3a and b). The power reduction due to these processes generates, in the target direction, a region of low-temperature plasma where MAR can be significant, as illustrated by the yellow regions in panels b) and c), until eventually, the temperature is low enough that EIR processes increase strongly, further reducing particle fluxes to the target (panels c and d).

The third parameter appearing in the extended-2PM, f_{cond}, is also affected by these processes. A part of its dependence on the temperature is captured by the Spitzer-Härm conductivity in the heat conduction equation

$$
q_{\parallel,cond}(l) = -\kappa_{0e} T(l)^{5/2} \frac{dT(l)}{dl}
\tag{1.28}
$$

Here $\kappa_{0e} T(l)^{5/2}$ is the Spitzer-Härm conductivity, and l is a coordinate along the flux tube, as used in figure 1.7. Reducing the temperature along the flux tube can cause heat transport to be dominated by convection (flows), gradually surpassing conduction, i.e. reducing f_{cond} and increasing f_{conv}. When convection dominates, temperature gradients can no longer be sustained and further temperature reductions become more difficult to achieve, as presented in equation 1.23.

In conclusion, we have seen in this section that the atomic and molecular processes involved in divertor detachment increase all the loss factors within the 2PM, successfully driving down

T_t, Γ_t and $q_\parallel$, ensuring the safety of the machine walls. This regime is so promising that, at least for partial attainment [72], it is currently thought to be obligatory to manage the power and particle fluxes that will reach ITER's divertor targets and likely those of the following nuclear fusion reactors.

Significant advances were made over the last decade in exploring the effects of divertor geometry on detachment in so-called *alternative divertor configurations* [53, 54, 73–75], of increased plasma neutral interaction provided by neutral baffling [76, 77], together with plasma control advances [78, 79]. Significant progress was also made in the field of SOL simulations [80, 81], with tools under continual development that aim to predict how divertor heat flux will behave in fusion reactor conditions.

The power exhaust challenge, however, persists, and more profound knowledge of detachment physics is needed. In particular, diagnostic tools and techniques that assess the detachment state and provide insight into the underlying physical process are fundamental in evaluating the fidelity of available simulation codes, as reported, for example, by Wensing et al. (2020) [82] and De Oliveira et al. (2022) [83].

1.3.3 Relevance of this work

The main object of this thesis is the first of this kind measurement of several species ion and neutral temperatures, performed with a high-resolution plasma spectroscopy diagnostic as a function of distance from the target, following the evolution of the divertor from an attached towards a detached regime. The integration of these measurements with other diagnostics allows for a detailed characterisation of the entire outer leg, following its evolution from an attached towards a detaching scenario.

This thesis is structured as follows. In chapter 2, we give an overview of the plasma edge and divertor research studies carried out in TCV. The main diagnostics used in this thesis framework are described in detail, focusing on the Divertor Spectroscopy System hardware upgrade, which was a fundamental step for the development of the subsequent chapter.
Chapter 3 describes the physics underlying the spectral line-shape broadening measured by the Divertor Spectroscopy System and the analysis techniques used to deduce information on the ion and neutral species temperatures from their spectral lines shape.
Chapter 4 describes the experimental scenario where the data were recorded. We approach the detachment of the divertor leg by injecting deuterium into TCV's divertor chamber. This causes plasma density to increase across the discharge, observed by a ramp in the plasma core density. We also exploited TCV's signature flexibility to create a geometry where the outer divertor leg intersected the Thomson Scattering system line of sight across most of its length within the divertor volume to measure reference parameters for the divertor characterisation, i.e. T_e and n_e. The tomographic reconstruction of spectral lines emissivity, made available by the Multispectral Advanced Narrowband Tokamak Imaging System diagnostic, completed the picture by providing a 2-D poloidal map of the observed species emissivity along and across

the entire divertor legs during their evolution towards detachment.

Lastly, in chapter 5, we discuss the main results of these experiments. They address the observation of ion-electron thermalisation and the determination of a characteristic electron temperature commonly used as a proxy for divertor detachment attainment from *C III emission*. The evolution of the divertor regime is directly observed as a pressure drop along the leg and with a gradual disappearance of electron thermal conductivity in the far SOL across the density ramp. Temperature profiles along the flux tubes in the divertor leg are finally compared to those predicted by the 2PM, testing the model validity and tracking the detachment evolution by the estimations of f_{power}, f_{mom} and f_{cond}.

Even though a large part of the thesis focuses on the Divertor Spectroscopy System development and the description of its data, its interpretation would have been impossible without the organic integration of other plasma edge diagnostics. This work proves that when exploiting the strengths of each diagnostic, we can go further in describing the processes leading to divertor detachment, with each diagnostic providing an additional view of the problem. Here we tested the multi-diagnostic data against a simplified model for impurity transport in the divertor by including many of the experimental quantities described above. This integration provides the basis for a new advance when comparing divertor experimental data to plasma modelling efforts. If regularly applied, these techniques may be able to identify any physical processes not included in the simulation codes or reassess their relative importance, improving the diagnostic-model comparison and, eventually, contributing to the successful design and development of upcoming nuclear fusion reactors.

2 Plasma edge research and diagnostics at TCV

Plasma edge research at TCV, in recent years, focused on detachment physics, alternative divertor solutions and the role of turbulent transport in the SOL, combining state-of-the-art diagnostics with modelling. Detachment physics is studied by a wide range of diagnostics: wall-embedded Langmuir probes [84, 85], are used to measure target parameters, such as the particle flux, T_e and n_e at the divertor strike points; InfraRed cameras [86] can infer the heat flux deposited on the targets from measurements of the target temperature; a radiation camera [87], including a bolometry system, is used to measure the radiative power losses. It is possible to acquire 1D and 2D profiles of relevant plasma parameters in TCV divertor volume, with two sets of reciprocating Langmuir probes systems [88, 89] for measurements of T_e, n_e, V_{pl} and their fluctuations, or with the Multispectral Advanced Narrowband Tokamak Imaging System [90] for measurements of a selection of spectral lines emissivity. Electron temperature and density are also measured by a Thomson Scattering system [91] over a narrow region defined by its laser beams. Passive spectroscopy in the divertor region, performed by the Divertor Spectroscopy System [92] is usually added to this diagnostic bouquet for detachment studies. The information from the whole diagnostic ensemble is essential to understand the physics as no reliable interpretation is considered achievable from a single diagnostic.

The main diagnostics used in this thesis are presented in more detail in the following sections.

2.1   DSS - the Divertor Spectroscopy System

The Divertor Spectroscopy System provides spatially and temporally resolved measurements of divertor plasma spectra for the determination of various plasma parameters, such as n_e, T_e and T_i.

The Divertor Spectroscopy System, in this thesis referred to by its acronym DSS, is used at TCV over a broad range of scopes. In the next paragraph, we give a quick overview of the existing lines of research based on DSS analysis, since its installation on TCV to the present times.

The DSS provides time-resolved, line-integrated spectra of the divertor plasma simultaneously

across many lines of sight (LOSs). It provides spectroscopic information on naturally abundant elements, such as D, C, B, and O, and on injected impurity species, such as He, N, Ne, Ar, and Kr, using broadband medium spectral resolution spectroscopy. Since its installation during K. Verhaegh's PhD thesis (2018) [58], DSS measurements have been used in the determination of the electron temperature T_e using intensity ratios of deuterium Balmer transitions (see Verhaegh et al. (2019)[59]), providing quantitative estimations of reaction rates, as well as power and particle balance information within TCV's divertor region. More recent analysis techniques, described in Verhaegh et al. (2021) [71], investigate the strength of plasma-molecule interactions on the divertor detachment through DSS data (Verhaegh et al. (2021) [93]). These works also employed Stark broadening measurements of high-n deuterium Balmer lines, such as $D_{7 \to 2}$, for electron density n_e estimation. A new analysis procedure for the DSS Stark broadening measurements was recently implemented in the framework of N. Maaziz's Master thesis [94], following new simulations of Stark broadening of high-n Balmer transition for tokamak relevant plasma and B-field parameters (see Rosato et al. (2017) [95]). The resulting tables, combined with the hardware upgrade described in the next section, accounted for the effect of the magnetic field on the Stark broadening, reducing the uncertainty on the n_e estimation.

After a significant hardware upgrade performed during this thesis work and described in [92], ion temperature T_i measurements of impurity species, and of neutral deuterium, became accessible as part of the DSS observation toolkit. The hardware upgrade will be described in the following paragraphs, while the novel analysis techniques, developed for T_i measurements, are the main object of chapter 3.

2.1.1   DSS - Hardware upgrade

The DSS hardware upgrade included: I) replacing lens-based optics with a mirror system, II) installation of a triple fibre bundle array, III) polarisation-resolved measurements, and IV) the addition of two high-resolution spectrometers.

Figure 2.1 presents a schematic overview of the main upgraded diagnostic's hardware components, designed thanks to the invaluable collaboration of Y. Andrebe and H. Elaian. Following the light path from its emission in the TCV divertor to its collection on the detector - i.e. following the elements in figure 2.1 from left to right - we find the following sequence of hardware components constituting the DSS diagnostic.

The mirror assembly

The mirror-based collection optics is composed of four copper mirrors. Those indicated in figure 2.1 as M2, M3 and M4 are spherical mirrors, with their corresponding curvature radii shown in the sketch. M1, instead, is a toroidal mirror, with two curvature radii to correct for the astigmatism resulting from off-axis reflection from the spherical mirrors in the assembly.
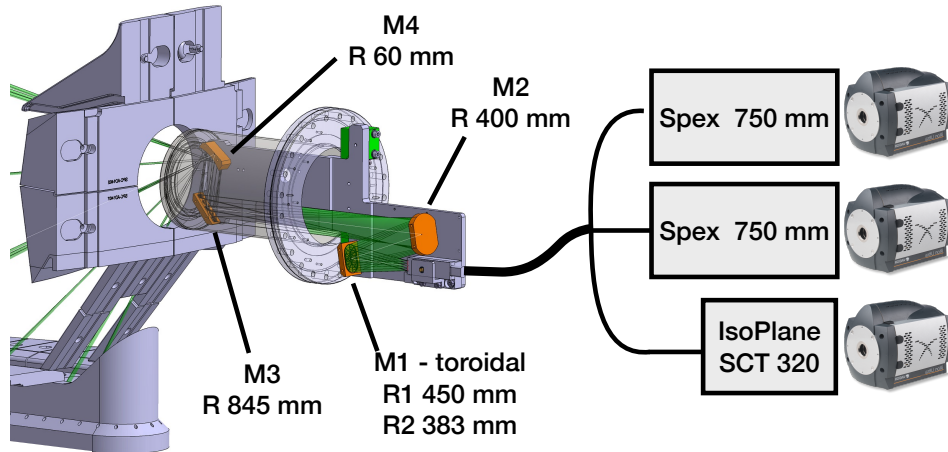
Figure 2.1: Cad drawing of the mirror relay optics and a schematic representation of the optical fibres, spectrometers and cameras (not to scale).

They are mounted on a metallic support held inside a cylindrical re-entrant port and observe the plasma through an N-BK7 window. They employ an aluminium reflector coated with a dielectric that protects them from oxidation and improves their reflection of broadband visible and UV light. The metallic support was designed to accommodate other diagnostics, previously hosted within that port, without obstructing their fields of view. A photodiode, two optical systems for the Ocean spectroscopy diagnostic and a microwave detector are also installed here.

Photos of the DSS collection optics set-up and its support are shown in figure 2.7 with different views: 2.7a and 2.7d are taken from the front, with M3 and M4 being the closest mirrors, while 2.7b is taken as from the side, indicating the ray-tracing trajectory of the light emitted by the plasma for a given LOS.

The position of the mirror assembly inside the re-entrant port and the small curvature radius of M4 allows for a wide field of view in the poloidal plane - here 67°. In figure 2.2, we compare the legacy DSS LOSs, shown in blue, that employed a lens-based collection optics situated at the exterior of the same port, with those from the upgraded mirror-based set-up, shown in orange. The new set of LOSs allows for spectral line measurements along the divertor legs over a wide range of divertor geometries, in most cases encompassing the entire leg length, from the configuration's X-point to the wall target. The wish to observe many of the divertor configurations that TCV can achieve was one of the main drivers for this hardware upgrade.

A second advantage provided by using mirrors is an absence of chromatic aberrations: N-BK7 lenses would generate different LOSs for each wavelength, as their refractive index is a function of λ. Achromatic lenses were considered in the design phase but were rejected due to their transmission cut-off for $\lambda < 370$ nm. Moreover, lenses with customised curvature radii, necessary to provide the LOSs sketched in 2.2b, would have been considerably more expensive
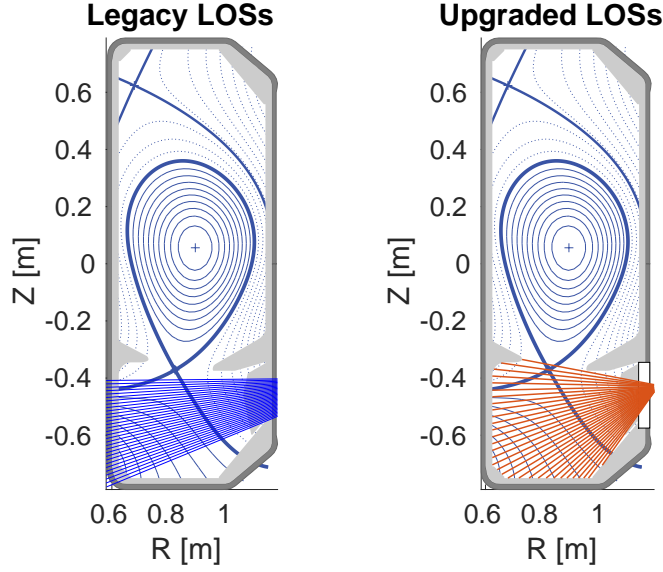
than the mirrors.

Figure 2.2: Comparison of legacy and upgraded LOSs, referenced to a typical lower single-null divertor studied in TCV.

The fibre bundle array

The LOSs presented in figure 2.2b result from the combination of the mirror system and the optical fibre bundle array. The sketch of the fibre bundle shown in figure 2.3 was designed in collaboration with CeramOptec GmbH.

As seen in figure 2.3A), the fibre bundle consists of three columns of 32 fibres each, held inside a rectangular aluminium ferrule. This is installed onto a metallic support next to mirror M2, as seen in figure 2.7c. The length of each fibre is 22 m [*] and they are installed under the TCV vessel, across two walls, to the spectrometers. Four meters before the fibres end at the spectrometers' locations, the three fibre columns are separated and directed to separate spectrometers, retaining the mirror end order. This side of the bundle is represented by the elements B, C and D of figure 2.3.

All fibres have a core diameter of 400 μm $\pm$5% of pure fused silica. This material was chosen as it provides high transmission in the UV range. The fibre cladding is of fluorine-doped fused silica, with a diameter of 440 μm $\pm$3%. Protective jackets of 130 μm thickness cover each fibre individually but are removed at their extremities to achieve the ferrule's packing. The fibres have a numerical aperture NA of 0.12$\pm$0.02, such that each fibre collects the light from a relatively narrow spatial region. This value of NA was identical to that designed in [58],

---

[*]Considering $3 \times 32 \times 22$ m, the entire optical fibre length is 2.1 km.

as it allows for minimising the stray light in the spectrometers and for the imaging of well-defined regions of interest at the IsoPlane spectrometer's focal plane, where EMCCD sensors are installed (see next paragraphs). In addition, the relatively low NA allows for employing small-size optical elements, such as the mirror system described above, that can fit inside the re-entrant port without obstructing the other diagnostics' field of view. More information on the properties of the fibres can be found in the Optran UV/ Optran WF technical sheet [96], while their main parameters are summarised in table 2.1.
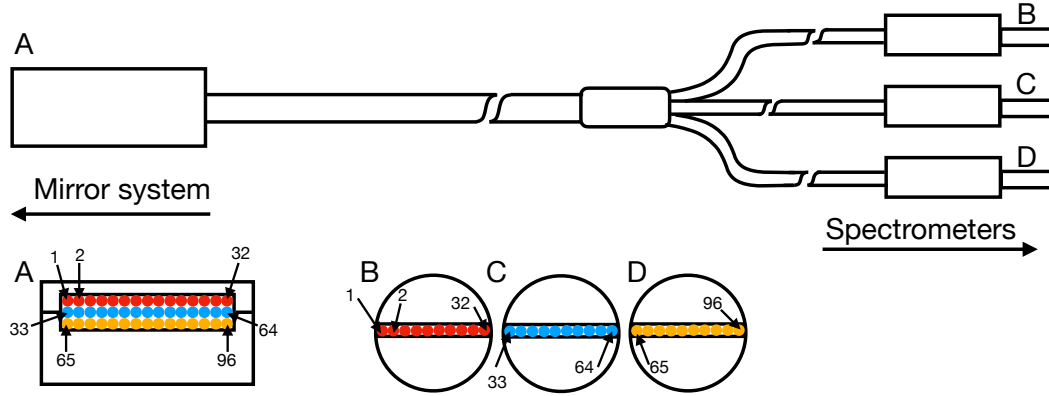

Figure 2.3: Simplified sketch of the triple fibre bundle with its side view drawn above and its front views below. This sketch is not to scale.

The fibres' setup and their alignment to the mirrors are such that, other than a slight angular difference in the toroidal plane, the three sets of LOSs are identical. After bundle separation into three branches, the fibres carry light to three independent spectrometers that, effectively, observe the same plasma volume. The simultaneous observation of three wavelength regions of the same plasma emission region, increasing the information acquired during a single discharge and limiting the need for diagnostic repeat discharges, was another motivation for the DSS hardware upgrade.

The light polariser

A wire grid light polariser was installed between mirror M1 and the fibre head (element A of figure 2.3) during a further part of this upgrade. The motivating intuition came from the preliminary results of the spectral line-shape analysis described in section 3.2. This significantly increased the DSS's sensitivity to Doppler broadening, by reducing the Zeeman splitting contribution to the line-shape due to TCV's magnetic field by selecting light characterised by a polarisation $\parallel \vec{B}$. Its effect will be described in detail in sections 3.1.3 and 3.2.2, comparing the observed spectral lines before and after the polariser installation. Although this innovation halved the total recorded signal intensity, it only slightly reduced the intensity of the central, analysed, π-component, signal.

The documentation on the polariser can be found in the instrument's datasheet [97], and its

implementation is visible in figure 2.7c.

The spectrometers

The legacy DSS system, at the start of this PhD, employed two IsoPlane SCT 320 spectrometers from Princeton Instruments. Detailed information can be found in the IsoPlane SCT 320 data sheet [98] and in K. Verhaegh's PhD thesis [58], where the spectrometer specifications and working principles are thoroughly described in chapter 5. The IsoPlane SCT 320 houses a triple turret grating, allowing a choice of grating parameters that determine the spectral resolution and the centre of the observed wavelength interval - before each plasma discharge. An 1800 l/mm groove grating provides the highest resolution available, and the grey dashed line in figure 2.4a plots its dispersion relation. The spectral resolution measured at $\lambda_{D7\rightarrow2}$ = 3969 Å, provided by the FWHM of the instrumental function in figure 2.4b, and employed for Stark broadening measurements on the $D_{7\rightarrow2}$ transition, is ≈0.8 Å.
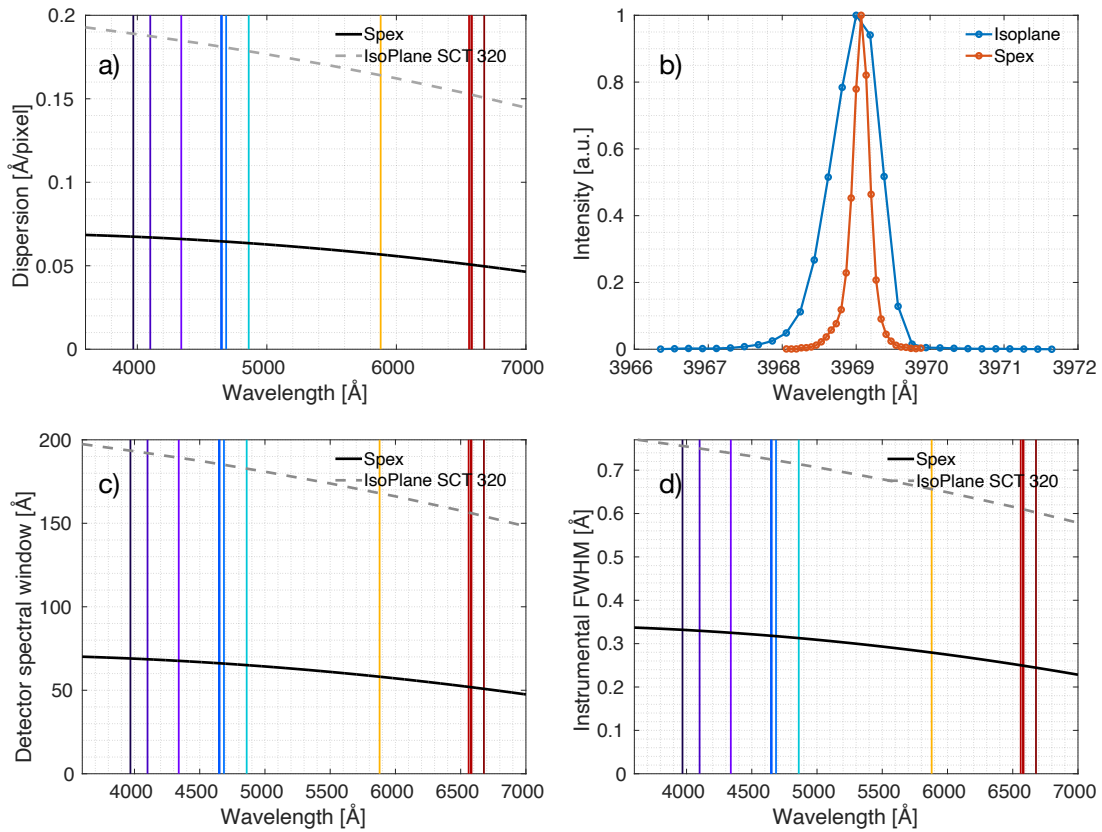

Figure 2.4: a): Comparison of IsoPlane and Spex dispersion relation. The higher dispersion is reflected on panel b), showing the difference in the instrumental functions associated with the $D_{7\rightarrow2}$ spectral line (see section 3.1.1 for more details). Panel c) plots the detector spectral window observable around each central wavelength; panel d) plots the spectral resolution, considered as the instrumental FWHM, as a function of wavelength.

With these settings, the DSS can cover a wavelength range of $\sim$ 19 nm (see figure 2.4c), ranging from a minimum of $\approx$350 nm to a maximum of $\approx$700 nm. This interval is wide enough to simultaneously monitor several deuterium and impurity spectral line intensities depending upon the central wavelength. The strengths of this instrument are characterised by a high flexibility in changing settings and relatively high light throughput, but primarily by aberration suppression of the grating angle, achieved by its Schmidt-Czerny-Turner design. The IsoPlane spectrometer is shown in figure 2.7e.

For the DSS hardware upgrade, only one IsoPlane spectrometer was retained. The two other fibre bundles were coupled to two Spex spectrometers, previously employed for high-resolution, but relatively low F-number, CXRS measurements presented in C. Marini's PhD thesis (2017) [99]. Unlike the compact IsoPlanes, the Spex spectrometers feature a Czerny-Turner design, with a 750 mm focal length -vs the IsoPlane's 320 mm- and a single holographic grating with 2400 l/mm. These provide a considerably higher dispersion and wavelength resolution: the Spex's dispersion relation is plotted by a black line in figure 2.4a, and an example instrumental function, at the $D_{7\to2}$ spectral line, in panel 2.4b, is over-drawn in red. Compared to the IsoPlane's instrumental function, the Spex's instrumental FWHM is $\approx$ 2.5$\times$ narrower across the visible spectrum, i.e. as in figure 2.4d. The highest spectral resolution is achieved at high wavelengths, where the Spex instrumental function's FWHM is $\approx$ 0.22 Å. This opened new avenues for the DSS: the line-shape analysis of the measured spectral lines, described in chapter 3.

If the Spex's spectral resolution is higher than the IsoPlane, it comes at the price of signal strength: Spex's aperture ratio -or F number- is $\approx$7.5, higher than the 4.6 provided by the IsoPlane, exacerbated by a lower grating reflection efficiency. Combined, this requires a longer integration time when operating the Spex spectrometer to obtain sufficient signal-to-noise ratios (SNR). For instance, the signal from weak spectral lines, such as $D_{7\to2}$, has to be integrated over a $\sim$ 3$\times$ longer integration time -e.g. $\gtrsim$30 ms, and high electron multiplication gains (see next paragraph) i.e. 30$\times$ have to be applied. On the other hand, other bright lines (e.g. $D_{3\to2}$, $D_{4\to2}$ or a C III triplet at 4650 Å), that in the legacy setup required the use of 0.5 up to 2.0 neutral-density filters to avoid signal saturation, were observable using integration times of 6-15 ms, depending on the plasma discharge parameters.

The cameras

A detailed description of the camera's specification is found online in the Andor iXon Ultra manual [103], in the user guide to software development kit [104] and in F. Bagnato's PhD thesis [105], with whom I shared the task of maintaining and updating the camera acquisition and control software, that is not repeated herein, for brevity.

A cooled EMCCD camera -manufactured by Andor, model iXon Ultra 888- is installed at each spectrometer's focal plane. The detection area of the cameras consists of 1024$\times$1024 pixels array, each of 13$\times$13 μm size, yielding a total image area of 13.3$\times$13.3 mm^2. The most
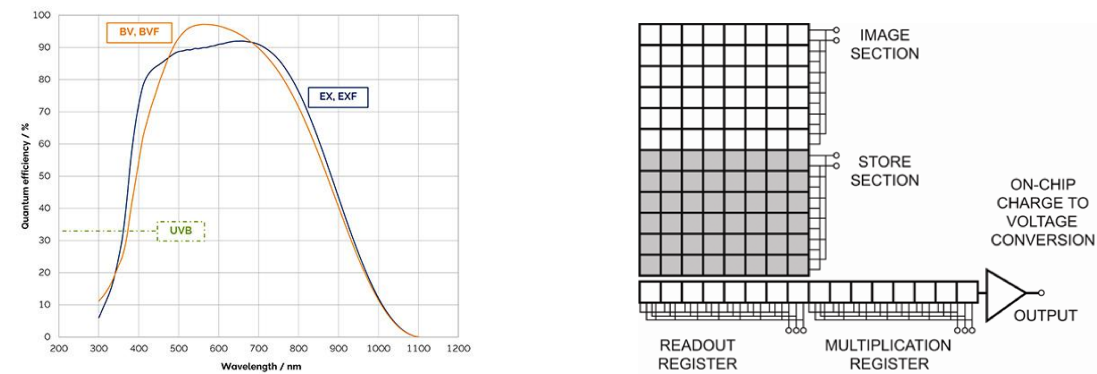
(a) Characterisation of the CCD's quantum efficiency. The yellow curve applies to the camera used in this application. Image source [100].

(b) Sketch of the EMCCD sensor structure, highlighting the image and the storage sections. Image source [101].
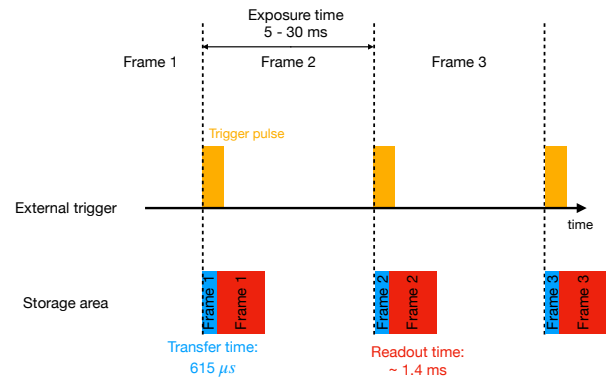
(c) Simplified acquisition cycle, not to scale. Image adapted from [102].

Figure 2.5: Illustrations of some Andor iXon Ultra properties.

important camera features for our application are the following:

- *Back-illuminated sensor* with >80% quantum efficiency in the 450-700 nm wavelength range relevant for DSS operations, drawn in figure 2.5a.

- *Sensor cooling*, reducing the dark current to negligible levels. Even for our longest integration time - of ~30 ms - the dark current is $\ll 1\ e^-$/pixel/frame at the typically set temperature of $T_{sensor=} - 50\ °$C, and, therefore, negligible. The sensor can, in principle, be cooled down to $T_{sensor=} - 95\ °$C using water-assisted heat exchange. Water-assisted heat exchange is not required at this temperature, significantly facilitating the camera installation and operation[†].

- *Fast frame transfer*: the CCD consists in two equal adjacent 2D pixel arrays, displayed in figure 2.5b. One is exposed to the light, called *image section*, while the other, called *storage section*, is masked to visible light. At the end of the exposure time, the photo-electrons generated in the image section are transferred to the storage section, and then the readout process starts. At the same time, the image section is ready for a new exposure. The frame transfer allows for fast acquisition without compromising the light collection efficiency and for increasing the readout frequency -but, therefore, also the noise associated with this process. In our application, we chose to operate at the fastest frame transfer speed, of 0.6 μs per row, which results in a total $1024 \times 0.6 = 615\ \mu$s frame transfer time. The typical -simplified- acquisition sequence is illustrated in figure 2.5c.

- *Electron multiplication*: this feature, the 'EM' in EMCCD, is applied before the charge-to-voltage conversion. Besides the readout register, the camera sensor is also equipped with a multiplication register, indicated in figure 2.5b. Here the photo-electrons of each pixel (or each binned pixel) are multiplied by a predefined factor by an impact ionisation process during their passage through the multiplication register. The advantage of using electron multiplication is an increased signal-to-read-out noise ratio since the signal is amplified, but the readout noise is unaffected. It should be noted that if the low SNR origin is from the photon statistics, the SNR cannot be improved by electron multiplication, as signal and shot noise would ideally be equally amplified, although, in practice, the EM process generates some additional noise.

- *Sensor binning:* it is possible to bin the sensor image rows to maximise the acquisition rate and reduce the readout noise. Since at the spectrometer's entrance slit we have a linear array of fibres, each of whose diameter corresponding to ~30 pixels at the focal plane (see table 2.1 at the end of this section), the image of each fibre on the sensor occupies ~30 pixels in the vertical direction, i.e. parallel to the fibre array direction, as shown in figure 2.6. Rows corresponding to the same fibre contain identical spectroscopic information and, therefore, their photo-electrons can be summed in the readout register and read as a single row, minimising the readout time and noise, always assuming the fibres images are perfectly vertically aligned.
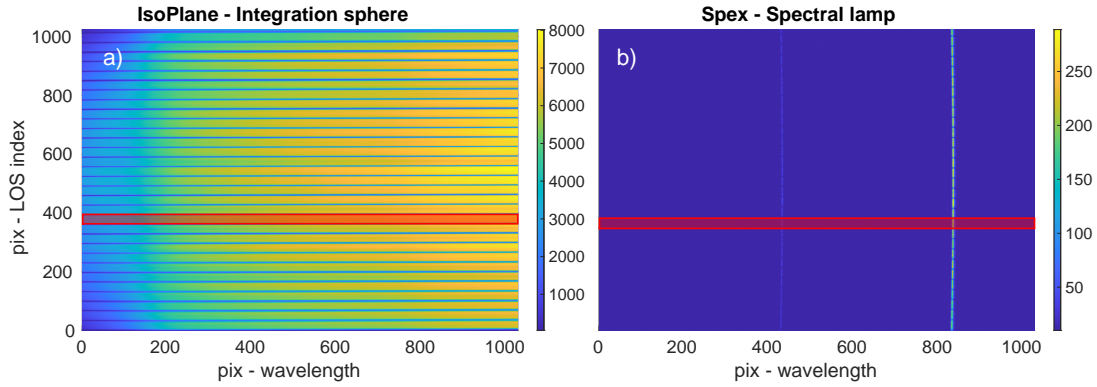

[†]Especially during pandemics.

Figure 2.6: Full-frame figures of the EMCCD sensors acquired during calibrations with the red boxes highlighting two ROIs -or *tracks*- as a reference, each corresponding to the region illuminated by a single fibre. a) Image of the integration sphere as recorded by the camera installed onto the IsoPlane spectrometer, in the range of 667-729 nm; b) Image of two Xe spectral lines at 469 and 473 nm, generated by a calibration spectral lamp, acquired by the camera installed onto one of the Spex spectrometers.

- *A large sensor area*, relative to other EMCCD models, allows maximising both the observed spectral range width and the LOS×fibre size product.

- *High dynamic range* allows for a simultaneous recording of very low and very bright spectral lines signal. For the typical camera settings i.e. readout rate 30 MHz, and pre-amplifier gain #2, the dynamic range is ~ 3000.

| Mirrors		Optical Fibres	
Surface polish [μm]	0.007 Ra	Wavelength	190-1200 nm
Coating	Alu UV SW	NA	0.12 ± 0.02
	175/Sw190	Core diameter	400 μm
Refl. at 370.0 nm	91.7 %	Transmission at 364.5 nm	~75.2 %
Refl. at 486.0 nm	92.4 %	Transmission at 486.0 nm	~90.2 %
		Total length	22 m
SPEX		IsoPlane	
Grating	2400 l/mm	Grating	1800 l/mm
F#	~ 7.5	F#	~ 4.6
Focal length	750 mm	Focal length	320 mm
Spectral coverage	70 Å	Spectral coverage	190 Å
Dispersion	$\approx$0.05-0.07 Å/pix	Dispersion	$\approx$0.15-0.20 Å/pix
Andor iXon Ultra		Resolution	
N pixels	1024x1024	Spatial resolution (vertical)	~ 1 cm
Pixels size	13×13 μm^2	Temporal resolution	5-30 ms
EM gain	2 - 100×	Spectral resolution	~ 0.20 Å
CCD detection range	3000-10000 Å	Spectral range of interest	3600 - 7000Å
Vertical shift speed	0.6 μs		
Horizontal shift rate	30 MHz		
Frame transfer	~615 μs		
Readout time	~1.4 ms		

Table 2.1: Standard DSS specification
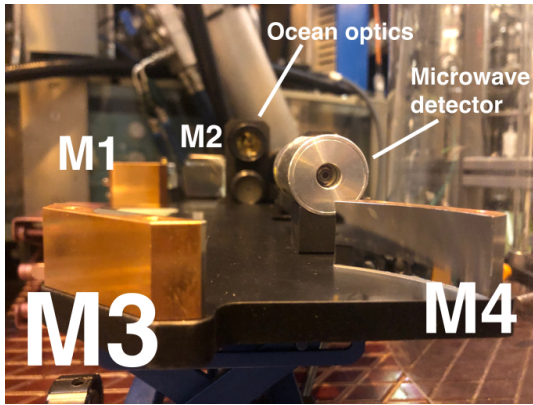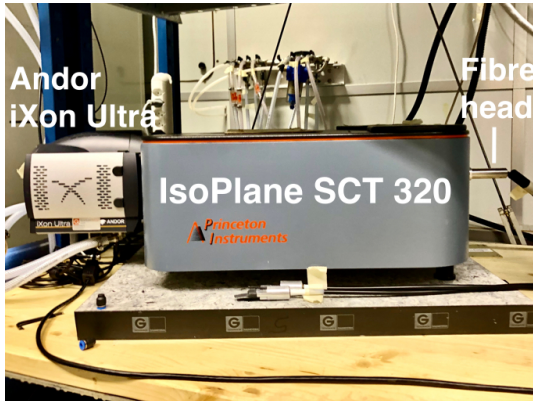
(a) Mirror assembly - front view.
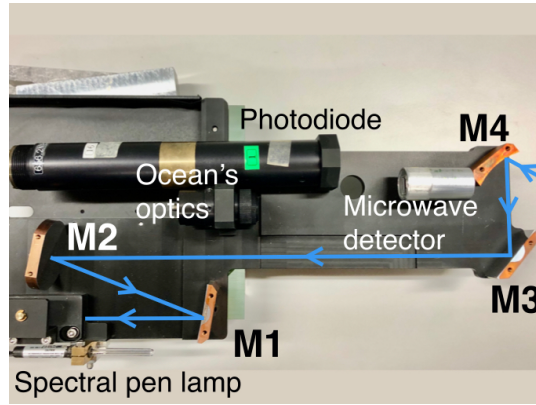
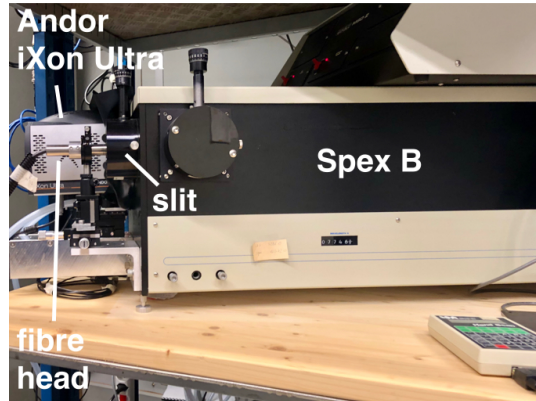(b) Mirror assembly - side view.
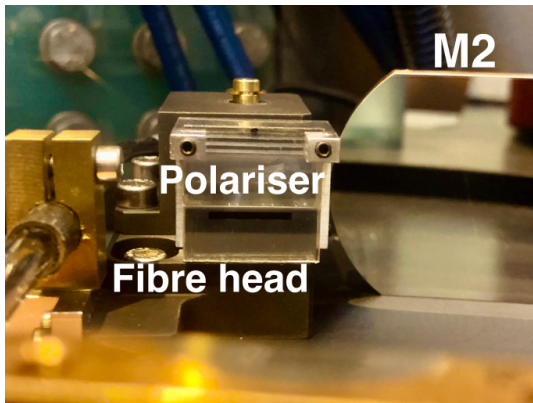
(c) Details of fibres head and polariser.
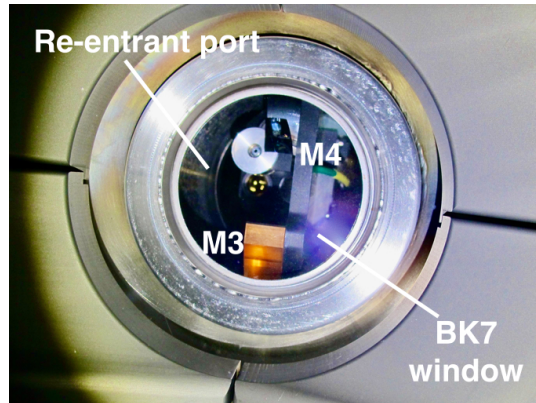
(d) View from inside TCV.

(e) Coupling to IsoPlane spectrometer.

(f) Coupling to SPEX spectrometer.

Figure 2.7: Photos of DSS hardware elements.

2.2   TS - the divertor Thomson Scattering system

The Thomson Scattering extension in the divertor region is able to measure T_e down to 0.6 eV for n_e down to $1.5 \cdot 10^{19}$ m^{-3} when its view lines intersect the divertor leg. The combination of the signal from its three lasers is used to compose radial profiles of T_e and n_e.

The TCV Thomson Scattering system, in this work referred to as TS, is the reference diagnostic for the study of T_e and n_e spatial profiles. These are measured along three, almost co-linear, vertical Q-switch Nd:YAG laser beams, crossing TCV poloidal cross-section at R= 0.9 m. The lasers deliver pulses of ≈1.5 J energy within 10 ns, at a wavelength of $\lambda = 1064$ nm. As its name suggests, this diagnostic exploits the Thomson scattering of the lasers' photons on the unbounded electrons in the plasma. The electrons' velocity distribution affects the distribution of the scattered light spectrum due to a Doppler effect, whose FWHM is proportional to $\sqrt{T_e}$ under the assumption that the total scattered light intensity is proportional to n_e.

Three wide-angle camera lenses collect the cross-beam scattered light and focus it on 117 chords, coupled to optical fibres, each observing a different vertical portion of the laser beams, defining *observation* or *probing* volumes. The covered region is between $Z = -0.692$ m to $Z = 0.536$ m, with several values of spatial resolution along the beam length. The fibres convey the scattered light to the filter polychromators, each equipped with up to five spectral channels, that are chosen to cover the expected T_e range in the observed region. The measurement of signal ratios from spectral channels with sufficient signal-to-noise ratio is used to estimate the 2nd moment of the Gaussian distribution describing the electron temperature, as in figure 2.8. These polychromators are optimised to measure T_e across four orders of magnitude, between 0.6 eV and 20 keV.
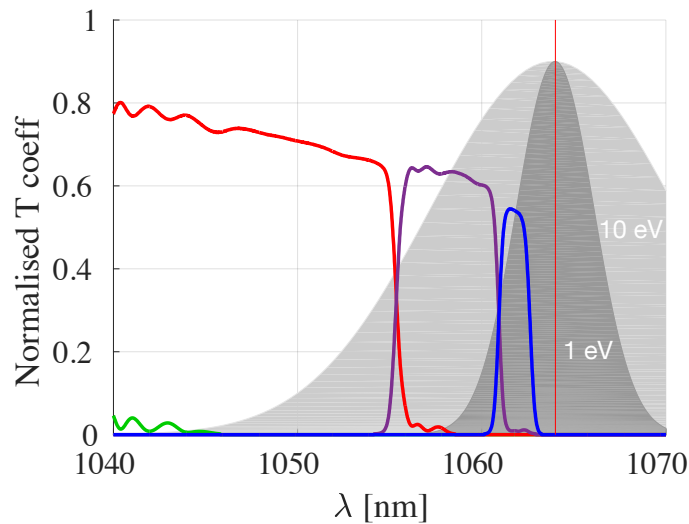

Figure 2.8: The green, red, purple and blue lines indicate the polychromators' transmission curves, while the two grey Gaussians indicate the scattered light spectral intensity distribution for plasma temperatures of 10 and 1 eV. Image source: P. Blanchard et al. (2019) [91].

An extension of TS in the TCV divertor region was implemented in 2019 - described in P. Blanchard et al. (2019) [91] - to study the divertor plasmas, focusing on alternative divertor configurations. This upgrade added twenty more channels, extending the spatial coverage in the divertor region. The corresponding filter polychromators of the divertor TS channels were optimised to low T_e values, allowing measurements of $T_e \approx 0.6$ eV. The new TS LOSs and their corresponding probing locations are illustrated in red in figure 2.9.
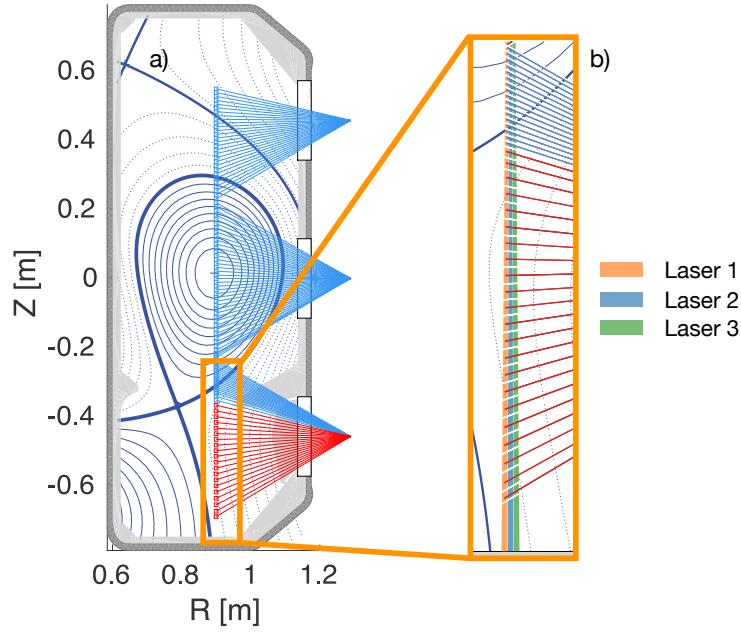

Figure 2.9: Panel a) shows the TS lines of sight and probing volumes in the TCV poloidal cross-section. The divertor extension described in [91] is illustrated in red. In panel b), a close-up of the divertor system, with the three laser beams and the corresponding probing volumes illustrated in orange, blue and green. Courtesy of B. Vincent.

The measurement of n_e requires an absolute calibration of the system, usually performed after TCV openings using Raman scattering on N_2. In dedicated, limited, calibration discharges, the so-called *yo-yo* discharges, the line-integrated density is benchmarked against that measured by TCV's fourteen-channel Far Infra-Red interferometer (FIR). We will see in section 4.1 how these two diagnostics can indicate different values for line-averaged density (noted as nel) due to some inclusion of divertor plasma in the FIR nel for the geometry chosen in the presented experiments. Conversely, TS measures this contribution separately, providing measurements accounting for the core density alone. Indeed, one of the main differences between TS and FIR is the crossed-beam nature of the former, opposed to the beam-integrated measurements of the latter.

Two more properties should be noted to facilitate understanding of the following chapters, related to the TS spatial and temporal resolution. First, we mentioned that the three high-power Nd:YAG lasers are *almost* co-linear: the slight misalignment of these elements in the poloidal plane is illustrated in the divertor TS detail of figure 2.9b), where it is shown that the

three lasers do not overlap within the divertor region. The probed volumes indicated in figure 2.9b by the orange, blue and green quadrilaterals are well characterised, with their position in the poloidal plane - and thus their distance from the plasma flux surfaces- well known.

It is possible, in principle, to fire the lasers simultaneously to maximise the detection SNR, effectively summing the scattered light originated by all three probing volumes observed by each TS LOS. This approach is recommended when operating at low plasma densities but is not necessary in the scenario used in this thesis work, described in section 4.1. Here, instead, we exploit the spatial separation of the lasers, collecting the signal originating from three different radial locations within the divertor region observed by each TS LOS by firing each laser, separated in time. Two different approaches are possible when choosing this acquisition mode, depending on a pre-defined inter-laser time. Indeed, although the laser pulse length is of $\Delta t \approx 10$ ns, each laser requires 50 ms before being able to fire again. For instance, one could increase the TS repetition rate to an effective 60 Hz with equally spaced laser pulses. The opposite approach, exploited in the experiments described in section 4.1, minimises the inter-laser time by keeping the laser triggering separate - i.e. not simultaneous, effectively measuring three different radial locations in the divertor leg. The three lasers are triggered in bursts with a 1ms inter-pulse delay, that samples the plasma every 50 ms. In this independent laser triggering acquisition mode, also referred to as *burst mode*, the 1 ms inter-laser separation is the shortest allowed time to complete a laser pulse signal and background acquisition. The burst mode tracks the longer time scale dynamics driving detachment of the divertor leg, observing significant variations from one burst to the next, but is blind inter-burst dynamics. These two properties are used to obtain detailed radial profiles of T_e and n_e across the divertor SOL.

2.2.1 Treatment of uncertainties

The TS uncertainty on T_e is calculated in the following way. First, a background signal is acquired ≈ 200 μs after each laser pulse. The signal-to-noise ratio, SNR, with respect to the active signal acquired during the laser pulse, is calculated for each polychromator channel using the background fluctuations acquired over the time interval around the measurement. This time window can depend on the laser firing mode. T_e is estimated by computing the signal ratios of several spectral channels for which the SNR is sufficiently high. A signal uncertainty is calculated as $\sigma_I = 2 \cdot \sqrt{(5.5\%)^2 + SNR^2} \cdot I$, where I is the TS signal intensity, and the factor 2 is included to account for the 95% confidence interval in the estimated value. The factor 5.5% indicates the minimum value of signal uncertainty provided by the system. Ratios including $\pm \sigma_I$ are also computed, providing the expected upper and lower limits of the ratio. An estimation of T_e for each of the available signal ratio is obtained using calibration curves computed within the hypothesis of a Maxwell-Boltzmann electron velocity distribution function. The final output for the TS T_e is given by the weighted average computed with all the ratios, weighted inversely to their uncertainties.

The estimated n_e varies linearly with the signal level collected by each channel. The n_e estimates from Thomson scattering are considered reliable; however, one must note that

TCV's Thomson scattering diagnostic is calibrated using the Raman scattering signal on N_2, for which the absolute scattering cross-section is only known with an uncertainty of 8%. This error will, however, only affect the absolute scaling, not channel ratios.

2.3 MANTIS - the Multispectral Advanced Narrowbad Tokamak Imaging System

MANTIS employs a single pupil and spectrally filtered camera images to generate tomographic inversions of up to ten spectral lines in the TCV poloidal plane. Their emissivity profiles are put in relation with the T_e and n_e profiles obtained from TS.
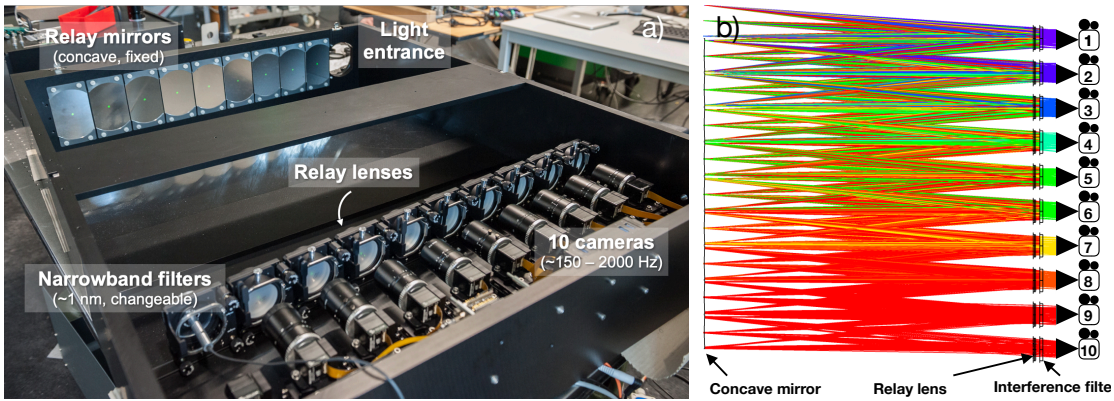

Figure 2.10: a) MANTIS cavity and relay optics, courtesy of A. Perek. b) ray tracing in the MANTIS cavity, with rays' colour corresponding to their wavelength. Image source: [90].

The Multispectral Advanced Narrowband Tokamak Imaging System, known as MANTIS, hardware description can be found in [90], and its main components are shown in figure 2.10a). MANTIS was designed in collaboration between MIT, DIFFER and EPFL, where it is now installed on the TCV tokamak.

Visible radiation emitted by the plasma is relayed to the cavity entrance, where an image of the plasma is formed. The light travels from the first relay lens to a corresponding narrowband interference filter. The filter transmits the radiation within the ≈ 1 nm range to the first camera, recording that spectral wavelength of the complete image. The rest of the light is reflected by that filter, via a concave mirror, to the next relay lens and its interference filter. This process, illustrated in figure 2.10b), is repeated (ten times), enabling MANTIS to record simultaneous 2D images of ten spectral wavelength channels of the same initial image. Figure 2.11 illustrates three images recorded by the cameras filtered for spectral lines of C III, D_β and D_α for discharge #74213. Many tokamak and divertor features can be identified in these figures, where the viewing aperture is positioned near tangentially to the plasma's toroidal direction.
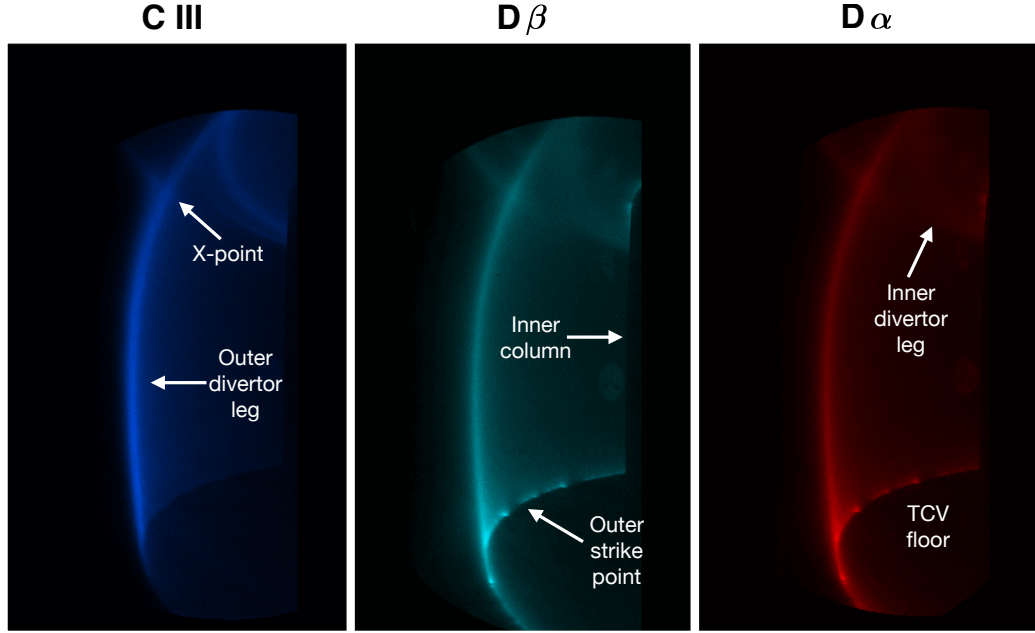
Figure 2.11: MANTIS raw images acquired for discharge #74213 at $t = 1$ s.

MANTIS images can be analysed in real-time, during a TCV plasma discharge, and some of the deduced parameters are made part of the shot's control algorithm. This was exploited in the works by T. Ravensbergen et al. (2021) [78] and more recently by J. Koenders et al. (2023) [106], where the radiation of impurity species, such as C III or N II, is used as an observer that the control algorithm employs to adjust the gas flux fuelling the plasma in TCV. By acting on the gas flux, one can control the distribution of such impurity radiation, e.g. the position of the radiation front - where the radiation intensity, along the divertor leg, extinguishes. We will see in section 5.2 that this is equivalent to controlling the position in the divertor leg of a characteristic temperature, effectively a proxy for divertor detachment, in a controlled manner.

But MANTIS can yield more information through tomographic inversions, that estimate poloidal-plane spectral line emissivity distributions. The present inversion algorithm is described by A. Perek et al. [107], and was used in A. Perek's PhD thesis (2022) [108] and by B. Linehan et al. (2023) [37] to extrapolate 2-D maps of T_e, n_e and n_0 in the plasma SOL, respectively exploiting known relationships between absolutely calibrated deuterium and/or neutral helium emissivity line ratios. This capability is key to this diagnostic, and it was extensively exploited in the experiments presented in this thesis, as will be described in chapters 4 and 5. In particular, we will reconstruct emissivity radial profiles of several spectral lines and relate them to the T_e and n_e radial profiles provided by the TS to build an organic model describing the divertor leg plasma state as it evolves from an attached towards a detached regime, as described in section 1.3.1.

2.4 Other diagnostics

While the data from DSS, TS, and MANTIS represent the core of this thesis, the information provided by other TCV edge diagnostics was fundamental to complete the description of the divertor state during its evolution towards a detached regime. In this section, we briefly present the main other diagnostics used to complement the analysis of the experiments presented in chapter 4 and 5.

2.4.1 LPs - the Langmuir Probes

Wall-embedded Langmuir probes (LPs) are routinely used to measure target plasma parameters and their profiles, such as the ion saturation current, target temperature and density. A detailed description of this diagnostic can be found in O. Février et al. (2018) [84] and in H. De Oliveira et al. (2019) [85]. TCV is equipped with 194 wall-embedded LPs, covering almost the complete poloidal cross-section, as illustrated in figure 2.12a.

LPs are the reference diagnostic to asses the attainment of divertor detachment, as they can estimate the target particle flux and those particles' temperature at the target, the two primary quantities we aim to minimise using this regime. The target particle flux is derived from measurements of the *ion saturation current*, obtained by biasing the probes to negative voltages, i.e. -100 V, and assuming that only ions can penetrate the sheath. The electron temperature can be inferred by characterising the $I(V)$ curve, obtained by sweeping the bias voltage between -120 to 80 V. For further details on the LPs analysis, refer to O. Février et al. (2018) [84].

2.4.2 Bolometry system

A radiation camera system (Radcam) combining foil bolometers, AXUV diodes and soft X-ray diodes was implemented in TCV in 2021. Details about this diagnostics are described in U. Sheikh et al. (2022) [87].

The bolometry system, in this thesis used for measuring the radiated power from the core and divertor region, consists of 120 lines of sight, displayed in figure 2.12b. The energy radiated from a region in TCV poloidal cross section is measured from the temperature change of a material that absorbs that radiation. The temperature of that material is, in turn, measured by the change in resistivity of a temperature-dependent electrical resistor, called *thermistor*, in thermal contact with the radiation absorber. Regions that strongly radiate can be determined by tomographic inversions of the bolometer array. For further details on the Radcam analysis, refer to U. Sheikh et al. (2022) [87].
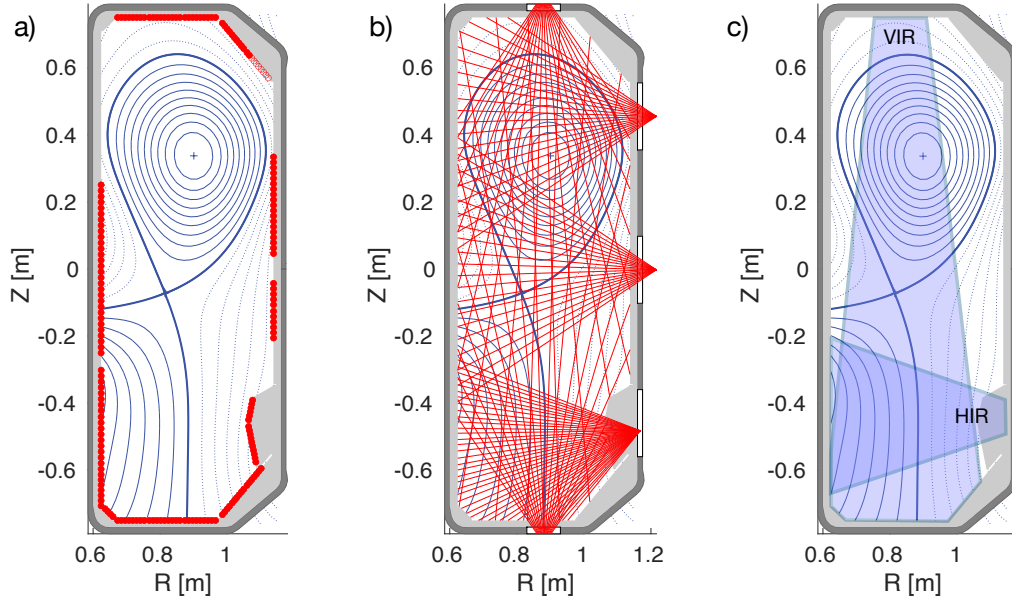
Figure 2.12: TCV poloidal cross sections illustrating in a) the location of wall-embedded Langmuir probes; in b) the bolometry system's lines of sight, and in panel c) the field of view of two infra-red thermography systems. For comparison, a magnetic equilibrium reconstructed by Liuqe [38] is also shown in the poloidal cross sections.

2.4.3   IR - Infra-Red thermography

TCV is equipped with three infrared thermography systems, used to measure the heat fluxes deposited on TCV's floor and onto the inner and outer divertor walls. In section 5.3, we will use data from the vertical system, whose field of view is illustrated in figure 2.12c indicated as *VIR*.

The infrared cameras measure the wall surface temperature by assuming a value of emissivity ε associated with the graphite tiles. This is then used to deduce the heat loads deposited at the targets by employing the THEODOR code, presented in J. Márki's PhD thesis [109]. Further insight into the infrared thermography analysis can be found in R. Maurizio's PhD thesis [86].

3 Line-shape broadening and data analysis

Section 3.1 presents an overview of the effects of the instrumental hardware, intrinsic atomic physics, and plasma parameters on the shape of observed spectral lines. Here the zoology of atomic transitions employed throughout this thesis work is also introduced. The data analysis process used to extract the ion temperature from the measured line-shapes is described in section 3.2, expanding that described in L. Martinelli et al. (2022) [92].

3.1   Line-shape broadening mechanisms

The wavelength of a spectral line is determined by the energy difference between the excited -or *upper-* and de-excited -or *lower-* levels that characterise the atomic transition. Indicating with E_u and E_l the energies associated with the upper and lower states, respectively, the characteristic angular frequency ω_0 and wavelength λ_0 of the transition are given by

$$\omega_0 = \frac{E_u - E_l}{\hbar}, \qquad \lambda_0 = \frac{hc}{(E_u - E_l) \cdot n_{\mathrm{medium}}} \tag{3.1}$$

where $\hbar = h/2\pi$ is the reduced Planck constant and n_{medium} is the refractive index of the medium through wich the photon is transmitted (e.g. $n_{\mathrm{air}} \simeq 1.0003$). However, the spectral line's measured frequency, or equivalently, its measured wavelength, cannot be monochromatic. Observed spectral lines are characterised by a frequency distribution in the vicinity of ω_0, called *broadening*, determined by multiple factors, such as the finite lifetime of the excited upper and lower levels, the emitter's surrounding environment (e.g. the presence of external electric or magnetic fields), the emitter's velocity projected along the observing LOS, and the transition structure, i.e. for multiplet transitions. By studying these frequency distributions, resulting in specific *line-shapes*, or *line-profiles*, we can learn about the emitter's velocity distribution and some properties of the surrounding plasma. Furthermore, even when the transition frequency can be considered monochromatic, the measured line-shape would be affected by instrumental effects, some of which are described in section 3.1.1.

In this section, we first present how DSS hardware affects the profiles, introducing characteris-

tic instrumental functions. We continue by illustrating how intrinsic atomic physics and the plasma surrounding the emitters affect the observed shape of the spectral lines. Examples of each individual broadening mechanism are illustrated for the deuterium $n = 7 \rightarrow n = 2$ (D_ε, or $D_{7\rightarrow2}$) and the ionised helium $n = 4 \rightarrow n = 3$ (He II) transitions, at $\lambda_{D\varepsilon} = 3968.99$ Å and $\lambda_{HeII} = 4865.8$ Å respectively. These are simulated for typical TCV divertor plasma parameters and compared to the DSS SPEX instrumental functions employed to measure each spectral line. This can be used to assess their contribution to the final line-shape.

3.1.1 Instrumental function

This broadening mechanism indicates the instrument response to an incoherent monochromatic source, and it is caused by the properties and settings of the spectrometers and cameras that constitute the DSS diagnostic.
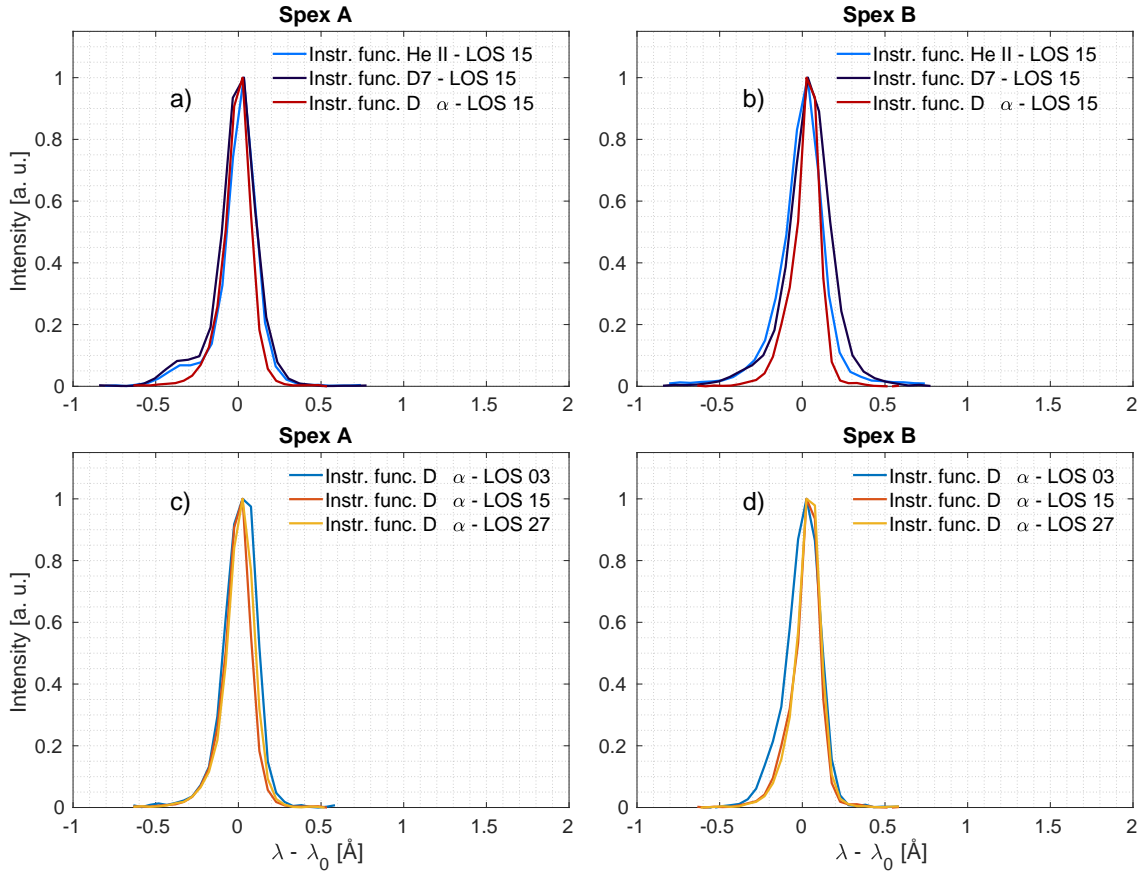

Figure 3.1: Instrumental functions of Spex A and B associated with different spectral lines and LOSs.

The parameters of the DSS components (i.e. spectrometers and cameras) that can affect the diagnostic instrumental function are numerous, i.e. the spectrometer entrance slit width,

the spectrometer optical elements performance, the detector pixel size and cross-talk, the electronic characteristics and the spectrometer's theoretical resolution limit, that, for the SPEX, is given by the Czerny-Turner mount. The images of the spectral lines on the EMCCD sensor vary with the grating angle and their 2D position on the sensor. Therefore, the instrumental functions associated with any spectral lines for a specific LOS are unique, preventing the use of a generalised shape (e.g., Gaussian) in the line-shape analysis described in section 3.2. While these variations can be challenging to simulate, due to the complexity of the optical system, they can be directly acquired experimentally and characterised.

To measure each instrumental function associated with a specific observation, we used pencil-style calibration spectral lamps [110] and set the spectrometer's grating angle to put their image on the same part of the detector where it would be observed during experiments. These lamps are used for measuring the hardware contribution to the line broadening alone, ruling out all the other field and plasma contributions (see sections 3.1.3, 3.1.4 and 3.1.5) as their emission comes from cold, low-density plasmas in the absence of magnetic field, making them ideal for this characterisation. Their natural broadening (see section 3.1.2) is also negligible with respect to the instrumental one so that these sources can be considered *monochromatic* except for their small fine structure. For example, the measurement of the instrumental function associated with the He II spectral line, illustrated in figure 3.1a and b in blue, used the emission of a Xe calibration lamp at $\lambda_{Xe} = 4671$ Å. The spectrometer grating angle settings were such to image the Xe line on the position of the He II line at $\lambda_{He\,II} = 4685.8$ Å (i.e. on the left-hand side of the EMCCD sensor). Apart from the integration time, which was $\approx 5 - 20\times$ longer to compensate for the low intensity of the lamp compared to the plasma, the EMCCD acquisition parameters were identical to those used during experiments. Similar procedures were used to characterise the instrumental functions associated with all the other spectral lines analysed in this thesis, employing Hg, Ne and Ar calibration spectral lamps. During these characterisations, conducted before each experimental campaign, the fibre head was homogeneously illuminated by the spectral pen lamp, conveying the light through an integrating sphere placed in front of mirror M4. This characterisation process allows for precise accounting of the instrumental broadening contribution to the observed line-shapes, reducing the uncertainty on the determination of the Doppler broadening component (see section 3.1.4) for the ion temperature estimations.

It is important to note that the broadening introduced by the instrumental function represents the narrowest detectable line-shape. Interpolation between pixels, provided sufficient photon statistics, is however possible, making the DSS sensitivity better than what is defined by the instrumental FWHM.

Figure 3.1 represents a collection of instrumental functions of both Spex A and Spex B spectrometers. Those illustrated in figures 3.1a and b are associated with He II, $D_{7\rightarrow2}$ and D_α. In standard experimental settings, D_α is imaged on the centre of the EMCCD sensor. He II is positioned on its far left to simultaneously measure other spectral lines of interest, such as a C III triplet and a N II spectral line. This difference in the horizontal position on the

detector surface causes slight but significant, variations in the instrumental functions that are characterised herein. One additional, and essential, difference between these functions comes from the dependence of the spectrometer dispersion d on the grating settings (see figure 2.4a). When calculated at $\lambda_{\text{He II}} = 4685.8$ Å, $d = 0.064$ [Å/pixel], while at $\lambda_{\text{D}\alpha} = 6561.01$ Å, $d = 0.050$ [Å/pixel]: this makes the instrumental function for the D_α transition narrower than that for He II when displayed as a function of wavelength. The D_α transition is, therefore, more sensitive to other broadening mechanisms.

The line-shapes of the Ne I transition at 6620 Å, shown in figures 3.1c and d, are all instrumental functions associated with D_α acquired for different DSS LOSs, i.e. at different vertical positions on the EMCCD. Due to a curved focal plane being imaged on a flat detector, the slit image is better focused on the spectrometer's optical axis and smears out when moving away. For this reason, the instrumental functions acquired on the EMCCD centre (i.e. associated with LOS 15) are characterised by a smaller FWHM than those acquired towards the edge of the sensor (e.g. LOS 3 or 27).

3.1.2 Natural broadening

This broadening mechanism is related to the finite lifetime of the transition's upper state.
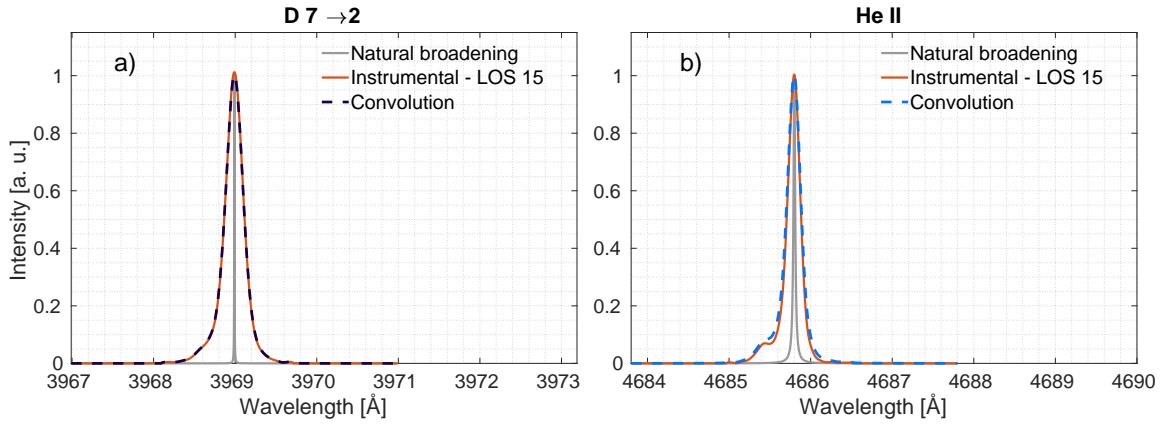
Figure 3.2: Natural broadening of $\text{D}_{7\to 2}$ (3.2a) and He II $n = 4 \to n = 3$ (3.2b) transitions, in grey, compared to the respective DSS SPEX instrumental functions, in red.

This section describes the natural broadening using a semi-classical picture of the atomic radiation process. A fully quantum treatment of this problem can be found in *The Quantum Theory of Radiation* by W. Heitler [111] chapter 18 and in *Principles of Plasma Spectroscopy* by H. Griem [112] chapter 2.7.

Considering a transition from a upper atomic state u to a lower atomic state l, their lifetimes τ

are given by

$$\tau_u = \frac{1}{\sum_{k<u} A(u \to k)} = \frac{1}{A(u \to)}, \qquad \tau_l = \frac{1}{\sum_{k<l} A(l \to k)} = \frac{1}{A(l \to)} \tag{3.2}$$

where $A(u \to k)$ and $A(l \to k)$ are called *Einstein coefficients*, representing the probability of spontaneous emission respectively from u and l towards a lower state k. The simplified wave-function of the electron undergoing the transition can be written as a superposition of u and l as

$$\psi = \alpha(t)\psi_u(\vec{r})e^{-i\omega_u t} + \beta(t)\psi_l(\vec{r})e^{-i\omega_l t} \tag{3.3}$$

where $\psi_u(\vec{r})$ and $\psi_l(\vec{r})$ are the eigen-functions of the u and l levels. The coefficients $\alpha(t)$ and $\beta(t)$ are related to the Einstein coefficient and can be expressed as

$$\alpha(t) = e^{-A(u\to)t}, \qquad \beta(t) \approx e^{-A(l\to)t} \tag{3.4}$$

Using equation 3.3, we can find the charge density probability, of which oscillatory term determines the properties of the radiation:

$$\begin{aligned} e|\psi|^2 &= \rho_e(t,\vec{r}) \\ &= \alpha^2(t)|\psi_u(\vec{r})|^2 + \beta^2(t)|\psi_l(\vec{r})|^2 + \alpha(t)\beta(t)\psi_u(\vec{r})\psi_l(\vec{r})\cos(\omega_0 t) \end{aligned} \tag{3.5}$$

where $\omega_0 = \omega_u - \omega_l$ is the characteristic frequency of the transition. The oscillatory contribution to equation 3.5 is represented by the term $\alpha(t)\beta(t)\psi_u(\vec{r})\psi_l(\vec{r})\cos(\omega_0 t)$ only. A damped oscillatory function gives the time dependence of the radiation electric field

$$E(t) \propto e^{i\omega_0 t} e^{-[A(u\to)+A(l\to)]t/2} \tag{3.6}$$

To observe the effect of the finite lifetime of the u and l states on the line-shape, we apply a Fourier transform to the time-dependent expression of $E(t)$ to find

$$\begin{aligned} \tilde{E}(\omega) &\propto \int_{-\infty}^{+\infty} \exp\left[-\left(\frac{[A(u\to)+A(l\to)]}{2} + i(\omega-\omega_0)\right)t\right] dt \\ &= -\frac{1}{[A(u\to)+A(l\to)]/2 + i(\omega-\omega_0)} \end{aligned} \tag{3.7}$$

The intensity $I(\omega)$, corresponding to what is measured experimentally, is proportional to $|\tilde{E}(\omega)|^2$, and given by

$$I(\omega) \propto |\tilde{E}(\omega)|^2 \propto \frac{1}{(\omega-\omega_0)^2 + 1/4\big(A(u\to)+A(l\to)\big)^2} \tag{3.8}$$

Therefore, the natural broadening of the line-shape exhibits a Lorentzian profile, with its FWHM given by $\Delta\omega_{\text{nat, FWHM}} = A(u\to) + A(l\to)$, or, in the wavelength units used throughout

the thesis,

$$\Delta\lambda_{\text{nat, FWHM}}[\text{Å}] = [A(u \rightarrow) + A(l \rightarrow)] \cdot \lambda_0^2[\text{Å}] \cdot 10^{-10}/(2\pi c) \tag{3.9}$$

Figure 3.2a and 3.2b illustrate the natural broadening, plotted in grey, of the $D_{7\rightarrow2}$ and He II transitions compared to their associated instrumental function, in red. A convolution of the two curves is shown with the dashed lines to simulate what the DSS would observe in the presence of natural broadening only. The natural broadening FWHM of $D_{7\rightarrow2}$ is $\Delta\lambda_{\text{nat, FWHM}} \approx 4 \cdot 10^{-3}$Å, while that for He II is $\Delta\lambda_{\text{nat, FWHM}} \approx 18 \cdot 10^{-3}$Å. In both cases, the natural broadening is negligible compared to the SPEX instrumental functions ($\Delta\lambda_{\text{instr, FWHM}} \approx 0.2$Å). Indeed, in figure 3.2, the convoluted curve is indistinguishable from the instrumental function. Natural broadening, thus, will not be referenced when discussing the analysis technique used to extract the ion temperature from the spectral line-shapes in section 3.2.

3.1.3 Zeeman splitting

This broadening mechanism is caused by the splitting of degenerate atomic energy levels in the presence of a magnetic field.

To calculate the energy splitting of the atomic levels in the presence of a magnetic field, it is often possible to express the Hamiltonian of the system as

$$\hat{H}_Z = \hat{H}_0 + \hat{H}_B \tag{3.10}$$

where $\hat{H}_0$ is the unperturbed Hamiltonian of the atomic system and $\hat{H}_B$ represents the interaction of the atomic system with the external magnetic field. $\hat{H}_B$ has the form

$$\begin{aligned}
\hat{H}_B &= \mu_B\left(\hat{\vec{L}} + g_S\hat{\vec{S}}\right) \cdot \vec{B} \\
&= \mu_B\left[B_x(\hat{L}_x + g_S\hat{S}_x) + B_y(\hat{L}_y + g_S\hat{S}_y) + B_z(\hat{L}_z + g_S\hat{S}_z)\right]
\end{aligned} \tag{3.11}$$

where $\mu_B = e\hbar/2m_e$ is the Bohr magneton, $\hat{\vec{L}}$ is the orbital angular momentum, $\hat{\vec{S}}$ the spin angular momentum and $g_S \approx 2$ is the gyromagnetic ratio of the electron's magnetic momentum to its spin angular momentum. The effect of the magnetic field is to split an atomic energy level characterised by a total angular momentum $\hat{\vec{J}} = \hat{\vec{L}} + \hat{\vec{S}}$, into $2j+1$ non-degenerate states. These energy sub-levels are characterised by the m_j quantum number, representing the projection of $\hat{\vec{J}}$ along the magnetic field direction.

Figure 3.4 represents an example of an energy diagram with Zeeman splitting for the C III 2s3p $^3P_2$ - 2s3s $^2S_1$ transition, yielding a simplified version of the splitting pattern illustrated in figure 3.15a. Here, the dashed arrow between the solid black lines represents the transition in the absence of magnetic fields. The red arrows show the transitions characterised by $m_{j,u} - m_{j,l} = 0$, while those in blue by $m_{j,u} - m_{j,l} = \pm 1$. The energy splitting, simplified in
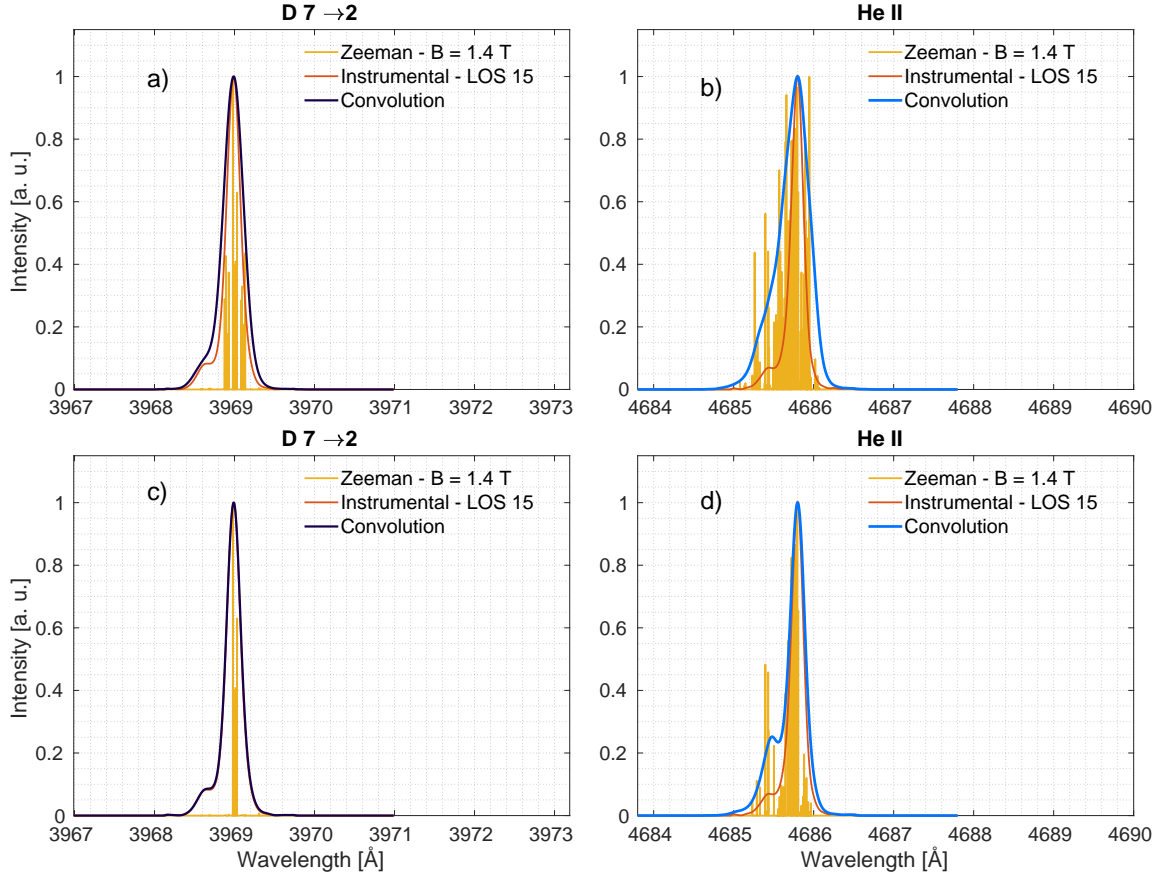
Figure 3.3: Zeeman splitting patterns, plotted in yellow, for the $D_{7\to2}$ (3.3a and 3.3c) and He II $n = 4 \to n = 3$ (3.3b and 3.3d) transitions, compared to the respective DSS SPEX instrumental functions, in red. Figures 3.3c and 3.3d are as in 3.3a and 3.3b respectively but after the installation of the linear light polariser in the optical chain.

this illustration, is approximated using a Landé factor, which is justified when the Zeeman interaction is much smaller than the spin-orbit interaction, yielding $\Delta E_u \approx \frac{3}{2} m_j \mu_B B$ and $\Delta E_l \approx 2 m_j \mu_B B$.

This approximation may be suitable for the illustrated C III transition but not for the He II transition studied throughout this thesis, where neither the low-field limit nor the high-field limit of Zeeman splitting, i.e. the Paschen-Back effect, can be employed. However, no approximation is used in this thesis to calculate the Zeeman splitting pattern affecting the shape of the spectral lines. Here, we follow this recipe:

1. We choose a basis for which the representation of the Hamiltonian $\hat{H}_0$ of equation 3.10 is diagonal, with the atomic levels energy taken from the NIST atomic database [113]. These atomic states are eigenvectors of the set of commuting operators $\{\hat{L}^2, \hat{S}^2, \hat{J}^2, \hat{J}_z\}$. The $\hat{\vec{L}}$ and $\hat{\vec{S}}$ operators used in the calculation of $\hat{H}_B$ are represented on the same basis.
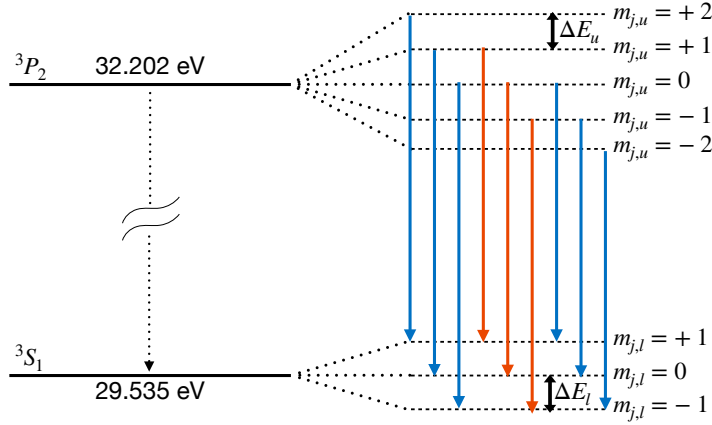
Figure 3.4: Diagram of the atomic energy splitting for the C III transition in an external magnetic field.

2. The diagonalisation of the Hamiltonian $\hat{H}_Z$ is numerically performed using Matlab software for both the upper ($\hat{H}_{Z,u}$) and lower ($\hat{H}_{Z,l}$) energy level that characterise the transition. $\hat{H}_{Z,u}$ and $\hat{H}_{Z,l}$ are given by:

$$\hat{H}_{Z,u} = \hat{H}_0 + \mu_B \left[B_x(\hat{L}_{x,u} + g_S \hat{S}_{x,u}) + B_y(\hat{L}_{y,u} + g_S \hat{S}_{y,u}) + B_z(\hat{L}_{z,u} + g_S \hat{S}_{z,u}) \right]$$
$$\hat{H}_{Z,l} = \hat{H}_0 + \mu_B \left[B_x(\hat{L}_{x,l} + g_S \hat{S}_{x,l}) + B_y(\hat{L}_{y,l} + g_S \hat{S}_{y,l}) + B_z(\hat{L}_{z,l} + g_S \hat{S}_{z,l}) \right] \quad (3.12)$$

The Zeeman-split position of the spectral lines is then given by $\Delta E_{u,l} = E_u(l_u, s_u, j_u, m_{ju}) - E_l(l_l, s_l, j_l, m_{ju})$, where $E_u(l_u, s_u, j_u, m_{ju})$ and $E_l(l_l, s_l, j_l, m_{ju})$ are the eigenvalues of $\hat{H}_{Z,u}$ and $\hat{H}_{Z,l}$ respectively. The wavelength of these spectral lines is given by:

$$\lambda_{u,l,\text{Zeeman}}[\text{Å}] = \frac{\hbar c}{\Delta E_{u,l}(l_u, s_u, j_u, m_{ju}, l_l, s_l, j_l, m_{jl})} \cdot 10^{10} \quad (3.13)$$

3. To generate the Zeeman splitting pattern, together with the energy levels splitting, it is necessary to obtain the transition probabilities between each upper and lower state. The dipole transition probabilities between each upper-lower state pair are calculated using the relation between the integral of spherical harmonics' triple product and the Wigner 3j symbols [112]. First, the dipole operators are calculated in the basis diagonalising $\hat{H}_{0,u}$ and $\hat{H}_{0,l}$, then they are represented in a new basis following the diagonalisation of the $\hat{H}_u$ and $\hat{H}_l$ Hamiltonians.

4. Finally, the Zeeman splitting pattern is modified to include the effect of the polariser (see the DSS hardware description in section 2.1). We express the polarisation state of each transition emission for each LOS using Stokes vector parametrisation [114]. Then,

the Muller matrix representing the polariser is applied to the Stokes vectors associated with each upper-lower pair transition.

Figure 3.3 illustrates the Zeeman splitting pattern, in yellow, for the $D_{7 \to 2}$ (figures 3.3a and 3.3c) and He II (figures 3.3b and 3.3d) transitions, calculated for an external magnetic field of $B = 1.4$ T in the toroidal direction (i.e. almost $\perp$ to the DSS LOS). The convolution of the Zeeman splitting pattern with the respective instrumental function is shown for both transitions, simulating what the DSS would measure in the presence of the magnetic field effect alone. Figures 3.3c and 3.3d differ from 3.3a and 3.3b respectively only by the introduction of a polariser, filtering the component of the light with polarisation $\perp \vec{B}$ ($\sigma-$component) through the DSS optics, selecting the component with polarisation $\parallel \vec{B}$ (π-component). The polariser greatly simplifies the Zeeman splitting pattern, making the overall line-shape FWHM smaller, as indicated by the convolution curves. Analogously to the argument in section 3.1.1, reducing the contribution of the Zeeman splitting to the overall line-shape makes the DSS more sensitive to other broadening mechanisms.

line	λ_0 [Å]	M [a.m.u]	Z	$\Delta\lambda_{\text{Zeeman}}$ [Å] for $B = 1.4$ T
D_α	6561.01	2	0	0.28
D_β	4860.00	2	0	0.14
D_γ	4339.28	2	0	0.12
D_ε	3968.99	2	0	0.10
He I - triplet	5875.62	4	0	0.23
He I - singlet	6678.15	4	0	0.29
He II	4685.80	4	1	0.14
C II	6578.04	12	1	0.28
	6582.88			
C III	4647.42	12	2	0.14
	4650.25			
	4651.47			

Table 3.1: Comparison of Zeeman splitting contributions to the shape of the spectral lines observed in this work. Here $\Delta\lambda_{\text{Zeeman}}$ is estimated considering an energy split of $\Delta E = \mu_B \cdot B$ with $B = 1.4$ T.

3.1.4 Doppler broadening

The thermal motion of the emitting atoms causes this broadening mechanism.

This section follows the description of Doppler broadening as treated in *Atomic Physics in Hot Plasmas* by D. Salzman [115] chapter 7.4.

The emission frequency ω of an emitting ion moving in the laboratory reference frame with a velocity v projected along the observing LOS is shifted from its emitter rest frame frequency
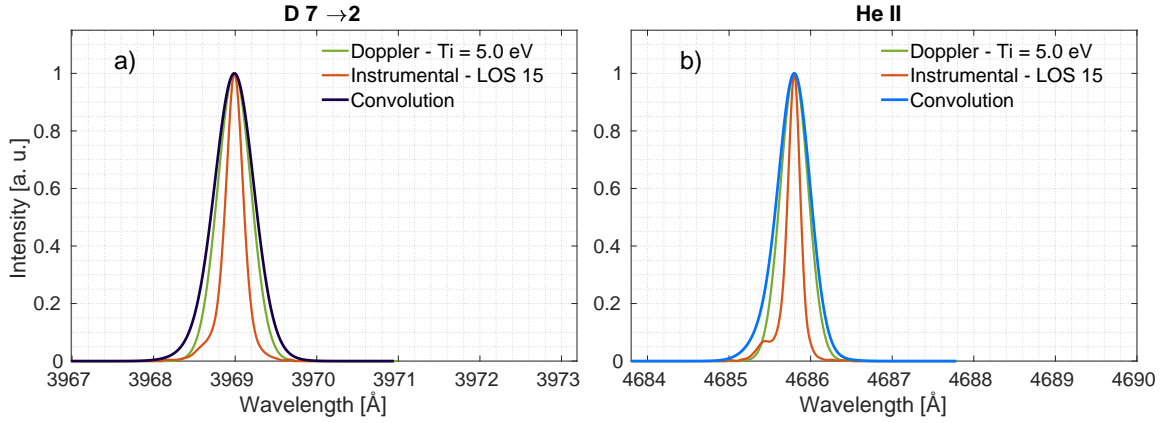
Figure 3.5: Doppler broadening, plotted in green, for the $D_{7 \to 2}$ (panel a), and He II $n = 4 \to n = 3$ (panel b) transitions, compared to the respective DSS SPEX instrumental functions, in red.

ω_0 by the Doppler effect

$$\omega = \omega_0 \sqrt{\frac{1 + v/c}{1 - v/c}} \tag{3.14}$$

When $v \ll c$, equation 3.14 yields a Doppler shift

$$\Delta \omega = \omega - \omega_0 = \omega_0 \frac{v}{c} \tag{3.15}$$

where c is the speed of light. When v exhibits a Maxwell-Boltzmann distribution, i.e.

$$f_v(v) dv = \left(\frac{M}{2 \pi k_B T} \right)^{1/2} \exp\left(-\frac{M v^2}{2 k_B T} \right) dv \tag{3.16}$$

where M and T are the mass and the temperature of the emitting ion, we can calculate the distribution of the emission frequencies by substituting equation 3.15 into 3.16. The probability $\mathscr{P}$ of detecting a shift of $\Delta \omega$ from ω_0 is given by

$$\mathscr{P}(\omega - \omega_0 = \Delta \omega) d(\Delta \omega) =$$
$$\mathscr{P}\left(v = c \frac{\Delta \omega}{\omega_0} \right) d(\Delta \omega) = \tag{3.17}$$
$$f_v\left(v = c \frac{\Delta \omega}{\omega_0} \right) dv = \left(\frac{M}{2 \pi k_B T} \right)^{1/2} \exp\left(-\frac{M c^2}{2 k_B T} \left(\frac{\Delta \omega}{\omega_0} \right)^2 \right) \frac{c}{\omega_0} d(\Delta \omega)$$

By substituting

$$\sigma^2 = \frac{k_B T \omega_0^2}{M c^2} \tag{3.18}$$

we can write the ω distribution as a Gaussian:

$$\mathscr{L}(\Delta\omega)d(\Delta\omega) = \frac{1}{\sqrt{2\pi}\sigma}\exp\left(-\frac{1}{2}\left(\frac{\Delta\omega}{\sigma}\right)^2\right)d(\Delta\omega) \tag{3.19}$$

Translating the definition in eq. 3.18 in terms of wavelengths and solving for T, gives us a direct relation between Doppler broadening measured by the DSS and the temperature of the emitting atom/ion:

$$T_i = \frac{Mc^2}{8k_b\ln 2}\frac{\Delta\lambda^2_{\text{Doppler,FWHM}}}{\lambda_0^2} \tag{3.20}$$

or, in more convenient units,

$$T_i[eV] = 1.7\cdot 10^8 \cdot M[\text{a.m.u.}]\frac{\Delta\lambda^2_{\text{Doppler,FWHM}}[\text{Å}]}{\lambda_0^2[\text{Å}]} \tag{3.21}$$

Instead of the Gaussian standard deviation σ we use its FWHM. They are related by

$$\text{FWHM} = 2\sqrt{2\ln 2}\sigma \tag{3.22}$$

Figure 3.5 illustrates the Doppler broadening, plotted in green for the $D_{7\rightarrow 2}$ and He II transitions, calculated for $T_i = 5$ eV. For each transition, a convolution of the Doppler broadening with the respective instrumental illustrates what DSS would measure in the presence of an ion thermal velocity alone. The $\Delta\lambda_{\text{Doppler,FWHM}}$ is larger for $D_{7\rightarrow 2}$ than for He II due to its lower nuclear mass. Values of $\Delta\lambda_{\text{Doppler,FWHM}}$ are listed in the last column of table 3.2 for all the spectral lines observed in this thesis work, for a reference $T_i = 5$ eV temperature.

line	λ_0 [Å]	M [a.m.u]	Z	$\Delta\lambda_{\text{Dopp,FWHM}}$ [Å] for $T_i = 5$ eV
D_α	6561.01	2	0	0.78
D_β	4860.00	2	0	0.59
D_γ	4339.28	2	0	0.52
D_ε	3968.99	2	0	0.48
He I - triplet	5875.62	4	0	0.50
He I - singlet	6678.15	4	0	0.57
He II	4685.80	4	1	0.40
C II	6578.04	12	1	0.33
	6582.88			
C III	4647.42	12	2	0.23
	4650.25			
	4651.47			

Table 3.2: Comparison of Doppler broadening contribution to the shape of the spectral lines observed in this thesis work.
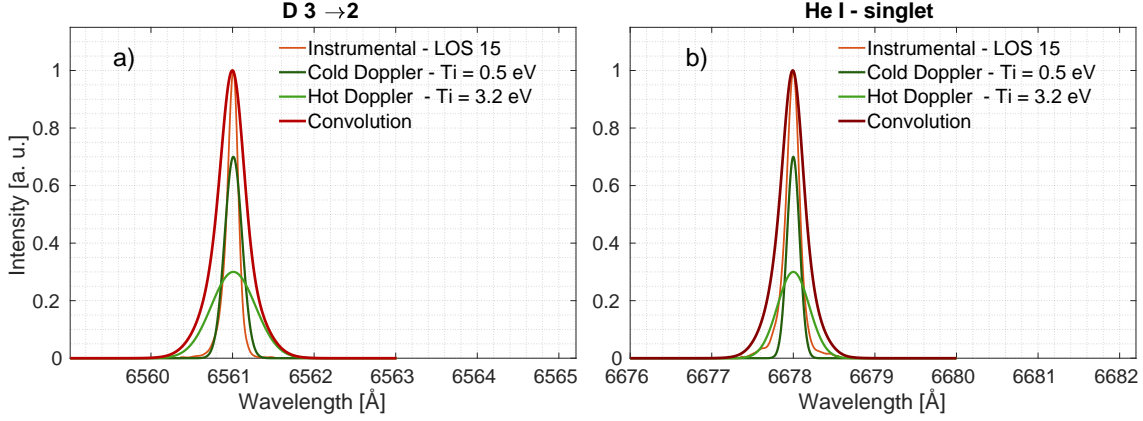
Remark on neutral atoms spectral lines

Figure 3.6: Neutral deuterium and helium spectral lines, simulated considering two temperature components.

Regressing the line-shapes with a Gaussian distribution assumes that the emitters follow a Maxwellian distribution. Therefore, the term *temperature* is well-defined for these particles. However, during numerous experiments in this thesis, measured line-shapes of neutral atoms spectral lines, such as D_α, D_β and the He I singlet, could not be explained by a single Gaussian distribution. In these cases, we fit these line-shapes taking two Gaussian distributions. Although this choice provides reasonable agreement with the experiments, it does not necessarily imply the presence of emitters' populations with distinct temperatures, i.e. with two independent Maxwellians, along the DSS LOS. In principle, it is possible that the distribution function of the neutrals is not Maxwellian since their energy transfer frequencies are relatively low, as will be discussed in section 4.2.3.

A justification for the employment of two Gaussian distributions is presented in section 3.2 in figure 3.12 where a comparison of single and double Gaussian models is shown for the D_α measured line-shape. A tentative explanation of the nature of this double temperature emission is presented in section 4.4.2, where DSS experimental results, distinguishing between the hot and cold components, are presented.

Figure 3.6 represents two of these examples. Here the line-shapes were modelled using a *hot* temperature component (e.g. $T_{i,\mathrm{hot}}$ = 3.2 eV) and a *cold* temperature component (e.g. $T_{i,\mathrm{cold}}$ < 1 eV). We note that the width of the sub-eV Doppler broadening component is comparable to that of the instrumental function, demonstrating that this diagnostic can provide reliable measurements even at such low ion temperatures.

3.1.5   Stark broadening

This broadening mechanism is caused by the electric micro-fields induced by the charged plasma particles' motion in the surrounding of the emitting atom.
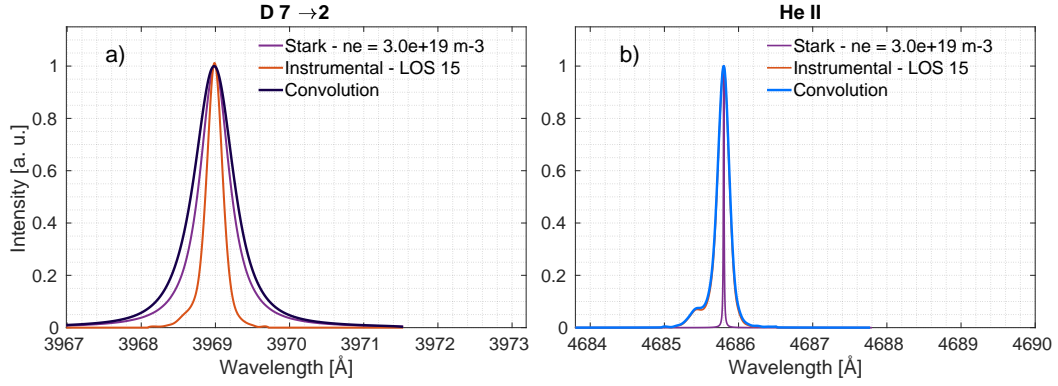

Figure 3.7: Stark broadening, plotted in purple, for the $D_{7\to 2}$ (3.7a) and He II $n = 4 \to n = 3$ (3.7b) transitions, compared to the respective DSS SPEX instrumental functions, in red.

This section follows the description of Stark broadening as treated in *Atomic Physics in Hot Plasmas* by D. Salzman [115] chapter 7.5 and by Rosato et al. (2020) [116]. Further details can be found in *Introduction to Plasma Spectroscopy* by H. Kunze [117] chapter 9.2.4.

The Stark broadening of a line-shape results from the interaction of the free plasma electrons and ions with the radiating atom or ion. Depending on the charged particle, two different approximations can be employed in its description: *electron impact broadening*, for which the broadening is dominated by interactions with free electrons that satisfy $1/\tau_{int} \gg 1/\Delta\omega$, where τ_{int} is the typical interaction time of the e^- with the emitters and $\Delta\omega$ is the typical Stark splitting due to this interaction - or *quasi-static broadening*, where a slow-moving nearby ion causes a perturbation. In both cases, the description of the general interaction of the radiator with the plasma particles is complicated. However, several approximations are possible. For instance, it is often taken that the perturbation is dominated by the interaction with the nearest neighbour to the radiator, that the charged particles' trajectories can be approximated as rectilinear, or finally, that the scattering is assumed elastic, with no transitions between the radiator energy levels leading to line-radiation. Descriptions of the Stark broadening contribution to the spectral line profiles can be obtained by computer simulations, considering both the ions' dynamics and the collisional effect of electrons, as performed in Rosato et al. (2020) [116].

A detailed modelling of $D_{7\to 2}$ Stark broadening based on the work of Rosato et al. (2017) [95], was implemented in the framework of N. Maaziz's master thesis [94] at the SPC to analyse DSS data. The model provides tables of computer-simulated line-shapes for deuterium Balmer lines from D_α to D_ε, directly accounting for Stark and Zeeman effects. A quasi-static contribution to the Startk broadening is calculated by simulating the time-varying micro-fields

$\vec{E}(t)$ generated by a linear ion motion. At the same time, the effect of the electrons is accounted for via a collision operator. These simulations are run by randomising the charged particles' initial conditions to obtain a statistical line-shape distribution.

Using this model, assuming plasma quasi-neutrality and $Z = 1$, it is possible to extract the plasma density from the Stark broadening contribution to the measured spectral lines.

When such detailed calculations are unavailable, approximating the Stark broadening profile with a Lorentzian distribution is often fruitful. In this approximation, tables relating Lorentzian's FWHM to the electron density, as in the *Plasma formulary interactive* by Stambulchik and Maron (2011) [118] and in the *STARK-B database* by Sahal-Bréchot et al. [119], can be used.

Figure 3.7 illustrates the Stark broadening, in purple, of the $D_{7\rightarrow2}$ and He II transition, calculated for $n_e = 3 \cdot 10^{19}$ m^{-3}. Stark broadening of $D_{7\rightarrow2}$ (i.e. figure 3.7a) is calculated using Rosato et al. (2017) [95] line-shape simulations, for $B = 0$ and $T_e = 0.31$ eV. The Stark profile for He II (i.e. figure 3.7b) is a Lorentzian function with a FWHM calculated using the Plasma Formulary Interactive as in [118], $\Delta\lambda_{\text{Stark,FWHM}} = 0.011$ Å, which is negligible compared to the DSS instrumental function.

In table 3.3, we present the contribution of Stark broadening to the shape of the spectral lines observed in this thesis work. $\Delta\lambda_{\text{Stark,FWHM}}$ for deuterium and He II transitions are taken from [118], while for He I, C II and C III from [119]. In these cases, only the Lorentzian approximation was used.

We note that due to the Lorentzian-like shape of this broadening mechanism, prominent at the wing on the line-shape, a different parameter than the FWHM would be more appropriate in representing the Stark broadening contribution to the line-shape. For instance, the broadening at $1/10^{th}$ of the line-shape's maximum, highlights its effect in the spectral wings. However, with these considerations, Stark broadening remains negligible for all of the lines presented in section 3.2 and the rest of the thesis. For example, tables from Rosato et al. (2017) [95] were used to generate Stark broadening on D_α spectral lines for the typical values of n_e observed in the experiments presented in chapter 4, i.e. $n_e \approx 2 \cdot 10^{19}$ m^{-3}, resulting in a $\approx 10\times$ smaller broadening than that of the instrumental function and has a negligible effect on the overall line-shape, even the wings of D_α, over the considered spectral ranges of the simulation.

3.1.6 Putting everything together...

The line-shapes observed by the DSS are affected by all the broadening mechanisms listed above.

Figure 3.8 represents the line-shapes of $D_{7\rightarrow2}$ and He II transitions where $T_i = 5$ eV, B = 1.4 T and $n_e = 3 \cdot 10^{19}$ m^{-3}. Neglecting natural broadening (that is indeed negligible) the line profile is given by the convolution of instrumental function, Zeeman splitting (here simplified by the polariser effect), Doppler and Stark broadening. This figure aims to convey the complexity of isolating the Doppler and Stark broadening components for T_i and n_e measurements. When

line	λ_0 [Å]	upper level	lower level	Z	$\Delta\lambda_{\text{Stark,FWHM}}$ [Å] for $n_e = 3 \cdot 10^{19}$ m^{-3}
D$_\alpha$	6561.01	3	2	0	0.03
D$_\beta$	4860.00	4	2	0	0.14
D$_\gamma$	4339.28	5	2	0	0.22
D$_\varepsilon$	3968.99	7	2	0	0.45
He I - triplet	5875.62	1s3d	1s2p	0	$8.4 \cdot 10^{-4}$
He I - singlet	6678.15	1s3d	1s2p	0	$2.2 \cdot 10^{-3}$
He II	4685.80	4	3	1	0.01
C II	6578.04	2s^{2}3p	2s^{2}3s	1	$2.3 \cdot 10^{-4}$
	6582.88				
C III	4647.42	2s3p	2s3s	2	$1.6 \cdot 10^{-4}$
	4650.25				
	4651.47				

Table 3.3: Comparison of Stark broadening contribution to the shape of the spectral lines observed in this thesis work. We note that the Lorentzian-like Stark shapes have wider wings than the other non-Lorentzian-like broadening mechanisms. Therefore, more significant parameters to evaluate the broadening can be given by the full width at 1/10 or 1/5 of the maximum.

dealing with the Doppler broadening measurement only, a few assumptions and techniques can aid, such as:

1. As mentioned in section 3.1.1, the instrumental function associated with the spectral line is fully characterised;

2. The Stark broadening of low-n Balmer lines (i.e. D$_\alpha$ and D$_\beta$) and non-hydrogen-like ions is negligible compared to the instrumental function. This can be seen from table 3.3;

3. The Zeeman pattern can be modelled if measurements of the magnetic field in the emission region(s) along the DSS LOSs are provided.

In the next section 3.2, we will see how these elements combined are used to measure T_i associated with the emitting ion or atomic species.
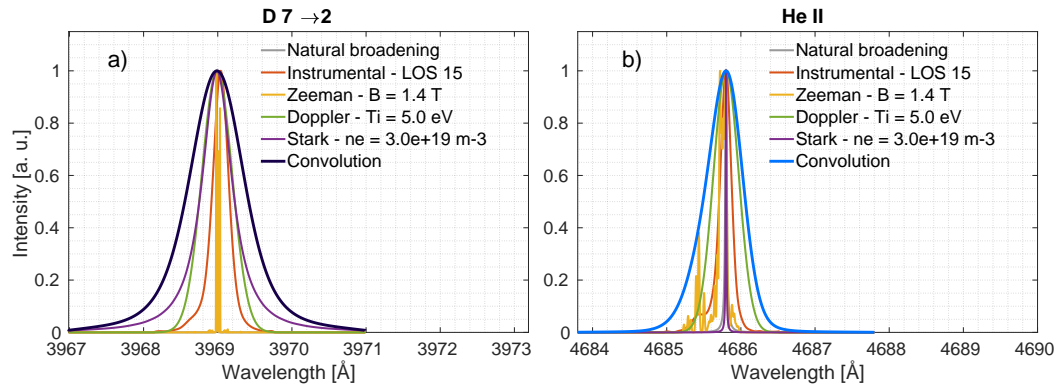
Figure 3.8: Line-shapes of the $D_{7\to2}$ and He II transition accounting for all the broadening mechanisms listed in section 3.1.

3.2 DSS line-shape analysis

This section presents the analysis technique developed during this thesis for T_i measurements from DSS data. Here we expand section III of Martinelli et al. (2022) [92], providing examples of the analysis applied to several spectral lines and listing the primary sources of uncertainty affecting the T_i estimations.

3.2.1 Analysis technique

Measuring the ion temperature by isolating the Doppler broadening component to the overall line-shape.

The ion temperatures are determined from the Doppler broadening of the observed transitions given by the thermal motion of the emitters. To best estimate T_i including the sub-eV temperature range, we regress the measured high-resolution line shapes after accounting for other non-negligible broadening mechanisms described earlier in this chapter, namely the Zeeman splitting and the instrumental profiles for each observed transition and LOS.

While the instrumental functions are fully characterised by the procedure described in 3.1.1, the Zeeman splitting modelling requires information on the magnetic field at, or over, the emission region, in particular its toroidal (B_{tor}) and poloidal (B_z, B_r) components. These are provided by LIUQE, TCV's magnetic equilibrium reconstruction code described in J. M. Moret et al. (2015) [38], that deduces the magnetic field components at any point inside the machine, by default averaged over ≈ 1 ms - a time scale that is considerably lower than typical DSS integration times. As the emission region of the observed spectral lines originates from a narrow region around the separatrix (see section 4.3 illustrating MANTIS data), B_{tor}, B_z and B_r are taken at the intersection point between the separatrix and each DSS LOS. This procedure introduces an approximation: we use a single value for B instead of its distribution over the emissivity region. The consequences of this approximation are discussed in 3.2.2.
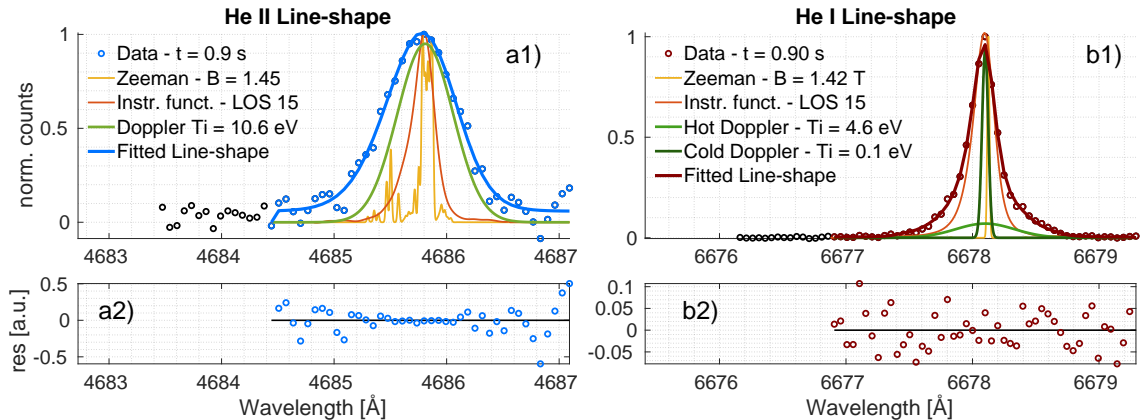

Figure 3.9: Line-shape fits and their residuals for He II and He I spectral lines.

The calculated Zeeman pattern is then convolved with the instrumental function associated with the selected LOS, interpolating the latter using a cubic spline on the wavelength grid used for the Zeeman pattern calculation. Here, a light polariser that selects the radiation π-component significantly improves the diagnostic's sensitivity, determined by the obtained convolution curve, as mentioned in section 3.1.3. As illustrated in figure 3.3, this narrows after the installation of the polariser, making the DSS more sensitive to Doppler broadening, and thus, lower T_i.
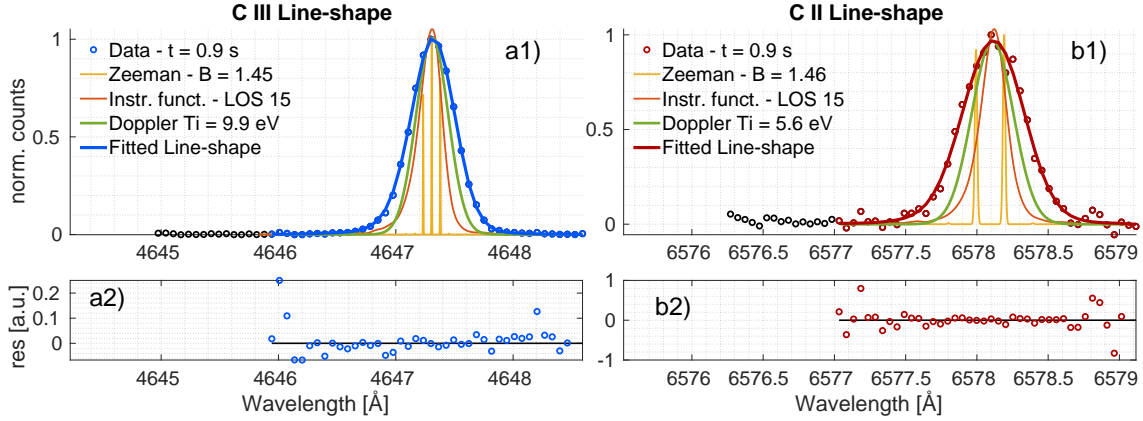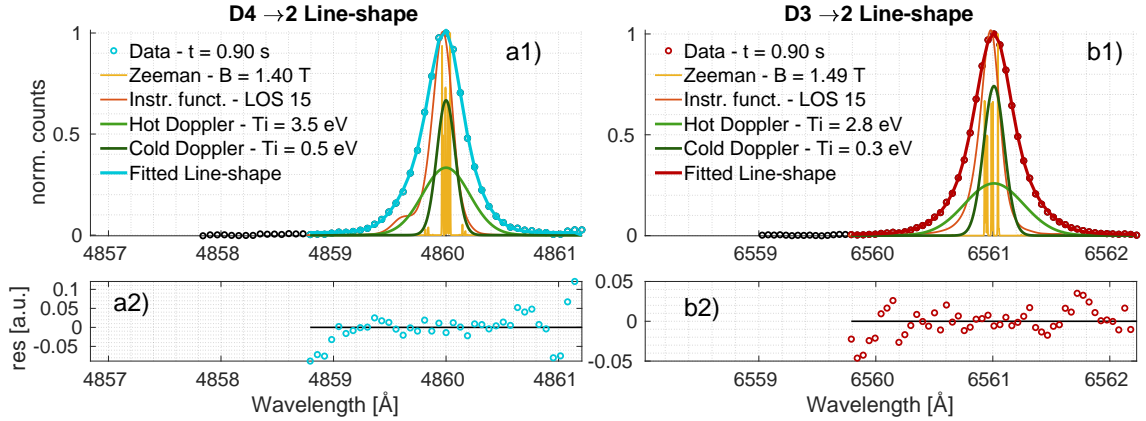

Figure 3.10: Line-shape fits and their residuals for C III and C II spectral lines.

The broadening mechanism left undetermined is the Doppler broadening, which we find by regressing the modelled curves, or more correctly their parameters, to the DSS data. Here, a Gaussian profile is convolved with the Zeeman-Instrumental function and the resulting error is minimised by a gradient expansion algorithm in a least-squares sense. The Zeeman-Instrumental function is passed as a fixed parameter, so only the Gaussian profile parameters are determined. The regression algorithm used in this thesis is described in *Data reduction and Error Analysis for the Physical Science* by P. R. Bevington (1969) [120], pages 156-160.

As mentioned in section 3.1.4, single and double ionised species, such as He II, C II and C III, are well described by a single Gaussian Doppler broadening component. The regression parameters used in these cases are: 1) λ_0, the central wavelength of the transition; 2) A, the amplitude; 3) $\Delta\lambda_{\mathrm{FWHM}}$, the Gaussian's FWHM that is related to T_i using equation 3.21; and 4) a background/offset level.

The regression parameters are free to vary within predefined intervals. While λ_0 and A should, in principle, be fixed by the model (since the central wavelength of the spectral line is known - assuming no significant bulk motion is present along the LOS - and the line's amplitude is normalised to 1) they are allowed to vary to accommodate for slight wavelength miscalibrations, for the finite pixel size and small perturbations in the amplitude due to detector noise, particularly for low-emissivity observations. For neutral species emission lines, additional parameters are needed to describe the two apparent Doppler components. The list of regression parameters used here becomes: 1) $\lambda_{0,\mathrm{Hot}}$, central wavelength of the *hot* component 2) A_{Hot},

Figure 3.11: Line-shape fits and their residuals for D_β and D_α spectral lines.

amplitude of the *hot* component; 3) $\Delta\lambda_{\text{FWHM, Hot}}$, FWHM of the *hot* component; 4) $\lambda_{0,\text{Cold}}$, central wavelength of the *cold* component; 5) $\Delta\lambda_{\text{FWHM, Cold}}$ FWHM of the *cold* component; 6) an offset level.

The amplitude of the cold component, A_{Cold} is defined by A_{Hot}, using the constraint

$$A_{\text{Hot}} + A_{\text{Cold}} = 1 \tag{3.23}$$

This constraint on the two Gaussian amplitudes is equivalent to another on their intensity. Calling I_{Hot} and I_{Cold} the intensity of the hot and cold components, respectively, we can write the relation

$$
\begin{aligned}
I_{\text{Hot}} &= \int A_{\text{Hot}} e^{\frac{2(2\ln 2)\cdot x^2}{\text{FWHM}_{\text{Hot}}^2}} dx = A_{\text{Hot}}\sqrt{\frac{\pi\,\text{FWHM}_{\text{Hot}}^2}{4\ln 2}} = \sqrt{\frac{\pi}{4\ln 2}}\cdot A_{\text{Hot}}\cdot \text{FWHM}_{\text{Hot}} \\
I_{\text{Cold}} &= \int A_{\text{Cold}} e^{\frac{2(2\ln 2)\cdot x^2}{\text{FWHM}_{\text{Cold}}^2}} dx = A_{\text{Cold}}\sqrt{\frac{\pi\,\text{FWHM}_{\text{Cold}}^2}{4\ln 2}} = \sqrt{\frac{\pi}{4\ln 2}}\cdot A_{\text{Cold}}\cdot \text{FWHM}_{\text{Cold}}
\end{aligned}
\tag{3.24}
$$

And therefore

$$A_{\text{Hot}} + A_{\text{Cold}} = 1 \Rightarrow \frac{I_{\text{Hot}}}{\text{FWHM}_{\text{Hot}}} + \frac{I_{\text{Cold}}}{\text{FWHM}_{\text{Cold}}} = \sqrt{\frac{\pi}{4\ln 2}} \tag{3.25}$$

More intuitively, this constraint means that the sum of the two Gaussian components' intensities must equal the intensity of the spectral line.

The regression model allows for adding other emission lines within the wavelength region of interest. Their profiles are treated as Gaussian distributions by adding three more fitting parameters: $\lambda_{0,\text{imp}}$, A_{imp} and $\Delta\lambda_{\text{FWHM, imp}}$. This option is only employed when necessary, for instance, when another emission line is clearly discerned from the regression's residuals since adding three more parameters will make the regression less stable, especially when λ_0 and $\lambda_{0,\text{imp}}$ are close. In this case, the main line's resulting $\Delta\lambda_{\text{FWHM}}$ becomes sensitive to the initial

guess parameters provided to the fitting routine.

Figures 3.9, 3.10 and 3.11 show examples of the regressed line-shapes observed during the experiments described in chapter 4, respectively for He, C and Deuterium transitions. Each figure shows the measured data, indicated by coloured dots, and a solid line of the same colour represents the regressed line-shape. The same panel also indicates the Zeeman splitting pattern in yellow, the instrumental function in red and the Doppler broadening component(s) in green. The regression residuals are shown in the same colour of the data below each panel. Here they are defined as

$$res(\lambda) = \frac{y(\lambda) - f(\lambda)}{\sqrt{f(\lambda)}} \tag{3.26}$$

where y indicates the normalised measured data and $f(\lambda)$ the normalised curve output of the regression routine. The term $\sqrt{f(\lambda)}$ indicates a re-normalisation on the expected *shot noise* at each point of the fitted curve. When the residuals are statistically distributed around the black line, indicating $res = 0$, they suggest that the chosen model well describes the measured data, as fluctuations around 0 indicate the statistical extraction of all information provided by the data. The residuals' absolute value depends on the SNR for the specific spectral line: typical values are $|res(\lambda)| \lesssim 0.05$ for bright lines such as D_α, D_β and C III, but they can increase to $0.1 - 0.2$ when the spectral lines are of relatively low intensity, such as for C II, He I and He II.

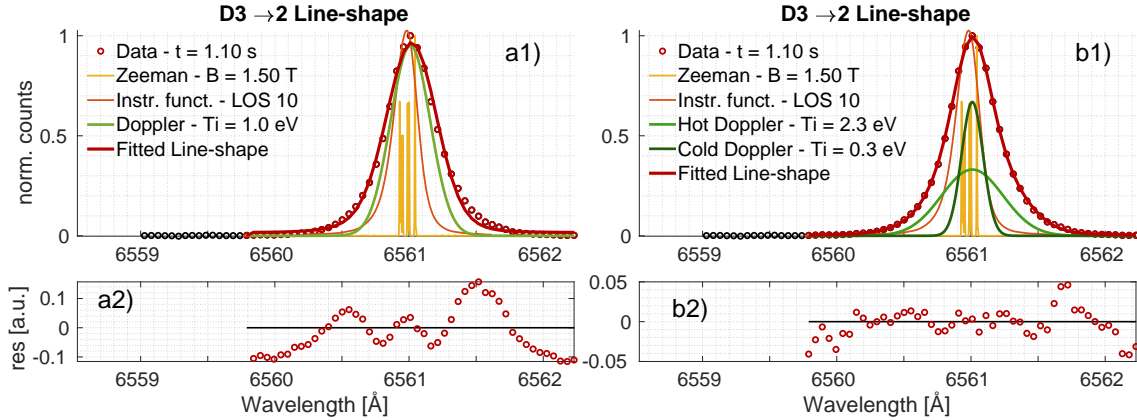**Remark on neutral atoms spectral lines - continuation**

Figure 3.12: Line-shape fits and their residuals for D_α using one and two Doppler components.

Using two Gaussians to describe the Doppler broadening of neutral spectral lines is well exemplified by figure 3.12. Here the same line-shape, acquired for the D_α transition at 1.10 s, LOS 10 on discharge # 74216, is regressed on two models: a single Gaussian, in figure 3.12a, and two Gaussians, in figure 3.12b. Not only are the residuals of the second fit smaller in magnitude but they are also evenly distributed around 0 with no clear wavelength dependence.

The structures in the residuals in panel a2) are typical where a single Gaussian is unable to simultaneously model the centre of the line-shape, here narrower than modelled, and the spectral wings, where the width is underestimated.

It could be argued that with enough Gaussians, one could fit an elephant. Here, we added a little more complexity to the model to significantly improve the regression quality, introducing parameters that appear related to physics processes, as we argue in section 4.4.2. Using more than two Gaussian components did not significantly improve the residual distribution symmetry nor its amplitude.
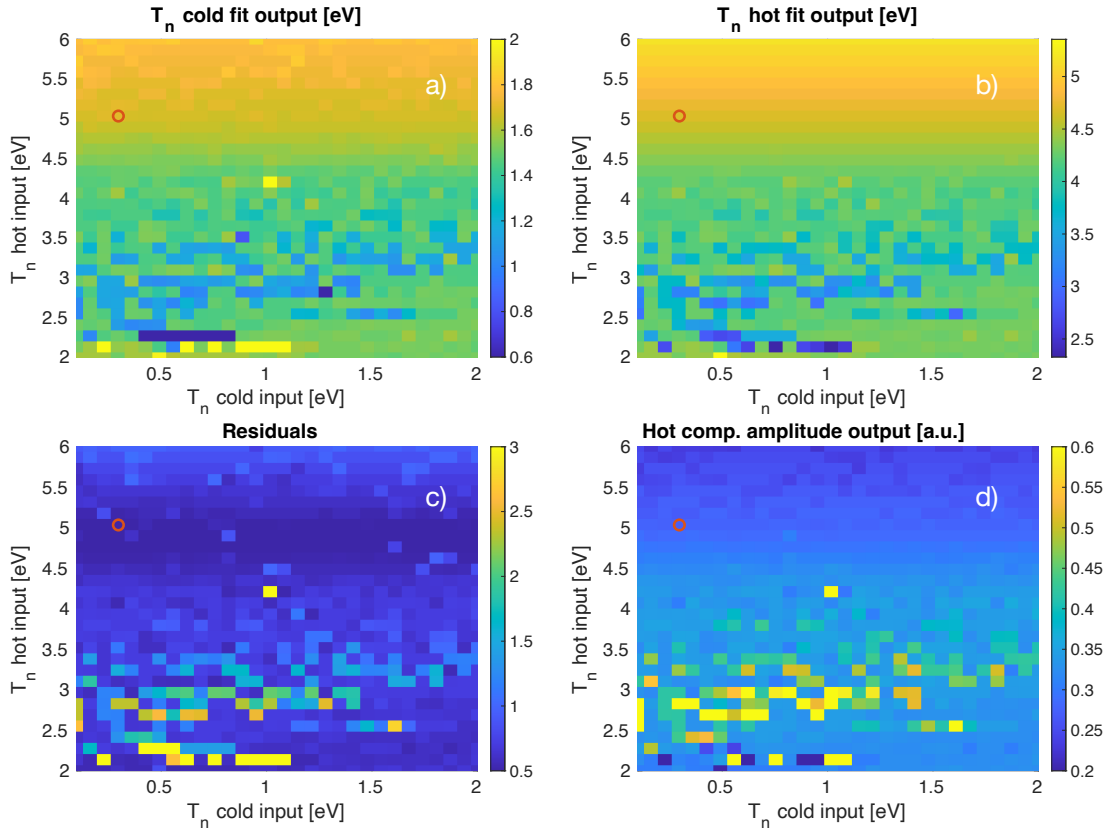

Figure 3.13: Scan of fit input parameters on a reference D_α line-shape. The red circle indicates the parameters for which the minimum sum of residuals is obtained.

One may wonder about the dependence of the Gaussians' parameters upon the initial parameters chosen for the regression. To address this, figure 3.13 presents a scan of the *hot* and *cold* Gaussian components' input values for the D_α line-shape acquired at $t = 1.10$ s at LOS 10 for discharge # 74216. Figure 3.13a) shows the regression algorithm output value for the *cold* Gaussian FWHM following a scan of the two input values. Similarly, in figure 3.13b) and d), the output of the *hot* Gaussian component's FWHM and amplitude are presented. Figure 3.13c) shows the sum of the absolute value of the residuals, expressed as in equation 3.26, for each regression. The FWHM values are expressed as T_n temperatures, using equation 3.21.

We note that all the fit parameters are correlated. For example, when the *hot* Gaussian component's FWHM is large (e.g. $T_n > 5$ eV), its amplitude is low, and vice versa. Surprisingly, the *hot* and *cold* components' FWHMs appear to be positively correlated. However, no input parameter pairs are able to describe the line-shape in the same way: the sum of the residuals presented in panel c) shows a region of superior fit quality for $T_{n,\,hot} \approx 4.5 - 5$ eV. Here, the *cold* component's output FWHM is relatively insensitive to the choice of input value. In each panel of figure 3.13, a red circle indicates the values of output parameters obtained by the regression corresponding to the residuals' global minimum. From this exercise, we conclude that the choice of input parameters is not determinant in the temperature estimates presented in this work.

3.2.2   Main sources of uncertainty

Low signal-to-noise ratio is the primary source of uncertainty in the regression of low-intensity spectral lines. The polariser decreases the uncertainty of the Zeeman splitting pattern. However, when possible for the experiments presented in this thesis, the standard deviation over repeats with similar conditions was considered to be a more reliable estimate of the T_i uncertainties.

The treatment of the main sources of uncertainty is reported in [92] section V. Here we distinguished three main contributions to the T_i uncertainty: 1) approximation of the Zeeman pattern due to taking a single representative magnetic field value, 2) fluctuating intensity of other impurity lines close to the regressed line-shape, 3) uncertainty in the regression routine itself. In this work, we also discuss a fourth contribution due to the machine's conditions.

To illustrate the contribution on the T_i uncertainty given by the approximation of the Zeeman pattern, we use the following example. Figures 3.14a and b represent the radial distribution of C III and He II emissivity, respectively recorded at 1.00 s and 1.60 s. The left panels present the MANTIS tomographic inversions in the TCV poloidal cross section for discharge # 74212, part of the experimental series that are extensively analysed in chapter 4. These are obtained on a custom grid with the procedure described in Perek et al. (2019) [90]. The magnetic equilibrium, reconstructed by LIUQE [38], is over-plotted in orange, while the DSS LOSs are represented in grey, except for LOS 12 and 8, highlighted in orange. The right panels present the MANTIS emissivity of the C III triplet centred at $\lambda_{\text{C III}} = 4650$ Å and of the He II transition at $\lambda_{\text{He II}} = 4686$Å as observed by the DSS, in blue, by taking the inversion grid cells associated to their respective DSS LOSs and projecting the emissivity in the radial direction. The red curve, referring to the right-hand side axis, plots the toroidal magnetic field component showing its $1/R$ dependence. These figures show the magnetic field and the emissivity radial distributions.

To estimate the effect of the variation of the magnetic field on the line-shape, we can consider, as an example, the magnetic field values at the radial positions defining the FWHM of the emissivity distributions, indicated by black dashed lines. These values are used to generate the Zeeman splitting patterns (with and without polariser) represented in figure 3.15 for C III and in figure 3.16 for He II, convoluted with their respective instrumental functions. Here,
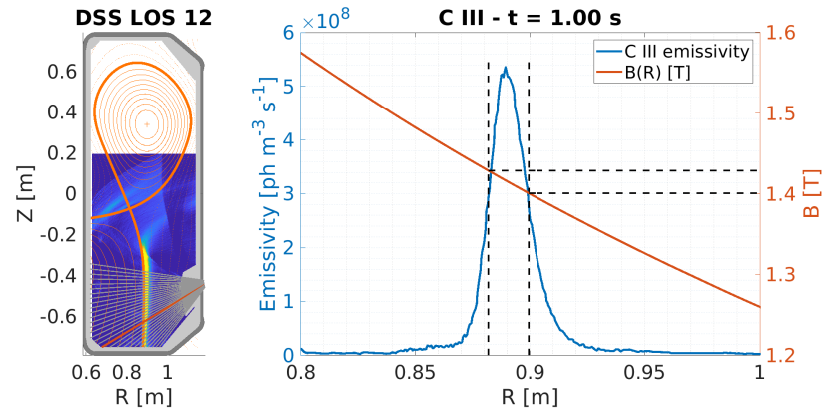
(a) In blue, the C III emissivity relative to DSS LOS 12 at 1.00 s. The magnetic field, referring to the r.h.s. axis, is plotted in orange.
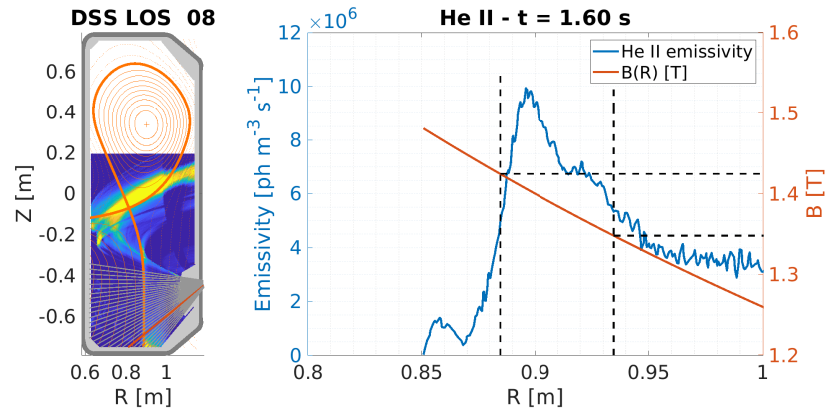
(b) In blue, the He II emissivity relative to DSS LOS 08 at 1.60 s. The magnetic field, referring to the r.h.s. axis, is plotted in orange.

Figure 3.14: The toroidal component of the magnetic field can vary across the radial profile of the spectral line emissivity, in particular when this is observed to be spatially broad, as in the case of He II in figure 3.14b.

in the lower panels, a curve representing the difference between the Zeeman-Instrumental function calculated for the two values of B is plotted in purple.
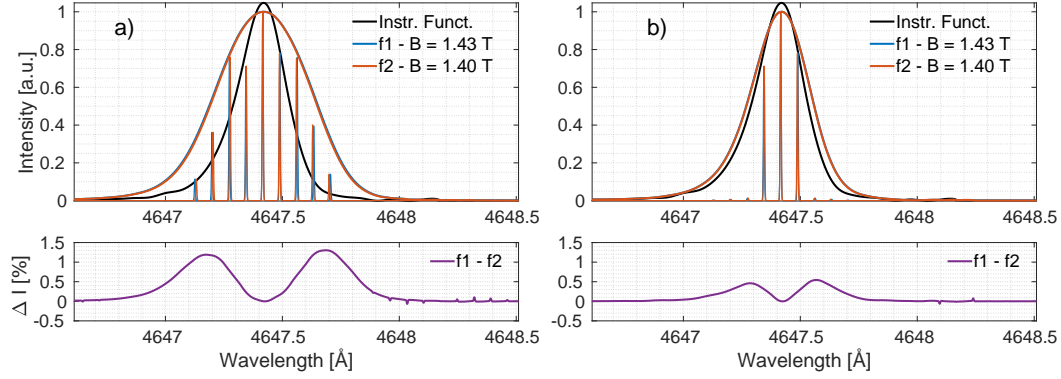

Figure 3.15: Zeeman patterns of C III and their convolution with the instrumental function for the two values of B indicated in figure 3.14a. Case a) is without the polariser, and case b) is with the polariser.

When considering relatively spatially narrow emissivity region, such as that for C III at 1.00 s, i.e. figure 3.14a, the effect of the magnetic field distribution is negligible (i.e. $\lesssim 1\%$) regardless of the presence of the polariser. When, instead, observing radially wider emissivity distributions, such as the case of He II at 1.60 s plotted in figure 3.14b, we see that the presence of the polariser dramatically reduces the difference between the two Zeeman-Instrumental functions, i.e. by comparing figures 3.16a and b. Choosing a single magnetic field value to calculate Zeeman patterns only introduces significant uncertainties in the case of radially wide emission regions recorded without polariser, as was the case in [92]. This uncertainty can be considered negligible for the experiments described in chapter 4, performed after the installation the polariser.
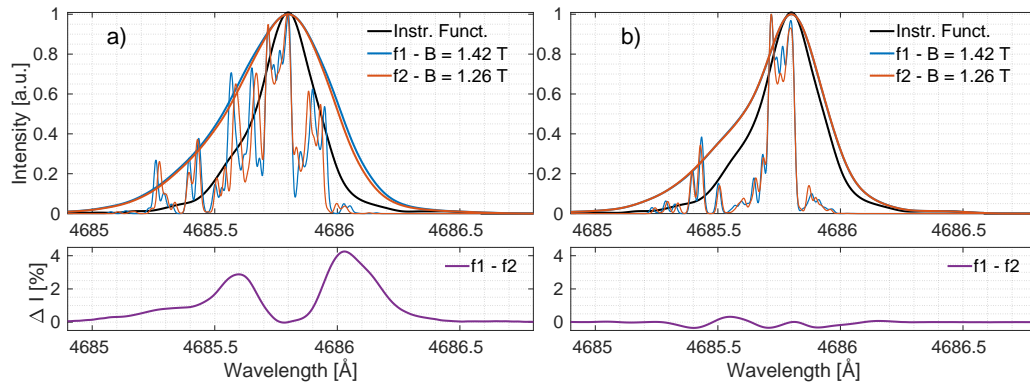

Figure 3.16: Zeeman patterns of He II and their convolution with the instrumental function for the two values of B indicated in figure 3.14b. Case a) is without the polariser, and case b) is with the polariser.

Additional -usually relatively weak- lines near the studied transition might also cause uncertainty in the ion temperature determination. Figure 3.17 presents He II data from LOS 16, acquired for discharge # 73912, also from the experiments presented in chapter 4. The data were regressed using the procedure presented in section 3.2.1, but, despite corresponding to nearly consecutive time frames, acquired only 30 ms apart, resulted in T_i differing by > 2.3 eV. This discrepancy was ascribed to an unknown spectral feature residing on the left wing of the He II spectral line, here highlighted with the red circle, even though, in this particular case, it is not fully resolved. The regression would sometimes ignore this feature, i.e. as referred to by the blue line, but sometimes would consider it part of the line-shape, i.e. red line. This always leads to overestimating the ion temperature and a significant scattering in the temperature values as a function of time.
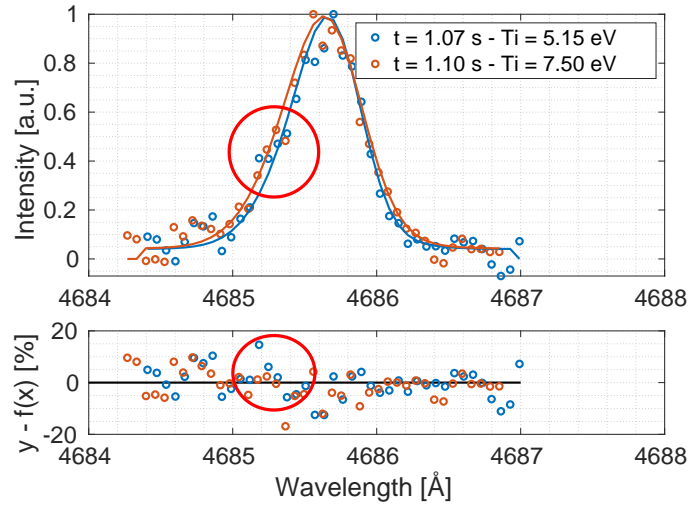

Figure 3.17: An example of an undefined faint line on the left-hand side of the He II transition and its effect on the obtained best fit and, consequently, on the inferred He II temperature. Ignoring this features leads to a temperature estimation of T_i(He II)= 5.15 eV, while in the example where this is considered as part of the spectral line width, it leads to a temperature estimation of T_i(He II)= 7.50 eV.

These effects are only relevant for low-intensity spectral lines, such as He II in the $T_e = 12 - 4$ eV range or for C III when T_e approaches the C III radiation front temperature (see section 5.2), but can lead to an uncertainty > 20%.

It is however possible to mitigate this contribution to the uncertainty by using some *escamotage* to increase these lines' signal-to-noise ratio (SNR). The DSS integration time is to be optimised by choosing a trade-off between a high SNR - i.e. long integration time - and the temporally evolving physics - i.e. short exposure times. EM-CCD gains are also able to increase the SNR, provided the sensor receives sufficient photons. Unfortunately, these options are not always available: when low-intensity lines are acquired in the same wavelength window of very bright ones -e.g. He II with C III - this can lead to saturation of the latter, with consequent

loss of information on the C III temperature and intensity. In the experiments reported in chapter 4, we used exposure times tailored to the higher spectral line's intensity. Later, we post-processed the data by applying a moving time average over consecutive time frames to reduce the uncertainty on the low-intensity line-shape which resulted in a corresponding reduction in the temporal resolution.
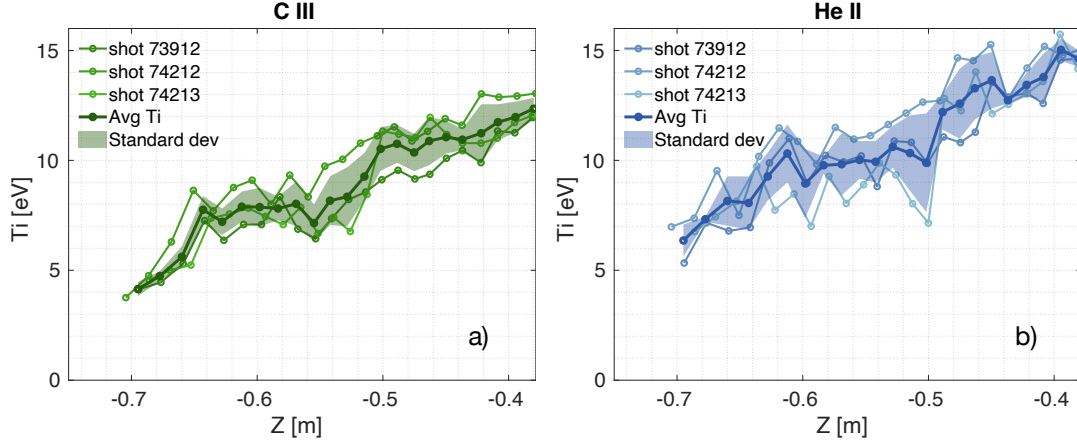

Figure 3.18: Calculation of average and standard deviation of C III and He II ion temperatures, acquired from discharge repeats and plotted for a the same core density value as function of TCV coordinate Z.

The regression routine calculates a third source of uncertainty directly, following the treatment presented in [120], pages 156-160. Here the inverse of the *curvature matrix*, which in the algorithm measures the curvature of the χ^2 hypersurface, is taken as an *error matrix*. Its diagonal terms are used to evaluate the uncertainty in the regression parameters. However, experimentally, this numerical contribution is negligible compared to those listed above.

One last contribution to the T_i uncertainty is given by any variation of the machine's conditions for discharges that would otherwise be considered exact repeats. This does not affect the regression algorithm uncertainty itself but rather the estimation of the ion temperatures in the context of the experiments presented in chapter 4. For example, the experiments described in chapter 4 were all designed with the same plasma parameters, i.e. constant plasma current, constant $\vec{B}$ field, and the same geometry, as reported in table 4.1. We assume that the primary observer tracking the divertor physics we aim to study is the core plasma density, that in these experiments is steadily increased across the discharges in so-called *density ramps* (more details will follow in chapter 4). The T_i measured by the DSS is taken to depend upon the core density and measurement location: for a given core density, a particular DSS LOS should measure the same T_i. Figure 3.18 shows the values of T_i(C III), in panel a, and T_i(He II), in panel b, as a function of TCV's coordinate Z, sampled for the same value of core density across three repeat discharges. Here, the differences between the measured values of T_i for the same

species are of the order of 15-25%. In the same figure, a thicker and darker line plots the average T_i(C III) and T_i(He II) across three repeat discharges, while a shaded region represents the standard deviation. Despite the limited statistic sample, we decided to use this standard deviation to assess the uncertainty due to the machine's conditioning, and the average as the T_i value representing the ion species in section 4.4. In chapter 4 and 5, these are further regularised by applying 2-D smoothing.

We note that this uncertainty includes the contribution due to any fluctuating spectral features mentioned above, that are smoothed in the averaging process. This uncertainty contribution can be reduced by running the repeat discharges consecutively.

Concluding, the polariser drastically reduced the uncertainty due to the choice of a single magnetic field value for the Zeeman pattern reconstruction. From a single discharge point of view, the main source of uncertainty on the DSS T_i is given by the low SNR of low-emissivity spectral lines. But in a *frequentist* approach, when a large number of repeat discharges is considered, these are reduced and dominated by the variation of the machine conditions over time.

We note that a study of the effect of instrumental function uncertainties on the temperature estimates was not discussed in this work. However, it could become non-negligible for C III at T_i(C III) $\lesssim$ 3.8 eV and for He II at T_i(He II) $\lesssim$ 1.2 eV, if the Doppler broadening becomes comparable to that of the instrumental function. These uncertainties can arise from shifts in the spectral line position due to uncertainty in the grating position reproducibility or possibly following differences in the integration times used in the instrumental function characterisation with respect to those used experimentally. We shall see, however, that these temperature limits are not problematic in the experiments presented in chapters 4 and 5. The statistical uncertainties discussed in this section are, thus, the dominant contribution to the uncertainty in the ion temperature measurements used herein.

4 Experimental results

As introduced in chapter 2, the physics of divertor plasma detachment is extensively studied at TCV using numerous diagnostics. Fil et al. (2018) [67] and Février et al. (2020) [35] present the two main methods for attaining detachment in TCV: the first increases the core plasma density, often through injecting additional working gas (i.e. *density ramp*) while in the second injects impurity species, again often gaseous, that enhance the radiated power losses in the divertor region (i.e. *impurity seeding*). SOLPS-ITER simulations in Smolders et al. (2020) [121] illustrate the main differences between these methods. Both processes feature a reduction of the power fluxes at the target, the main objective of divertor detachment, but this is attained in different ways. In density ramps, we observe an increase in the target particle flux with a substantial, simultaneous, decrease in the target temperature. Conversely, impurity-seeded detachment maintains a relatively high particle temperature at the target but features a significant reduction of the target particle flux. From the recent advances presented in Verhaegh et al. (2021) [93], we also know that plasma-molecular interactions represent a primary particle sink process in density ramps by molecular-assisted recombination, but their role is lessened in impurity-seeded discharges. These interactions affect divertor detachment physics becoming increasingly important at relatively low temperatures.

The analysis technique presented in section 3.2 allows us to measure the ion and neutral temperatures associated with the observed species. This is useful in detachment-related experiments, where the DSS provides temporal evolutions and 1-D spatial measurements of several species' T_i. Indeed, the ions do deliver power to the target, but a complete picture of the evolution from an attached to a detached regime also requires information on the electron temperature T_e and density n_e, as they are the main parameters responsible for excitation and ionisation processes. DSS data provides part of this information that is complemented by the other diagnostics data, and, as collisionality increases in the detachment experiments later presented in this chapter, T_i will be directly compared with T_e (see section 5.1).

As an example, the electron temperature T_e and density n_e can be measured by the divertor extension of the TS system, but only for plasma locations in the laser's beam path, while the MANTIS diagnostic can provide 2D poloidal information on the spectral lines' emission

profiles. TS and MANTIS data can be fruitfully combined to study the electron temperatures for which particular atomic transitions occur or extinguish, as we will see, for instance, in the case of the C III radiation in section 5.2, that has long been used as a detachment proxy.

4.1 Discharge scenario

The studied discharges featured deuterium density ramps, leading the divertor towards the onset of detachment. The chosen divertor leg geometry allowed the TS system to sample n_e and T_e in the SOL and obtain these quantities profiles using repeat discharges.

Main experimental parameters							
discharge #	73912	73914	73942	74212	74213	74215	74216
R_t [m]	0.888	0.880	0.900	0.866	0.880	0.906	0.855
I_p [kA]				250			
B_{tor} [T]			~ 1.4 (at the divertor leg radius)				
field direction				reversed			
heating				ohmic			
confinement mode				L-mode			
main species				D, C (natural impurity)			
He puff			6×10^{19} particles/s from 0.300 to 0.400 s				
FIR max nel [10^{19} m^{-3}]	9.70	9.63	10.37	11.66	11.70	14.28	13.23
HR-DSS settings							
Spex A	He I	D_α C II	D_β	D_β	C II	He I	D_α
Spex B	C III He II	D_γ	D_ε	C III He II	C III He II	D_ε	D_ε

Table 4.1: Main parameters of the studied discharges.

This thesis studies the evolution of the TCV divertor evolving toward a detached scenario using a set of seven deuterium density ramps. These were characterised by a 250 kA plasma current, a reversed $\vec{B}$ field direction (i.e. with the ion ∇B drift pointing away from the X-point, making the configuration unfavourable to H-mode access), and featured the long-legged divertor geometry shown in figure 4.1a), where an orange solid line indicates the configuration separatrix position. The main plasma species is deuterium, while carbon is often the most abundant impurity due to TCV's graphite tile erosion. A small helium gas injection enhances the emissivity of helium spectral lines, over that remaining for the inter-discharge He glow discharge cleaning, facilitating the line-shape analysis illustrated in 3.2 by increasing the signal strength.

This gas is injected from $t = 0.300 - 0.400$ s before the final magnetic equilibrium is established, with a flux of $6 \cdot 10^{19}$ particles per second, for a total of $\approx 6 \cdot 10^{18}$ He atoms injected. This value is a trade-off between signal strength and the wish to keep He as a trace impurity that does not affect the detachment physics we wish to study. Experimental parameters for this discharge
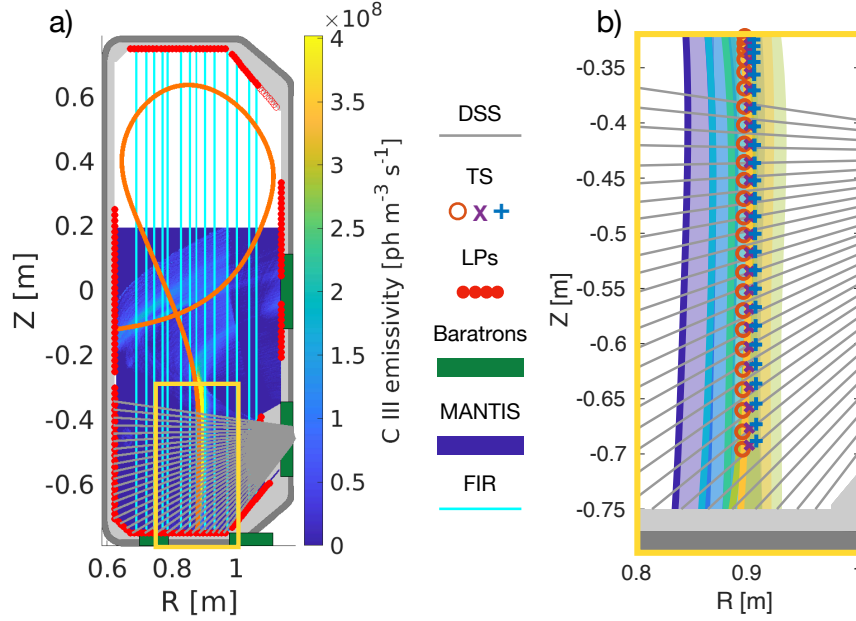
set are given in table 4.1.

Figure 4.1: a) An example of a magnetic equilibrium used in the experiments described in this chapter is plotted in orange. The solid grey lines in the divertor region represent the DSS LOSs. The blue area indicates the MANTIS field of view in the poloidal plane, for the C III 4650 Å emission intensity shown with the blue to yellow colour map. Wall-embedded Langmuir probes and baratron gauges are indicated with red dots and green rectangles. The fourteen FIR vertical beams are plotted in cyan. Panel b) is a zoom of the yellow rectangle enclosing the divertor leg. Here the TS probing locations, indicated by the o, x and + symbols, are over-plotted on the outer divertor legs. Thicker lines represent the separatrix, while the shaded area represents a section of the SOL relative to each separatrix. A representation of the complete repeat discharges set is represented in figure 4.2

.

TCV's signature flexibility in creating precisely positioned magnetic configurations is exploited to align the outer divertor leg position to the TS probing locations and, through discharge repeats, to scan the leg's radial position, R_t, across ~ 6 cm. The position of the leg is re-constructed by Liuqe [38], with an accuracy of $\lesssim 1$ cm in the divertor region. However, the agreement with other independent diagnostics e.g. MANTIS and LPs, on the evaluation of the separatrix position and of the strike points, makes this uncertainty considerably smaller. A close-up of the outer divertor leg region is drawn in figure 4.1b). Here the outer divertor leg position of each discharge is shown by coloured solid lines, with the dark blue indicating $R_t = 0.855$ m and the bright-yellow $R_t = 0.906$ m, the two extremities of the radial scan. The fixed TS probing volumes -with respect to the machine vessel-, located at ~ $R = 0.9$ m, are indicated with the o, x and + symbols illustrating the three lasers paths of the TS system.

These were independently fired in bursts with a 20 Hz cycle frequency throughout the density
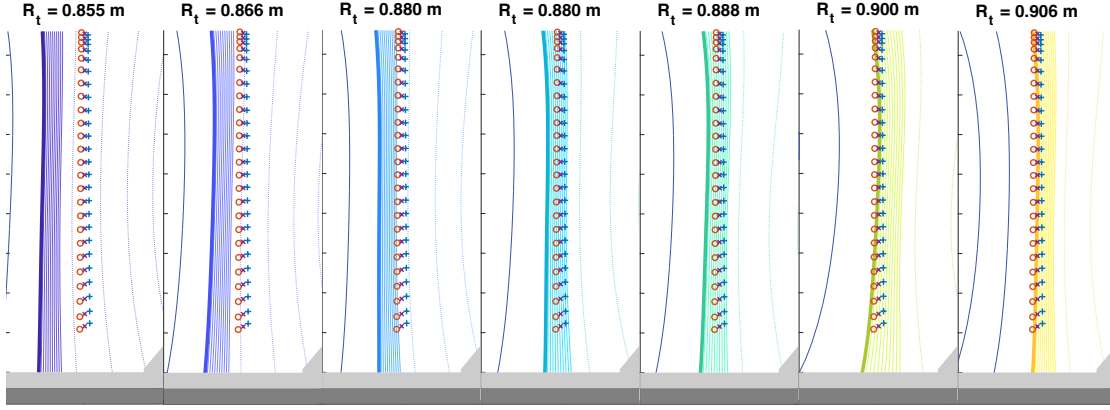
Figure 4.2: Expansion of figure 4.1b, separately displaying the outer divertor leg of each discharge. The TS probing volumes are also shown to indicate the relative distance from the separatrix for each repeat discharge.

ramps. The time interval between three consecutive laser triggers of one cycle is set to its minimum of 1 ms (i.e. *burst mode*). Using this firing mode, the evolution of the plasma within the 3 ms triggering cycle is considered negligible. In contrast, gradual variations are observed between consecutive cycles. Figure 4.2 illustrates how the fixed TS laser beams observe different portions of the plasma divertor SOL across the repeat discharges. The displacement of the separatrix is such that they move from observing the far SOL in the blue separatrix case, i.e. $R_t = 0.855$ m, to the private flux region in the yellow case, i.e. $R_t = 0.906$ m.

The discharges listed in table 4.1 are considered repeats of the same scenario, with only R_t varied. Indeed, the plasma current I_p and the neutral pressure measured by the divertor baratron gauge show highly similar temporal traces for the discharges, in figures 4.3a) and 4.3b). However, some differences can be observed in figures 4.3c) and 4.3d) by, respectively, the line-averaged density, or *nel*, averaged over all the Far InfraRed (FIR) beams and the average core density measured by the FIR chord at the TS radius, corrected by the TS measurements of n_e in the core.

The central beam of the FIR diagnostic was used as the real-time observer in the feedback-controlled density ramps, acting on the D_2 fuelling flux. However, the magnetic equilibrium is such that a large part of the measured line-integrated density, up to $\approx 50\%$, can result from the divertor plasma, depending on the portion of SOL observed by the central FIR channel during the R_t scan. This can affect the D_2 fuelling rates of otherwise identically programmed density ramps depending upon the divertor leg position. A more reliable parameter in parameterising the core density is provided by TS, since, as mentioned in section 2.2, it separately evaluates core and divertor densities, due to its cross-beam measurements. The real-time feedback control on the FIR core density resulted in up to a 20% deviation between the repeat discharges, as shown in figure 4.3d).

The target particle flux represented in figure 4.3e) and f) is measured by wall-embedded

Langmuir probes on the TCV floor and in some of the tilted tiles. As discussed in section 1.3, this is one of the critical parameters in estimating divertor detachment. In detachment-relevant density ramps, detachment follows three phases. At first, the ion saturation current is observed to linearly increase with the core density, until a *saturation* level. The onset of detachment is usually taken to occur when a particle flux *rollover* -a decrease in the ion saturation current- is observed when further increasing the core density, as in [53, 77, 122]. No particle flux rollover was observed in these discharges. However, as shown in figure 4.3f), a saturation occurs in all the repeat discharges for similar values of core density, at $n_{e,core} \approx 5 - 5.5 \cdot 10^{19}$ m^{-3}.

In conclusion, these experiments are unsuitable for probing the physical processes associated with the detached state. Still, we will see in sections 4.3, 4.4 and in chapter 5 how they can illustrate in detail the evolution of many parameters of interest (e.g. T_e, n_e, p_e, T_i,...) along the entire divertor leg as we evolve towards a detached regime.
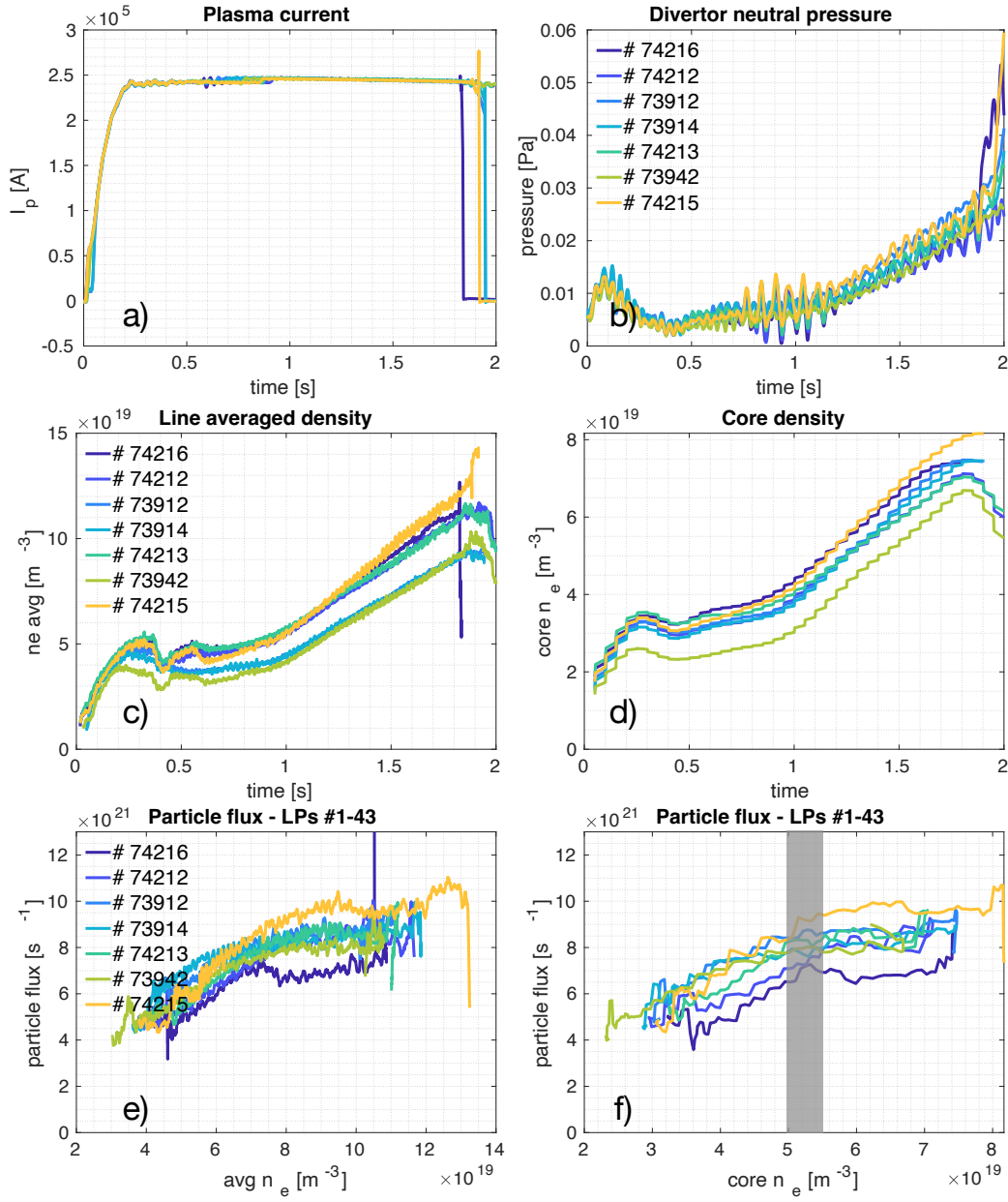
Figure 4.3: Time traces of a) plasma current, b) neutral pressure measured by the divertor baratron, c) line averaged density measured averaged over all the FIR beams, and d) average core density measured by FIR and corrected by TS. Panel e) and f) show the target particle flux measured by the floor LPs, respectively plotted as a function of line averaged density and average core density. In the last panel, the shaded region marks the transition to the saturated ion flux regime, taking place at similar values of core density.

4.2 Characteristic times of relevant processes in the divertor plasma

In chapter 5, we compare electron and ion temperatures. To understand the experimental findings, it is first necessary to show the various time scales of the plasma processes relevant to this study. In this section, these are divided into processes involving the main plasma, the impurities and neutral particles.

4.2.1 Time scales for main plasma particles

Electron-electron energy transfer is the fastest of the considered interactions, while the thermalisation between ions and electrons occurs over an $\approx 2000\times$ longer time scale.

Equations 4.1 report the typical energy and momentum transfer frequencies, indicated by $v_{E_k}^{j/k}$ and $v_p^{j/k}$ respectively, between the projectile species j interacting with the target species k. The treatment used to derive the equations shown in eq. 4.1 is illustrated in chapter 9 of *Plasma Physics and Fusion Energy* by J. Freidberg [123].

$$
\begin{array}{cccc}
\text{Particles} & \text{Energy} & & \text{Momentum} \\
e \to i & v_{E_k}^{e/i} = n_i \dfrac{Z^2 e^4}{2\pi \varepsilon_0^2} \dfrac{\ln \Lambda}{m_i m_e v_e^3} & & v_p^{e/i} = v_{E_k}^{e/i} \dfrac{m_i}{2m_e} \\[2ex]
i \to e & v_{E_k}^{i/e} = n_e \dfrac{Z^2 e^4}{2\pi \varepsilon_0^2} \dfrac{\ln \Lambda}{m_i m_e v_i^3} & & v_p^{i/e} = \dfrac{1}{2} v_{E_k}^{i/e} \\[2ex]
i \to i & v_{E_k}^{i/i} = n_i \dfrac{Z^2 e^4}{2\pi \varepsilon_0^2} \dfrac{\ln \Lambda}{m_i^2 v_i^3} & & v_p^{i/i} = v_{E_k}^{i/i} \\[2ex]
e \to e & v_{E_k}^{e/e} = n_e \dfrac{Z^2 e^4}{2\pi \varepsilon_0^2} \dfrac{\ln \Lambda}{m_e^2 v_e^3} & & v_p^{e/e} = v_{E_k}^{e/e}
\end{array}
\tag{4.1}
$$

where n_i and n_e are respectively the ion and electron densities, m_i and m_e the ion and electron masses, v_i and v_e the ion and electron velocities, ε_0 the vacuum permittivity and e the electron charge. The quantity $\ln \Lambda$ is the Coulomb logarithm,

$$
\Lambda \approx \frac{12\pi \varepsilon_0^{3/2} T_e^{3/2}}{n_e^{1/2} e^3}
\tag{4.2}
$$

where $\ln \Lambda \approx 10$ for divertor relevant parameters, i.e $n_e = 2 \cdot 10^{19}$ m^{-3}, $T_e = 20$ eV. Equations 4.1 provide the collision frequencies for particles of a given velocity. However, plasma particles -at least in the divertor region- are characterised by a velocity distribution, that is usually assumed to be Maxwellian, characterised by a temperature T.

$$
f(\vec{v}) = \left(\frac{m}{2\pi kT} \right)^{3/2} 4\pi v^2 \exp\left(-\frac{mv^2}{2kT} \right)
\tag{4.3}
$$

A Maxwellian velocity distribution represents an ensemble of particles in thermal equilibrium, for which a *temperature* is well defined. Averaging equation 4.1 over a Maxwellian distribution results in equation 4.4, derived in the *Kinetic theory of plasmas lecture notes* by A. Fasoli [124]

Particles	Momentum	Energy	
$e \to i$	$\bar{v}_p^{e/i} = \dfrac{1}{3}\sqrt{\dfrac{2}{\pi}} n_i \dfrac{Z^2 e^4}{4\pi\varepsilon_0^2} \dfrac{\ln\Lambda}{m_e^{1/2} T_e^{3/2}}$	$\bar{v}_{E_k}^{e/i} = \dfrac{2m_e}{m_i}\bar{v}_p^{e/i}$	
$e \to e$	$\bar{v}_p^{e/e} \simeq \dfrac{1}{\sqrt{2}}\bar{v}_p^{e/i}$	$\bar{v}_{E_k}^{e/e} = \bar{v}_p^{e/e}$	(4.4)
$i \to e$	$\bar{v}_p^{i/e} \simeq \dfrac{n_e m_e}{n_i m_i}\bar{v}_p^{e/i}$	$\bar{v}_{E_k}^{i/e} = 2v_p^{i/e}$	
$i \to i$	$\bar{v}_p^{i/i} \simeq \dfrac{1}{\sqrt{2}}\sqrt{\dfrac{m_e}{m_i}}\left(\dfrac{T_e}{T_i}\right)^{3/2}\bar{v}_p^{e/i}$	$\bar{v}_{E_k}^{i/i} = \bar{v}_p^{i/i}$	

Using Maxwellian averaged momentum and energy transfer frequencies between charged particles, we show a hierarchy of characteristic time scales $\tau = \bar{v}^{-1}$, sketched in figure 4.4. The fastest time scales of the main plasma collision processes are given by electron momentum transfer on ions, $\tau_p^{e/i}$, and electron-electron momentum and energy transfer, of the order of $\sqrt{2}\bar{\tau}_p^{e/i}$. The electrons can be considered thermalised in a time scale of $\bar{\tau}_{E_k}^{e/e}$. The intermediate time scales are given by ion-ion momentum and energy transfer, of the order of $\bar{\tau}_p^{i/i}$ and $\bar{\tau}_{E_k}^{i/i}$. Finally, the longest time scales of the main plasma collisional processes are given by the electron-ion and ion-electron energy transfer, of the order of $\bar{\tau}_{E_k}^{i/e}$. Figure 4.5 plots the energy transfer times calculated using equations 4.4 for a deuterium plasma, i.e. $Z = 1$, for two plasma regimes relevant to the experiments presented in section 4.1.
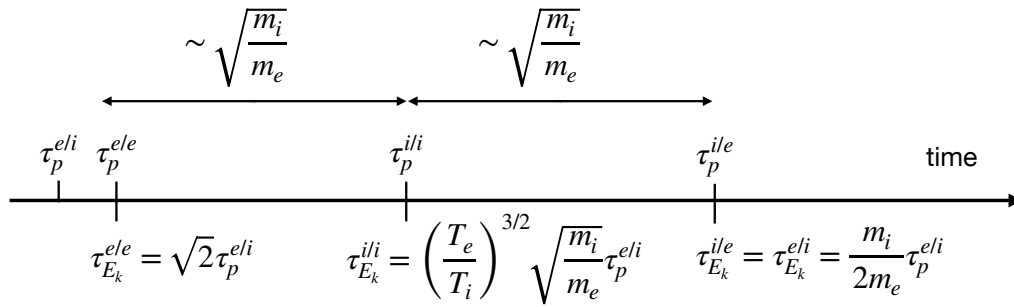

Figure 4.4: Hierarchy of momentum and energy transfer characteristic time scales. Sketch adapted from [124]. Time scales of other representative time scales are illustrated in figure 4.9 for typical divertor plasma parameters, displaying the separation between them.
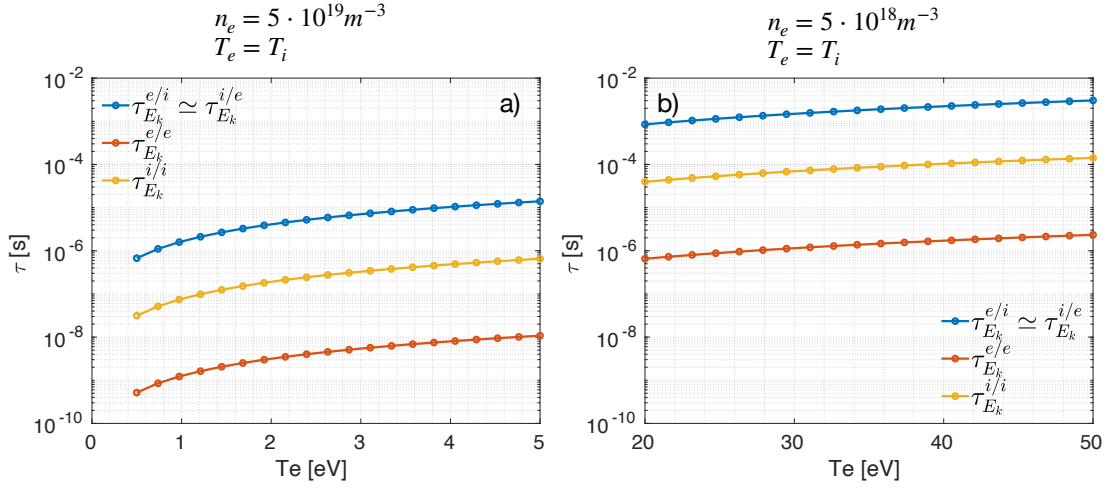
Figure 4.5: Energy transfer time as in equations 4.4 for $e \longrightarrow e$ in red, $i \longrightarrow i$ in yellow, and $i \longrightarrow e$ and $e \longrightarrow i$ in blue for two regimes. In panel a), we calculate the τ_{E_k} for typical detachment-relevant plasma parameters, e.g. $T_e < 5$ eV and $n_e = 5 \cdot 10^{19}$ m^{-3}, while in panel b) for parameters typical of attached plasmas e.g. $T_e > 20$ eV and $n_e = 5 \cdot 10^{18}$ m^{-3}.

4.2.2 Time scales for impurity ions

Impurity particles thermalise faster with deuterium nuclei than with electrons. Thermalisation and ionisation are the two main processes considered for understanding impurity particles' temperature evolution.

The energy transfer frequency between impurity ions and main plasma species, i.e. deuterium ions and electrons, is given by equation 4.5, from the NRL Plasma Formulary by J. D. Huba (1998) [125], indicating with the subscript α the parameters related to the impurity ions and with the subscript β those related to deuterium or electrons:

$$\bar{\nu}_{E_k}^{\alpha/\beta} = 1.8 \cdot 10^{-19} \frac{\sqrt{m_\alpha m_\beta} Z_\alpha^2 Z_\beta^2 n_\beta \lambda_{\alpha\beta}}{\left(m_\alpha T_\beta + m_\beta T_\alpha\right)^{3/2}} \tag{4.5}$$

where $\lambda_{\alpha\beta}$ is defined as

$$\lambda_{\alpha\beta} = 23 - \log\left(\frac{Z_\alpha Z_\beta (m_\alpha + m_\beta)}{m_\alpha T_\beta + m_\beta T_\alpha} \cdot \sqrt{\left(\frac{n_\alpha Z_\beta^2}{T_\alpha} + \frac{n_\beta Z_\alpha^2}{T_\beta}\right)}\right) \tag{4.6}$$

and where m_α and m_β are expressed in g, n_α and n_β in cm^{-3}, T_α and T_β in eV. Finally, the thermalisation time is given by

$$\bar{\tau}_{E_k}^{\alpha/\beta} = 1/\bar{\nu}_{E_k}^{\alpha/\beta} \tag{4.7}$$
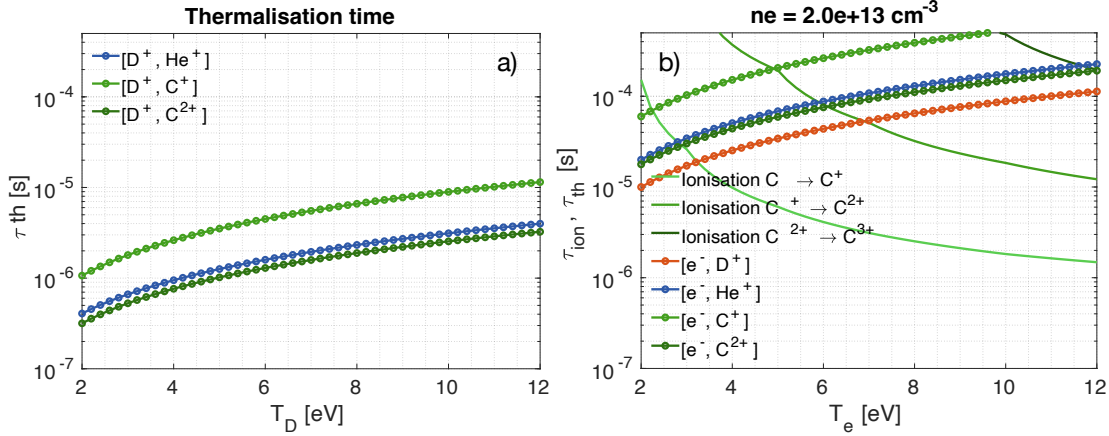
Figure 4.6: Ionisation and thermalisation times for several species plotted as a function of temperature. In panel a), we consider the thermalisation of carbon and helium ions born at $T_i = 0.5$ eV with deuterons. In panel b), we consider the thermalisation of the same species of panel a) and deuterium born at $T_i = 0.5$ eV with electrons, comparing them with C species ionisation times.

In figure 4.6a) we show the thermalisation time of C II, C III and He II impurity ions with D^+ as a function of D^+ temperature, while in figure 4.6b) the thermalisation time of electrons with ion species, including deuterium, plotting the results as a function of T_e. In these calculations, we take the ions' initial temperature of $T_i = 0.5$ eV. However, the choice of the initial T_i has only a small effect on the thermalisation time. In this calculation, we assumed that the plasma densities of $n_\beta = n_{D^+} = n_{e^-} = 2 \cdot 10^{19}$ m^{-3}, from TS. The impurity density $n_\alpha = n_{C\ II} = n_{C\ III} = n_{He\ II}$ was assumed to be 1% that of deuterium ions and electrons. For such densities, the thermalisation times $\tau^{C\ II/C\ III}$, $\tau^{C\ III/C\ II}$, $\tau^{C\ II/He\ II}$, ..., are more than $10\times$ longer than the thermalisation times of the impurity ions with D^+. Therefore, direct interactions between impurities alone can be neglected.

Figures 4.6a and b show that impurity ions thermalise with $D^+ \approx 50 - 100 \times$ times faster than with the electrons so that if $T_{D^+} \neq T_e$, they will tend to a distinct D^+ temperature. Therefore, in certain conditions, the measurement of impurity ions' temperature may be used as an indirect determination of the D^+ temperature in the divertor.

In chapter 5, we will consider the evolution of the fractional abundance based on an ionisation balance model and temperature evolution of the impurity and neutral particles in the divertor leg plasma and show how this affects the DSS measurements. Therefore, another important time scale to consider herein, and to be compared to the thermalisation time, is the ionisation time of such impurities. Figure 4.6b presents the ionisation times of C, C^+ and C^{2+} as a function of T_e, computed from the *effective ionisation coefficients* (SCD files) from the Open Adas database [126]. By comparing figures 4.6a and b, we see that ionisation happens on shorter time scales than those for impurity thermalisation with D^+ only at relatively high T_e.

4.2.3   Time scales for neutral atoms

The two main processes involving neutral particles are their ionisation and the crossing of the divertor leg, occurring on similar time scales. For neutral deuterium, charge exchange with D^+ has to be considered. Conversely, the thermalisation of neutral particles with the plasma ions occurs on the longest time scales.

The divertor plasma we observe with the MANTIS and DSS systems is characterised by significant neutral deuterium and helium radiation (probably also from carbon, but no C I line exists in the spectral range of our systems) despite the relatively high T_e. This observation is a strong indication of the presence of a substantial inflow of neutrals within the divertor plasma, and therefore, neutral species and their interaction with the charged particles must be included in the plasma ensemble description.

As our plasma is highly ionised and we are interested in the thermalisation of neutrals with D^+ in the divertor leg plasma, we can write a formula for the neutral-to-D^+ energy transfer in the following way

$$\bar{v}_{E_k}^{n/D^+} = n_{D^+} \cdot \sigma_s^{D^+|n} \cdot v_{th,D^+} \cdot \frac{2m_D}{m_D + m_n} \tag{4.8}$$

where subscript n indicates neutral quantities. The formula applies for $\sqrt{\frac{kT_n}{m_n}} < \sqrt{\frac{kT_{D^+}}{m_{D^+}}}$, where T_n and m_n are respectively the neutral temperature and mass. The cross-section $\sigma_s^{D^+|n}$ of hydrogen atoms and molecules interacting with neutral and plasma particles are presented in [127], where they were calculated by approximating the plasma-neutral scattering as a hard-sphere collision. Here, from the point of view of the charged particle, the neutral atoms can be approximated by a sphere with a Van Der Waals radius. A list of Van Der Waals radii for several neutral species is presented in [128]. For deuterium, helium, and carbon, these are respectively $r_D = 1.2$ Å, $r_{He} = 1.4$ Å and $r_C = 1.7$ Å.

Figure 4.7a) illustrates the thermalisation times of neutral deuterium, helium and carbon atoms with deuterium ions computed with equation 4.8. Here we used $n_e = 2 \cdot 10^{19}$ m^{-3}, from TS measurements. These time scales are to be compared to the time taken for neutrals to cross the divertor leg, e.g. transit time, and to the time scales of neutral ionisation. Transit times computed using thermal velocities for neutral deuterium, helium, and carbon are illustrated in figure 4.7b) as a function of neutral temperature. These were calculated considering a leg width $\Delta L = 3$ cm, referring to FWHM of the pressure radial profiles illustrated in figure 4.14 and 4.15 and an average length travelled by neutrals of $\Delta L / \sin(\pi/4)$.

Figure 4.8 compares the characteristic times of neutral deuterium, helium and carbon. The data for deuterium are illustrated in panel a). Here, for $T_e \gtrsim 10$ eV, ionisation is faster than thermalisation and the atomic transit time across the divertor plasma. For $5 \lesssim T_e \lesssim 10$ eV, depending upon the incoming velocity of the neutral particles, ionisation and transit across the divertor leg occur on similar time scales, implying a finite probability of relatively *hot*
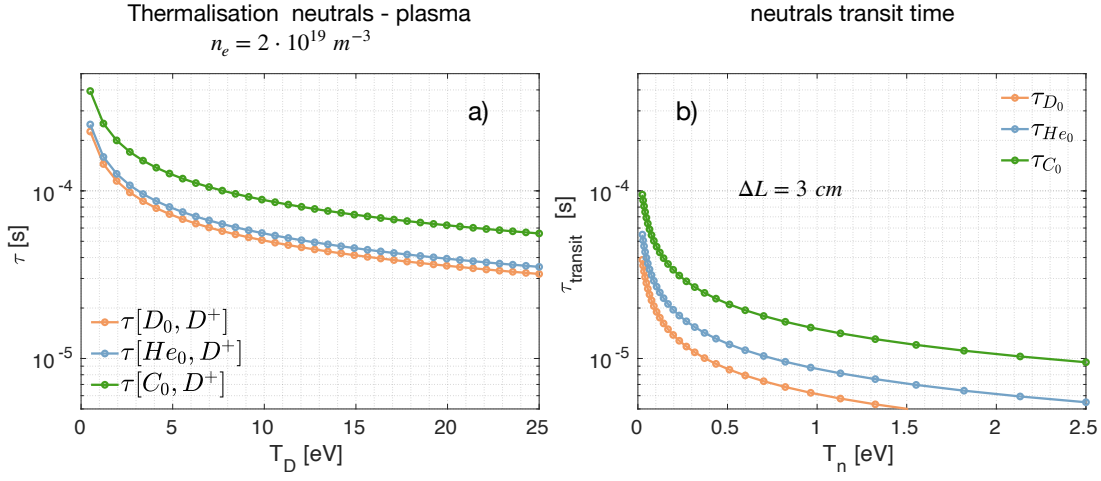
Figure 4.7: thermalisation time a) transit time b)
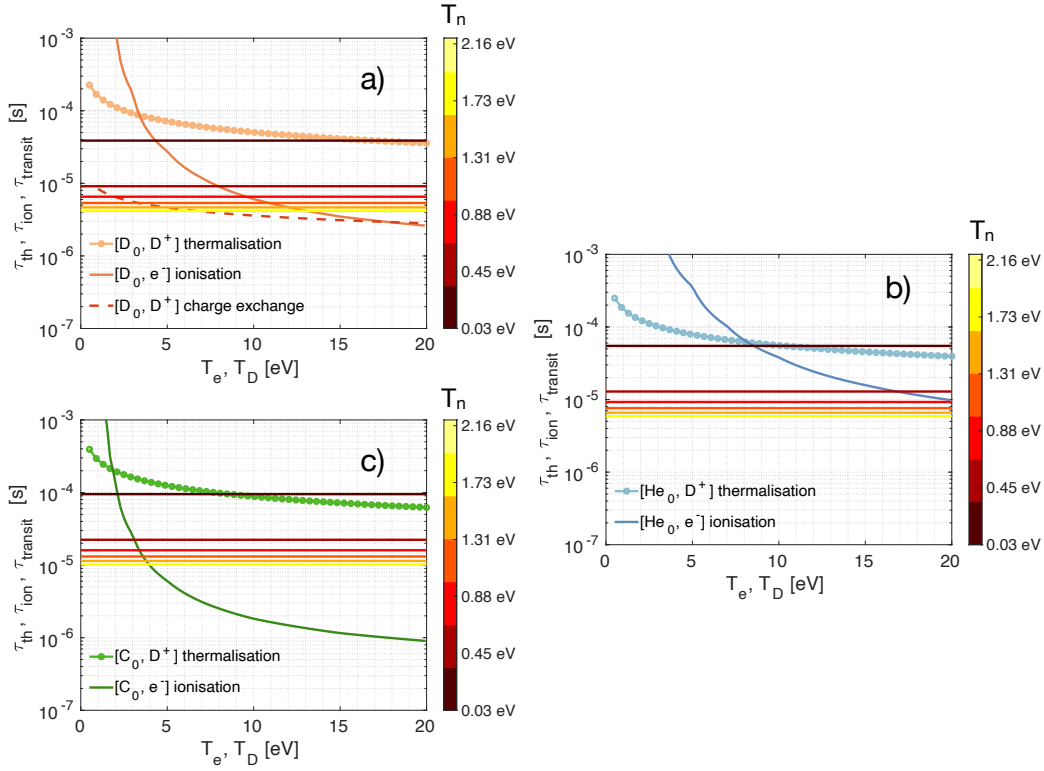
Figure 4.8: Neutral deuterium (a), helium (b) and carbon (c) ionisation, thermalisation with plasma and transit across the divertor leg characteristic times. The temperature of the neutral particles used to compute the transit times is indicated by the colourmap on the right of panel c), ranging from wall temperature i.e. $T_n \approx 0.03$ eV to $T_n \gtrsim 2$ eV. The data used for computing the ionisation times as a function of T_e are taken from OPEN-ADAS [126], and plotted for $n_e = 2 \cdot 10^{19}$ m^{-3}. The charge exchange of D$_0$ with D$^+$, indicated in panel a, is taken from [129].

neutrals, i.e. $T_n \approx 1$ eV, to cross the leg without being ionised. Thermalisation of neutrals by ionised deuterium occurs on significantly longer time scales than the two other processes in the considered range of T_D. For deuterium, a fourth relevant reaction is considered: charge exchange CX between cold neutrals and D^+ ions that occur on similar time scales of transit and ionisation. The data illustrated in panel a) for this CX reaction are taken from Swaczyna et al. (2019) [129], while it can be neglected for C and He neutrals with D^+. Panel 4.8b) illustrates the reaction time scales for neutral He. This element is characterised by a higher ionisation energy than deuterium and thus by an ionisation time in the explored T_e range that is over $\approx 10\times$ longer. This implies that neutral He particles have a high probability of crossing the divertor leg without ionising or thermalising with the divertor plasma. Finally, neutral carbon data are reported in panel c). This element ionises on faster time scales than helium and deuterium for the same T_e, and for $T_e \gtrsim 4$ eV, this is the fastest process involving neutral carbon atoms.

Following these considerations, the thermalisation of neutral particles within the divertor leg ions can be ruled out, as it occurs on longer time scales than those required for ionisation or in the crossing of the divertor leg. Depending upon the energy at which the neutral particles arrive, they can cross the divertor leg without ionising: in that case, the emission measured by the DSS would be that of a cold neutral species through their excitation by the divertor leg plasma. This is true under the assumption that the emission mainly originates from electron-impact excitation. If neutrals arrive with low kinetic energy, i.e. at wall temperature, they will have a high probability of ionising within the divertor leg. These particles will then contribute to the emission of the ionised species, but at least initially, with a temperature close to that of the neutral particles. Once ionised, the cold particles will fast thermalise with deuterium ions, on time scales of $10^{-7} - 10^{-5}$ s -referring to figure 4.6- contributing to decreasing their temperature.

Figure 4.9 visually summarises this section, comparing the time scales of the considered processes of all the species treated in this thesis. The characteristic time scales are calculated for $n_e = 2 \cdot 10^{19}$ m^{-3} and electron temperature in the range of $T_e = 2$ - 12 eV. $e - e$ thermalisation is, by a large margin, the fastest process. The T_e measured by TS can therefore be taken as *the* temperature for the electrons at the probing location. Despite occurring on longer time scales than e-e thermalisation, D^+-D^+ thermalisation and D^+-impurity ions thermalisation are faster than the other relevant processes. This makes the T_i measured by the DSS also well-defined. The emission lines of neutral atoms, instead, would carry the information on the neutral atoms excited while crossing the divertor leg but also, in the case of deuterium, on those resulting from CX reactions with typically hotter D+ ions.
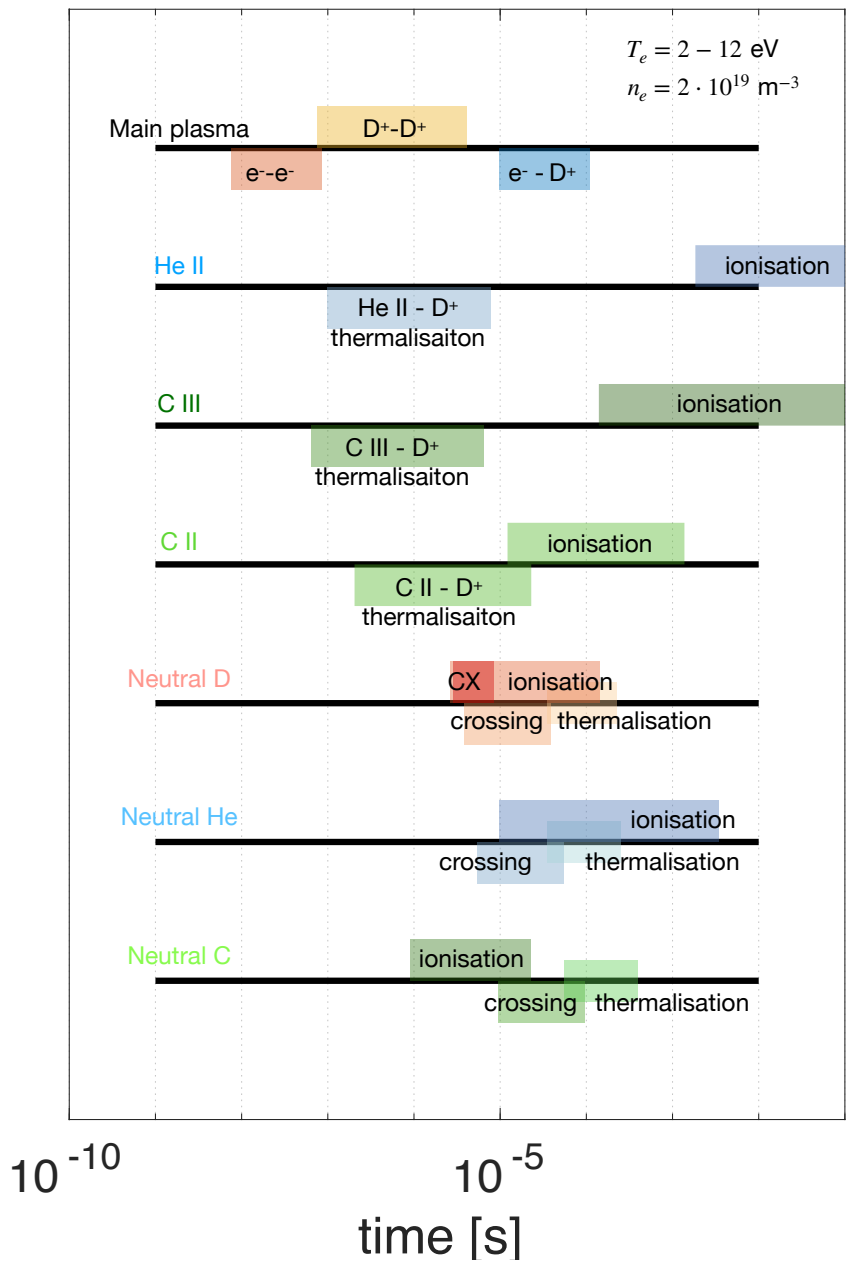
Figure 4.9: Hierarchy of the time scales for the relevant processes occurring in the divertor.

4.3 Measurements of plasma parameters poloidal profiles with MANTIS and TS

The leg position radial scan offers the unique opportunity to reconstruct, in a non-invasive way, T_e and n_e and to compare these to several species' emissivity radial profiles. It is also possible to directly derive profiles of the electron pressure p_e. T_e and p_e are observed to decrease across the density ramp, while n_e increases in the target vicinity.
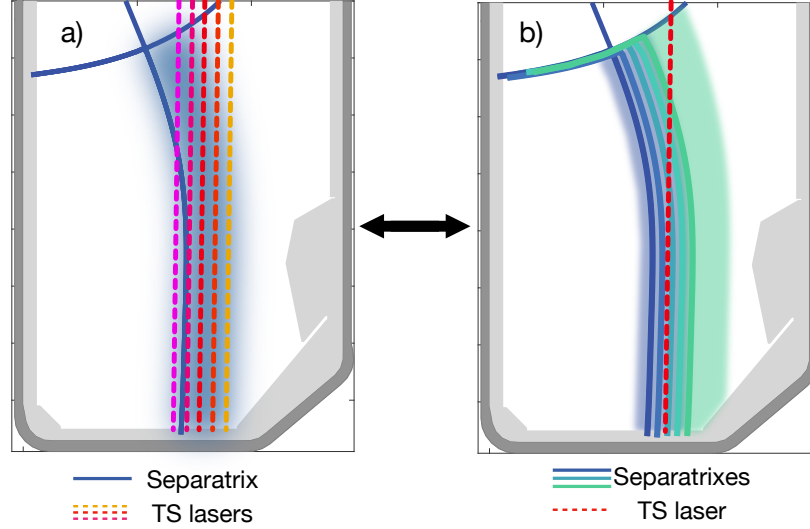

Figure 4.10: Panel a) represents five virtual TS laser beams probing the entire SOL width, indicated by the blue shaded region next to the separatrix. Panel b) represents multiple magnetic equilibria for which a single TS laser beam probes multiple SOLs. During a leg position scan, as done in these experiments, the fixed TS lasers probed different open flux surfaces according to the relative distance between the separatrix and the beam. This is equivalent to probing the entire SOL using many lasers, each positioned at a different distance to the plasma separatrix.

We have seen in section 2.2 that the TS system's divertor extension has three laser beams, positioned separately in the reference frame of the TCV vessel. As illustrated in figure 4.1b), the R_t of each radial divertor chord allows the TS system to probe three different major radii in the plasma SOL when independently firing the lasers. Using repeat discharges to generate the same plasma conditions, it is possible to reconstruct radial and vertical profiles of T_e and n_e by combining the TS data array for the same values of the core density.

This is illustrated in figure 4.11. Here, panel a) illustrates a close-up of TCV's poloidal cross-section of the divertor leg region, similar to that of figure 4.1. The TS probing volumes, the divertor leg and the DSS LOSs are plotted over the C III emissivity 2D map reconstructed by MANTIS for a core density of $5 \cdot 10^{19} \, \mathrm{m}^{-3}$.

To compare the reconstructed plasma profiles to the DSS measurements, we consider the TS
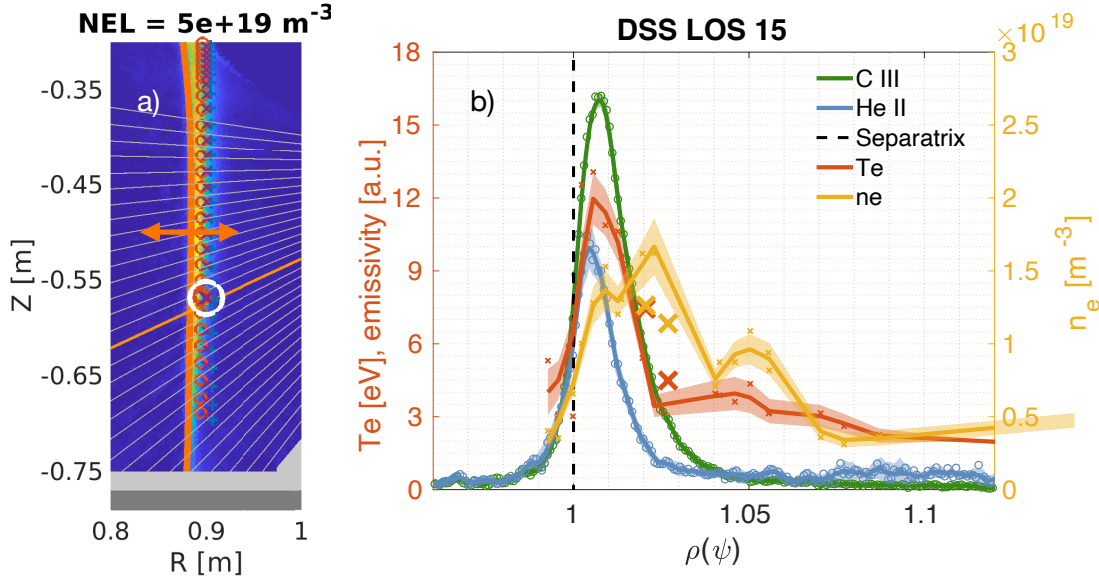
Figure 4.11: Panel b) represents, with the red and yellow lines respectively, the radial profiles of the TS T_e and n_e, acquired over the seven repeats at the TS probing locations enclosed in the white circle of panel a), for an average core density of $5 \cdot 10^{19}$ m^{-3}. The solid lines represent an interpolation of the measured data, which are indicated by the small crosses of the same colours. The larger symbols highlight the data collected in the configuration chosen for this example and are represented in panel a). The double arrow indicates the radial displacement of the separatrix in the other repeats, enabling TS to sample the rest of the data series. The green and blue lines represent the radial profiles of MANTIS C III and He II normalised emissivity measured along the DSS LOS 15, highlighted in orange in panel a), acquired for the same value of core density. The same colour code is used in figures 4.12 and 4.13.

probing volumes closest to the intersection between the DSS LOS and the separatrix, where MANTIS indicates the peaking of the species' emissivity.

Both MANTIS and DSS chords are observing the same plasma volumes. This is made explicit in panel a) where the DSS LOS 15 is highlighted in orange: this line crosses the separatrix in the proximity of the TS probing volumes enclosed in the white circle, of which data is represented by the large 'X' symbols in panel b). Repeating this procedure over the repeat discharges allows us to compose the profiles illustrated in panel b). The data measured by TS are represented in figure 4.11b) with the red and yellow crosses, respectively, indicating T_e (LHS) and n_e (RHS) data points. The red and yellow solid lines interpolate the TS data to generate a smooth radial profile for both quantities while preserving any possible secondary profile peak. The TS data are, in this thesis, considered to be the *truth*, the base upon which the validation of the DSS T_i measurements is posed, and upon which the divertor state is characterised.

The profiles are plotted as a function of the normalised poloidal flux

$$\rho(\psi) = \sqrt{(\psi - \psi_0)/(\psi_{LCFS} - \psi_0)} \tag{4.9}$$

where ψ_0 and ψ_{LCFS} are the poloidal flux values at the magnetic axis and at the separatrix. The latter, corresponding to $\rho(\psi) = 1$, is indicated with a dashed black line.

Additionally, to T_e and n_e, the emissivity radial profile of the observed spectral lines is reconstructed poloidally by MANTIS tomographic inversions, associated with the same DSS LOS. In figure 4.11b), we chose to plot C III, in green, and He II emissivity, in blue, with the same $\rho(\psi)$ coordinate. The MANTIS data are reconstructed using the inversions of a single discharge, #74213, on a custom grid. The emissivities are normalised to each species' global maximum, to compensate for the changes in the intensities of the spectral lines (e.g., in attached divertor conditions, C III is $\approx 30\times$ brighter than He II) and to the maximum T_e, for representation purposes only, to meaningfully plot them on the same T_e axis.
In résumé, figure 4.11b) represents a snapshot of such radial profiles, acquired for $n_{e,core} = 5 \cdot 10^{19}$ m^{-3} and to a vertical distance from the target of ≈ 18 cm, associated with the DSS LOS #15.

In figures 4.12 and 4.13, on page 90 and 91, we can see other examples of this plot, using the same colour coding, representing the data acquired for four, increasing, core densities at three locations along the outer divertor leg.

To visualise the evolution of the profiles in the divertor when increasing their degree of detachment, we can picture these two pages as a single figure - or as a table - composed of four rows and four columns. The TCV poloidal cross sections in the first row indicate the three DSS LOSs with the orange lines and their associated TS probing volumes, each enclosed in the numbered white circles. From left to right, they capture the divertor at four increasing values of core density. The MANTIS inversions for the C III emissivity are also shown. The colour bar is omitted, as the relative change in intensity, rather than its absolute value, is the critical parameter in our description. The chosen normalisation is the same as in figure 4.11. Following the increase in core density from $4 \cdot 10^{19}$ m^{-3} to $7 \cdot 10^{19}$ m^{-3}, MANTIS 2D data clearly shows the most intense C III emissivity region retreating from the target towards the X-point as the density increases: this phenomenon is known as *C III radiation front movement*, associated with the C III emission at 465 nm, and will be the object of section 5.2.

The other panels, indicated by the letters from e) to p), represent the TS and MANTIS radial profiles corresponding to the indicated DSS LOS and the value of core density. Examining these figures column by column - i.e. taking, for example, figures 4.12e), i) and m) - we see their poloidal variation from upstream to downstream, recorded for the same value of core density. Alternatively, row by row - i.e. panels e), f), g) and h) - we see the profiles' variation with increasing core density at a fixed distance from the target and X-point.
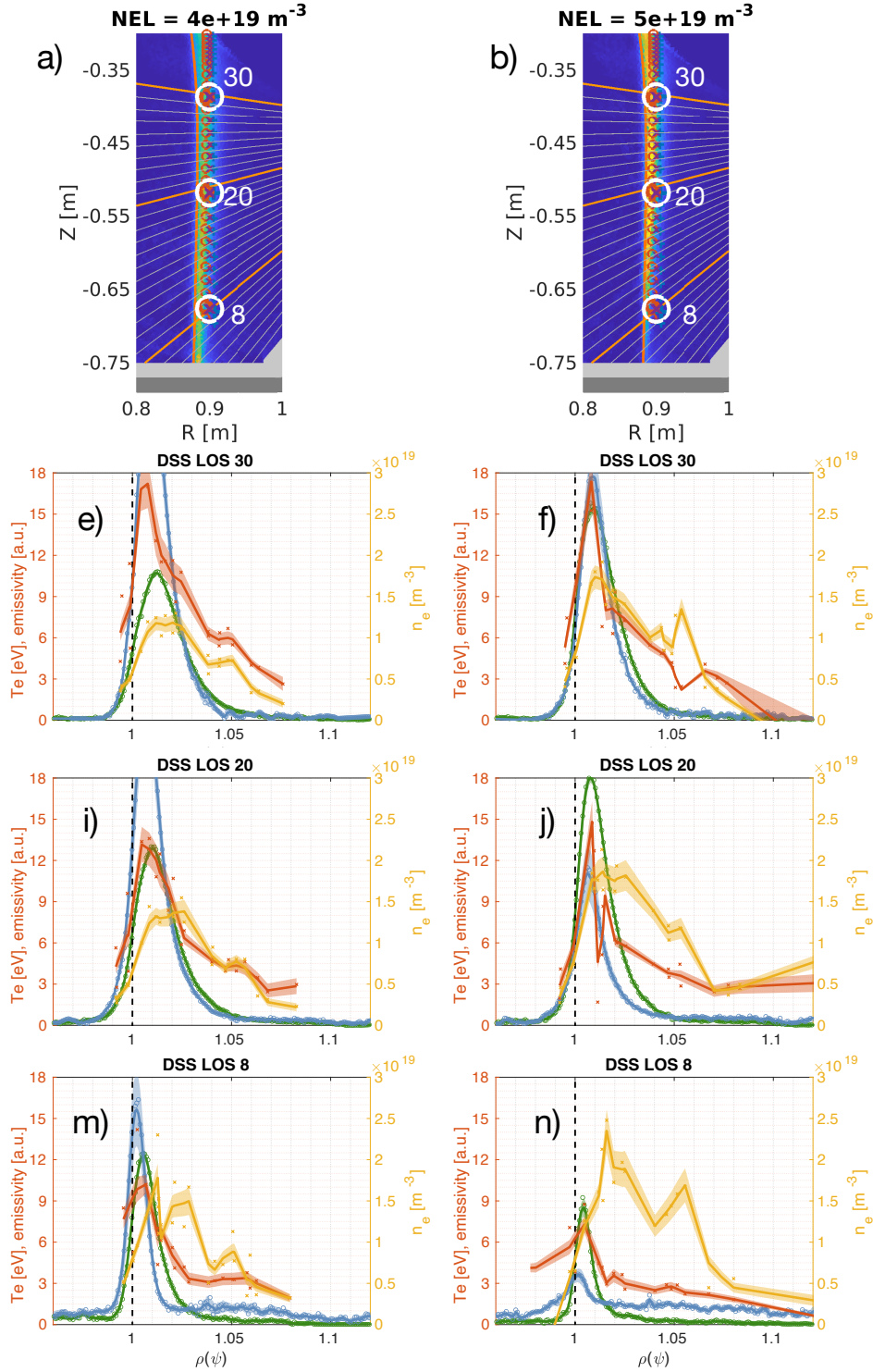
Figure 4.12: Reconstructions of the TS T_e, plotted in red, n_e, plotted in yellow and referring to the r.h.s. y axis, obtained by combining the data measured at the positions highlighted in panels a) and b) across all the repeats. C III, in green, and He II, in blue, normalised emissivity radial profiles obtained by MANTIS inversions for discharge #74213 along the highlighted DSS LOSs are plotted referring to the l.h.s. y axis.

Figure 4.13: Same data representation of figure 4.12, but for higher core density.

Figure 4.14: Reconstructions of the static pressure p_e, using the TS T_e and n_e data, obtained combining the data measured at the highlighted positions across all the repeats.

Figure 4.15: Similar to figure 4.14 but for higher core density.

4.3.1 Electron temperature and density profiles evolution

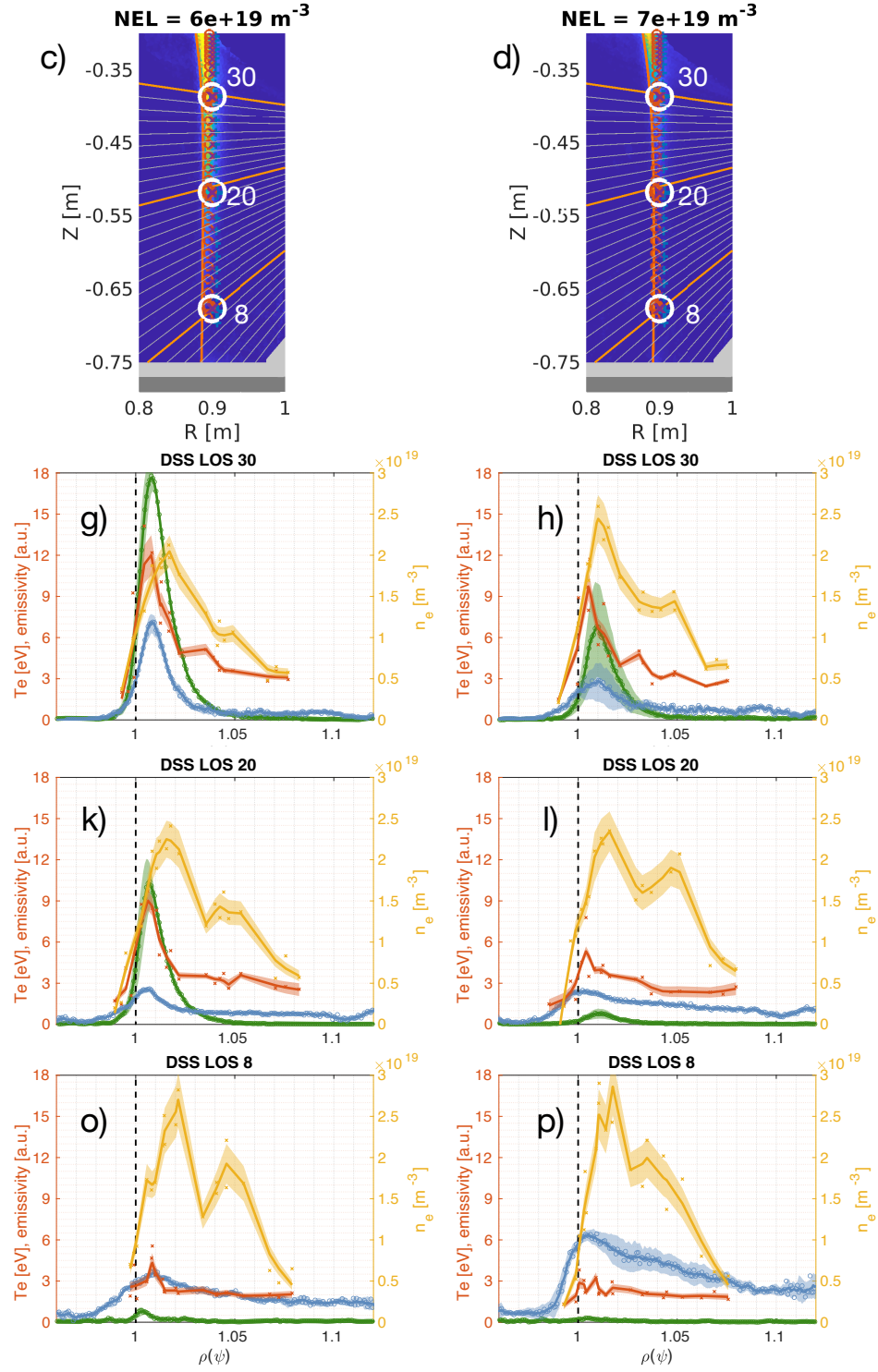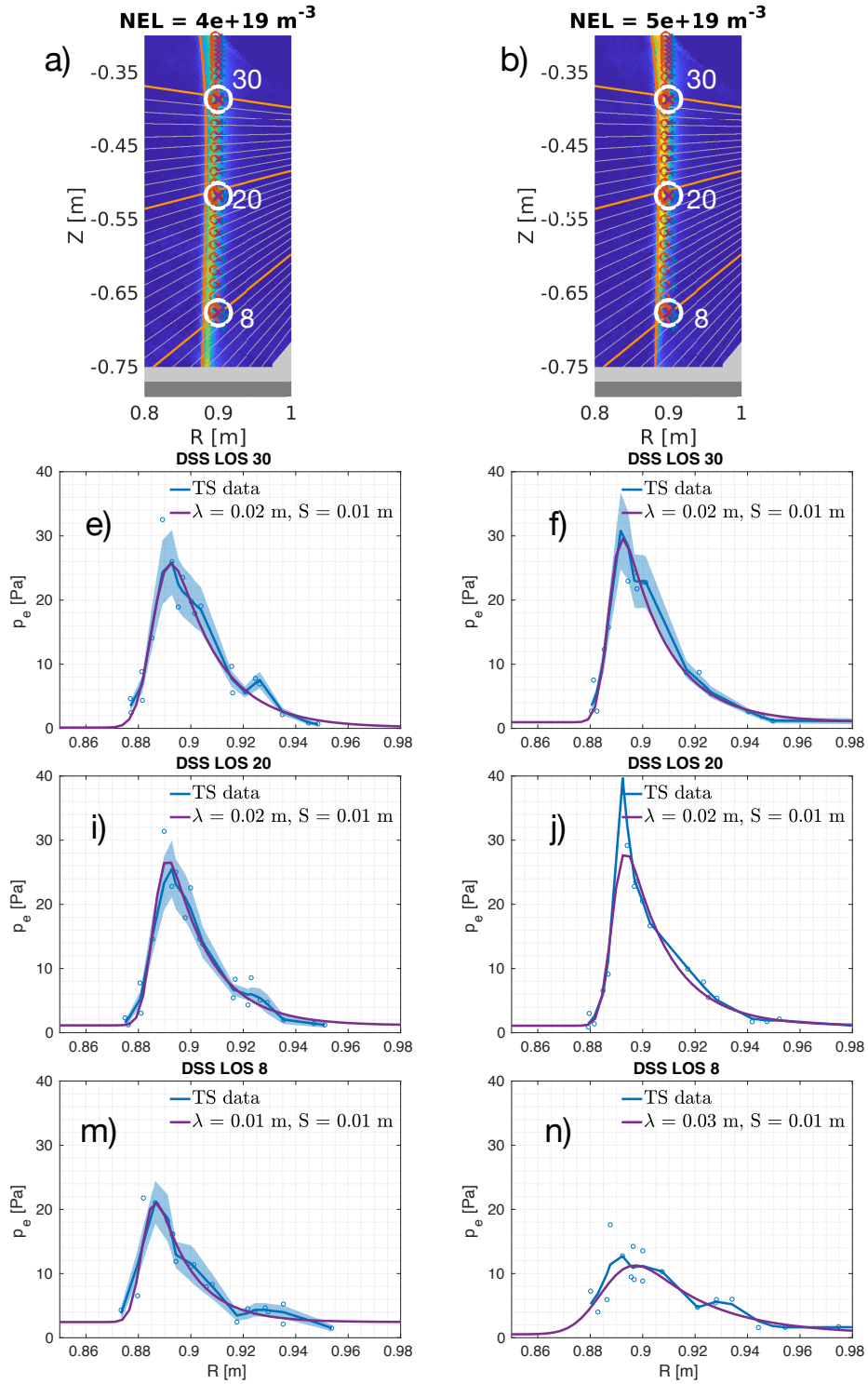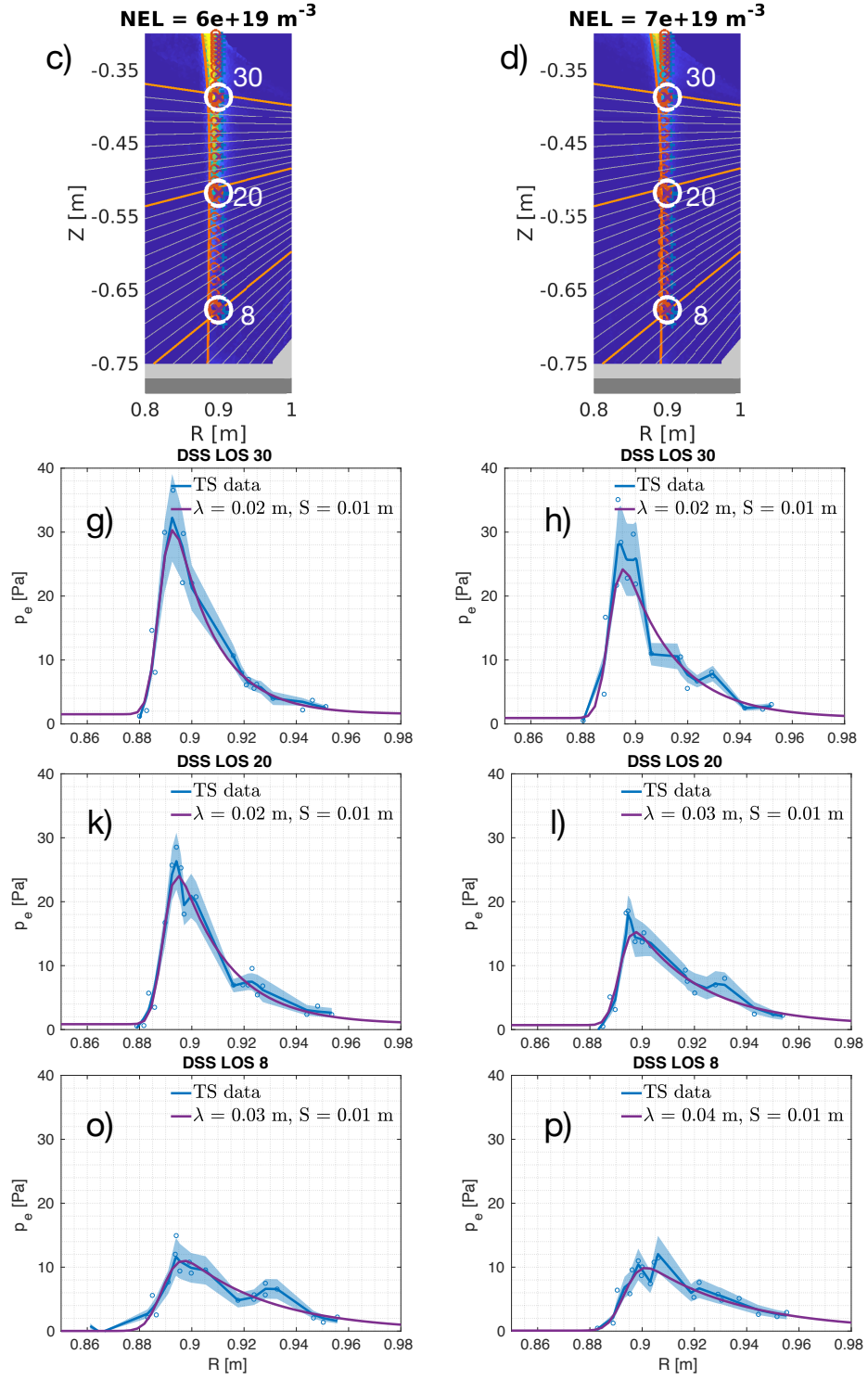During the density ramps, the temperature profiles change radically. The peak values generally decrease, i.e., at the most upstream considered location $T_{e,peak}$ goes from the 17 eV of panel e) to the 10 eV of panel h); lower in the divertor, the drop can be even more significant, as illustrated in panels m) to p), in which the $T_{e,peak} \approx 11$ eV at low core density is reduced to $T_{e,peak} \approx 3$ eV at high core density. Similar observations can be made for the profiles' poloidal variations at a given value of core density: for core density of $5 \cdot 10^{19}$ m^{-3}, moving from higher in the divertor toward the target, i.e. from panel f) to n), $T_{e,peak}$ drops from 18 eV to 8 eV. However, at later stages across the density ramp, the T_e profiles show less variation in the poloidal plane, at least in the region above the target extending to the higher divertor, i.e. comparing panel l) to p).

With the decrease in $T_{e,peak}$, the radial profiles also flatten: moving diagonally from panel e) to panel p), we see that, initially, the profile tail shows a near exponential decay, with its extremity in the far SOL becoming increasingly flatter and extending toward the separatrix with density and when towards the target. Eventually, the profiles, at the target for high core density, display a nearly flat T_e profile.

The position of $T_{e,peak}$, in each of these panels, is located near the separatrix, at $\rho(\psi) \approx 1.01$.

Referring to figures 4.12 and 4.13, on page 90 and 91, we can also observe variations in the n_e radial profiles. A first observation is that the position of $n_{e,peak}$ is located radially outward with respect to that of $T_{e,peak}$, at around $\rho(\psi) \approx 1.02$. This radial shift was also observed in SOLPS-ITER simulations, as, for instance, those reported in M. Wensing's PhD thesis [81], and was attributed to $\vec{E} \times \vec{B}$ drifts in the reversed field configuration.

Comparing profiles acquired for the same core density, we see that n_e increases toward the target. Moreover, a secondary peak in this region appears at $\rho(\psi) \approx 1.05$, which becomes increasingly prominent with increasing core density. At the highest core density, the secondary peak extends into the upper divertor region (i.e. for the DSS LOS #20 to #30, for a vertical distance from the target of 20-30 cm), also visible in panels h), k) and l). A similar feature is also observed on the ion saturation current J_{sat} measured by the wall-embedded LPs at the target, as shown in figure 4.16.

SOLPS-ITER and UEDGE codes are able to catch the density double-peak, i.e. as in N. Christen (2017) [130]. Similar experimental findings were also observed at JET, as described by A. V. Chankin (2001) [131], and also ascribed to the action of $\vec{E} \times \vec{B}$ drifts. The rise of the secondary n_e peak may also be attributed to a pressure balance mechanism: indeed, as in figures 4.14 and 4.15, and as will be explained in the following paragraph, the product $p_e = n_e \cdot T_e$ remains a smooth function of $\rho(\psi)$. The increased n_e, therefore, compensates for the drop in T_e in the radial profiles, thus conserving the static pressure in the flux tube.

Further observations on the trends of the TS-derived profiles are reported in sections 5.3.2 and 5.3.3.
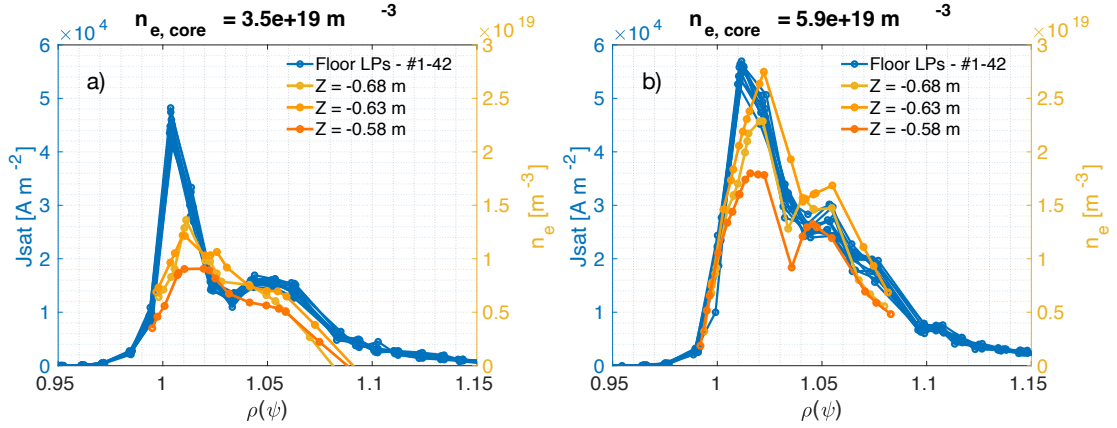
Figure 4.16: Radial profile of LP's J_{sat}, on the l.h.s. axis, and TS's n_e for three vertical distances from the target on the r.h.s. axis, represented for two values of core density.

4.3.2   Electron pressure profile evolution

The availability of TS profiles augments our divertor description: it is possible to compute the static component of plasma pressure following the ideal gas law:

$$p = n \cdot T \qquad \longrightarrow \qquad p_e[\text{Pa}] = n_e[\text{m}^{-3}]\, T_e[\text{eV}]\, 1.602 \cdot 10^{-19}[\text{J/eV}] \qquad (4.10)$$

The electron pressure profiles are shown in figures 4.14 and 4.15, reconstructed using the raw and the interpolated TS data of T_e and n_e of figures 4.12 and 4.13, respectively shown by the blue dots solid lines. The evolution of p_e profiles is relatively clear: the peak decreases both with increasing core density and towards the target; they simultaneously spread in the radial direction.

To provide a quantitative evaluation of these changes, we regressed these profiles using an Eich function [132], illustrated in the same figures by solid purple lines. The Eich function is here defined as

$$f(x) = \frac{I}{2} \cdot \exp^{\left(\frac{S_p}{2\lambda_p}\right)^2 - \frac{x - x_0}{\lambda_p}} \cdot erf\left(\frac{S_p}{2\lambda_p} - \frac{(x - x_0)}{S_p}\right) \qquad (4.11)$$

where I represents the intensity of the function, S_p a Gaussian spreading parameter, λ_p and exponential fall-off length and x_0 the peak position, here the separatrix. To give a physical interpretation to the λ_p and S_p, these profiles were remapped in TCV coordinates to a physical length. This profile parametrisation is often used to describe the heat fluxes in power exhaust studies, as in R. Maurizio's PhD thesis (2020) [86], where S indicates a diffusive-like profile spreading and λ a characteristic fall-off length. The Eich regressions only approximate the shape of the p_e profiles but do so relatively well. The parameters can help describe the profile evolution in the proximity of a detached regime, as, instead of taking shape as its whole, it is

possible to track the variation of each Eich parameter as a function of core density or distance from the target, as in section 5.3.2. The evolution of the Eich parameters can indicate the effect of momentum redistribution between flux tubes, associated with an increase of S_p or λ_p, effectively linked to the f_{mom} factor, discussed in section 1.3.1.

4.3.3   Emissivity profiles
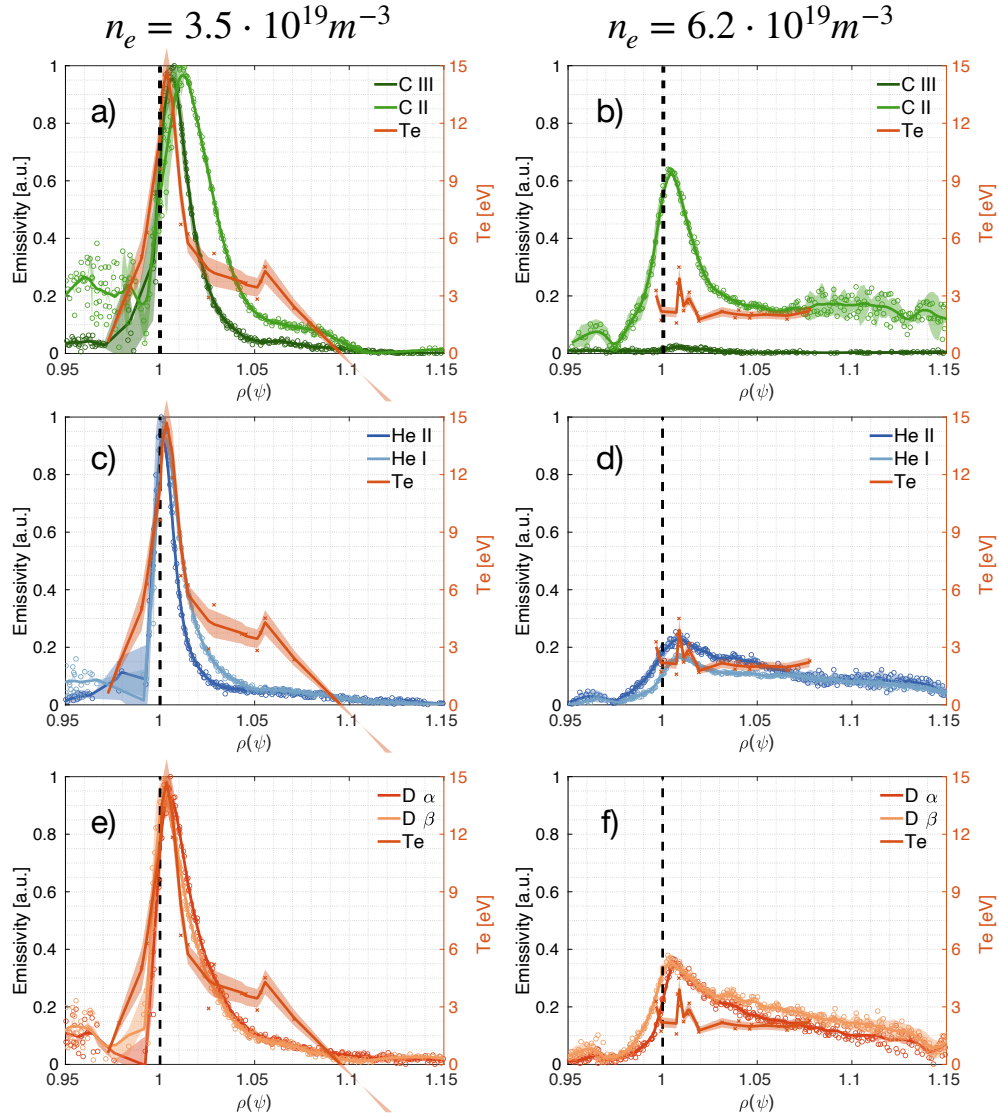

Figure 4.17: MANTIS emissivity radial profiles of ionised and neutral species, relative to DSS LOS 9, illustrated for the case of an attached divertor and for a divertor with a higher degree of detachment.

Significant changes in the emissivity profiles are seen across the density ramp for ionised and neutral species from the MANTIS reconstructions. For clarity's sake, figures 4.12 and 4.13

display MANTIS data only for C III and He II, but all the ion and neutral species spectral lines observed by DSS, were available from MANTIS for discharge #74213. Those described here are shown in figure 4.17, sorted by element. The two columns show the profiles reconstructed along the DSS LOS 9, corresponding to an attached and a detaching divertor, respectively acquired for a core density of $\approx 3.5 \cdot 10^{19}$ m^{-3} and $\approx 6.2 \cdot 10^{19}$ m^{-3}. The profiles have been normalised to their attached peak intensities, to highlight relative intensity variations.

At the beginning of this section, we briefly described the C III radiation front movement. A more explicit representation of this phenomenon can be observed in figure 4.17: comparing panels a) and b), we clearly see how the C III emissivity diminishes drastically when evolving towards a detached regime. C III emissivity sharply decreases in the region of electron temperatures in the range of $T_e \approx 3-5$ eV. Further detail on this will be presented in section 5.2. On the other hand, He II and C II radial emission profiles broaden considerably, as in figure 4.17b) and d), emitting radiation from the entire SOL. Depending on T_e in the separatrix region, C II can conserve a peaked emissivity radial profile, but a long emission tail still significantly contributes to the total C II emissivity. We also stress that He II *does not* completely extinguish, in contrast to what one might expect from simple excitation energy considerations. The presence of He II emissivity in the region where $T_e < 3$ eV is indicative of recombination reactions occurring, involving He^{2+} ions in the cold divertor [92]. We will also see in next section 4.4 and later, in section 5.1, how this continual He II emission can be exploited to access information about the low temperature of a detaching divertor using the DSS line-shape analysis of section 3.2.

Figure 4.17 also presents emissivity profiles of He I, D$_\alpha$ and D$_\beta$, from plasma neutrals i.e. particles not confined to magnetic field lines. We observe that their radial emissivity profiles behave similarly to those of He II and C II. However, we have seen in section 3.1.4 that their line shapes are often better described by two Gaussian distributions, corresponding to two neutral temperatures. Interestingly, no clear radial splitting of the emissivity profiles is observed in the MANTIS inversions, suggesting that the two measured neutral temperatures originate from different neutral populations at two separate temperatures in the same location.For the record, the MANTIS diagnostic would have the spatial resolution to measure such a splitting and similar phenomena are observed in other conditions, as shown in Perek et al (2021) [107]. More insight on the interpretation of this DSS observation will be given in section 4.4.2.

4.4 Ion and neutral temperature measurements with DSS

Ion and neutral temperatures were measured by the DSS using the technique illustrated in section 3.2. The different charge state of the emitting species leads to different behaviour for the temperature evolution of the ionised and neutral species.
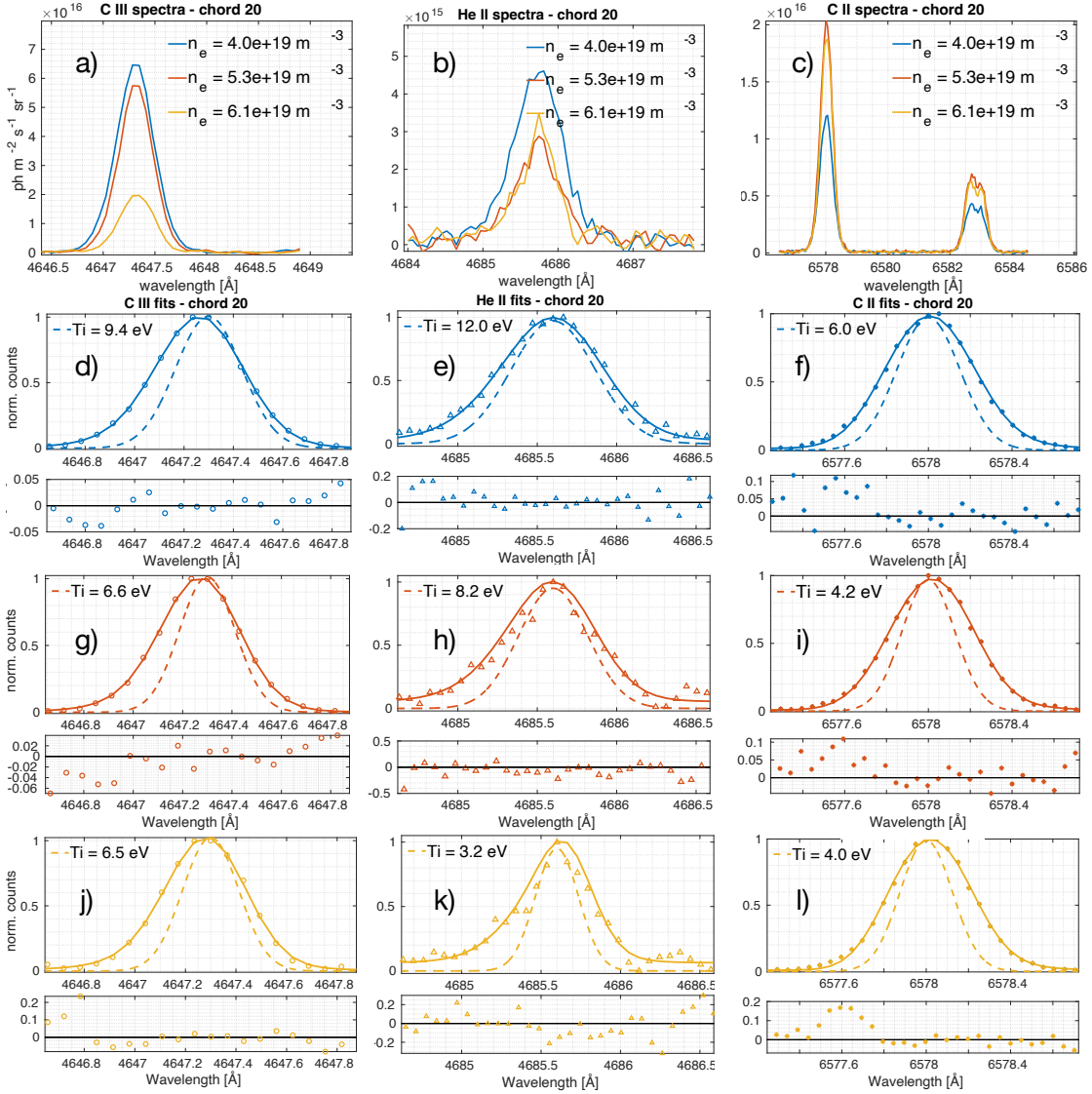
Figure 4.18: Panels a), b), and c) show examples of the C III, He II and C II spectra acquired along DSS LOS # 20 for three core density values. In the case of the C III triplet, only the brightest line at 4647.3 Åis regressed, while the peaks of the C II doublet are independently regressed, and only the brightest one is displayed in this figure. Panels d) to l) indicate the resulting Gaussian components with the dashed lines, using different colours for the three values of core density, showing how the DSS interprets the small differences in the ion temperature. The fit residuals are presented below each panel.
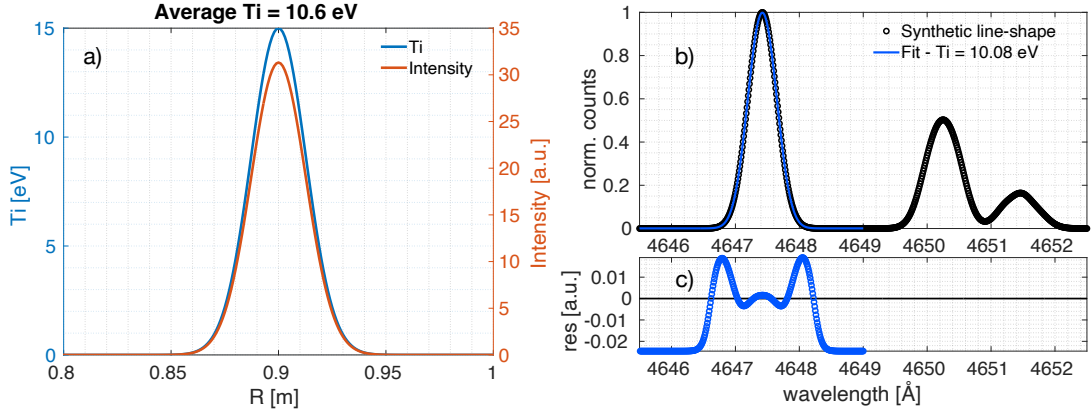
Figure 4.19: Panel a) represents the ion temperature and emissivity radial profiles used to generate the synthetic line-shape illustrated with the black dots in panel b), courtesy of A. Renggli. This is fitted with the procedure described in section 3.2, and the solid blue line illustrates the output. The blue dots in panel c represent the fit residuals).

The visible emission measured by the MANTIS diagnostic, of which a selected cut along the DSS LOS #9 is plotted in figure 4.17, is also captured by the DSS in a line-integrated fashion. The DSS's high spectral resolution analysis of the spectral line-shape can be used to infer the emitters' temperatures, as described in section 3.2.

The ion -or neutral- temperature of a species α measured by the DSS is line-averaged along the LOS and corresponds to

$$T_i(\alpha) = \frac{\int_{LOS}\varepsilon_\alpha(\rho)\,T_{i,\alpha}(\rho)\,d\rho}{\int_{LOS}\varepsilon_\alpha(\rho)\,d\rho} \tag{4.12}$$

Here $\varepsilon_\alpha(\rho)$ is the emissivity of the species α, i.e. that measured by the MANTIS tomographic inversions, acting as a weight on the ion temperature contribution at that $\rho(\psi)$ coordinate. The integral along the DSS's LOS includes the entire SOL width, along which the plasma emits albeit at different n_e, T_e - as presented in figures 4.12 and 4.13, and T_i.

The DSS's LOS integration makes the measured line-shape that of a radial sum of the ion temperature profiles across the SOL, proportionally weighted by the observed species emissivity radial profile. This view was tested in the framework of A. Renggli's semester project, supervised by D. Mykytchuck, where synthetic line-shapes of C III and He II were numerically generated from the radial distributions of temperature and emissivity across the DSS's LOSs. These line-shapes were then regressed, as described in section 3.2, using a simplified Gaussian instrumental function for both the synthetic line-shape generation and the regression. Figure 4.19 compares the average ion temperature weighted on the emission intensity radial distribution with that resulting from the regression. This is a simplified case where both distributions

- Gaussian - centred at R = 0.90 m gave a weighted average ion temperature of 10.6 eV. The synthetic line-shape of panel 4.19b) was generated using the complete intensity, temperature and magnetic field profiles, while the regressed line-shape only considers averaged values of these parameters, yielding as a result T_i(C III) = 10.08 eV. The difference between the two is within 5%, supporting the interpretation of the ion temperatures given by equation 4.12.

This section presents the experimental results obtained by analysing the discharges listed in 4.1, separating ionised and neutral species.

4.4.1   Ion temperature measurements

Ion temperatures measured by the DSS are observed to decrease with the increasing core density. However, different species exhibit different sensitivities and temperatures.
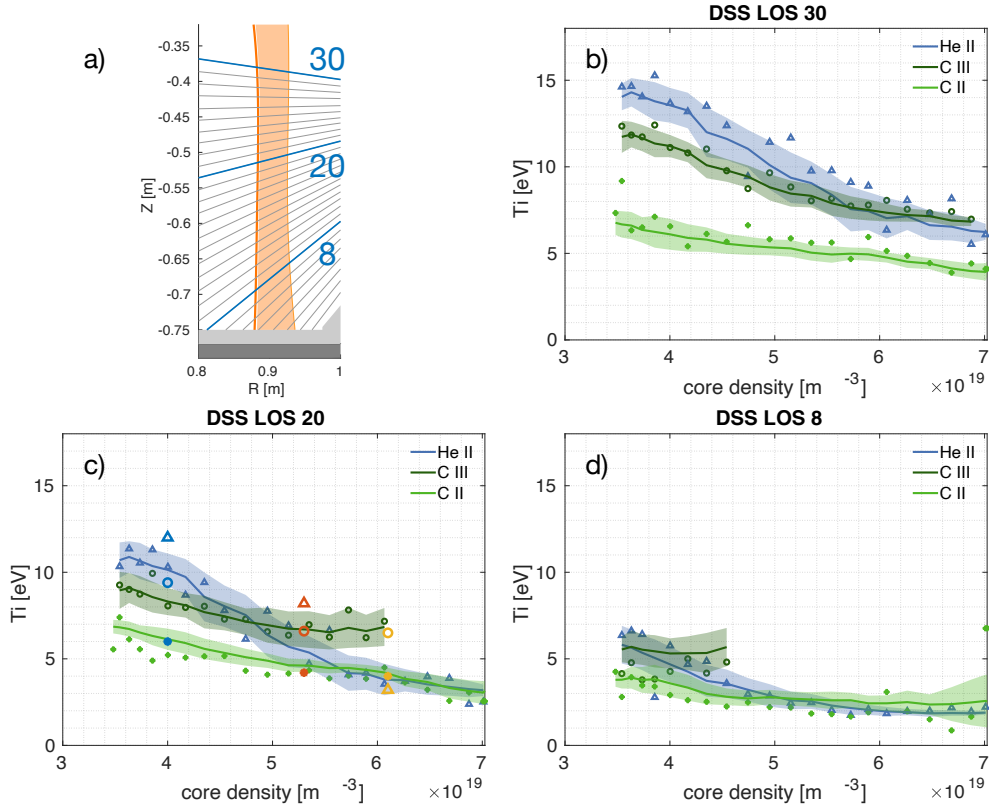
Figure 4.20: Ion temperature measurements for three selected DSS LOSs, plotted as a function of core density through a working gas density ramp. The symbols represent the T_i from the averaging of repeat discharges, while the solid lines originate from the 2-D smoothing of this average. The shaded areas, representing the uncertainty on the T_i, are also given by a 2-D smoothing of the standard deviations calculated across the repeat discharges. The representative data of figure 4.18 are reported in panel c) in the corresponding symbols and colours.

Figure 4.20 presents three ion species' DSS ion temperature measurements along three of the thirty available DSS LOSs. Panel a) is similar to figure 4.1b), representing part of the SOL in the TCV poloidal cross-section. The DSS LOSs are plotted in grey, except for those chosen to be representative of the data in panels b), c) and d), which are highlighted in blue. Figures 4.20b), c) and d) illustrate the ion temperatures of the He II, C II and C III species measured, along the indicated DSS LOSs, as a function of the increasing core density.

Through the seven repeat discharges, DSS's high-resolution spectrometers were set to observe the species indicated in table 4.1, with several of these, e.g. He II, C II, C III, D_α and D_β, observed multiple times. Observations of the same spectral line across similar density ramp discharges can also be used to estimate an average and a standard deviation of the deduced ion temperatures. Here and in the following sections, where possible, the indicated DSS ion temperatures will be those resulting from averaging over the discharges in which they were observed, using the procedure described at the end of section 3.2.2. For example, in the C III and He II cases, the data is given by an average of the T_i acquired for the same values of core density over discharges #73912, #74212 and #74213. C II data similarly comes from the average of three T_i sets, from discharges #73914 and #74213. In discharge #74213, this transition was observed alone and the camera's exposure time and EM gains were tailored to optimise the SNR for both doublet's line-shapes; however, in #73914, C II was observed together with the much brighter D_α, so that only the brightest line in the C II doublet was considered in the analysis of T_i(C II).

The averaged data is shown in figure 4.20 by the coloured series, using different symbols for the three species. A 2D smoothing function was applied to the ion temperature measurements, across the density and across the vertical distance from the target. The smoothed data is represented by the solid lines in figure 4.20 and by the dotted series later in figure 4.21. The uncertainty bounds in these figures reflect the standard deviations calculated for the same values of core density over the repeat discharges, as described at the end of section 3.2.2, to reflect the intrinsic variations of TCV's divertor conditions over the time of the repeat discharges.

In panels b), c) and d) of figure 4.20, T_i(He II), T_i(C II) and T_i(C III) are observed to decrease with the increasing core density. This behaviour is expected, as it is predicted for T_e by the 2PM and observed in [53]. However, different species can exhibit different gradients and different T_i. Another observation from figure 4.20d) is that, sufficiently close to the target, T_i(C II) and T_i(He II) are equal and do not decrease below 2 eV. This apparent lower temperature limit could explain the absence of a clear detachment in these discharges, indicated by the saturated Γ_t as a function of core density presented in figure 4.3. However, the reason for this temperature saturation is not clear.

It is also possible to examine the spatial dependence of the ion temperatures, in figure 4.21. Here, the vertical distance from the target, indicated by TCV's coordinate Z in the poloidal cross-section, is taken from the intersection of the DSS LOSs with the separatrix in the LFS
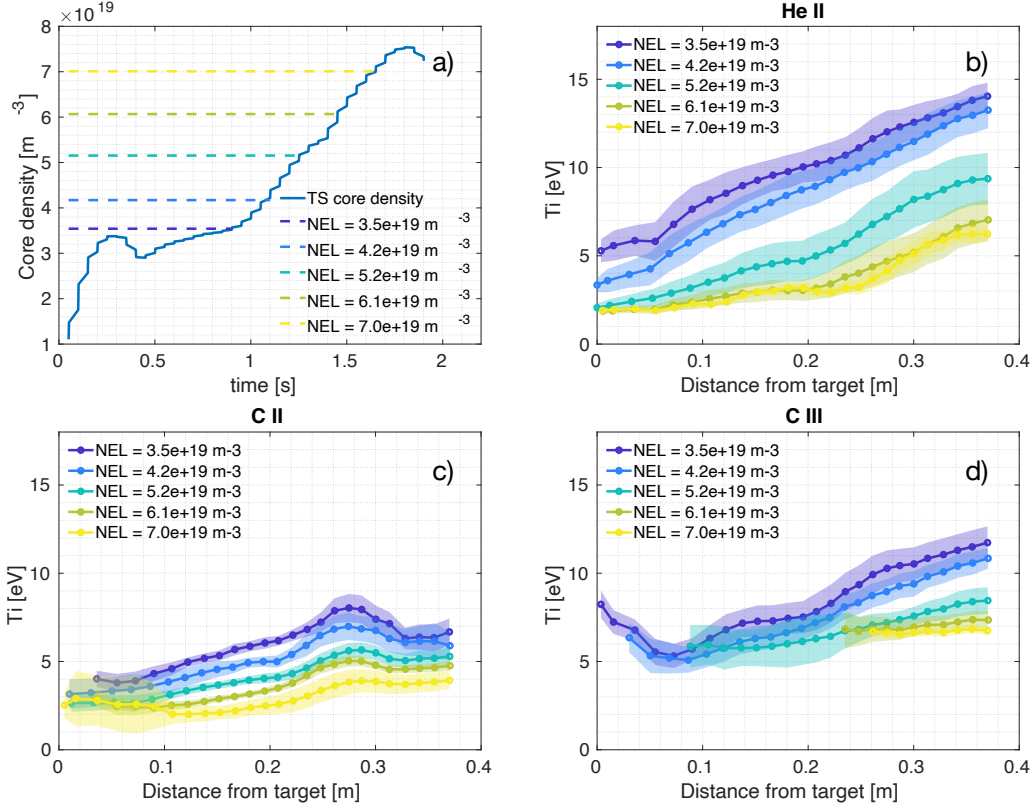
Figure 4.21: Ion temperature measurements for five selected values of core density, plotted as a function of vertical distance from the target.

divertor leg, as illustrated in figure 4.20a). Figure 4.21a) is representative of a typical core density ramp, with the coloured horizontal dashed lines indicating the values of core density used in the data of panels b), c) and d), indicated by the colourmap, from the lowest core density case of $3.5 \cdot 10^{19}$ m^{-3} in dark blue to a bright yellow, indicating a $n_{e,core} = 7.0 \cdot 10^{19}$ m^{-3}.

Panel b) shows the evolution of T_i(He II) as a function of distance from the target for the selected core densities. Here we observe a strong temperature gradient early in the ramp, with temperatures ranging from T_i(He II) $\approx$ 15 eV at the highest DSS LOS, to T_i(He II) $\approx$ 5 eV at the target. This gradient gradually flattens as the density increases until an extended flat temperature region extends from the target. This is indicated by the yellow line, that plots T_i(He II) $\approx$ 2 eV extending up to $\approx$20 cm from the target. From there, a temperature gradient resumes. These findings will be explored in more detail in section 5.3, using a 2PM interpretation.

Panels c) and d) present the data of T_i(C II) and T_i(C III). The evolution of the former is somewhat similar to that of T_i(He II), with slightly lower temperatures and lower gradients. This singly ionised element also displays a near-constant T_i region extending from the target upwards of $\approx$20 cm in the SOL at high core density. The "bump" observed at $Z \approx$ 28 cm is likely

due to artefacts observed on the C II data for the discharge #74213. This feature persists across the entire density ramp and it is considered not physical during the following analysis. Finally, C III also supports this ion temperature evolution observed for the other species: temperature gradients are present at low core density but they too flatten across the density ramp. In this panel, C III data is only shown where reliable fits were obtained, excluding the frames where the C III intensity was below a chosen threshold (25 % of the global maximum intensity). C III does not provide more information on the flat temperature region.

A clear difference between the ion temperatures of different species is observed. This can be partly explained by referring to the spatial extent of their emissivity in the SOL, illustrated in figures 4.12 and 4.13 for He II and C III, in view of equation 4.12 for the DSS ion temperature. He II emissivity profiles are more peaked than those of C III at low core density, thus more strongly weighting the hotter portion of the divertor leg - see equation 4.12. They progressively broaden with increasing core density, adding observation weighting from the far SOL region, thus probing lower temperatures than that at the separatrix. Conversely, the C III profiles remain peaked at $\rho(\psi) \approx 1.01$, probing the same SOL region throughout the density ramp, which remains at higher T_e than the SOL external region. This will be extensively discussed in section 5.1, by combining TS and MANTIS measurements.

4.4.2   Neutral temperature measurements

Several neutral species were observed across the discharge repeats. We report in this section the data regarding the D_α, D_β, and triplet He I spectral lines. The analysis technique used on their line-shapes is the one described in section 3.2.1 for neutral species, characterised by the use of two Gaussian distributions describing two temperature components. Figure 4.22 presents the temperature evolution of D_α, D_β, and He I recorded on the DSS LOSs illustrated in figure 4.20a, separating between a *hot* component, $1.5 \lesssim T_{n,hot} \lesssim 10$ eV and a *cold* component, $0.2 \lesssim T_{n,cold} \lesssim 1.5$ eV. No clear evolution is observed for the hot component's temperature as a function of core density, remaining flat across the density ramp. The cold component's temperature of D_α and D_β does, however, evolve, showing a 50-100% increase depending on the LOS.

Figure 4.23, is similar to figure 4.21, but shows the data of neutral temperatures as a function of vertical distance from the target for several densities. These are displayed by a colour map, with the dark blue lines referring to the low core density case and the yellow lines to the high core density case.

He I temperature components are illustrated in panels a) and b). The hot component shows a gradual decrease as a function of density in the region within ≈ 0.2 m from the target, considering a vertical distance only. Here $T_{n,hot}$(He I) decreases from ≈ 5 to ≈ 3 eV across the density ramp, while, above this region, it remains relatively constant at $T_{n,hot}$(He I) ≈ 5 eV. $T_{n,cold}$(He I) appears to be close to the wall temperature, measuring in the range of 0.02 to 0.05 eV. The effective temperature of this component is below the spectroscopic resolution,
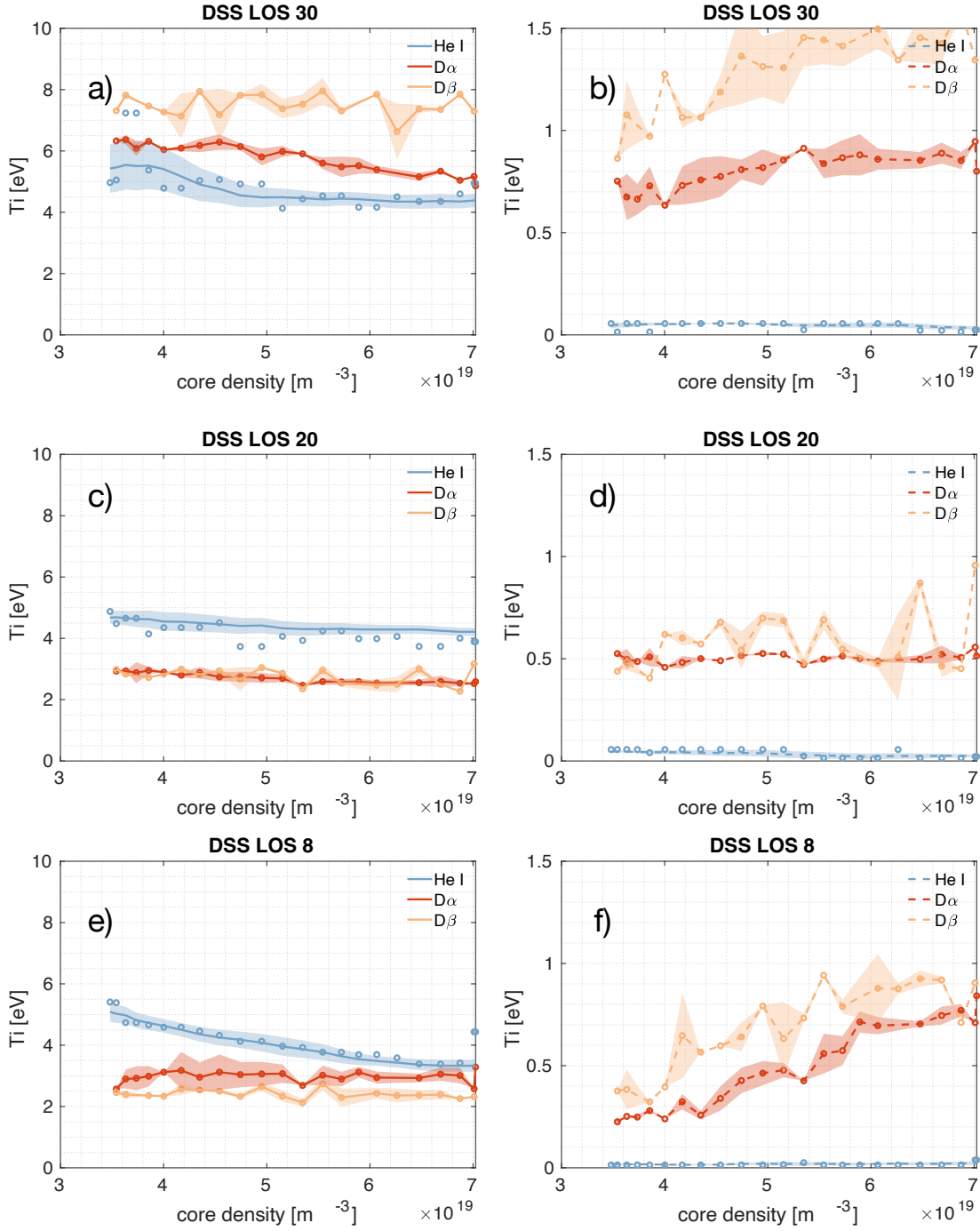
Figure 4.22: Similar to figure 4.20, but illustrating the evolution of the neutral species D_α, D_β and He I temperatures with the increasing core density for DSS LOSs 30, 20 and 8. The left-hand side of the figure represents the *hot* components, while the right-hand side represents the *cold* ones.
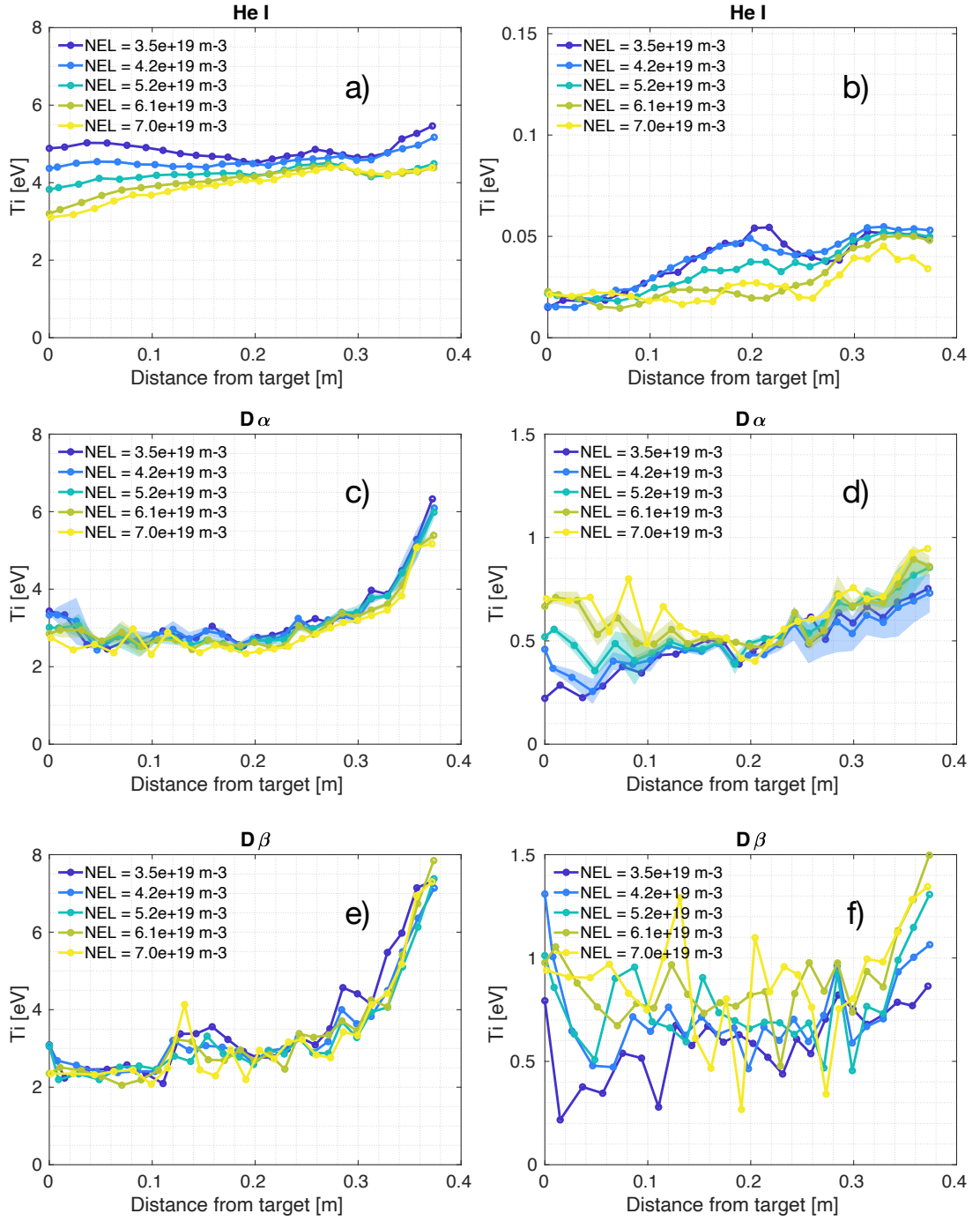
Figure 4.23: Similar to figure 4.21 but for D_α, D_β and He I. The left-hand side of the figure represents the *hot* components, while the right-hand side represents the *cold* ones.

of ≈ 0.5 eV, but it remains more symptomatic of the vessel temperatures than that of the plasma. Turning to the D_α and D_β temperatures, in figure 4.23 panels c) and e), the hot components of D_α and D_β are observed to depend upon the distance from the target but little on the core density, as all the lines are nearly superimposed. Until a vertical distance of ≈ 0.3 m from the target, these temperatures are near constant through the density ramp at $T_{n,hot}(D_\alpha) \approx T_{n,hot}(D_\beta) \approx 2.5 - 3$ eV. A sharp increase in the hot temperature component is observed for both species in the region above ≈ 0.3 m from the target, reaching values up to 6-8 eV. Here again, little dependence is discernible on the core density.

Conversely, the temperature of the cold component of D_α and D_β increases with the core density in the target region, up to a distance of ≈ 0.1 m from the target. The cold temperature of D_β, presented in panel f), appears consistently higher than that of D_α, in panel d), however, a much larger scatter affects these data. Both species' cold components temperatures increase slightly when moving away from the target: 0.2 to 0.9 eV for $T_{n,cold}(D_\alpha)$, and ≈ 0.2 to ≈ 1.5 eV for $T_{n,cold}(D_\beta)$.

Figure 4.24: D_α signal components: panel a) represents the intensity of the line, panel b) indicates the *cold* component contribution to the intensity, panel c) shows the temperature associated with the *hot* component and panel d) the temperature associated to the *cold* one. The data are plotted as a function of vertical distance from the target, with different colours, from blue to yellow, indicating increasing core density values.

While little or no dependence on the core density is observed on the temperature values of the neutral deuterium species, it is interesting to examine whether an evolution, or a spatial dependence, of the intensity associated with these components, is observed. This is illustrated in figure 4.24 and 4.25, for D_α and D_β respectively. In these figures, panels c) and d) report the same data of figure 4.23, but for all the analysed time frames. Panels a) and b), instead, refer to the overall intensity and the cold component's contribution. Despite a higher scatter in the D_β data, similar trends and temperature values are observed for both species. The overall intensity increases at the target across the density ramp, simultaneously with an increase in the cold component intensity and temperature. The furthest region from the target, above $\approx$ 0.3 m, where $T_{n,hot}$ increases, shows a corresponding drop in the hot component contribution to the spectral line intensity, as the cold component increases from 40% to 60% for D_α and to nearly 70% for D_β. The poloidal dependence of the hot component's temperature and intensity, and, at the same time, its independence from the other plasma parameters, is not understood and requires further investigation.
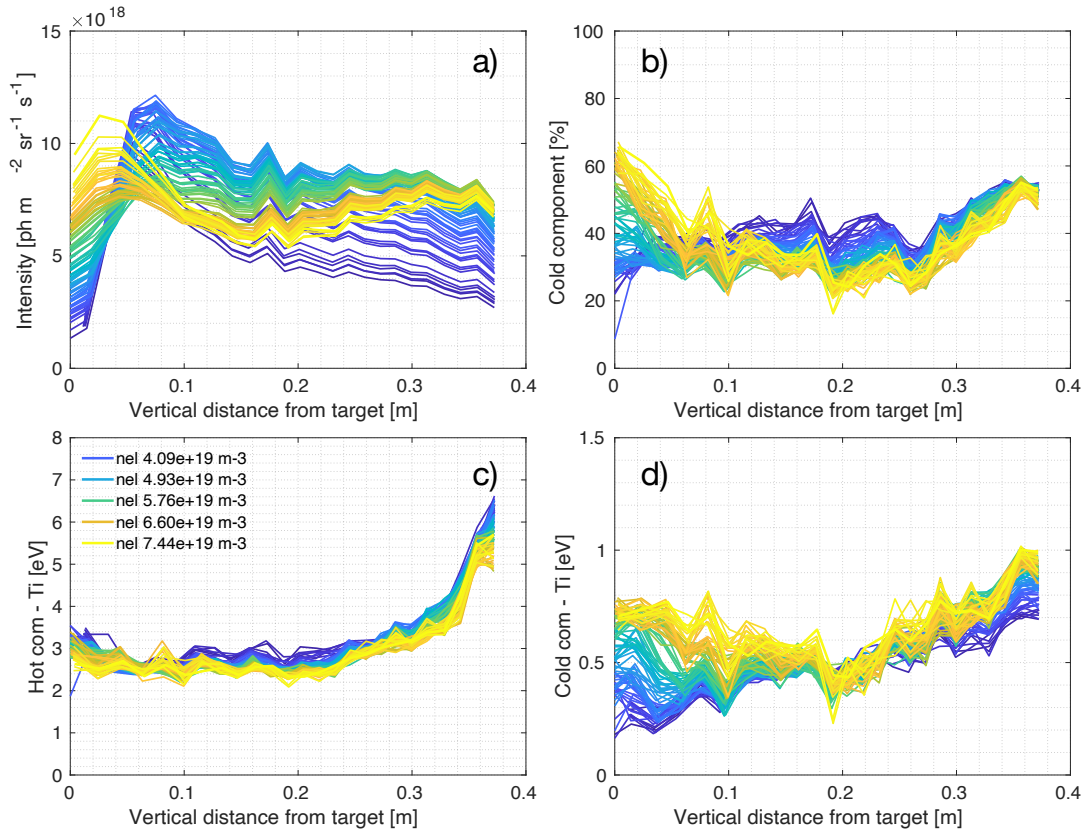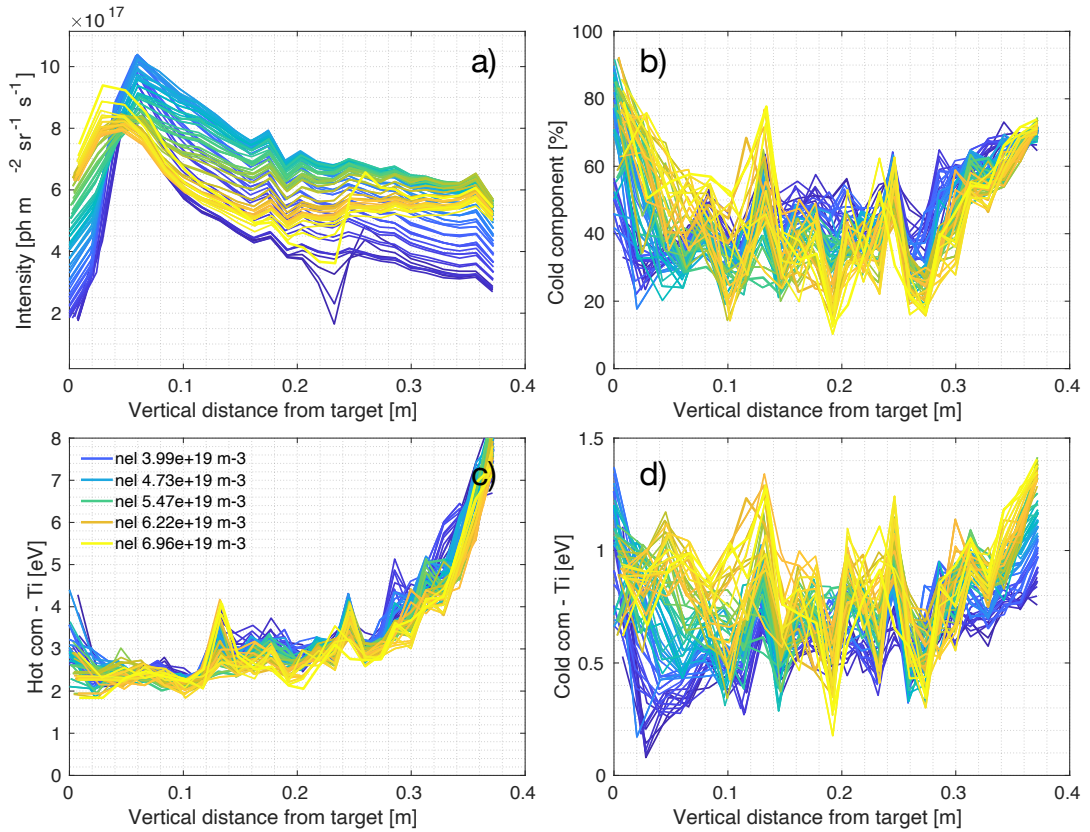

Figure 4.25: D_β signal components: panel a) represents the intensity of the line, panel b) indicates the *cold* component contribution to the intensity, panel c) shows the temperature associated with the *hot* component and panel d) the temperature associated to the *cold* one. The data are plotted as a function of vertical distance from the target, with different colours, from blue to yellow, indicating increasing core density values.
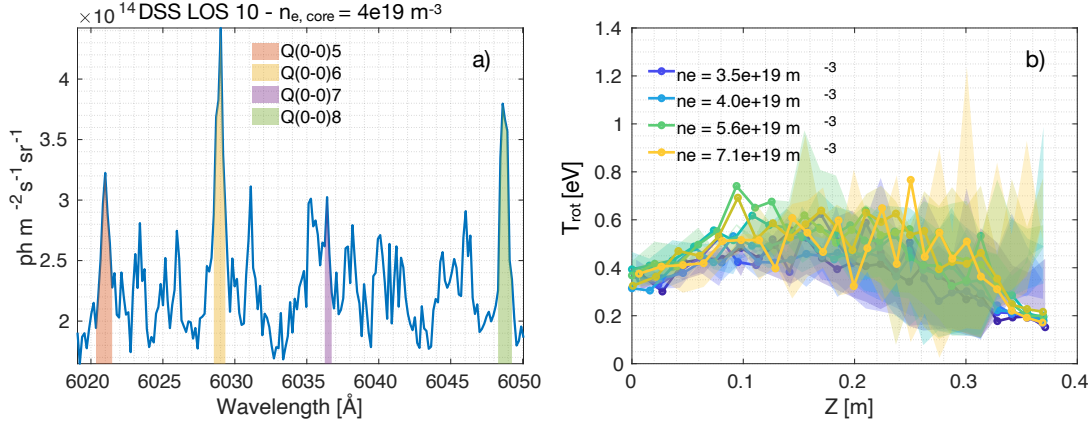
Figure 4.26: Panel a) shows the Fulcher band emission detected by the DSS medium-resolution system, highlighting the intensity of the *Q-braches* used to analyse the D_2 rotational temperature in the vibrational ground state, mapped to the electronic ground state, presented in panel b).

From the considerations expressed in section 4.2, the temperatures observed for neutral particles do not reflect that of a tokamak plasma. Thermalisation of neutral particles with the deuterium ions in the divertor leg plasma has relatively long time scales (i.e. figure 4.9) so neutrals either cross the leg or are ionised, depending on the energy at which they reach the divertor and the electron temperature in the divertor leg. If a particle gets ionised, it thermalises with the ions and emits light that corresponds to the next ionisation state of that element, or no light in the case of the singly charged working gas. Conversely, if the neutrals cross the leg without ionising, their temperature is little affected by the divertor leg plasma. In this model, light originating from electron-ion recombination (EIR) processes is neglected because of the relatively high electron temperatures measured by TS, i.e. $T_e > 2$ eV. If EIR was strong, the temperature of the neutral emission would be close to that of the next higher ionisation state and to that of the plasma particles, as the *parent* particle would be thermalised with the plasma in the divertor leg.

The observation of two temperatures for neutral particle emission, suggests that two populations of neutrals are present in the TCV divertor region. Estimations of the rotational temperature of D_2 molecules, calculated by N. Osborne from the absolute intensity ratio of spectral lines belonging to the D_2 Fulcher band measured by the DSS' IsoPlane spectrometer, similarly to what discussed in N. Osborne (in preparation)[133], are associated with the *gas temperature*, reported in figure 4.26. We note that the order of magnitude of this temperature is similar to that measured for the cold component of D_α and D_β, both being $\lesssim 1$ eV, despite showing a different spatial dependence. The cold atoms in thermal equilibrium with the gas molecules contribute to the recorded cold temperature for the neutral deuterium atomic spectral lines emitted when crossing the divertor leg.
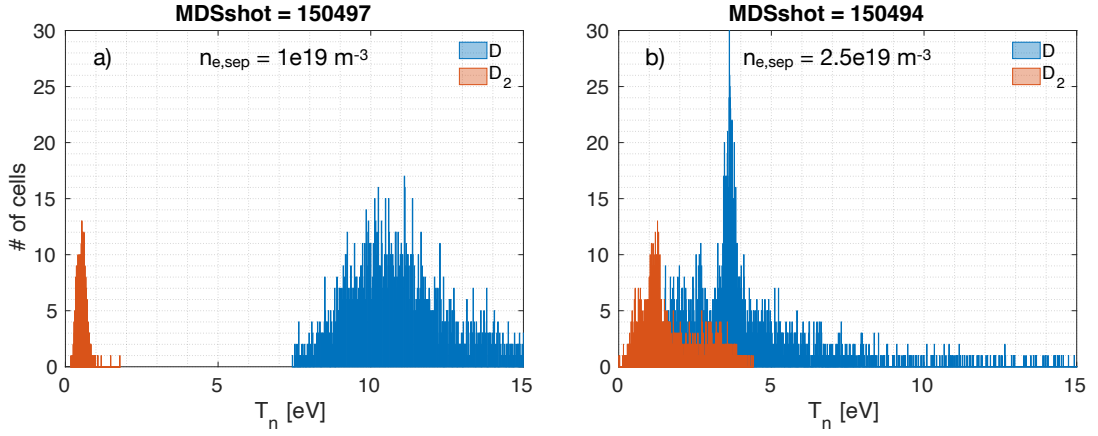
Figure 4.27: Neutral atoms' and molecules' energy distribution in SOLPS-EIRENE simulations carried out in the framework of M. Wensing's PhD thesis (2021) [81], courtesy of E. Tonello.

Regarding the hot temperature component, a similar line of reasoning holds, but the origin of this neutral population must be ascribed to other mechanisms, resulting in neutral atoms with a constant temperature of $\approx$ 2.5-3 eV, independently of their position in the divertor or the plasma density. A possible mechanism for this could be through molecular dissociation, the reaction described in equation 1.27. The work of K. Verhaegh et al. (2023) [69] highlighted the importance of plasma-molecule interaction in detach*ing* plasma, indicating that a large part of the D_α and, to a lesser extent, of D_β, is given by neutral atoms produced by that reaction. Moreover, E. de la Cal et al. (2008) [134] and N. Bisai et al. (2018) [135] mention the H_2^+ dissociation reaction as a channel for the production of cold and hot neutral atoms. The proposed temperatures are, however, different from those found here experimentally. More recent studies, presented by R. Friedl et al. (2020) [136], also showed line-shapes of deuterium Balmer lines dominated by two Gaussian components, linking them to the atomic and molecular processes causing their emission. This possibility merits further investigation with the aid of specific analysis tools, such as that presented in [71] and SOLPS-ITER modelling, which uses the Eirene suite to track neutral particles. An example of SOLPS-ITER modelled post-processed data for the neutral particles' energy distribution across the entire divertor chamber is shown in figure 4.27. These are taken from simulations in the framework of M. Wensing's PhD thesis (2021) [81], for a different magnetic equilibrium and different plasma parameters, but, still, highlight the possibility of separate neutral particle energy populations. These histograms should be considered as an interesting direction to follow, but would not be enough to explain the observed spatial dependence of the *hot* component in our experiments. Further insight would be required before drawing firmer conclusions.

The hypothesis of the two neutral particles population born at different temperatures could also explain why no spatial separation in D_α and D_β emissivity radial profiles is observed by

MANTIS, as in figure 4.17e and f. If the emission were caused by two different plasma processes that generate neutral atoms at different temperatures, a dependence on the T_e radial profiles would likely follow and be reflected on the species' emissivity radial profiles. Conversely, if the emission mechanism is caused by neutral atom excitation during their transit across the divertor leg, and arrived at the divertor leg at, say, two different effective temperatures before crossing the leg, little spatial separation should occur in the emissivity due to the two neutral populations. These would lead to an emissivity that would appear to have two temperatures from the same plasma region, as we appear to have measured in our experiments.

5 Discussion

Knowledge of the divertor ion temperature gives insight into, among other processes, the charge exchange rates [129] and the physical sputtering at the target [137]. The measurements presented in section 4.4.1, which are novel in their kind, need further interpretation before being used to draw conclusions on the temperature of the impurity ions. The radial profiles of T_e, n_e and impurities emissivity, reconstructed in section 4.3, are the framework used to interpret the DSS ion temperatures. In section 5.1, we use these reconstructions to define an *emission-weighted electron temperature T_e^**, that is the analogy of the ion temperature measured by the DSS, to study the thermalisation of main plasma particles and impurity species as the divertor plasma evolves towards a detached regime. The differences between the ion temperatures of different species, presented in section 4.4.1, are interpreted using this T_e^* variable and an ionisation-balance code. Section 5.1 will present a validation exercise necessary to understand the meaning of these DSS measurements to reply to many of the points raised in the previous chapters. For instance, we shall see that the often used $T_e = T_i$ assumption (see, for instance, section 1.3.1) does not always hold, and even how different ion species will exhibit different ion temperatures when measured at the same time from the same plasma volume. Most importantly, using the arguments presented in section 4.2, we will see how the DSS ion temperatures indirectly provide estimations of the main plasma ions. Once validated and interpreted, DSS, MANTIS and TS data will be used in section 5.2 to determine characteristic temperatures of the C III 4650 Å emission front, which, in TCV and other C-walled machines, is routinely used as a proxy of *low-temperature* attainment, and from that, detachment proximity. Using this framework, we are able to determine T_e at the C III emission front position, which stays constant as this front moves from the target towards the X-point, justifying its use as a proxy *thermometer* in detachment-relevant experiments. Showing that $T_i(\text{C III}) \approx T_e^*(\text{C III})$, DSS measurements can effectively provide information on T_e at the front position for many of the divertor geometries that are achievable on TCV that the TS laser beams cannot probe due to their fixed laser trajectory geometry. Lastly, in section 5.3, we follow the evolution of the divertor state from an attached towards a detached regime, estimating the f_{power}, f_{mom} and f_{cond} loss factors of the 2PM presented in section 1.3.1. These are estimated considering the static pressure profiles presented in section 4.3.2

and the electron and ion temperatures representative of different SOL regions, complemented by measurements of radiated power and heat loads at the target. In this last section, DSS and TS data are compared with the model presented by Siccinio et al. (2016) [55], that shows an encouraging qualitatively good agreement.

Throughout this chapter, we will highlight a few applications enabled by the DSS hardware upgrade presented in section 2.1.1. The experiments presented in chapter 4 are a natural test-bed for SOL model validation (i.e. SOLPS-ITER), as they collect a wide range of SOL plasma quantities. We would like to highlight that many of the findings presented in this section are relevant to a much broader range of TCV experiments, most notably related to detachment, aiding the interpretation of the divertor regimes even when the reconstructions presented in this work are not allowed by the divertor geometry. In particular, we note that TS laser beams would typically (e.g. refer, for example, to figure 2.2) provide n_e and T_e measurements only at a single location in the outer divertor leg. DSS can also access T_e from T_i(He II) at higher densities, given high collisional diveror conditions. The T_e values accessed by these measurements can provide reliable values when line ratios techniques of deuterium Balmer lines [138] and/or neutral helium [37] from MANTIS data, mentioned in section 2.3, are no reliable, although little information on n_0 can be inferred by DSS measurements alone.

5.1 Comparison of electron and ion temperatures

The comparison of electron and ion temperatures for different $n_{e,core}$ values at different positions along the leg may be used to understand the plasma processes affecting them. For example, at first sight, one would expect T_e to be lower than T_i since electrons effectively lose their energy by inelastic collisions leading to excitation and ionisation, while ions transfer their thermal motion energy to the free electrons, equalising both temperatures. However, as it will be shown in this section, this is not observed in the experiments presented in this thesis. Moreover, the temperature of different ion species observed within the same plasma volume can differ from the corresponding electron temperature. Therefore, more processes, besides radiation, should be considered. Here we suggest that due to a high influx of low-temperature deuterium and impurity neutrals into the plasma volume, the temperature of ions can be lower than that of the electrons, as will be shown in section 5.1.2

The apparent ion temperature of a species α measured by the DSS, line-averaged along the LOS, was defined in equation 4.12 as

$$T_i(\alpha) = \frac{\int_{LOS} \varepsilon_\alpha(\rho) T_{i,\alpha}(\rho) d\rho}{\int_{LOS} \varepsilon_\alpha(\rho) d\rho} \tag{5.1}$$

For comparison purposes, we define this effective electron temperature of the same species α

as

$$T_e^*(\alpha) \equiv \frac{\int_{\rho_1}^{\rho_2} \varepsilon_\alpha(\rho)\, T_e(\rho)\, d\rho}{\int_{\rho_1}^{\rho_2} \varepsilon_\alpha(\rho)\, d\rho} \tag{5.2}$$

where $\varepsilon_\alpha(\rho)$ is the emissivity profile of the species α, here measured by the MANTIS tomographic inversions, acting as a weight on the $T_e(\rho)$ measured by TS. ρ_1 and ρ_2 represent the integration boundaries defined by the inner and outermost radial locations probed by TS. The tomographic inversions indicate that these radial boundaries include most of the SOL. $T_e^*(\alpha)$ is defined in such a way to represent the most appropriate T_e value to be compared with the $T_i(\alpha)$ measured by DSS. The physical interpretation of an effective electron temperature is that of the electron temperature in the SOL region where the species radiates the most: e.g. considering figures 4.12 and 4.13, showing a highly peaked C III emissivity profile around $\rho(\psi) = 1.01$, we conclude that $T_e^*(\text{C III})$ is indicative of T_e in the proximity of the separatrix. The He II radiation distribution provides another example: although it also peaks at the separatrix for low core density -i.e. figure 4.17c, its emissivity profile significantly broadens across the density ramps, especially close to the target, as in figure 4.17d. In this case, the interpretation of $T_e^*(\text{He II})$ is closer to an average T_e across a large region of the SOL.

We present an experimental comparison of $T_i(\alpha)$ and $T_e^*(\alpha)$ in section 5.1.1, while in section 5.1.2 we implement a model to interpret these measurements.

5.1.1 Experimental observations

Electrons and ions reach thermal equilibrium for relatively high core density and when observed sufficiently far from the divertor targets.

Figures 5.2 and 5.3 plot a comparison of $T_e^*(\alpha)$ to the respective DSS T_i for $\alpha = $ C II, C III, He I and He II. The data are represented for the same lines of sight used in figures 4.12 and 4.13 and are plotted as a function of core density across a density ramp.

$T_e^*(\alpha)$ are obtained using equation 5.2, interpolating over missing, omitted or corrupted data points and applying some 2D smoothing (1D over the average density and the other over the vertical distance from the target). This procedure is illustrated in figure 5.1, where we show the example of $T_e^*(\text{He II})$ data. The uncertainty is obtained by propagating the uncertainties on TS T_e and MANTIS emissivity reconstruction.

Figure 5.2 compares electron and ion temperatures relative to two ionisation states of carbon, with C II in the first column and C III in the second. We observe significant differences between the two species. First, $T_e^*(\text{C II})$ is slightly, but consistently, higher than its corresponding ion temperature, $T_i(\text{C II})$, over most of the density ramp. The difference is more pronounced for higher $T_e^*(\text{C II})$, as in figure 5.2a. Conversely, we observe $T_e^*(\text{C II}) \approx T_i(\text{C II})$ for sufficiently low $T_e^*(\text{C II})$, as in panels c) and d) at high core density. For C III we conversely observe that the $T_i(\text{C III}) \approx T_e^*(\text{C III})$ when sufficiently far from the divertor target (e.g. figure 5.2b)) or well into
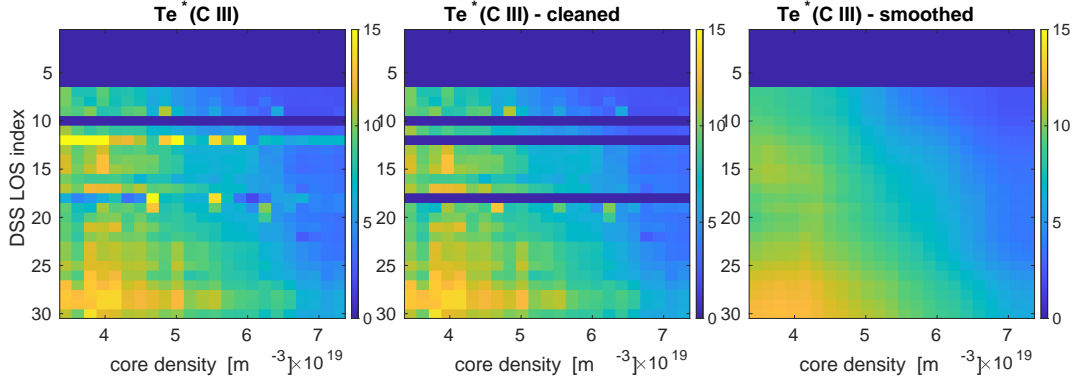
Figure 5.1: T_e^*(C III), expressed in eV. On the leftmost panel, *raw* data expressing the weighted average calculation according to eq. 5.2. In the central panel, unphysical data are discarded. The missing data are interpolated and a 2-D smoothing is applied on the rightmost panel to obtain the T_e^*(C III) represented in figure 5.2. No data is present for DSS LOS < 7 as no TS coverage is provided for these LOS.

the density ramp (e.g. end of the data series plotted in figure 5.2d)). C III ions are also observed to be generally hotter than the C II. This is not observed when probing C III temperatures close to the target, where T_i(C III)< T_e^*(C III), for all data points where C III line-shapes fitting was considered reliable, i.e. before C III emissivity reached 25% of its global maximum. In general, the emission from He II indicates T_i(He II) $\approx$ T_e^*(He II), for most of the DSS LOSs and all core densities, except for the LOS near the target and $n_{e,core} < 5 \cdot 10^{19}$ m^{-3}, as in figure 5.3f).
We attempt to explain the observation of T_i(C III) < T_e^*(C III), T_i(He II) < T_e^*(He II) for chords near the target and $n_{e,core} < 5 \cdot 10^{19}$ m^{-3} in section 5.1.2 by arguing that at this LOS and value of core density $T_i(D^+) < T_e$. Therefore, T_i(C III) and T_i(He II) represent indirect measurements of $T_i(D^+)$ weighted over the C III and He II emission profiles.

The He I temperature is surprisingly constant throughout the core density ramp along the whole divertor leg. We have seen in section 4.4.2 that D$_\alpha$ and D$_\beta$ spectral lines behave similarly, where we argued that the measured characteristic temperatures are due to different neutral particle populations, possibly determined by molecular processes. For the He I case, no in-depth analysis was made to investigate a possible role of molecules on T_i(He I), however, the striking similarity with the deuterium lines would indicate such an approach.

5.1.2 Thermalisation of ions and electrons, and the influence of cold particle influx from the target

The discrepancy between T_i(C II) and T_e^*(C II) can be ascribed to an influx of cold neutral C, while $T_i(\alpha) < T_e^*(\alpha)$ observed near the target for α = He II, C III indicates that $T_i(D^+) < T_e$.

The observation of $T_i(\alpha) \approx T_e^*(\alpha)$ indicates that the observed species α thermalised with

Figure 5.2: Comparison of T_e^* (C II), left column, and T_e^* (C III), right column, to their respective T_i measured by DSS for the LOSs highlighted in figures 4.12 and 4.13, plotted as function of core density. To the C III plots, two vertical lines are added, representing for which density the C III reaches 75% and 50% of its intensity, respectively, at the given DSS LOS. The T_i (C III) data series is plotted until C III emission intensity reaches 25% of its global maximum.

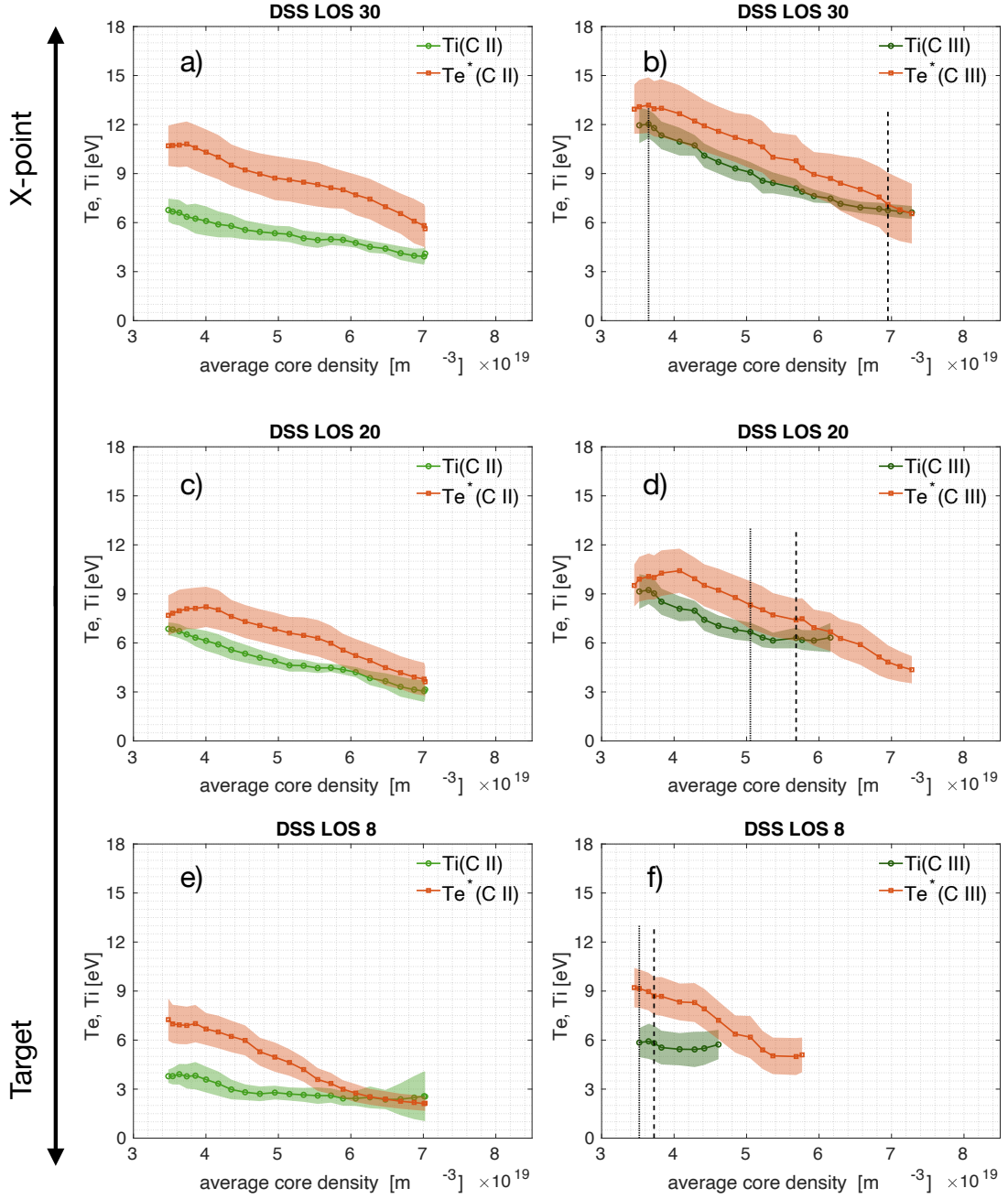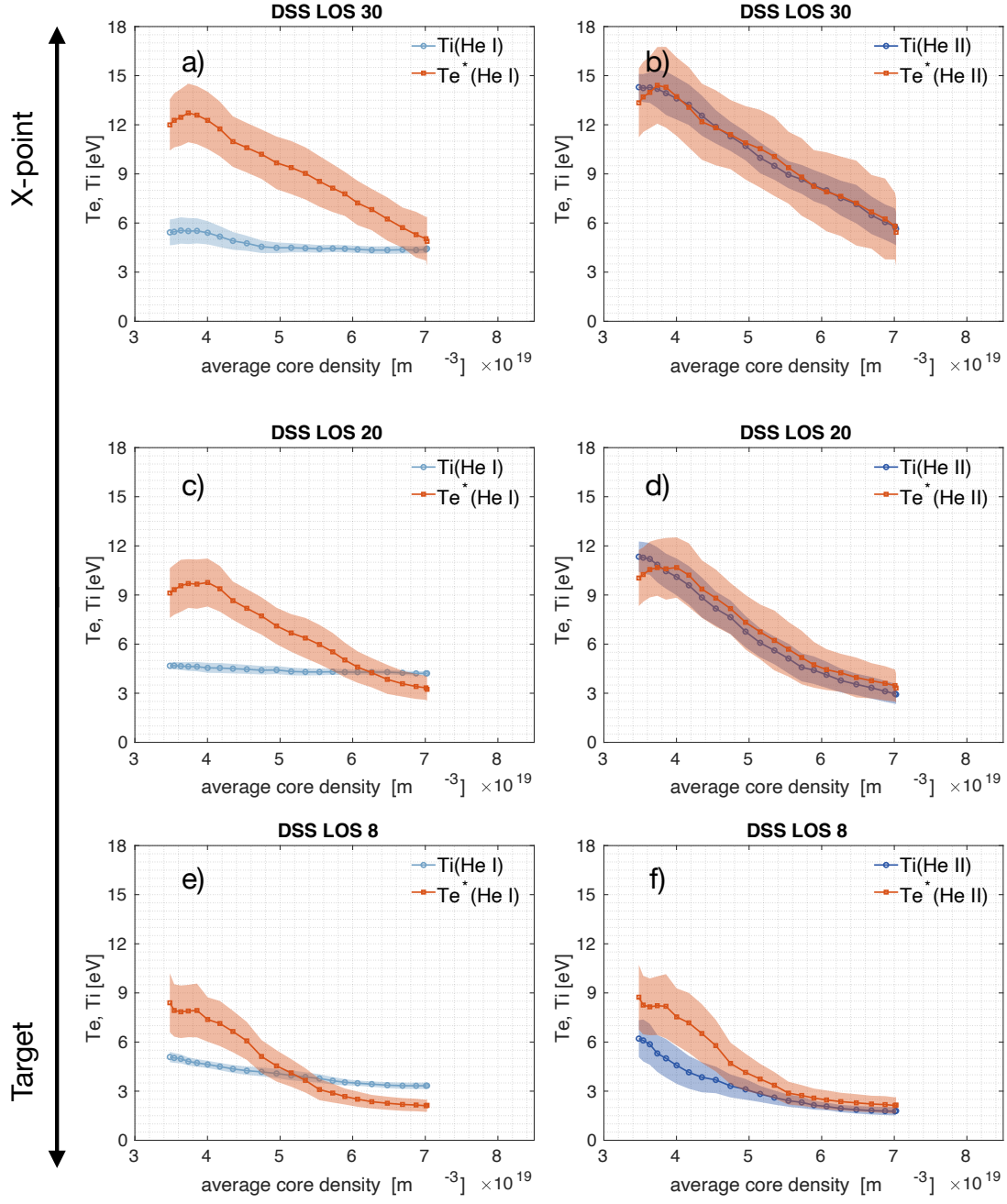Figure 5.3: Comparison of T_e^* (He I), left column, and T_e^* (He II), righ column, to their respective T_i measured by DSS for the LOSs highlighted in figures 4.12 and 4.13, plotted as function of core density.

the electrons. However, it must be noted that the considerably smaller mass difference between impurity ion species and deuterium ions, compared to that between impurity ions and electrons, implies that the impurity ions' temperature will always tend to that of the deuterium ions.

The consistent observations of $T_i(\text{C II}) < T_e^*(\text{C II})$ in figure 5.2 led to the hypothesis of the presence of a cold carbon particle influx entering the divertor from the target and surrounding walls. To estimate the effect of a cold C I neutral influx on the C II ion temperature, we use an ionisation-balance (IB) model for carbon that includes a constant source of C I neutrals in the ground state at wall temperature (≈ 0.03 eV). We notice that even if the initial C I temperature were higher than wall temperature (e.g. ≈ 1 eV range), i.e. from molecular dissociation of carbohydrates, the resulting C II temperatures presented in figure 5.5 would differ by $< 10\%$. We will see how the introduction of this cold influx of neutral carbon atoms can explain the difference between $T_i(\text{C II})$ and $T_e^*(\text{C II})$ observed along the entire divertor leg. However, the modelled cold neutral C flux practically does not affect the C III ion temperature, which satisfies $T_i(\text{C III}) \approx T_i(D^+)$ for all plasma parameters here considered, confirming that when $T_i(\text{C III}) < T_e^*(\text{C III})$ is observed, $T_i(D^+) < T_e$ is implied.

In this model, the evolution of the carbon ionisation states is calculated using the following:

- *effective recombination coefficients* (ACD)

- *effective ionisation coefficients* (SCD), and

- *charge exchange effective recombination coefficients* (CCD)

interpolated over a set of n_e and T_e, using data provided by ADAS-OPEN [126].
The emissivities of the selected C II and C III transitions are then calculated using the ionisation state distribution and photon emission coefficients (PECs - [126]). To obtain the PECs for the selected n_e and T_e, we interpolated between the values again provided by the OPEN-ADAS database.
The evolution of the C II and C III ion temperatures is calculated by considering the thermalisation processes with electrons, deuterons and the influx of cold C I particles that are subsequently ionised to higher carbon charge states. Here we omit thermalisation between carbon charge states by assuming that the carbon density is negligible compared to the deuterons.

The set of equations used in the model is:

Discussion

- *Ionisation states evolution:*

$$\frac{dn_0}{dt} = \left(\alpha_{ACD}^{(1)}(n_e, T_e) \cdot n_e + \alpha_{CCD}^{(1)}(n_e, T_e) \cdot n_D\right) \cdot n_1 - \alpha_{SCD}^{(0)}(n_e, T_e) \cdot n_0 \cdot n_e + S_{C\,I}$$

$$\vdots$$

$$\frac{dn_Z}{dt} = \alpha_{ACD}^{(Z+1)}(n_e, T_e) \cdot n_e \cdot n_{Z+1} + \alpha_{CCD}^{(Z+1)}(n_e, T_e) \cdot n_D \cdot n_{Z+1} + \alpha_{SCD}^{(Z-1)}(n_e, T_e) \cdot n_e \cdot n_{Z-1} -$$
$$\left(\alpha_{ACD}^{(Z)}(n_e, T_e) \cdot n_e + \alpha_{CCD}^{(Z)}(n_e, T_e) \cdot n_D + \alpha_{SCD}^{(Z)}(n_e, T_e) \cdot n_e\right) \cdot n_Z$$

$$\vdots$$

$$\frac{dn_6}{dt} = \alpha_{SCD}^{(5)} \cdot n_e \cdot n_5 - \left(\alpha_{ACD}^{(6)} \cdot n_e + \alpha_{CCD}^{(6)} \cdot n_D\right) \cdot n_6$$

(5.3)

where n_Z is the density of ions of charge state Z; $\alpha_{ACD}^{(Z)}$ is an effective recombination coefficient from ions of charge state Z to ions of charge state $Z-1$; $\alpha_{CCD}^{(Z)}$ is the effective charge exchange recombination coefficient of ions of charge state Z with hydrogen or deuterium to ions of charge state $Z-1$; $\alpha_{SCD}^{(Z)}$ is the effective ionisation coefficient from charge state Z to charge state $Z+1$; finally, n_e and n_D are the electron and the neutral densities. Metastable-resolved data are used in the calculation of the charge state distribution. The term $S_{C\,I}$ is a constant source of cold neutral carbon, added at each time step to the plasma volume. For example, with a $S_{C\,I} = 10^3$ s^{-1}, the number of C particles doubles every ms. It is important to note that, as described by these equations, the model does *not* account for any transport term.

- *Emissivity of the selected transitions:*

$$\varepsilon_\lambda^{(Z)}(t) = \alpha_{PEC}^{exc}(n_e, T_e, \lambda) \cdot n_e n_Z(t) + \alpha_{PEC}^{rec}(n_e, T_e, \lambda) \cdot n_e n_{Z+1}(t) +$$
$$\alpha_{PEC}^{cx}(n_e, T_e, \lambda) \cdot n_D n_{Z+1}(t)$$

(5.4)

where $\varepsilon_\lambda^{(Z)}(t)$ is the spectral line emissivity at wavelength λ; α_{PEC}^{exc} is the photon emission coefficient due to excitation for the selected transition; α_{PEC}^{rec} is the photon emission coefficient due to recombination and α_{PEC}^{cx} is for charge exchange processes;

- *Temperature evolution for the selected ions:*

$$\frac{dT_i^{(Z)}}{dt} = \frac{T_e - T_i^{(Z)}}{\tau_{ei}^{(Z)}} + \frac{T_D - T_i^{(Z)}}{\tau_{Di}^{(Z)}} + \frac{\alpha_{SCD}^{(Z-1)} \cdot n_e \cdot n_{Z-1}}{n_Z} \cdot (T_i^{(Z-1)} - T_i^{(Z)}) +$$
$$\frac{(\alpha_{ACD}^{(Z+1)} \cdot n_e + \alpha_{CCD}^{(Z+1)} \cdot n_D) \cdot n_{Z+1}}{n_Z} \cdot (T_i^{(Z+1)} - T_i^{(Z)})$$

(5.5)

where $T_i^{(Z)}$ is the temperature of the ion with charge state Z; T_e the electron temperature; T_D the deuteron temperature; $\tau_{ei}^{(Z)}$ the thermalisation time of the ion with charge state Z with the electrons [125] and $\tau_{Di}^{(Z)}$ the thermalisation time of the ion with charge state

Z with the deuterons. Since in our plasmas $\tau_{Di}^{(Z)} \ll \tau_{ei}^{(Z)}$, and $T_D \approx T_e$, in principle, the first term of the r.h.s. of equation 5.5 can be neglected compared to the second one.

The charge state density distribution, transition emissivities, and C II and C III ion temperatures are calculated for $n_e = 2 \cdot 10^{19}$ m^{-3}, T_e in the range of $T_e = 0.5 - 15$ eV, for several values of C I flux, and for several values of neutral deuterium density. It is important to note that in all the calculations described here, we assume $T_i(D^+) = T_e$. The plasma density used here is symptomatic of that typically measured by TS close to the target during the density ramp.

The IB model includes the presence of neutral deuterium atoms - in the form of a neutral fraction n_0/n_e - since it strongly affects the charge state distribution via charge exchange recombination reactions. This was found to be important in recent publications, as in Chen et al. (2020) [139], as part of the non-coronal effects affecting the C III emission, and it will be further elaborated in section 5.2.

The C I flux values shown in figure 5.5 represent the flux normalised to the C ion density ($n_{C\ II} + n_{C\ III} + n_{C\ IV}$...) per m^{-2}, i.e. ion density integrated radially across the divertor leg. In other words, these values represent the number of neutral C atoms entering the plasma volume per unit of time and per C ion particle. In the model, the C I particles enter the plasma volume at wall temperature.

Each species' ionisation distribution and thermalisation time are iteratively computed in steps of $\Delta t = 5 \cdot 10^{-8}$ s, considering the addition of the said cold particles into the plasma volume. The temperature of each species is also re-calculated at each time step. The model provides equilibration temperatures of C II and C III, obtained for each set of n_e, T_e, C I flux and n_0.

The evolution of the impurity ion temperatures and charge state distribution is represented in figure 5.4, for $S_{C\ I} = 10^1, 10^3$ s^{-1}, $n_0/n_e = 2\%$ and the constant value of $T_{D^+} = T_e$ set to 10 eV. The initial impurity ion temperature is set to $T_i^{(Z)}(t=0) = T_{D^+}$, and then the system, which includes an addition of cold C I particles, is left to evolve. An *equilibration temperature* is reached for all ion species after ≈ 100 μs, with notably, $T_i(C\ II) < T_i(C\ III) \approx T_i(He\ II)$. The fractional abundances, illustrated in figures 5.4b and e, also reach an asymptotic value but on time scales that depend on the chosen $S_{C\ I}$. Figures 5.4c and f, instead, illustrate the fractional abundances normalised to that at $t = 0$ s, highlighting the effect of $S_{C\ I}$ in increasing the number of C particles.

This is presented in figure 5.5, where data for $T_i(He\ II)$ are calculated using an analogous approach, imposing a range of $S_{He\ I} = 0.2$ to 200. This was chosen to be lower than that of C to mimic the expected lower density of He impurities in the divertor region. The ion temperature values are taken after letting the system evolve for 500 μs when an equilibration temperature is reached for each species.

In figure 5.5, C III and He II ions curves adhere to the black dashed lines, indicative of $T_i = T_e$: these species are not affected by the cold influx. Conversely, the C II ion temperature
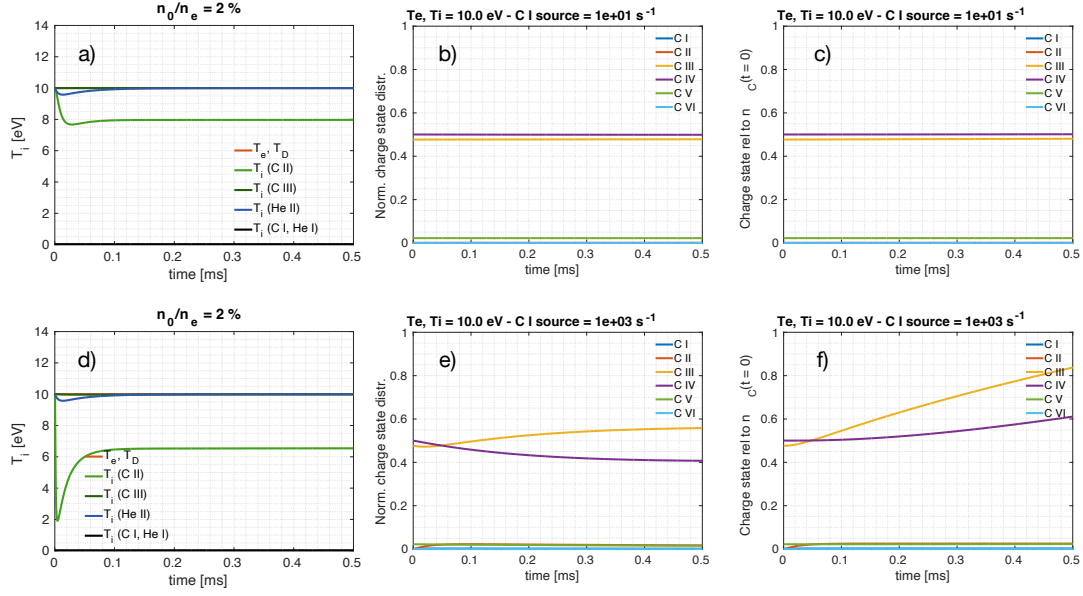
Figure 5.4: Evolution of $T_i^{(Z)}$, in panels a) and e) and of the C species charge state distributions, panels b), c), e) and f), as a function of time for two values of C I influx - 10 and 10^3 s^{-1}. In the second column, the charge state distribution is renormalised at each time step, while, in the third column, it is normalised to that at $t = 0$, highlighting the increase of C density due to the continuous cold C I influx.
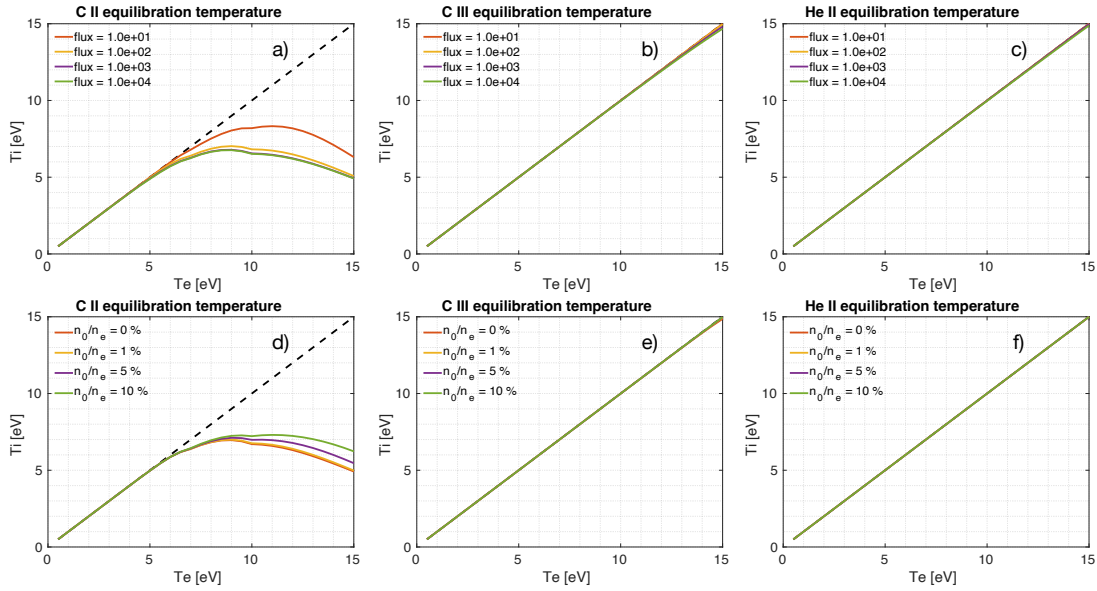
Figure 5.5: Equilibration temperatures of C and He ions when considering an influx of cold particles entering the plasma volume at wall temperature. Panels a) to c) illustrate the dependence of the model on the magnitude of the cold neutral flux, while panels d) to f) illustrate its dependence on the neutral deuterium density.

is observed to deviate from the $T_i = T_e$ reference in the region of T_e between 6 and 9 eV, depending on the magnitude of the cold flux, showing that $T_i(\text{C II}) < T_e$. A comparison of panels a) and b) also shows that $T_i(\text{C II}) < T_i(\text{C III})$ when $T_e > 6 - 9$ eV. This is indeed what is observed in figure 5.2: in panel a), when $T_e^*(\text{C II})$ is 11 eV, the corresponding $T_i(\text{C II})$ is of ≈ 6.5 eV, but across the density ramp, with the decreasing T_e, this difference also decreases. We observe $T_e^*(\text{C II}) \approx T_i(\text{C II})$ only when the former is sufficiently low i.e. close to the target and/or at high core density, as in panels 5.2c) and e).

Finally, the consistent observation of $T_i(\alpha) < T_e^*(\alpha)$ for $\alpha = $ C III and He II, close to the divertor target at the beginning of the density ramp, led to the hypothesis that $T_D < T_e$ in this region. Indeed, we know from section 1.3.2 that, in a regime of high recycling that precedes divertor detachment, the divertor target region is characterised by several cycles of ionisation and surface recombination of particles recycled from the machine wall. When these particles are recycled, they enter the divertor region at wall temperature, but the ionisation of such particles, and the subsequent *partial* thermalisation, or charge-exchange processes, can lead to the presence of localised cold D^+ ions in front of the target.

From the thermalisation times illustrated in figures 4.6a and b, it is reasonable to state that where $T_i(\alpha) \approx T_e^*(\alpha)$ is observed, the impurity species first thermalise with deuterium, that in turn, is thermalised by the electrons. Where this is not observed, and the measured $T_i(\alpha) < T_e^*(\alpha)$, it is reasonable to assume that $T_D < T_e$, as the He^+ and C^{2+} ion temperatures would be closer to that of D^+. Figure 5.6 supports this hypothesis. Here $T_i(\text{C II})$ and $T_i(\text{C III})$ are calculated by the CR model as a function of $T_i(D^+)$, for a fixed $T_e = 10$ eV and neutral fraction of 2%. The effect of the cold C I influx is recovered on $T_i(\text{C II})$, but we observe $T_i(\text{C III}) \approx T_i(D^+)$ even when the latter differs from T_e.

This is the case illustrated in figures 5.2f) 5.3f) representing the temperatures in the vicinity of the target: here we observe both $T_i(\text{C III}) < T_e^*(\text{C III})$ and $T_i(\text{He II}) < T_e^*(\text{He II})$, suggesting that $T_D < T_e$. When moving away from the target, we see that $T_i(\text{C III}) \approx T_e^*(\text{C III})$ and $T_i(\text{He II}) \approx T_e^*(\text{He II})$, with the equality increasing with increasing distance from the target, e.g. as in figures 5.2b) and d) and 5.3b) and d) suggesting that here $T_e \approx T_D$.
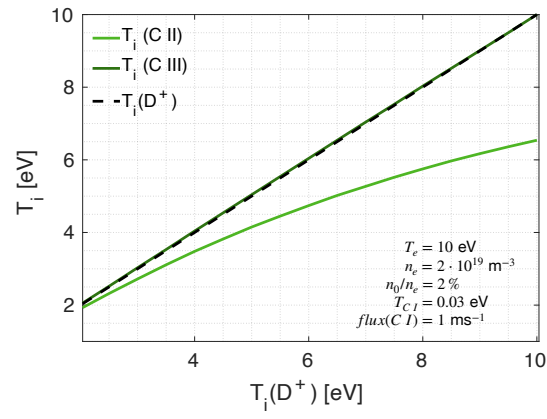
Figure 5.6: Equilibration temperature of C II and C III as a function of $T_i(D^+)$ for a fixed T_e.

5.2   C III emission front temperature determination

The measurement of constant characteristic temperatures along the C III emission at 465 nm front position during the evolution from an attached towards a detached divertor supports its use as a thermometer.

The C III line radiation observed in the experiments presented in chapter 4 and discussed in detail in section 5.1 is exploited by many C-walled magnetic confined fusion devices in detachment experiments. For instance, it is routinely used for impurity flow velocity measurements in DIII-D (Weber et al. (2013) [140]), MAST (Silburn et al. (2014) [141]) and more recently also in W7-X (Gradic et al. (2021) [142]). Moreover, using similar techniques to those illustrated in section 3.2.1, it is used in W7-X to measure the T_i associated with carbon impurities, as in the work of Gradic et al. (2022) [143].

Figures 4.12 and 4.13 show a gradual decrease of the C III intensity with divertor cooling. This is often used in detachment-relevant experiments as a proxy to indicate the attainment of *low T_e* in the region where the C III radiation intensity becomes negligible. In these scenarios, we identify the location between the X-point and target where the C III intensity drops to 50% of its maximum as the *C III radiation front*. This position is usually easy to define, as the intensity drops quite abruptly in this region of *low T_e*, even with a relatively low Te gradient. Since the transport of C III is unlikely to change abruptly, this change in emission intensity is associated with a reduction in T_e rather than one in N(C III). This front movement is tracked in many machines, such as in DIII-D (Wang et al. (2022) [144]). In TCV, its position can be analysed in real-time, as illustrated in the works of Ravensberger et al. (2021) [78] and Koenders et al. (2023) [106], to initiate and stabilise a cold plasma region in front of the target, thus facilitating controlled detachment attainment [*]. Measurements of the C III radiation front and its movement are well established in TCV and many experiments rely on it to evaluate the success in attaining a cold divertor temperature: some examples are in the recent studies on TCV divertor closure effect on detachment, reported in Reimerders et al. (2022) [42], or the role of different geometries on the detachment threshold, studied in Theiler et al. (2017) [53]; and on diverted negative triangularity, by O. Février (in preparation).

The works of Nakano et al. (2009) [145] and Harrison et al. (2017) [66] based, respectively, on collisional radiative codes and OMS-EIRENE and DIVIMP codes, evaluate the T_e at the C III radiation front location to be between 3-8 eV. However, in these experiments, we are able to directly measure the ion and electron temperatures involved from the profiles reconstructed in figures 4.12 and 4.13, including the information presented in section 5.1. Moreover, from the shape of the T_e profiles in the SOL, which was observed to be asymmetric and peaked at the separatrix, a single value of T_e to define the one at C III radiation front inevitably compresses the information contained in the radial profile. In this work, we instead present two simultaneous temperature values, used to determine a peak and an average T_e at the C III

---

[*]Although the C III emission region can be indicative of a low-temperature region, it is not a measure of detachment *per se*.

radiation front position, that retains part of the information on the T_e profiles in the SOL.

The X-point position is not included in the DSS field of view in the experiments presented in chapter 4. Therefore, it was impossible to define the C III radiation front the same way as done in the real-time control experiments, which consider emission along the entire leg length. In this section, we consider the radiation intensity within the DSS field of view across the density ramp. The difference in the two approaches is considered here to be small, since, as already mentioned, the drop in C III intensity is rather abrupt. A 2D representation of the C III intensity is plotted in panel a) of figures 5.7, 5.8 and 5.9, as a function of core density (horizontal axis) and vertical distance from the target (vertical axis). The colourmap indicates, in yellow, the region where C III line radiation is the most intense, and, with dark blue, where the C III emission is low. We can thus determine where, within the DSS's field of view, the C III radiation intensity decreases to 75% (figure 5.7), 50% (figure 5.8) and 25% (figure 5.9) of its global maximum across the entire density ramp. These percentages are referred to as *extinction factors*, indicated by a red line in panel a) of each of these figures, demonstrating that the radiation front moves away from the target with increasing core density.
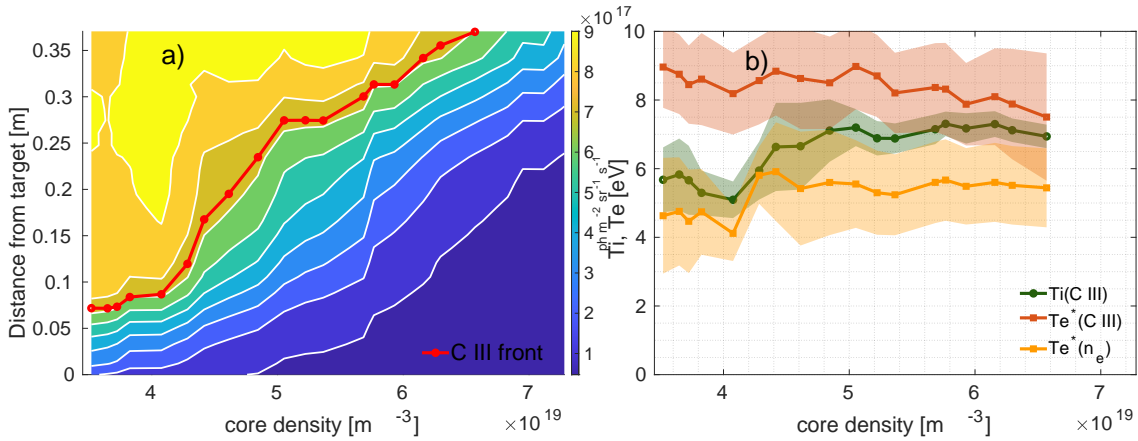
Figure 5.7: a) C III radiation intensity measured by DSS and the position of its 75% extinction factor (C III radiation front), plotted in red as a function of the increasing core density; b) the T_i(C III), T_e^*(C III) and the average T_e, weighted on n_e, all measured along the red line of panel a), following the C III radiation front as it moves towards the confined plasma core across the density ramp.

Panels b) of figures 5.7, 5.8 and 5.9 represent respectively the T_i(C III), T_e^*(C III), and T_e^*(n_e) measured along the red line of panel a) of each respective figure. We thus track all of these characteristic temperatures as a function of the C III front position during its movement.

In each case, these temperatures are relatively constant, except T_i(C III) and T_e^*(C III) close to the target, likely due to the process described in section 5.1: a cold influx of working gas (D) and C neutrals lowers the temperature of the carbon, that gradually thermalise as the average density increases and as the front moves away from the target. From the arguments presented in section 4.4.1, we associate the T_e^*(C III) with a *peak T_e*, as it is representative of
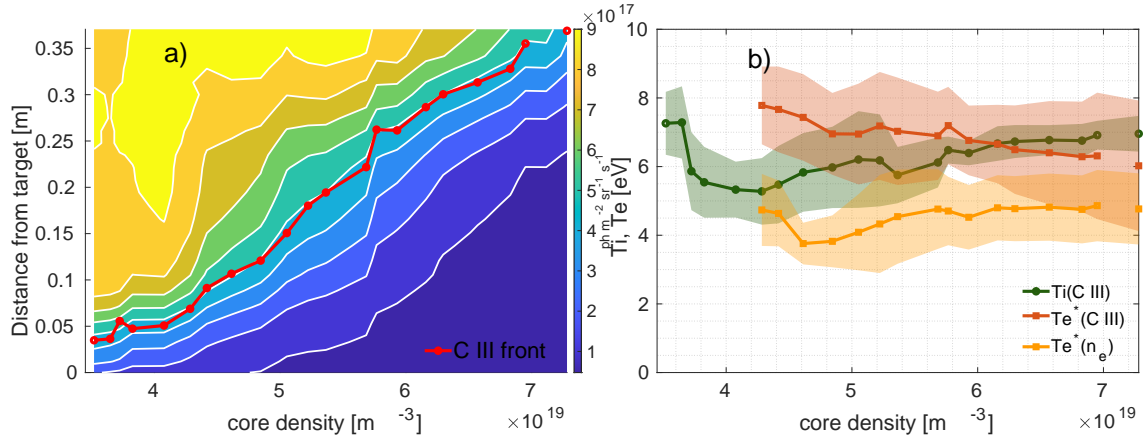
Figure 5.8: Similar to figure 5.7, but considering 50% of the intensity extinction factor.
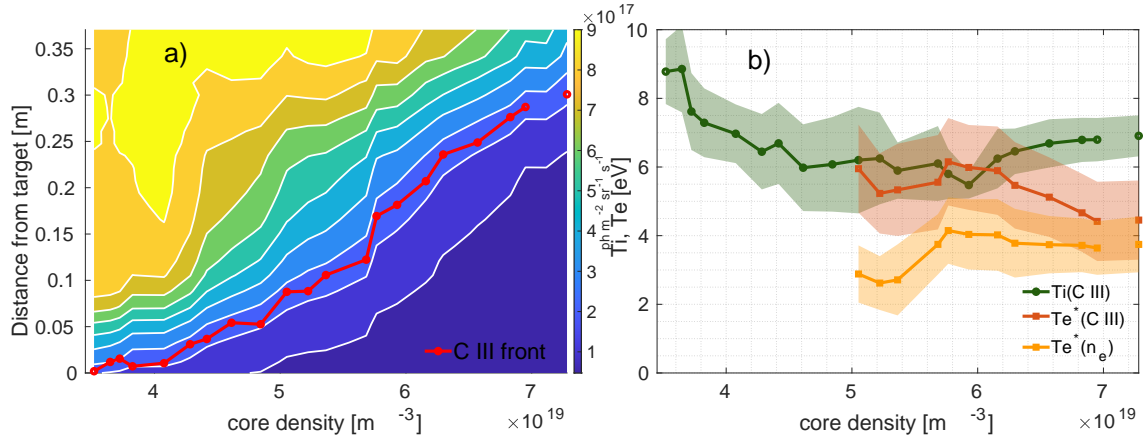
Figure 5.9: Similar to figure 5.7 and 5.8, but considering 25% of the intensity extinction factor.

the separatrix region, where T_e is observed to be peaked. Another characteristic temperature is represented in figures 5.7, 5.8 and 5.9: $T_e^*(n_e)$, which represents an average T_e weighted to the electron density n_e, that can be taken as an appropriate definition of *average T_e*, is seen to remain constant with the C III front movement, regardless the considered extinction factor (25%, 50% or 75%). The values of average and peak T_e at the C III radiation front position are reported in table 5.1 for three values of the extinction factor.

We now re-consider the lower T_e limit of the C III radiation. Further examples of the reconstructed radial profiles of C III emissivity and T_e are illustrated in figure 5.10, for additional DSS LOSs than those of figures 4.12 and 4.13. Here, a grey stripe marks the region of $T_e \approx 3 - 4.5$ eV. The T_e profile changes its gradient in this temperature region, flattening in the common flux region. Here, the C III spectral line's intensity decreases nearly completely; in other words, the C III radiation mostly comes from the SOL region where $T_e > 3 - 4.5$ eV. At high average density, as illustrated in the right-hand panels of figure 4.13, this region radially retreats towards

C III radiation front temperatures		
Exctinction facor	**Average** T_e	**Peak** T_e
75%	5.5 ±1 eV	8.5 ±1 eV
50%	4.5 ±1 eV	7.0 ±1 eV
25%	4.0 ±1 eV	5.5 ±1 eV

Table 5.1: Measured values of C III front temperatures for three extinction factors.
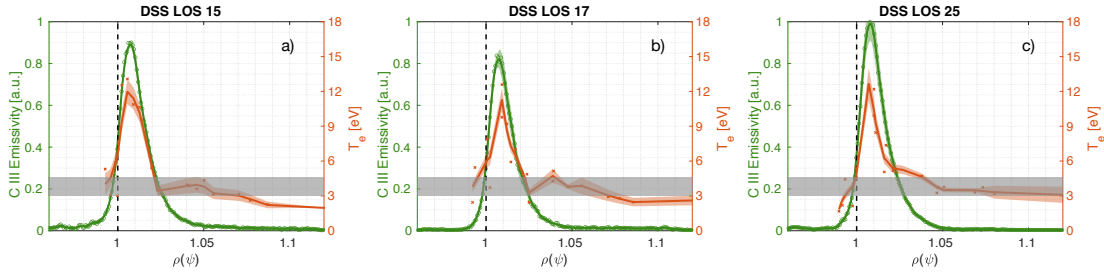
Figure 5.10: Reconstruction of normalised C III emissivity and T_e as in figures 4.12 and 4.13. Panel a) represents the data corresponding to DSS LOS 15 at nel = $4.7 \cdot 10^{19}$ m^{-3}; panel b) refers to DSS LOS 17 and nel = $5.3 \cdot 10^{19}$ m^{-3}; panel c) refers to DSS LOS 25 and nel = $5.7 \cdot 10^{19}$ m^{-3}. The grey shaded area represents the proposed threshold for C III emission, corresponding to $T_e \approx 3 - 4.5$ eV.
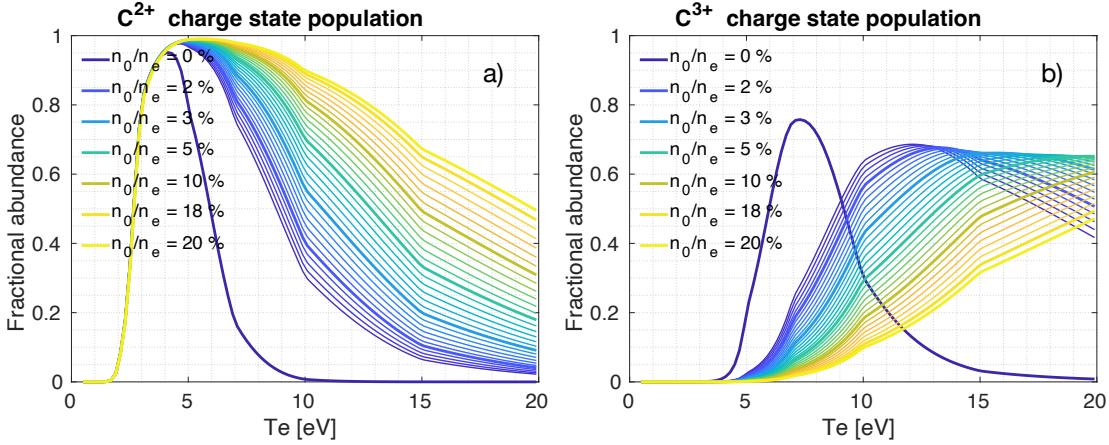
Figure 5.11: Charge state distribution of C^{2+} and C^{3+} ions as a function of T_e for different neutral fractions n_0/n_e.
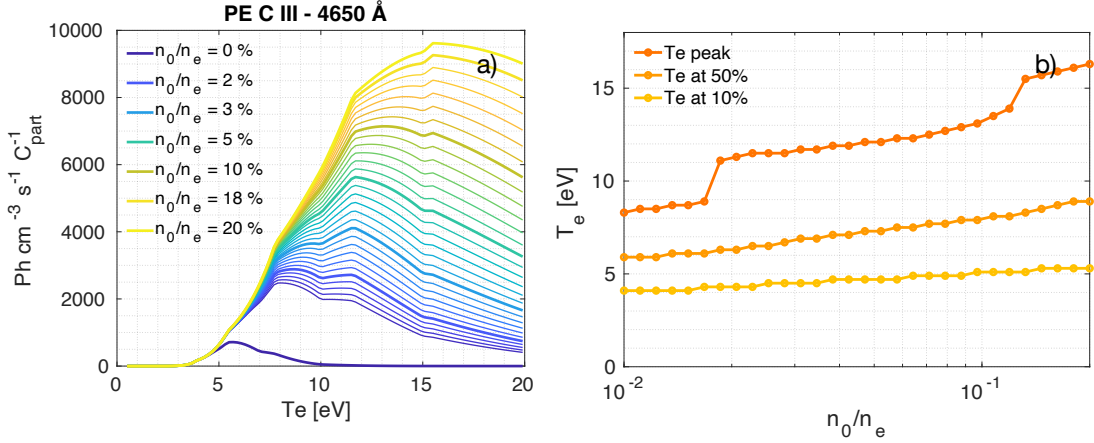
Figure 5.12: Panel a) shows the C III emissivity as a function of T_e for increasing values of neutral fraction n_0/n_e and a fixed $n_e = 2 \cdot 10^{19}$ m^{-3}. Panel b) shows the T_e at the emissivity peak, at its 50% and at its 10%, as a function of n_0/n_e, defining different *front* temperatures.

$\rho(\psi) \approx 1.01$ with the same behaviour reflected on the C III emissivity.

These observations can be used to test the simple IB model introduced in section 5.1.2. This tool can be used not only to compute the equilibration temperature in the presence of cold fluxes but can also provide the photon emissivity of the C III transition for several parameters - i.e. T_e, n_0/n_e. Panels a) and b) of figure 5.11 show the charge state distribution of C^{2+} and C^{3+} ions as a function of T_e for neutral fractions between 0% and 20%. From these figures, we notice that they are strongly affected by the neutral density, as charge exchange recombination of C^{3+} with neutral deuterium is responsible for populating the C^{2+} charge state at values of T_e that would otherwise not be accessible for this species. The curve representing the C^{2+} distribution for $n_0/n_e = 0\%$, illustrated in panel a by the darkest blue line, which corresponds to the case of no charge exchange recombination, is peaked at 4 eV and is characterised by a sharp decay as a function of T_e. When neutrals are introduced, the decay of the distribution becomes slower as the C^{2+} are populated for higher T_e. The emissivity of the C III line reflects the C^{2+} ion charge state distribution. This is illustrated in figure 5.12a, as a function of T_e for the same values of neutral density used to compute the data in figure 5.11. The C III emissivity increases in magnitude and its peak moves to higher T_e with increasing n_0/n_e, as indicated by the dark orange line in figure 5.12b. From these emissivities, it is also possible to calculate the electron temperature for which the emissivity is halved or reaches 10% of its peak - i.e. respectively a 50% and 90% extinction factor. These values are plotted in figure 5.12b as a function of n_0/n_e. The curve representing the T_e at the 90% extinction factor agrees with the experimental data of figure 5.10: no C III radiation is observed below the grey band between 3 eV and 4.5 eV because the C^{2+} ion charge state is no longer populated at these temperatures. The value of T_e^*(C III) illustrated in figure 5.8 for the 50% extinction factor case, and reported in table 5.1 as *peak T_e*, is also in good agreement with the 50% extinction factor curve of figure

127

5.12b, ranging from 6 to 9 eV depending upon the neutral fraction.
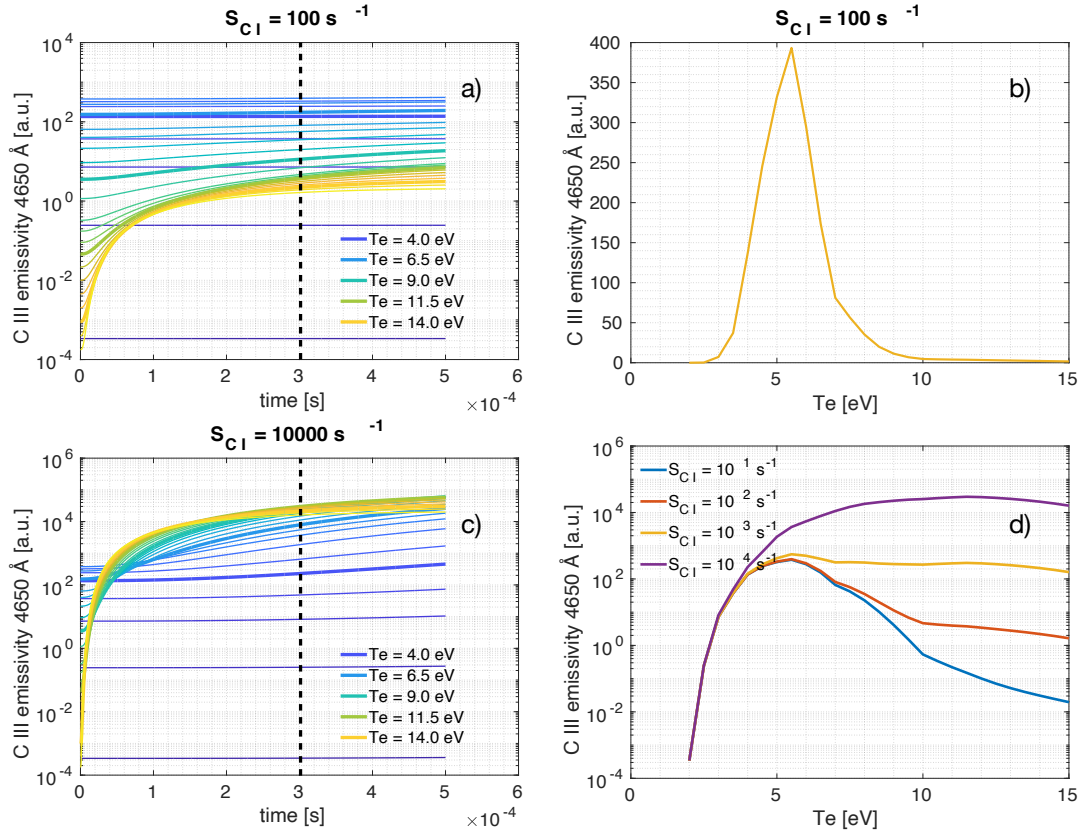
Figure 5.13: $S_{C\,I}$ effect on C III emissivity at 4650 Å calculated by the IB code. Panel a) and c) show the time evolution of the C III emissivity for several T_e values, starting at $T_e = 2$ eV - indicated by the dark blue lines - up to $T_e = 15$ eV - indicated by the bright yellow lines, for values of $S_{C\,I}$, 10^2 s and 10^4 respectively. Panels b) and d) present the same emissivity, here as a function of T_e, considering the values presented at $t = 300$ μs, corresponding to the dashed lines in panels a) and c).

We now discuss the effect of a constant C I source on the C III emissivity. The idea, as previously argued, is that when an ion enters a high-temperature plasma region, it takes a finite amount of time to ionise. Because of this, low-charged ions can still exist in relatively high-temperature plasma regions, resulting in significant emission. Figure 5.13 presents the outcomes of the IB code for the C III emissivity. Panels a) and c) are analogous to panels a) and d) of figure 5.4, this time showing the emissivity of C III at 4650 Å as we let the system evolve from the initial conditions. Here the colour map indicates low-T_e by dark blue lines and higher T_e by yellow ones. We see, for instance, that depending on the cold carbon source magnitude, the emissivity reaches a steady state at different T_e, largely because the C III charge state population reaches a different equilibrium (see figure 5.4b and e). To model the dependence of the emissivity on T_e we take a slice of the data at $t = 300$ μs, indicated by the black dashed line. An example of C III emissivity at 4650 Å plotted as a function of T_e is presented in figure 5.13c for the case of $S_{C\,I} = 10^2$ s^{-1}. Figure 5.13d, conversely, presents similar data for several

values of $S_{C\ I}$. Increasing $S_{C\ I}$ results in significantly increased C III emissivity at higher T_e, as presented by the purple curve of figure 5.13d. The transient population of C III ions is strongly excited by higher temperature e^-, causing C III emission before ionisation.

Therefore, this mechanism can also lead to a C III emissivity peak at $T_e \approx 12$ eV observed during the experiments presented in chapter 4. Experimentally disentangling the contribution of charge exchange from that from $S_{C\ I}$ is very challenging and outside the scope of this thesis. We have shown, however, that although transport is already taken into account in many applications and models (see, for instance, Kallenbach et al. (2013) [146] and Henderson et al. (2017) [147]), it remains important to include the effect of deuterium charge exchange recombination with impurity ions in the ionisation balance. To date, this reaction is *not* accounted for in SOL simulation codes, such as SOLPS-ITER. Here, the only considered CX reactions are those affecting the D^+ transport equations, but no analogous reaction is considered for the C ions transport equations [148, 149]. This likely leads to an overestimation of the impurity transport and to a misevaluation of the C III emission intensity and its emission front position.

5.3 Transition from attached to detaching divertor - comparison with the 2PM

The data presented in chapter 4 can also be used to test the theory of the Two Point Model presented in section 1.3.1, following Stangeby's description. The combination of T_e, n_e and p_e measurements can give precious insight into the three loss factors introduced in the 2PM to describe detachment, f_{power}, f_{mom} and f_{cond}.

Section 1.3.1 discussed how the interplay between momentum removal redistribution before the target, volumetric power losses, and heat transport via convection are ultimately required to observe a particle flux rollover and attain the detachment of the divertor leg. Despite this regime not being attained in the experiments presented in chapter 4 (see figure 4.3e and f), Γ_t does deviate from a linear growth before reaching a saturated value across the density ramp, indicating the presence of additional loss factors that are taking the divertor from an attached toward a detached regime. In the following sections, we investigate the presence of each of these loss factors and try to link them to the observations of p_e, T_e, T_i (He II), and the electron heat conductivity κ_e.

5.3.1 Volumetric power losses

During the density ramp volumetric power losses are observed to increase in the outer divertor leg region. The power deposited at the target is also observed to decrease, for a ≈ constant power entering the outer divertor leg. Therefore, f_{power} increases across the density ramp.
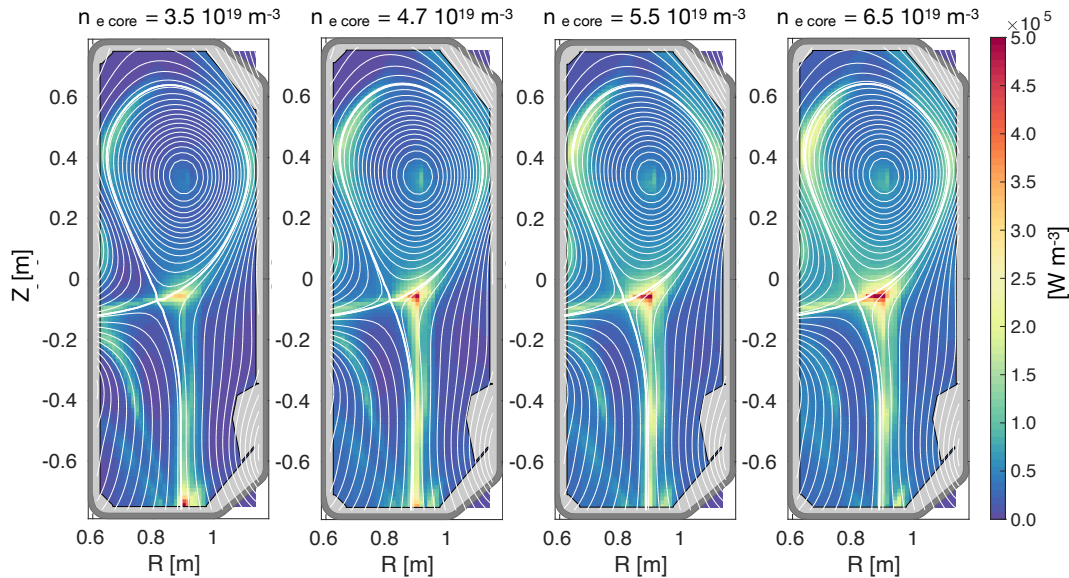

Figure 5.14: Power radiated in TCV poloidal cross-section reconstructed by Radcam's bolometry system tomographic inversions [87] across the density ramp, for discharge #74213.

Volumetric power losses are the first mechanism taking place in the transition from an attached regime towards a high recycling situation. These are required in the goal of decreasing the plasma temperature and redistributing the exhausted power onto the machine's walls, alleviating the heat loads at the divertor targets. Following the 2PM theory presented in section 1.3.1, the power density flux in the SOL can be modelled in the following way. We can write the continuity equation for the heat flux as

$$\vec{\nabla} \cdot \vec{q} = S \tag{5.6}$$

where S represents all power density sinks and sources. In this treatment, the dimensions of $q_{\parallel}$ are [$\mathrm{W\,m^{-2}}$] and S is in [$\mathrm{W\,m^{-3}}$]. As we are mainly interested in the parallel component of q in the SOL, where the main contributions to S are given by radiated power (S_{rad}) and charge exchange reactions (S_{CX}), so we can rewrite equation 5.6 as

$$\partial_{\parallel} q_{\parallel} = S_{rad} + S_{CX} \tag{5.7}$$

which can be integrated from upstream to the target as

$$\int_u^t \partial_{\parallel} q_{\parallel} \mathrm{d}s = \int_u^t (S_{rad} + S_{CX}) \mathrm{d}s \tag{5.8}$$

where s is the coordinate along the magnetic field line connecting the upstream location u to the target t. From this, we take the difference between the upstream and target heat fluxes to equal the integral along the SOL of the radiated power density and CX, I_{rad} and I_{CX} respectively, as

$$q_{\parallel}^t - q_{\parallel}^u = I_{rad} + I_{CX} \tag{5.9}$$

normalising by $q_{\parallel}^u$ we obtain an expression for f_{power} of equation 1.20

$$\frac{q_{\parallel}^t - q_{\parallel}^u}{q_{\parallel}^u} = \frac{q_{\parallel}^t}{q_{\parallel}^u} - 1 = f_{power} = \frac{I_{rad} + I_{CX}}{q_{\parallel}^u} \tag{5.10}$$

We note that, following the second 2PM approach presented in section 1.3.1, a third contribution should be added to $q_{\parallel}$. Indeed, ionisation of neutral particles requires a minimum E_{ion} energy to be spent. In absence of volumetric recombination, this is returned to the target as surface recombination, contributing with approximately 13.6 eV $\times \Gamma_t$.

The parameters in equation 5.10 can be directly measured, or estimated, in order to provide an estimation of the volumetric power losses occurring in the SOL across the density ramp. Equivalently, it is possible to compare volume-integrated measurements that are more easily

measured in TCV. The definition of f_{power} does not change, as

$$Q_\parallel^t = Q_\parallel^u (1 - f_{power})$$
$$Q_\parallel^t = Q_\parallel^u - P_{loss}$$
$$\frac{Q_\parallel^t}{Q_\parallel^u} = 1 - \frac{P_{rad} + P_{CX}}{Q_\parallel^u} = 1 - f_{power}$$

(5.11)

where now the quantities $Q_\parallel^t, Q_\parallel^u, P_{rad}$ and P_{CX} are in [W].

The power radiated in the SOL is directly measured by TCV's bolometry system. Figure 5.14 presents four snapshots of the power radiated in TCV's poloidal cross-section, reconstructed by Radcam tomographic inversions [87]. The radiated power density in the poloidal plane is mainly concentrated in the outer divertor leg and X-point, where $\approx 2/3$ of total the emissivity is reconstructed. However, as density increases, we observe significant amounts of radiation from the SOL surrounding the core plasma, likely due to interactions with the machine walls. When accounting for the volume from where this radiation originates, we obtain the data shown in figure 5.15b. Here the radiated power was separated between the three regions of interest enclosed by the three rectangles illustrated in panel a. The blue rectangle encloses the region observed within the DSS LOSs, with the red accounting for the entire divertor leg and X-point and the yellow one, the entire TCV volume.

The total radiated power increases across the ramp, from ≈ 130 to ≈ 240 kW. Despite representing $\approx 2/3$ of the total emissivity in the poloidal plane, when accounting for the volume in which this power is radiated, the contribution from the outer divertor leg and X-point is $\approx 45\%$ of the total.

It is possible to estimate the power entering the SOL, i.e. $Q_\parallel^u$, by combining the measurements of the plasma ohmic power P_{ohm}, the power radiated from the core $P_{rad,core}$, i.e. within the main plasma separatrix, and the energy stored in the plasma W, as

$$P_{SOL} = P_{ohm} - P_{rad,core} - \frac{\mathrm{d}W}{\mathrm{d}t}$$

(5.12)

where P_{ohm} is given by the product of V_{loop} and I_p, and $P_{rad,core}$ from bolometry. To estimate the power balance in the outer divertor leg, the radiated power in the SOL above the X-point is subtracted from this. A 50-50% power redistribution is assumed between the outer and inner divertor legs. Although this assumption is rather approximate, and several studies have been dedicated to assessing this, i.e. R. Maurizio (2020) [86], this choice does not affect the identified trend in f_{power} across the density ramp. The power entering the outer divertor leg is now calculated as

$$Q_\parallel^{u, out \, div} = \frac{P_{ohm} - \mathrm{d}W/\mathrm{d}t - P_{rad}^{above \, Xpt}}{2}$$

(5.13)
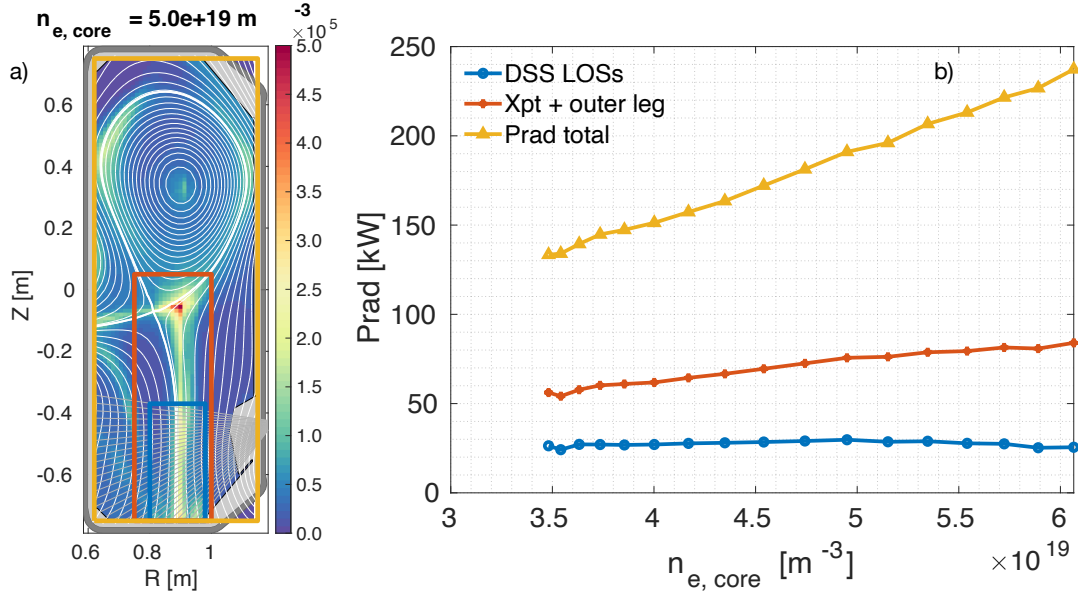
Figure 5.15: Radiated power in TCV volume, separated between different regions in the poloidal cross-section. The radiation emitted within the DSS LOSs is indicated in blue, while the one emitted in the outer divertor leg region, X-point included, is in red. The radiation coming from the entire TCV volume is shown in yellow.

The power deposited onto the outer target can be measured by the InfraRed thermography system, from the vertical field of view (VIR). In the calculation for the deposited power, the contributions due to the heat fluxes by radiation are removed by removing a constant offset observed on the measured heat flux profiles, as performed in [86], since this contribution is already accounted for by the bolometry system. Radial profiles of $q_\perp$, where in this nominal $\perp$ is referred to the tile's surface, are shown in figure 5.16a for several values of core density, while panel b illustrates the evolution of the power deposited at the target across the density ramp, that is observed to decrease.

The contribution to the volumetric power losses due to CX reactions in the SOL can only be estimated. The neutral fraction in TCV divertor was estimated as $n_0/n_e \approx 1-2\%$, from previous measurements from MANTIS, i.e. as presented in [138], and from the simple model where the C III emissivity is peaked at ≈ 12 eV, referring to figure 5.12. The reaction cross-section σ^{CX}, function of the deuterium ion temperature, is taken from P. Swaczyna et al. (2019) [129], as in section 4.2.3, while D^+ temperature and density are taken from TS measurements assuming Z = 1 and complete thermalisation between ions and electrons. The volumetric power losses due to charge exchange are then computed using

$$P_{CX} = \int \int \int n_{D^+} \sigma^{CX} \langle v_{th,D^+} \rangle n_0 \frac{3}{2} k_b T_{D^+} R \, dRdZd\phi \tag{5.14}$$

In this estimation, the neutral temperature is assumed to be of 2 eV, as in figure 4.27b. The

Figure 5.16: Heat flux radial profiles at the target measured by the VIR are shown in panel a). Panel b) shows the total power deposited at the target measured by the VIR.

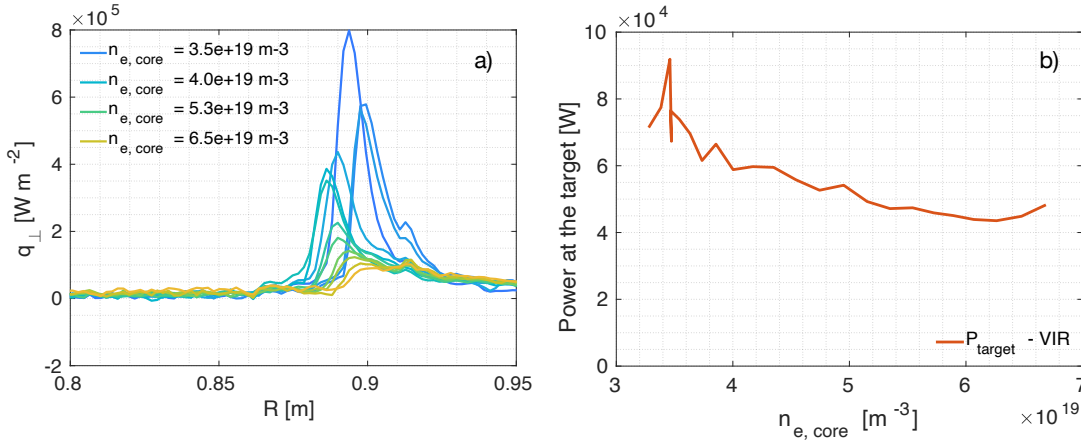calculation only accounts for CX losses within the DSS LOSs, i.e. in the blue box of figure 5.15a, as no measurement of TS n_e and T_e were available above this region, as the leg locus deviates from the TS laser beam paths. The estimated volumetric power losses due to CX reactions increase from $\approx$2.5 kW, at the start of the density ramp, up to $\approx$5 kW at the highest core density, i.e. $\approx$10% of the contribution due to radiation.

Panel a) of figure 5.17 represents the power entering the outer divertor leg, $Q_{\parallel}^{u,out\,div}$, in blue. This remains rather constant across the density ramp. Although it might be expected to increase, the rise in the Ohmic power appears to be compensated by stronger radiation above the X-point. The power deposited at the target, $Q_{\parallel}^{t}$, from IR thermography, is plotted in red. This power, in Stangeby's 2PM interpretation, accounts for the kinetic plasma plasma heat flux loading. However, the total heat flux also includes contributions from surface recombination, neutral and radiative power losses. Finally, the volumetric power losses are plotted in yellow. We note that, in principle, $Q_{\parallel}^{u,out\,div} = Q_{\parallel}^{t} + P_{loss}$, but this is not observed probably due to the number and quality of approximations used in this exercise. Panel b) of figure 5.17 plots the estimates of $1 - f_{power}$ calculated as $1 - f_{power} = 1 - P_{loss}/Q_{\parallel}^{u,out\,div}$, shown in blue, and as $1 - f_{power} = Q_{\parallel}^{t}/Q_{\parallel}^{u,out\,div}$, in red. The two curves disagree in value but not in their trend, as both indicate that the loss factor f_{power} increases during the density ramp, causing the divertor to approach a detached regime.

5.3.2 Momentum losses

The static component of the electron pressure is observed to decrease across the density ramp, and its radial profiles to broaden, effectively reducing the peak loads at the target. The momentum loss factor f_{mom}, estimated in this paragraph, increases with core density.

The second *loss factor* of the extended 2PM that we can estimate is f_{mom}, introduced in equa-
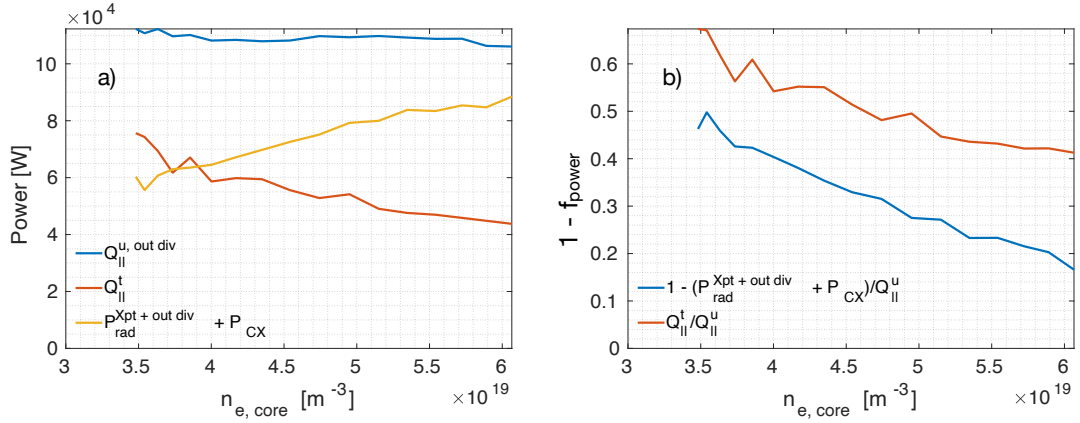
Figure 5.17: Panel a represents the power entering the outer divertor leg in blue, the one deposited onto the target in red, and the one leaving the divertor region via radiation and CX in yellow. Panel b shows two approaches to calculate f_{power} as in equation 5.11.

tion 1.21, linking the upstream static pressure to that evaluated at the target.

We mentioned in section 4.3.2 that the electron pressure measured by the TS scan was approximated using an Eich parametrisation. Despite the hint of a double peak lying over the p_e exponential decay - observed, for instance, in figure 4.14e) and i) or in figure 4.15l) and o) - and due to the more pronounced secondary peak of n_e at the same distance from the separatrix, this parametrisation is useful in tracking the evolution of the p_e peak, width and integral, as a function of both $n_{e,core}$ and the vertical distance from the target. Similar experiments were also performed in DIII-D, i.e. see McLean et al. (2015) [150] where 2D maps of T_e, n_e and p_e were reconstructed in the SOL. It should be noted that the pressure measured by TS represents the *static* contribution of equation 1.10.

Figure 5.18a) plots p_e evaluated at the separatrix where the peak of the profile is observed as a function of distance from the target. The colour map used in these figures indicates the data acquired at low $n_{e,core}$ with dark blue lines and that acquired at high $n_{e,core}$ with yellow lines, as indicated in the legend of panel 5.18a). The pressure at the separatrix decreases upon approaching the target across the entire density ramp. However, the gradient of this quantity becomes increasingly pronounced with the increasing density.

Figure 5.18c) and d) plot the information on the *shape* of the p_e radial profiles, indicating the evolution of the exponential fall-off length and the Gaussian contribution due to diffusion. λ_p starts with a flat profile along the divertor leg but steadily increases across the density ramp at the closest probed position to the target. Here, $\lambda_p \approx 1$ cm at the beginning of the discharge increases to $\lambda_p \approx 3.5$ cm at the highest core density. The parameter s_p follows a similar trend, but its value at the target is higher than that upstream, from the lowest density in the ramp. The profiles look more scattered, despite the applied data smoothing, but an increase of s_p as a function of density can be discerned. At the target, $s_p \approx 0.8$ cm at the beginning of the
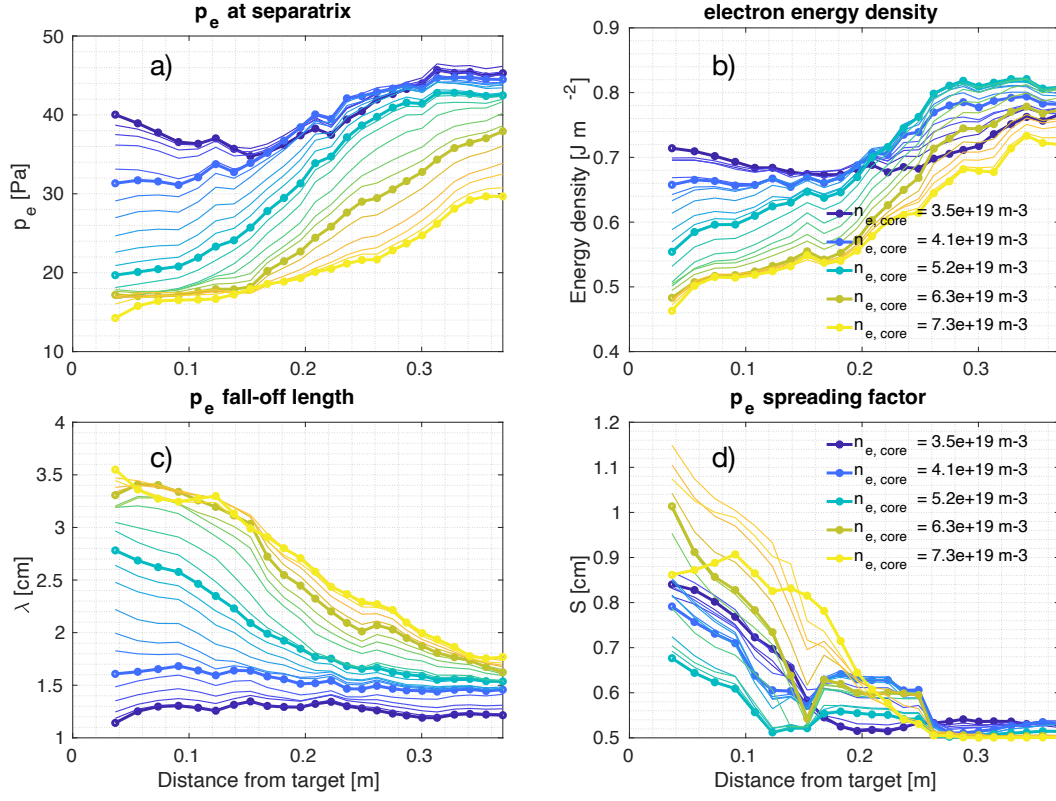
Figure 5.18: Evolution of the Eich curve parameters used for the p_e profiles fitting, plotted as a function of the vertical distance from the target. The colours are used to indicate different values of core density, with dark blue indicating a low $n_{e,core}$ and bright yellow a value close to the limit of the density ramp. Panel a) indicates the maximum of the p_e profile, measured at the separatrix; panel b) plots the electron energy density per m^{-2}, obtained by integrating the p_e profiles in the R direction; panel c) represents the p_e fall-off length, i.e. the exponential part of the Eich curve; panel d) plots the p_e spreading factor, i.e. the Gaussian part of the Eich curve.

discharge, growing to $s_p \approx 1.2$ cm at the highest chore density. The increase of these shape parameters, together with the decrease of p_e at the separatrix, shows how the static pressure is redistributed over a larger surface across the density ramp, effectively reducing the target load at the separatrix's flux tube position.

Finally, figure 5.18b) plots the evolution of the integral of the p_e radial profile. The physical meaning of this quantity is that of the energy carried by the electrons along the leg. Indeed, integrating the profiles in the radial direction allows one to write this quantity in units of [J m^{-2}]. As indicated by the dark blue line, at low density, the deduced energy carried by the electrons is near constant from upstream to the target. The slope of this curve increases with the core density as the energy reaching the target decreases, indicating the action of effective loss mechanisms. This parameter's evolution is summarised in figure 5.19, where the slope of each curve, assumed to be a straight line, is calculated as a function of the increasing core density.
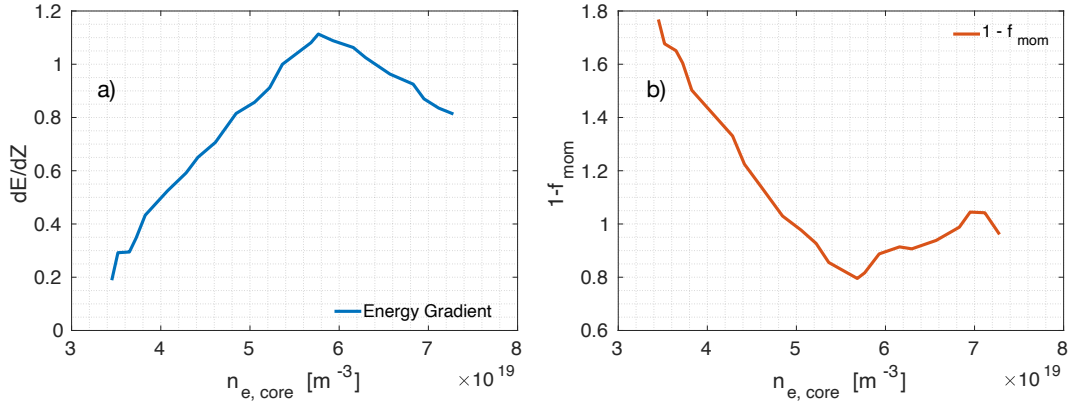
Figure 5.19: Panel a shows the electron energy gradient along the leg as a function of core density. This data is obtained by approximating the curves plotted in panel 5.18b) with a straight line and calculating its slope. Panel b plots the momentum loss factor as a function of core density.

The deflection around $n_{e,core} \approx 5.8 \cdot 10^{19}$ m^{-3} results from the rough approximation of considering each dependence linear. However, this plot provides some insight into when pressure gradients develop and their evolution when increasing the core density. In panel b of figure 5.19 we plot $1 - f_{mom}$, calculated using equation 1.21,

$$1 - f_{mom} = \frac{2 n_t T_t}{n_u T_u} \tag{5.15}$$

accounting for the values of n_t, n_u, T_t, T_u at the separatrix. As expected from the 2PM, f_{mom} increases across the density ramp, as we approach a detached regime. However, we note that the values obtained in this treatment are not really physical, as we should have obtained $0 < f_{mom} < 1$. The reason behind this is probably explained by the assumptions made to obtain

equation 1.21, i.e. as in equation 1.11: here the main assumption in the pressure balance is an absence of upstream flows. A new dedicated DSS viewing optic system, exploiting LOSs tangential to $\vec{B}_{tor}$, is currently being constructed to assess the presence of flows in the divertor SOL by measuring Doppler shift on impurity spectral lines, but we will already see in the next paragraph that the assumption of $v_u = 0$ may not be accurate, particularly with the progression of the core density, as heat transport by convection is seen to become important.

Another potential cause for the aphysical values of $f_{mom} < 0$ is the lack of coverage of n_e and T_e at the target, where n_t and T_t ought to have been evaluated. Were the TS values of n_t and T_t such that $n_t T_t \leq n_u T_u / 2$, the correct range of validity for f_{mom} would be recovered.

5.3.3 Conduction losses

In the divertor SOL, heat is transported by both conduction and convection, with the convection becoming dominant in the outer SOL at high core densities.

The remaining loss factor to be determined is that describing the heat transported by conduction, f_{cond}. This is estimated by exploiting the temperature profiles along the divertor leg reconstructed from TS and measured by the DSS.

The observation of a knee in the T_i(He II) profiles along the divertor leg measured by the DSS, present at all values of core density across the ramp, motivated us to use an approach similar to that reported in Siccinio et al. (2016) [55], where the SOL is divided into two regions. In the first region, heat is taken to be transported by conduction in the presence of temperature gradients and impurity radiation. In the second, heat is taken to be transported by convection alone, resulting in flat temperature profiles. The 2PM then becomes a *3PM*, with an intermediate position that marks the transition between the two regimes.

In this section, we estimate the spatial extent of the convection-dominant region and the contribution to convective heat transport in the conduction-dominant region. These estimations are performed using two characteristic temperatures: one represented by T_i(He II) and one by the electron temperature measured in the separatrix proximity, $T_{e,peak}$. In the following paragraphs, the estimation technique is exemplified by employing the T_i(He II) data.

The temperature profile T_i(He II, $s_\parallel$) in the conduction region can be described by equation 1.22 of the 2PM, where the term f_{cond} is included to model heat transport through convection as in the first region. We note that this equation provides estimates of the upstream temperature, but assumes that power losses only occur at the target. The temperature profile T_i(He II, $s_\parallel$) in the second region, dominated by convection, is modelled by a linear function of the distance from the target, with a strongly reduced positive slope to accommodate the small observed temperature gradients. An example of the data presenting this two-regime feature is shown in figure 5.20a) where T_i(He II), in blue, is plotted against the distance from the target calculated along the magnetic field lines, referred to as $s_\parallel$. The vertical dashed line marks the transition position between the two heat transport regimes: from $s_\parallel \approx 3$ m downstream,

heat transport is dominated by convection. This is described by the yellow line, fitting the data on the left of the dashed line. Upstream from that position, heat conduction develops temperature gradients, captured by the red line, modelled through equation 1.22.

The position of the transition region is chosen by recursively regressing the curve and moving the transition position between the two extremes. The position yielding the smallest χ^2 value is taken to best describe the separation between conduction and convection regions, as indicated in figure 5.20b).
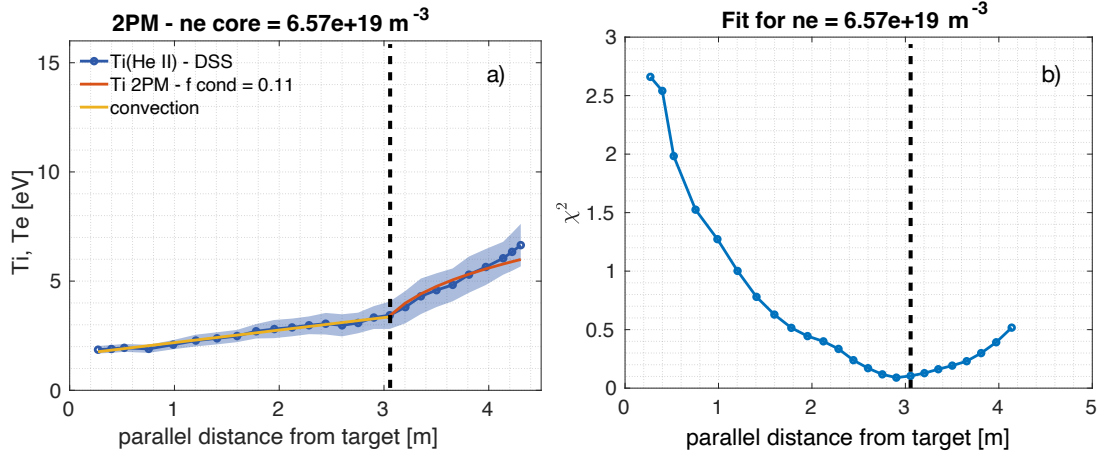
Figure 5.20: Determination of the spatial extent of the two regimes via a χ^2 minimisation.

Two critical pieces of information can be extracted: the extent of the convection region from the target and the remaining convection present in the region best described by conduction. While this procedure directly generates the first parameter, the second can only be estimated using several approximations, that start by estimating the $q_\parallel$ from equation 1.22. Here we follow the instructions presented in appendix A of Février et al. (2020) [35]: $q_\parallel$ can be estimated from the ratio between the total magnetic field and its poloidal component $\frac{B_{tot}}{B_{pol}}$, the heat flux decay length λ_q, the radial position of the separatrix R_{sep}, the power entering the sol that is carried toward the targets by the electron P_e^{tar}, and f, that indicates the fraction of this power carried to the outer target. With these elements, $q_\parallel$ is estimated as

$$q_{e,\parallel}^{peak} = \frac{1}{2\pi R_{sep}} \frac{f P_e^{tar}}{\lambda_q} \frac{B_{tot}}{B_{pol}} \tag{5.16}$$

While B_{tot}, B_{pol}, and R_{sep} can be easily determined by geometrical considerations, the other parameters must be obtained by further measurements and assumptions, some of which are rather approximate. For instance, as in section 5.3.1, we assumed $f = 0.5$, implying that the power entering the SOL is equally shared between the inner and outer divertor legs. P^{tar} is given by the difference between the Ohmic power P_{ohm}, and that radiated from the core, measured by bolometers [87], and that carried by the electrons is taken as half of that, $P_e^{tar} = 0.5 \cdot P^{tar}$. The main limitation of this assumption lies in taking radiation losses to only

occur in front of the target, as no power is assumed to be lost within the SOL, contrary to what is observed in section 5.3.1. A spatial distribution of f_{power}, if included in this model, would likely improve the quality of the fits presented in figure 5.20a, better describing the conduction-dominant region. A further approximation is represented by taking a value of λ_q, here assumed to be $\lambda_q = 5$ mm, to be constant across the density ramp. While this absolute value is consistent with other experiments, i.e. see Février et al. (2020) [35], it is expected to increase slowly with increasing core density.

The conduction fitting function is characterised by two fit parameters: the upstream temperature T_u and a constant f_{fit} uniting the estimated $q_{\parallel}$ and electron heat conductivity constant $\kappa_{0e} \approx 2000$ [W m^{-1} eV$^{-7/2}$]. The curve, describing the temperature as a function of parallel distance from the target, is

$$T(s_{\parallel}) = \sqrt[2/7]{T_u^{7/2} - f_{fit} \cdot s_{\parallel}} \tag{5.17}$$

Finally, f_{cond} is evaluated from the ratio between the fit parameter and the parallel heat flux estimation as

$$f_{cond} = f_{fit} / \frac{7}{2} \frac{q_{\parallel}}{\kappa_{0e}} \tag{5.18}$$

As the 2PM describes the evolution of the plasma parameters within a given flux tube, it is interesting to see if any radial variation in the f_{cond} parameter is present by applying the regression to different characteristic temperature profiles along the divertor leg. For instance, the electron temperature evaluated at $\rho(\psi) \approx 1.01$, where all the T_e profiles reconstructed by TS are observed to peak, can be used to explore the extension of the convection region around the separatrix only. We refer to this temperature as $T_{e,peak}$. Conversely, T_i(He II), at higher core densities, is suitable to describe T_e^*(He II) over the entire SOL width, as we have observed in section 5.1 that T_i(He II) $\approx T_e^*$(He II). It is thus possible to use this for retrieving an *average* f_{cond} across the SOL.

Figure 5.21 presents the fits of this 3PM applied to $T_{e,peak}$ and T_i(He II) for three increasing values of core density. It should be noted that, before fitting, the $T_{e,peak}$ data was subjected to similar filtering and 2D-smoothing to that presented for T_e^*(He II) in figure 5.1, to exclude non-physical data and help regularise local gradients.

Figure 5.22 summarises the fit results of the two data series: panel a) plots the extracted value of f_{cond}, and panel b) plots the extension of the convection-dominant region, both as a function of the core density. Due to the significant uncertainty in the estimation $q_{\parallel}$, only the relative changes in f_{cond} should be considered. Indeed, values of $f_{cond} > 1$ can result from an underestimation of $q_{\parallel}$ from TCV measurements or may indicate the limitations in the model used to evaluate P_e^{tar} and/or the other parameters, such as neglecting the effect of the spatial profiles of f_{power}. On the other hand, the transition between conduction and
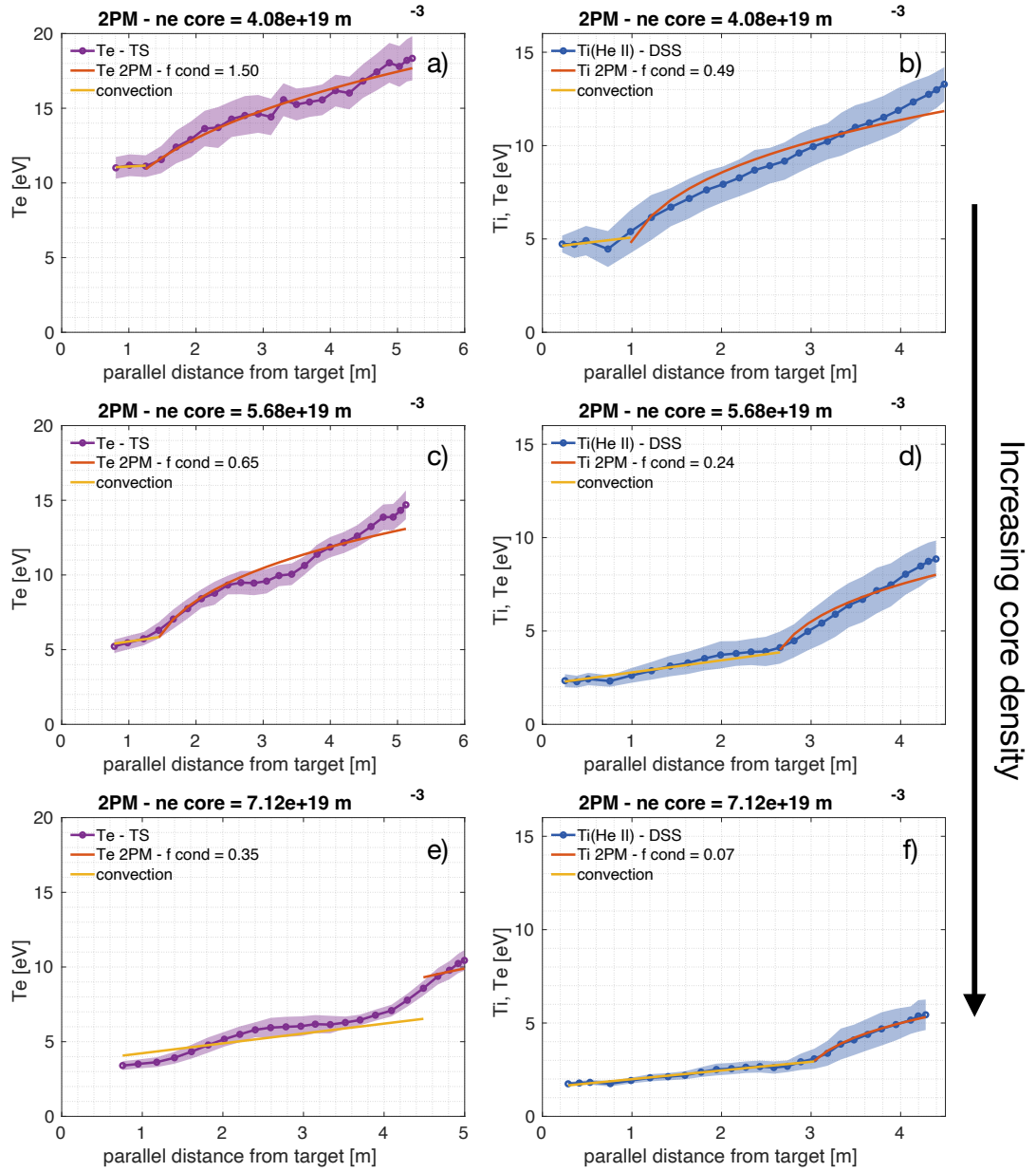
Figure 5.21: T_e measured at the separatrix (panels a, c, and e) and T_i (He II) (panels b, d, and f) along the divertor leg at three increasing core densities. The temperatures are regressed to two models, one describing the temperature predicted by 2PM, as in equation 1.22, plotted in red, and another representing a SOL in which heat transport is dominated by convection, resulting in small temperature gradients, plotted in yellow.

convection-dominant regions is reliable on the T_i(He II) profiles, where a knee is always evident. The determination of the convection-dominant region extension in the SOL is not affected by all the approximations mentioned above. Furthermore, the decreasing trend of f_{cond} as a function of core density, and the difference between f_{cond} calculated from $T_{e,peak}$ and T_i(He II), show that the heat transported by conduction decreases with the increasing density, with the far SOL - probed by the He II data but not by $T_{e,peak}$ - being more affected by convection than the separatrix region. This is also highlighted by figure 5.22b, which shows an extension of the convection-dominant region in the SOL. Here, the convection region, probed by the He II ion temperature, extends upstream, but the same clear extension is not recovered at the separatrix, indicated by the purple line. The last data points of this series are characterised by artefacts probably resulting from the smoothing algorithm, that make the $T_{e,peak}$ curve deviate from the 3PM description, e.g. in figure 5.21e.
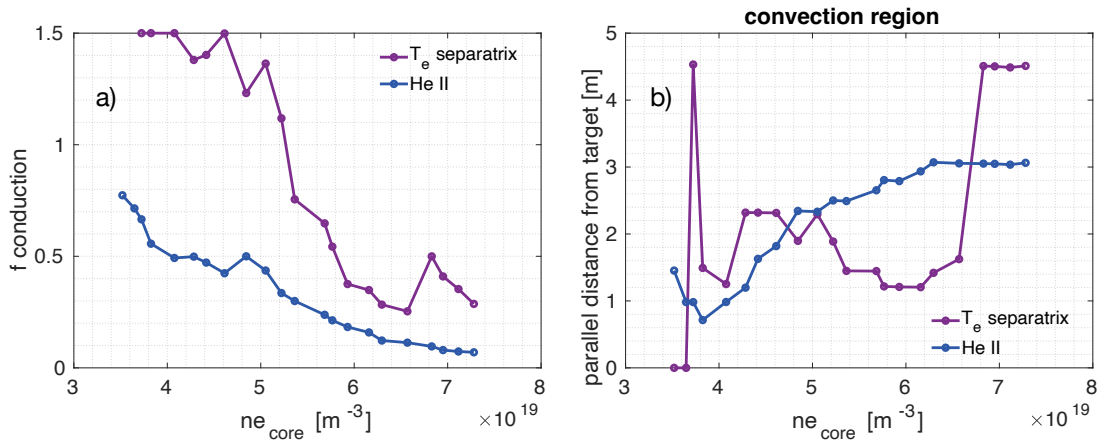
Figure 5.22: a) f_{cond} evolution across the density ramp and b) extension of the convection-dominated region in the divertor obtained from the fits presented in figure 5.21 for T_e measured at the separatrix and T_i(He II), as a function of core density.

Further information can be obtained by comparing the T_i(He II) and $T_{e,peak}$ profiles along the divertor leg with the TS radial profiles of T_e and n_e, as those in figures 4.12 and illustrated in figure 5.23. The radial T_e profiles reconstructed by TS are shown for three different DSS LOSs, i.e. 8, 18 and 28, each probing a divertor SOL with different f_{cond} and f_{conv}. At the higher divertor probed location, in panel d), $T_e \approx 16$ eV at the separatrix, and it follows a near exponential decay in further SOL, reaching $T_e \approx 3$ eV for $\rho(\psi) \approx 1.1$: here temperature gradients between nearby DSS LOSs are significant and conduction plays an important role in the heat transport. At the knee location in the T_i(He II) profile, at ≈ 2.6 m from the target along the $\vec{B}$ field line, illustrated in panel c), the T_e radial profile starts to flatten further in the SOL, and the secondary n_e peak becomes prominent. The 3PM would mark this point as the border between the heat transport regimes, however, no clear knee is present in the $T_{e,peak}$ profile at this location. As $T_{e,peak}$ probes the region close to the separatrix, we can state that conduction is still significant at the separatrix, but convection increasingly dominates in the

far SOL. The last probed location, corresponding to DSS LOS 8, illustrated in panel b), shows an almost completely flat T_e radial profile, of $T_e \approx 3$ eV, with an even larger secondary n_e peak, of $n_e \approx 1.6 \cdot 10^{19}$ m^{-3}. At this probing location, both the $T_{e,peak}$ and T_i(He II) profiles agree in indicating convection as the dominant transport mechanism.
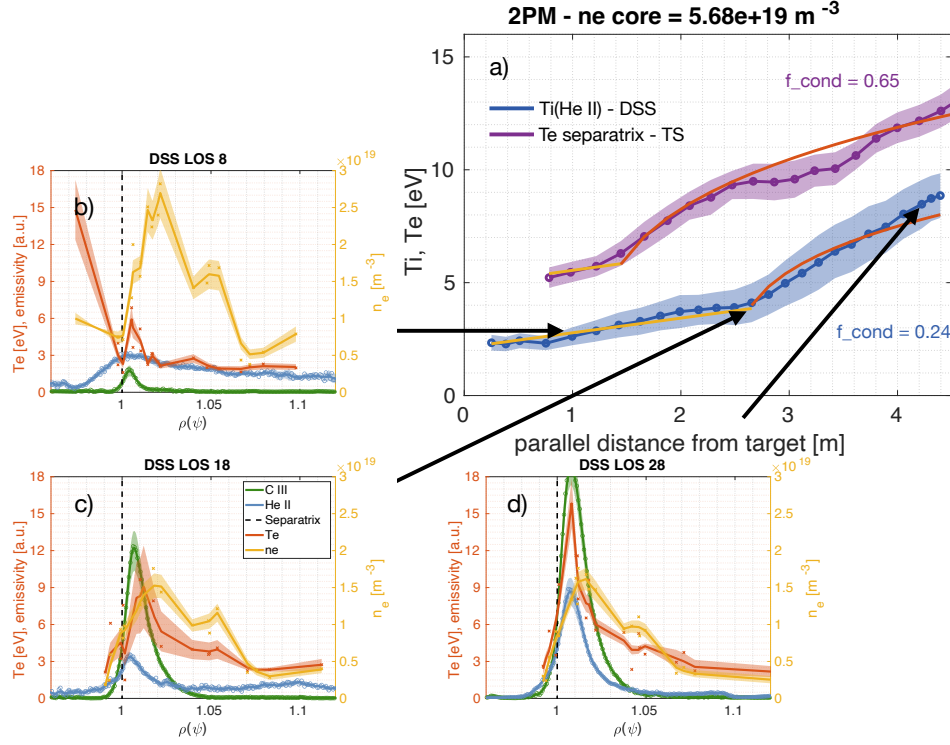
Figure 5.23: TS and MANTIS radial profiles in panels b), c) and d), as in figure 4.12 corresponding to the illustrated T_i(He II) profile along the divertor leg, in panel a), as in figure 5.21. The radial profiles in panel b) are representative of the convection-dominant region, while those in panel d) are of the conduction-dominant one. The data of panel c) are taken at the knee location of the He II temperature profile along the divertor leg and represent a smooth transition between the two regions.

Although some approximations were required, we have outlined in this section how the experimental framework presented in chapter 4 can be used to estimate power, momentum and conductivity fraction losses in the divertor during its evolution from an attached towards a detached scenario. Impurity radiation and plasma-neutral interactions (i.e. CX, ionisation) drive power losses along the divertor leg that decrease the plasma temperature. As the divertor progressively cools across the density ramp, we observe an increase in losses, with the estimated increase of f_{mom}, accompanied by an increase in convective heat transport. This limits the temperature gradients in the outer SOL and thus the attainment of the lower T_e necessary for enhancing volumetric recombination processes such as EIR. These mechanisms are coupled. The f_{power} and f_{cond} loss mechanisms display an approximately linear increase with the core plasma density. In contrast, f_{mom} appears to saturate at high core density, likely due to the decrease in the upstream pressure observed in figure 5.18a. The ability to estimate all

three of these contributions provides important insight into the changing divertor description for model validation, and tracking their evolution with that of the divertor state is especially important for model validation.

6 Conclusions

In this thesis, we presented a recent upgrade of TCV's divertor spectroscopy system - described in section 2.1.1. This encompassed the following elements. A mirror relay system inside a re-entrant port that replaced the legacy lens-based collection optics. This improved the transmission in the near-UV range, considerably increased the diagnostic field of view and resulted in an intrinsically achromatic system. A triple fibre bundle was installed in the collection optics focal plane, conveying the collected light to up to three separate spectrometers, allowing simultaneous measurements of the plasma emission in three different spectral ranges and/or different spectral resolutions. The upgrade included the installation of two additional imaging spectrometers that featured sufficient resolution to analyse low-Z elements' spectral line-shapes in much greater detail than that previously available.

The upgrade opened up a new use of the DSS as a spectroscopy diagnostic, enabling ion temperature measurements by determining the Doppler broadening component of the observed spectral lines. A new analysis technique, described in section 3.2, was developed and used to separate the Doppler broadening component from the two other main broadening mechanisms that interest impurity and low-n deuterium Balmer spectral lines, namely the Zeeman splitting and the instrumental broadening. A model for the Zeeman splitting pattern calculation was implemented for several charged and neutral species, e.g. deuterium Balmer lines, He I, He II, C II, and C III spectral lines. The instrumental broadening was instead characterised using spectral pen lamps, carefully reproducing experimental settings.

The analysis technique was applied to deuterium density ramp repeat discharges in a long outer divertor leg configuration to study the physical process occurring during the transition from an attached towards a detach*ing* divertor regime. A novel aspect of the experiments presented in chapter 4, was the characterisation of the outer divertor leg in terms of electron and ion temperatures, electron density and static pressure by the integration of the DSS, MANTIS and Thomson Scattering diagnostics, together with the high degree of divertor position control afforded by TCV's magnetic system.

Radial profiles of T_e and n_e were reconstructed during a radial scan of the outer divertor leg position with respect to the TS probing volumes over seven repeat core density ramps, while MANTIS tomographic inversions reconstructed the radial profiles of spectral line emissivities. Over the density ramp, described in section 4.3.1, T_e is observed to decrease and to exhibit different trends in two radial regions: in the first, around the separatrix, T_e remains peaked, and an exponential decay develops from $\rho(\psi) \approx 1.01$; in the second region, the T_e profile flattens in the farther SOL at $\approx 2 - 3$ eV. This second region is initially present only in the vicinity of the divertor target but then extends towards the inner SOL further from the target as the core density is increased by the ramp. With this flat T_e region, a secondary peak in the n_e profile, at $\rho(\psi) \approx 1.05$, is observed to develop, reaching up to $\approx 75\%$ of the primary n_e peak, located at $\rho(\psi) \approx 1.02$, by the end of the core density ramp. The mechanism driving this secondary peak is believed to be pressure conservation, as the secondary n_e peak corresponds to a region where the T_e radial profile drops faster than the exponential decay.

The information provided by the TS temperature radial profiles is combined with the MANTIS poloidal tomographic inversion of several atomic spectral lines to define an effective electron temperature T_e^* for each observed impurity species, as discussed in section 5.1. This quantity is suitable for comparison with the DSS ion temperature measurements to determine whether the observed species are thermalised within the divertor leg plasma. Following the discussion proposed in section 4.2, impurity ions thermalise quickly with deuterium ions regardless of the electron temperature. When $T_i(\alpha) \approx T_e^*(\alpha)$ is observed for $\alpha = $ C III, He II, α can be considered as thermalised with both deuterium ions and electrons. Conversely, when $T_i(\alpha) < T_e^*(\alpha)$, one can state that the species α thermalised with deuterium ions but not with the electrons. In section 5.1.2, we argue that this observation is due to a cold influx of neutral particles, lowering the temperature of the ionised species of the respective element. In particular, an influx of cold neutral carbon, originating from the target, is reflected on the temperature of C II ions, which consistently present $T_i($C II$) < T_e^*($C II$)$. In the target vicinity, at the start of the density ramp, $T_i(\alpha) < T_e^*(\alpha)$ for all the analysed species, suggesting the presence of a cold neutral deuterium influx that, once ionised, lowers the deuterium ion temperature, and consequently, the impurity temperatures. The hypothesis of a cold influx was probed using a simple ionisation-balance model that recovered the observed differences between $T_i($C II$)$ and $T_i($C III$)$, namely where $T_i($C II$) < T_i($C III$)$ for $T_D, T_e > 6 - 9$ eV.

The exercise presented in this thesis validated the line-shape analysis technique of chapter 3, providing clear insight into the different ion temperatures observed for the several analysed species. The new field of view introduced with the DSS hardware upgrade, presented in section 2.1.1, now offers T_i measurements for many of the divertor geometries achievable in TCV, with a focus on the alternative divertor configurations, such as those presented in [53], where TS can only probe a little or no portion of the divertor SOL. Despite not being observed in the experiments provided in this thesis, the DSS is able to probe ion temperatures in the interval of $T_i \approx 30 - 0.5$ eV using the He II spectral line broadening, as presented in [92]. Even though the combination of all these diagnostics remains the strongest option for the divertor

SOL characterisation, after this validation, it is possible to estimate LOS-averaged T_e values in case TS or MANTIS are not able to support their interpretation. More importantly, these experiments showed that, in detachment-relevant conditions, where plasma collisionality is particularly high, ions and electrons thermalise - if observed sufficiently far from the target. Impurity ion temperatures from DSS measurements can not only be representative of the main ion species, i.e. D^+, an interesting measurement already on its own, but also of the electron temperature in the region of the strongest measured spectral lines' emissivity. As an example, the C III spectral line width can provide information on the T_e representative of the separatrix region, while He II measurements are more representative of an average across the SOL.

The observations reported in section 4.3 were used in section 5.2 to track characteristic temperatures at the C III radiation front position as it moves towards the configuration's X-point with the density ramp. Due to the asymmetry of the T_e profiles measured by TS, we opted to use two values for its description, with one corresponding to the peak T_e, tracked with T_i(C III) and T_e(C III), and the other an averaged temperature, weighted upon the n_e profiles across the SOL. Using a 50% extinction factor, i.e. tracking where the line intensity reaches half of its global maximum between the X-point and the target, we find that

$$T_{e,avg} \approx 4.5 \pm 1 \text{ eV}$$
$$T_{e,peak} \approx 7.0 \pm 1 \text{ eV}$$

The same ionisation-balance model presented in section 5.1.2 highlighted the dependence of the C III emissivity and the C III radiation front temperature on the deuterium neutral density in the SOL. The measured $T_{e,peak}$, based on the C III emissivity radial distribution, is in good agreement with the temperature range suggested by the model for the 50% of C III emissivity, between 6 and 9 eV for n_0/n_e in the range of $10^{-2} - 2 \cdot 10^{-1}$. We note that the C III emission intensity was observed to strongly depend on the neutral deuterium density, which populates this ionisation state by CX recombination with C IV ions. Neglecting this process in SOL modelling can impact the estimation of carbon content, the role of impurity transport in the divertor, the C III radiation along the divertor leg and how these contribute to dissipating the power crossing the SOL. As the neutral density depends upon the divertor closure, the C III emission front properties, such as its T_e, can be directly influenced by neutral baffles, as those installed in TCV and modelled in Wensing et al. (2019) [151] or in Sun et al. (2023) [152] using SOLPS-ITER.

Finally, the DSS, TS, and MANTIS measurements were used in section 5.3 to probe a 0-D model describing heat transport in the SOL before detachment attainment, known as the two-point model. In this framework, we attempted to assess the role of power and momentum losses, together with heat transport by convection.
Radiative power losses, measured by TCV's bolometric system, increase through the density ramp. The evolution of radial static pressure profiles, presented in section 4.3.1, were regressed

onto an Eich parametrisation, used to track their fall-off length, peak and integral evolution across the ramp and spatially along the leg. A pressure gradient along the divertor leg length becomes stronger through the density ramp as the configuration approaches a detached regime, as exemplified by the gradual drop of p_e at the separatrix close to the target, which reached $\approx 50\%$ of its initial value at the end of the ramp. The fall-off length close to the target is observed to increase from 1 cm to 3 cm, and conversely, the energy density, calculated from the integral of the p_e profiles, decreases in the target region. Volumetric momentum losses are observed to increase across the density ramp and are a fundamental process for reducing the target pressure, which is a requirement for detachment, while maintaining higher pressure upstream.

A transition from heat transport dominated by conduction to convection is observed in the SOL across the density ramp. This was analysed using a similar model to that described in [55], which divided the divertor leg length into two regions. Convection dominates close to the target in a region that extends towards the configuration's X-point as the density increases. Conversely, the region dominated by conduction retreats towards the X-point position, simultaneously experiencing a reduction in the f_{cond} parameter, described using the 2PM. The difference in the f_{cond} value and in the extension of the convection region observed between the T_i(He II) and $T_{e,sep}$ profiles along the leg is ascribed to the different region of SOL probed by their two characteristic temperatures, as heat conductivity remains non-negligible at the separatrix but it reduces more strongly in the far SOL. TS T_e and n_e radial profiles and the MANTIS emissivity profiles of He II and C III exhibit different trends in the two regions. Where conduction remains non-negligible, T_e is peaked ($\rho(\psi) \approx 1.01$), and its decay in the SOL can be described by an exponential, as discussed in the previous paragraph. The emissivity of He II and C III peak at similar $\rho(\psi)$ values. Conversely, in the region described by convection, the radial T_e profiles are flat with low gradients observed for $T_{e,sep}$ and T_i(He II) along the divertor leg. Here, the He II emissivity profiles broaden in the SOL with the low remaining C III emissivity localised at the separatrix. The analysis was able to assess the presence and the evolution of the loss factors f_{power}, f_{mom} and f_{conv} described by the 2PM and to observe their growth across the density ramp qualitatively.

Additional experiments, and probably diagnostic views, would be required to answer the outstanding questions from this thesis. First, it is unclear why a deep detachment regime, previously identified by a clear target particle flux rollover, was not observed in these density ramps despite the increase in the 2PM loss factors. Second, the constant temperature measured for the neutral deuterium spectral lines, on D_α and D_β, is proposed to originate from molecular dissociation processes. One way to prove or refute this hypothesis would be to run similar analysis techniques to that used in [68] and study the correlation between the *hot* component intensity with the dissociation rates along the divertor leg and this across the density ramp. Integrating the BaSPMI analysis framework [68], able to estimate the plasma-molecule reaction rates from measurements of deuterium Balmer lines intensity, into the multi-diagnostic analysis presented in the thesis is suggested as the next logical step in this approach to improve our understanding of the atomic and molecular processes involved

in the power and particle balance, leading to strong detachment of the outer divertor leg. Secondly, this analysis, including the information on the D_2 Fulcher band presented in figure 4.26, should provide ionisation and recombination rates along the divertor leg. An evaluation of the ionisation front position, retreating towards the X-point as detachment is approached, is expected to correspond to the advancing convection-dominant region observed in section 5.3.3. This hypothesis will be tested by newly installed DSS tangential lines of sight, that are designed to measure both ion temperature and ion flow velocities, from the spectral line-shapes Doppler broadening and Doppler shift without all chords crossing the divertor leg location.

Some of these ideas are already in preparation for upcoming TCV experiments, promoted and guided by the results presented herein.

Bibliography

[1]   United Nations. *Day of Eight Billion*. 2022. URL: https://www.un.org/en/dayof8billion.

[2]   P. Conceição. *Human Development report 2021/22*. United Nations Development Programme (UNDP), 2022. URL: https://hdr.undp.org/system/files/documents/global-report-document/hdr2021-22pdf_1.pdf.

[3]   F. Faisal, T. Tursoy, and O. Ercantan. "The relationship between energy consumption and economic growth: Evidence from non-Granger causality test". In: *Procedia Computer Science* 120 (2017). 9th International Conference on Theory and Application of Soft Computing, Computing with Words and Perception, ICSCCW 2017, 22-23 August 2017, Budapest, Hungary, pp. 671–675. DOI: https://doi.org/10.1016/j.procs.2017.11.294.

[4]   E. E. Agency. *Correlation of energy consumption and GDP per person*. Feb. 2016. URL: https://www.eea.europa.eu/data-and-maps/figures/correlation-of-per-capita-energy.

[5]   I. E. Agency. *World Energy Outlook 2022, IEA, Paris*. License: CC BY 4.0 (report); CC BY NC SA 4.0 (Annex A). 2022. URL: https://www.iea.org/reports/world-energy-outlook-2022.

[6]   International Energy Agency. *CO2 Emissions in 2022, IEA, Paris*. License: CC BY 4.0. 2023. URL: https://www.iea.org/reports/co2-emissions-in-2022.

[7]   U. S. E. P. Agency. *Global Greenhouse Gas Emissions Data*. 2014. URL: https://www.epa.gov/ghgemissions/global-greenhouse-gas-emissions-data.

[8]   W. M. Organization. *State of the Global Climate 2022*. World Meteorological Organization (WMO), 2023. URL: https://library.wmo.int/doc_num.php?explnum_id=11593.

[9]   UNFCCC. *The Paris Agreement*. 2016. URL: https://unfccc.int/process-and-meetings/the-paris-agreement.

[10]   P. Shukla et al. *IPCC, 2022: Climate Change 2022: Mitigation of Climate Change. Contribution of Working Group III to the Sixth Assessment Report of the Intergovernmental Panel on Climate Change*. 2022. DOI: doi:10.1017/9781009157926.

Bibliography

[11] I. E. Agency. *Clean energy investment in the Stated Policies Scenario, 2015-2030, IEA, Paris*. Licence: CC BY 4.0. 2022. URL: https://www.iea.org/data-and-statistics/charts/clean-energy-investment-in-the-stated-policies-scenario-2015-2030.

[12] International Energy Agency. *World Energy Outlook 2022, IEA, Paris*. License: CC BY 4.0 (report); CC BY NC SA 4.0 (Annex A). 2022. URL: https://www.iea.org/reports/world-energy-outlook-2022.

[13] Federal Ministry for the Environment, Nature Conservation, Nuclear Safety and Consumer Protection. Press Release. Apr. 2023. URL: https://www.bmuv.de/en/pressrelease/germany-brings-era-of-nuclear-power-to-an-end.

[14] R. Pitts, R. Buttery, and S. Pinches. "Fusion: The way ahead". In: *Physics World* 19 (2006), p. 20. URL: https://physicsworld.com/a/fusion-the-way-ahead/.

[15] A. S. Eddington. "The Internal Constitution of the Stars". In: *Nature* 106 (1920). DOI: 10.1038/106014a0.

[16] P. Ball. "The chase for fusion energy". In: *Nature* (Nov. 2021). URL: https://www.nature.com/immersive/d41586-021-03401-w/index.html.

[17] EuroFusion. *European researchers achieve fusion energy record*. Press release. 2022. URL: https://euro-fusion.org/eurofusion-news/european-researchers-achieve-fusion-energy-record/.

[18] ITER organization. *ITER website*. URL: https://www.iter.org/.

[19] S. C. Cowley. "The quest for fusion power". In: *Nature Physics* 12 (May 2016). DOI: 10.1038/nphys3719.

[20] B. M. Andreev. "Separation of hydrogen isotopes in H2O-H2S system". In: *Separation Science and Technology* 36.8-9 (2001), pp. 1949–1989. DOI: 10.1081/SS-100104764.

[21] D. Fasel and M. Tran. "Availability of lithium in the context of future D–T fusion reactors". In: *Fusion Engineering and Design* 75-79 (2005). Proceedings of the 23rd Symposium of Fusion Technology, pp. 1163–1168. DOI: https://doi.org/10.1016/j.fusengdes.2005.06.345.

[22] A. Bradshaw, T. Hamacher, and U. Fischer. "Is nuclear fusion a sustainable energy form?" In: *Fusion Engineering and Design* 86.9 (2011). Proceedings of the 26th Symposium of Fusion Technology (SOFT-26), pp. 2770–2773. DOI: https://doi.org/10.1016/j.fusengdes.2010.11.040.

[23] D. Maisonnier et al. "Power plant conceptual studies in Europe". In: *Nuclear Fusion* 47.11 (Oct. 2007), p. 1524. DOI: 10.1088/0029-5515/47/11/014.

[24] H.-S. Bosch and G. Hale. "Improved formulas for fusion cross-sections and thermal reactivities". In: *Nuclear Fusion* 32.4 (Apr. 1992), p. 611. DOI: 10.1088/0029-5515/32/4/I07.

[25] J. D. Lawson. "Some Criteria for a Power Producing Thermonuclear Reactor". In: *Proceedings of the Physical Society. Section B* 70.1 (Jan. 1957), p. 6. DOI: 10.1088/0370-1301/70/1/303.

[26] C. Iliadis. *Nuclear physics of stars*. eng. Wiley-VCH, 2007. URL: https://worldcat.org/title/85897502.

[27] U. D. of Energy. *DOE National Laboratory Makes History by Achieving Fusion Ignition*. Press release. Dec. 2022. URL: https://www.energy.gov/articles/doe-national-laboratory-makes-history-achieving-fusion-ignition.

[28] J. Wesson. *Tokamaks; 4th ed.* International series of monographs on physics. Oxford: Oxford Univ. Press, 2011. URL: https://cds.cern.ch/record/1427009.

[29] J. G. Cordey. "A review of Non-Inductive current drive theory". In: *Plasma Physics and Controlled Fusion* 26.1A (Jan. 1984), p. 123. DOI: 10.1088/0741-3335/26/1A/311.

[30] A. Fasoli et al. "TCV heating and divertor upgrades". In: *Nuclear Fusion* 60.1 (Nov. 2019), p. 016019. DOI: 10.1088/1741-4326/ab4c56.

[31] A. N. Karpushov et al. "Upgrade of the neutral beam heating system on the TCV tokamak – second high energy neutral beam". In: *Fusion Engineering and Design* 187 (2023), p. 113384. DOI: https://doi.org/10.1016/j.fusengdes.2022.113384.

[32] A. N. Karpushov et al. "Neutral beam heating on the TCV tokamak". In: *Fusion Engineering and Design* 123 (2017). Proceedings of the 29th Symposium on Fusion Technology (SOFT-29) Prague, Czech Republic, September 5-9, 2016, pp. 468–472. DOI: https://doi.org/10.1016/j.fusengdes.2017.02.076.

[33] F. Bagnato et al. "Study of correlations between LOC/SOC transition, intrinsic toroidal rotation reversal and TEM/ITG bifurcation with different working gases in TCV". In: *Nuclear Fusion* 63.5 (Mar. 2023), p. 056006. DOI: 10.1088/1741-4326/acc115.

[34] N. Offeddu et al. "Gas puff imaging on the TCV tokamak". In: *Review of Scientific Instruments* 93.12 (2022), p. 123504. DOI: 10.1063/5.0126398.

[35] O. Février et al. "Nitrogen-seeded divertor detachment in TCV L-mode plasmas". en. In: *Plasma Phys. Control. Fusion* 62.3 (Feb. 2020). DOI: 10.1088/1361-6587/ab6b00.

[36] J. Decker et al. "Full conversion from ohmic to runaway electron driven current via massive gas injection in the TCV tokamak". In: *Nuclear Fusion* 62.7 (May 2022), p. 076038. DOI: 10.1088/1741-4326/ac544e.

[37] B. Linehan et al. "Validation of 2D and measurements made with Helium imaging spectroscopy in the volume of the TCV divertor". In: *Nuclear Fusion* 63.3 (Feb. 2023), p. 036021. DOI: 10.1088/1741-4326/acb5b0.

[38] J. M. Moret et al. "Tokamak equilibrium reconstruction code LIUQE and its real time implementation". In: *Fusion Engineering and Design* 91.0920-3796 (2015), pp. 1–15. DOI: {https://doi.org/10.1016/j.fusengdes.2014.09.019}.

Bibliography

[39] V. Philipps et al. "Overview of the JET ITER-like Wall Project". In: *Fusion Engineering and Design* 85.7 (2010). Proceedings of the Ninth International Symposium on Fusion Nuclear Technology, pp. 1581–1586. DOI: https://doi.org/10.1016/j.fusengdes.2010.04.048.

[40] A. Herrmann et al. "Solid tungsten Divertor-III for ASDEX Upgrade and contributions to ITER". In: *Nuclear Fusion* 55.6 (May 2015), p. 063015. DOI: 10.1088/0029-5515/55/6/063015.

[41] S. Coda et al. "Overview of the TCV tokamak program: scientific progress and facility upgrades". In: *Nuclear Fusion* 57.10 (June 2017), p. 102011. DOI: 10.1088/1741-4326/aa6412.

[42] H. Reimerdes et al. "Overview of the TCV tokamak experimental programme". en. In: *Nucl. Fusion* 62.4 (Apr. 2022), p. 042018. DOI: 10.1088/1741-4326/ac369b.

[43] G. Matthews. "Plasma detachment from divertor targets and limiters". In: *Journal of Nuclear Materials* 220-222 (1995). Plasma-Surface Interactions in Controlled Fusion Devices, pp. 104–116. DOI: https://doi.org/10.1016/0022-3115(94)00450-1.

[44] L. Spitzer. "The Stellarator concept". In: *The Physics of Fluids* 1.253 (1958). DOI: 10.1063/1.1705883.

[45] S. I. Krasheninnikov, A. S. Kukushkin, and A. A. Pshenov. "Divertor plasma detachment". In: *Physics of Plasmas* 23.5 (2016), p. 055602. DOI: 10.1063/1.4948273.

[46] G. Janeschitz et al. "The ITER divertor concept". In: *Journal of Nuclear Materials* 220-222 (1995). Plasma-Surface Interactions in Controlled Fusion Devices, pp. 73–88. DOI: https://doi.org/10.1016/0022-3115(94)00447-1.

[47] R. Pitts et al. "A full tungsten divertor for ITER: Physics issues and design status". In: *Journal of Nuclear Materials* 438 (2013). Proceedings of the 20th International Conference on Plasma-Surface Interactions in Controlled Fusion Devices, S48–S56. DOI: https://doi.org/10.1016/j.jnucmat.2013.01.008.

[48] H. Reimerdes et al. "TCV divertor upgrade for alternative magnetic configurations". In: *Nuclear Materials and Energy* 12 (2017). Proceedings of the 22nd International Conference on Plasma Surface Interactions 2016, 22nd PSI, pp. 1106–1111. DOI: https://doi.org/10.1016/j.nme.2017.02.013.

[49] P. Stangeby. *The Plasma Boundary of Magnetic Fusion Devices*. Institute of Physics Publishing, 2000. DOI: https://doi.org/10.1201/9780367801489.

[50] B. Labombard et al. "Experimental investigation of transport phenomena in the scrape-off layer and divertor". In: *Journal of Nuclear Materials* 241-243 (1997), pp. 149–166. DOI: https://doi.org/10.1016/S0022-3115(97)80037-2.

[51] P. Stangeby. "The roles of power loss and momentum-pressure loss in causing particle-detachment in tokamak divertors: I. A heuristic model analysis". In: *Plasma Physics and Controlled Fusion* 62.2 (Dec. 2019), p. 025012. DOI: 10.1088/1361-6587/ab51a9.

[52]   P. Stangeby. "The roles of power loss and momentum-pressure loss in causing particle-detachment in tokamak divertors: II. 2 Point Model analysis that includes recycle power-loss explicitly". In: *Plasma Physics and Controlled Fusion* 62.2 (Dec. 2019), p. 025013. DOI: 10.1088/1361-6587/ab51d6.

[53]   C. Theiler et al. "Results from recent detachment experiments in alternative divertor configurations on TCV". In: *Nucl. Fusion* 57.7 (July 2017), p. 072008. DOI: 10.1088/1741-4326/aa5fb7.

[54]   M. Carpita. "Reduction in benefits of total flux expansion on divertor detachment due to parallel flows". In: *In preparation* (2023).

[55]   M. Siccinio et al. "A 0D stationary model for the evaluation of the degree of detachment on the divertor plates". In: *Plasma Physics and Controlled Fusion* 58.12 (Nov. 2016), p. 125011. DOI: 10.1088/0741-3335/58/12/125011.

[56]   B. Lipschultz et al. "The role of particle sinks and sources in Alcator C-Mod detached divertor discharges". In: *Physics of Plasmas* 6.5 (May 1999), pp. 1907–1916. DOI: 10.1063/1.873448.

[57]   S. I. Krasheninnikov, A. S. Kukushkin, and A. A. Pshenov. "Divertor plasma detachment: roles of plasma momentum, energy, and particle balances". In: *Plasma Physics and Controlled Fusion* 64.12 (Nov. 2022), p. 125011. DOI: 10.1088/1361-6587/ac9a6f.

[58]   K. Verhaegh. "Spectroscopic investigations of detachment on TCV". Ph.D. thesis. University of York, Sept. 2018. URL: https://etheses.whiterose.ac.uk/22523/1/thesis.pdf.

[59]   K. Verhaegh et al. "An improved understanding of the roles of atomic processes and power balance in divertor target ion current loss during detachment". In: *Nuclear Fusion* 59.12 (Oct. 2019), p. 126038. DOI: 10.1088/1741-4326/ab4251.

[60]   K. Lackner and M. Keilhacker. "Divertor physics: summary of modelling and experiments". In: *Journal of Nuclear Materials* 128-129 (1984), pp. 368–377. DOI: https://doi.org/10.1016/0022-3115(84)90379-9.

[61]   M. Bernert et al. "X-point radiation, its control and an ELM suppressed radiating regime at the ASDEX Upgrade tokamak". In: *Nuclear Fusion* 61.2 (Dec. 2020), p. 024001. DOI: 10.1088/1741-4326/abc936.

[62]   T. Lunt et al. "Compact Radiative Divertor Experiments at ASDEX Upgrade and Their Consequences for a Reactor". In: *Phys. Rev. Lett.* 130 (14 Apr. 2023), p. 145102. DOI: 10.1103/PhysRevLett.130.145102.

[63]   N. Hosogane et al. "Divertor phenomena prior to density limit disruptions in JT-60U". In: *Journal of Nuclear Materials* 196-198 (1992). Plasma-Surface Interactions in Controlled Fusion Devices, pp. 750–754. DOI: https://doi.org/10.1016/S0022-3115(06)80136-4.

[64]   B. Lipschultz et al. "Divertor Physics Research on Alcator C-Mod". In: *Fusion Science and Technology* 51.3 (2007), pp. 369–389. DOI: 10.13182/FST07-A1428.

[65] H. Reimerdes et al. "TCV experiments towards the development of a plasma exhaust solution". In: *Nuclear Fusion* 57.12 (Sept. 2017), p. 126007. DOI: 10.1088/1741-4326/aa82c2.

[66] J. R. Harrison et al. "Detachment evolution on the TCV tokamak". en. In: *Nuclear Materials and Energy*. Proceedings of the 22nd International Conference on Plasma Surface Interactions 2016, 22nd PSI 12 (Aug. 2017), pp. 1071–1076. DOI: 10.1016/j.nme.2016.10.020.

[67] A. Fil et al. "Identification of the primary processes that lead to the drop in divertor target ion current at detachment in TCV". en. In: *Contributions to Plasma Physics* 58.6-8 (2018). DOI: 10.1002/ctpp.201700171.

[68] K. Verhaegh et al. "A study of the influence of plasma–molecule interactions on particle balance during detachment". In: *Nuclear Materials and Energy* 26 (2021), p. 100922. DOI: https://doi.org/10.1016/j.nme.2021.100922.

[69] K. Verhaegh et al. "The role of plasma-atom and molecule interactions on power & particle balance during detachment on the MAST Upgrade Super-X divertor". In: (2023). DOI: https://doi.org/10.48550/arXiv.2304.09109.

[70] K. Verhaegh et al. "Spectroscopic investigations of detachment on the MAST Upgrade Super-X divertor". In: *Nuclear Fusion* 63.1 (Dec. 2022), p. 016014. DOI: 10.1088/1741-4326/aca10a.

[71] K. Verhaegh et al. "A novel hydrogenic spectroscopic technique for inferring the role of plasma-molecule interaction on power and particle balance during detached conditions". In: *Plasma Physics And Controlled Fusion* 63.3 (2021), p. 035018. DOI: https://doi.org/10.1088/1361-6587/abd4c0.

[72] R. Pitts et al. "Physics basis for the first ITER tungsten divertor". In: *Nuclear Materials and Energy* 20 (2019), p. 100696. DOI: https://doi.org/10.1016/j.nme.2019.100696.

[73] B. LaBombard et al. "ADX: a high field, high power density, advanced divertor and RF tokamak". In: *Nuclear Fusion* 55.5 (Apr. 2015), p. 053020. DOI: 10.1088/0029-5515/55/5/053020.

[74] S. Gorno et al. "Power exhaust and core-divertor compatibility of the baffled snowflake divertor in TCV". In: *Plasma Physics and Controlled Fusion* 65.3 (Jan. 2023), p. 035004. DOI: 10.1088/1361-6587/acad26.

[75] H. Raj et al. "Improved heat and particle flux mitigation in high core confinement, baffled, alternative divertor configurations in the TCV tokamak". In: *Nuclear Fusion* 62.12 (Nov. 2022), p. 126035. DOI: 10.1088/1741-4326/ac94e5.

[76] H. Reimerdes et al. "Initial TCV operation with a baffled divertor". In: *Nuclear Fusion* 61.2 (Jan. 2021), p. 024002. DOI: 10.1088/1741-4326/abd196.

[77]   O. Février et al. "Divertor closure effects on the TCV boundary plasma". In: *Nuclear Materials and Energy* 27 (2021), p. 100977. DOI: `https://doi.org/10.1016/j.nme.2021.100977`.

[78]   T. Ravensbergen et al. "Real-time feedback control of the impurity emission front in tokamak divertor plasmas". en. In: *Nat Commun* 12.1 (Dec. 2021). DOI: `10.1038/s41467-021-21268-3`.

[79]   J. Koenders et al. "Systematic extraction of a control-oriented model from perturbative experiments and SOLPS-ITER for emission front control in TCV". In: *Nucl. Fusion* 62.6 (June 2022). DOI: `10.1088/1741-4326/ac5b8c`.

[80]   D. Galassi et al. "Numerical investigation of optimal divertor gas baffle closure on TCV". In: *Plasma Physics and Controlled Fusion* 62.11 (Sept. 2020), p. 115009. DOI: `10.1088/1361-6587/abb24f`.

[81]   M. Wensing. "Drift-related transport and plasma-neutral interaction in the TCV divertor". Ph.D. thesis. EPFL, Apr. 2021. URL: `https://doi.org/10.5075/epfl-thesis-8447`.

[82]   M. Wensing et al. "Experimental verification of X-point potential well formation in unfavourable magnetic field direction". In: *Nuclear Materials and Energy* 25 (2020), p. 100839. DOI: `https://doi.org/10.1016/j.nme.2020.100839`.

[83]   D. Oliveira et al. "Validation of edge turbulence codes against the TCV-X21 diverted L-mode reference case". In: *Nuclear Fusion* 62.9 (July 2022), p. 096001. DOI: `10.1088/1741-4326/ac4cde`.

[84]   O. Février et al. "Analysis of wall-embedded Langmuir probe signals in different conditions on the Tokamak à Configuration Variable". In: *Review of Scientific Instruments* 89.5 (2018), p. 053502. DOI: `10.1063/1.5022459`.

[85]   H. De Oliveira et al. "Langmuir probe electronics upgrade on the tokamak à configuration variable". In: *Review of Scientific Instruments* 90.8 (Aug. 2019). 083502. DOI: `10.1063/1.5108876`.

[86]   R. Maurizio. "Investigating Scrape-Off Layer transport in alternative divertor geometries on the TCV tokamak". 2020. DOI: `https://doi.org/10.5075/epfl-thesis-9893`.

[87]   U. A. Sheikh et al. "RADCAM—A radiation camera system combining foil bolometers, AXUV diodes, and filtered soft x-ray diodes". In: *Review of Scientific Instruments* 93.11 (Nov. 2022). 113513. DOI: `10.1063/5.0095907`.

[88]   H. D. Oliveira. "A fast-moving Langmuir probe array for the divertor of the Tokamak à Configuration Variable". 2021. DOI: `https://doi.org/10.5075/epfl-thesis-8407`.

[89]   C. K. Tsui et al. "Filamentary velocity scaling validation in the TCV tokamak". In: *Physics of Plasmas* 25.7 (July 2018). 072506. DOI: `10.1063/1.5038019`.

[90] A. Perek et al. "MANTIS: A real-time quantitative multispectral imaging system for fusion plasmas". In: *Review of Scientific Instruments* 90.12 (2019), p. 123514. DOI: 10.1063/1.5115569.

[91] P. Blanchard et al. "Thomson scattering measurements in the divertor region of the TCV Tokamak plasmas". In: *Journal of Instrumentation* 14.10 (2019). DOI: 10.1088/1748-0221/14/10/C10038.

[92] L. Martinelli et al. "Implementation of high-resolution spectroscopy for ion (and electron) temperature measurements of the divertor plasma in the Tokamak à configuration variable". In: *Review of Scientific Instruments* 93.12 (Dec. 2022). DOI: 10.1063/5.0114538.

[93] K. Verhaegh et al. "The role of plasma-molecule interactions on power and particle balance during detachment on the TCV tokamak". en. In: *Nucl. Fusion* 61.10 (Oct. 2021), p. 106014. DOI: 10.1088/1741-4326/ac1dc5.

[94] N. Maaziz. "Electron density determination of the TCV divertor plasma using Stark broadening of D_ε transition". en. MA thesis. Rte Cantonale, 1015 Lausanne, CH: EPFL, Sept. 2022.

[95] J. Rosato, Y. Marandet, and R. Stamm. "A new table of Balmer line shapes for the diagnostic of magnetic fusion plasmas". en. In: *Journal of Quantitative Spectroscopy and Radiative Transfer* 187 (Jan. 2017), pp. 333–337. DOI: 10.1016/j.jqsrt.2016.10.005.

[96] CeramOptec. *Optran UV/Optran WF technical sheet*. URL: https://www.ceramoptec.com/fileadmin/user_upload/pdf/pdf_data_sheets_neu_Sept2017/englisch_Sept2017/ceramoptec_EN_Optran_UV_WF.pdf.

[97] Thorlabs-Inc. *WP25L-VIS - 25.0 mm x 25.0 mm Wire Grid Polarizer, 420-700 nm*. URL: https://www.thorlabs.com/thorproduct.cfm?partnumber=WP25L-VIS.

[98] Princeton-Instruments. *IsoPlane data sheet*. URL: https://www.princetoninstruments.com/wp-content/uploads/2021/07/IsoPlane-Rev-C4-28-01-2022.pdf.

[99] C. Marini. "Poloidal CX visible light plasma rotation diagnostics in TCV". Ph.D. thesis. EPFL, Nov. 2017. DOI: https://doi.org/10.5075/epfl-thesis-8031.

[100] Oxford Instruments. *iXon Ultra EMCCD Cameras for Physical Science*. URL: https://andor.oxinst.com/products/ixon-emccd-cameras-for-physical-science.

[101] Oxford Instruments. *What is an EMCCD Camera?* URL: https://andor.oxinst.com/learning/view/article/electron-multiplying-ccd-cameras.

[102] Oxford Instrument. *iXon Ultra & Life 888 - Hardware Guide*. June 2022. URL: https://andor.oxinst.com/downloads/uploads/Hardware_Guide_iXon_Ultra_Life_888.pdf.

[103] Oxford Instruments. *Andor iXon Ultra Manual*. URL: https://andor.oxinst.com/assets/uploads/products/andor/documents/andor-ixon-ultra-emccd-specifications.pdf.

[104] Andor. *Andor User Guide to SDK - Software Development Kit*. URL: `https://andor.oxinst.com/downloads/uploads/Andor_Software_Development_Kit_2.pdf`. Oxford Instruments.

[105] F. Bagnato. "Study of impurity ion transport using charge exchange spectroscopy on TCV". Ph.D. thesis. École Polytechnique Fédérale de Lausanne, Oct. 2022. DOI: `https://doi.org/10.5075/epfl-thesis-9550`.

[106] J. Koenders et al. "Model-based impurity emission front control using deuterium fueling and nitrogen seeding in TCV". In: *Nucl. Fusion* 63.2 (Feb. 2023). DOI: `10.1088/1741-4326/aca620`.

[107] A. Perek et al. "Measurement of the 2D emission profiles of hydrogen and impurity ions in the TCV divertor". en. In: *Nuclear Materials and Energy* 26 (Mar. 2021), p. 100858. DOI: `10.1016/j.nme.2020.100858`.

[108] A. Perek. "Development and application of quantitative multispectral imaging in nuclear fusion research". English. Proefschrift. PhD thesis. Applied Physics and Science Education, Apr. 2022. URL: `https://pure.tue.nl/ws/portalfiles/portal/199138469/20220413_Perek_hf.pdf`.

[109] J. Márki. "Infrared Thermography of Divertor ELM Heat Loads on TCV". Ph.D. thesis. EPFL, Feb. 2012. URL: `https://doi.org/10.5075/epfl-thesis-5021`.

[110] Oriel-Instruments. *Typical Spectra of Oriel Instruments Spectral Calibration Lamps*. URL: `https://www.newport.com/medias/sys_master/images/images/h55/hfd/8797293281310/Typical-Spectra-of-Spectral-Calib-Lamps.pdf`.

[111] W. Heitler. *The Quantum Theory of Radiation*. Third. The International Series of Monographs on Physics. pp. 235-246. Oxford at the Clarendon Press, 1954.

[112] H. R. Griem. *Principles of Plasma Spectroscopy*. Cambridge Monographs on Plasma Physics. Cambridge University Press, 1997.

[113] A. Kramida et al. *NIST Atomic Spectra Database (ver. 5.10)*. 2022. URL: `https://physics.nist.gov/asd`.

[114] W. H. McMaster. "Polarization and the Stokes Parameters". In: *American Journal of Physics* 22.6 (Sept. 1954), pp. 351–362. DOI: `10.1119/1.1933744`.

[115] D. Salzman. *Atomic Physics in Hot Plasmas*. International Series of Monograph on Physics 97. Oxford University Press, 1998.

[116] J. Rosato, Y. Marandet, and R. Stamm. "Quantifying the statistical noise in computer simulations of Stark broadening". In: *Journal of Quantitative Spectroscopy and Radiative Transfer* 249 (July 2020), p. 107002. DOI: `10.1016/j.jqsrt.2020.107002`.

[117] H.-J. Kunze. *Introduction to Plasma Spectroscopy*. Springer Series on Atomic, Optical, and Plasma Physics 56. Springer, 2009. DOI: `10.1007/978-3-642-02233-3`.

[118] E. Stambulchik and Y. Maron. "Plasma formulary interactive". en. In: *J. Inst.* 6.10 (Oct. 2011), P10009–P10009. DOI: `10.1088/1748-0221/6/10/P10009`.

[119] S. Sahal-Bréchot, M. Dimitrijević, and N. Moreau. *STARK-B database*. Observatory of Paris, LERMA and Astronomical Observatory of Belgrade. 2023. URL: http://stark-b.obspm.fr.

[120] P. R. Bevington. *Data reduction and Error Analysis for the Physical Science*. Third. pp. 235-246. McGraw-Hill, 1969. URL: http://experimentationlab.berkeley.edu/sites/default/files/pdfs/Bevington.pdf.

[121] A. Smolders et al. "Comparison of high density and nitrogen seeded detachment using SOLPS-ITER simulations of the tokamak á configuration variable". In: *Plasma Phys. Control. Fusion* 62.12 (Dec. 2020). DOI: 10.1088/1361-6587/abbcc5.

[122] A. Loarte et al. "Plasma detachment in JET Mark I divertor experiments". In: *Nuclear Fusion* 38.3 (Mar. 1998), p. 331. DOI: 10.1088/0029-5515/38/3/303.

[123] J. Freidberg. *Plasma Physics and Fusion Energy*. Cambridge: Cambridge University Press, 2007. URL: www.cambridge.org/9780521733175.

[124] A. Fasoli. *Plasma Physics II - Kinetic theory of plasmas*. Lecture notes. 2010. URL: https://moodle.epfl.ch/pluginfile.php/3132694/mod_resource/content/1/Plasma_II_notes_Fasoli.pdf.

[125] J.D. Huba. *NRL Plasma Formulary*. (Joseph D. 1950). Washington D.C.: Naval Research Laboratory, 1998. URL: https://library.psfc.mit.edu/catalog/online_pubs/NRL_FORMULARY_13.pdf.

[126] H. P. Summers. *The ADAS User Manual*. version 2.6. 2004. URL: http://www.adas.ac.uk.

[127] J. S. Santoso. "Production of Negative Hydrogen Ions in a High-Powered Helicon Plasma Source". Ph.D. thesis. Australian National University, July 2018. URL: https://openresearch-repository.anu.edu.au/bitstream/1885/154254/1/Santoso%2020J%2020S%2020Thesis%202018.pdf.

[128] A. Bondi. "van der Waals Volumes and Radii". In: *The Journal of Physical Chemistry* 68.3 (1964), pp. 441–451. DOI: 10.1021/j100785a001.

[129] P. Swaczyna et al. "Angular Scattering in Charge Exchange: Issues and Implications for Secondary Interstellar Hydrogen". In: *The Astrophysical Journal* 887.2 (Dec. 2019), p. 223. DOI: 10.3847/1538-4357/ab5440.

[130] N. Christen et al. "Exploring drift effects in TCV single-null plasmas with the UEDGE code". In: *Plasma Physics and Controlled Fusion* 59.10 (Aug. 2017), p. 105004. DOI: 10.1088/1361-6587/aa7c8e.

[131] A. V. Chankin et al. "Possible explanation for doubly peaked profiles at the divertor target in JET". In: *Plasma Physics and Controlled Fusion* 43.3 (Mar. 2001), p. 299. DOI: 10.1088/0741-3335/43/3/305.

[132] T. Eich et al. "Inter-ELM Power Decay Length for JET and ASDEX Upgrade: Measurement and Comparison with Heuristic Drift-Based Model". In: *Phys. Rev. Lett.* 107 (21 Nov. 2011), p. 215001. DOI: 10.1103/PhysRevLett.107.215001.

[133] N. Osborne et al. "Initial Fulcher band observations from high-resolution spectroscopy in the MAST-U divertor". In: *In preparation* (2023).

[134] E. de la Cal et al. "Spatially resolved H_α-emission simulation with EIRENE in TJ-II to study hydrogen atomic and molecular physics in low density, high temperature fusion edge plasmas". In: *Nuclear Fusion* 48.9 (Aug. 2008), p. 095005. DOI: 10.1088/0029-5515/48/9/095005.

[135] N. Bisai and P. K. Kaw. "Influence of hot and cold neutrals on scrape-off layer tokamak plasma turbulence". In: *Physics of Plasmas* 25.1 (Jan. 2018). 012503. DOI: 10.1063/1.5002623.

[136] R. Friedl et al. "Dissociative recombination and its impact on the line profile of the hydrogen Balmer series". In: *Plasma Sources Science and Technology* 29.1 (Jan. 2020), p. 015014. DOI: 10.1088/1361-6595/ab5ae5.

[137] D. Smith. "Physical sputtering model for fusion reactor first-wall materials". In: *Journal of Nuclear Materials* 75.1 (1978), pp. 20–31. DOI: https://doi.org/10.1016/0022-3115(78)90025-9.

[138] A. Perek et al. "A spectroscopic inference and SOLPS-ITER comparison of flux-resolved edge plasma parameters in detachment experiments on TCV". In: *Nuclear Fusion* 62.9 (July 2022), p. 096012. DOI: 10.1088/1741-4326/ac7813.

[139] Z.-P. Chen et al. "SOLPS-ITER modeling of boosted carbon radiation through non-coronal effects in an X-divertor facilitating detachment in DIII-D". In: *Nuclear Fusion* 60.4 (Feb. 2020), p. 046005. DOI: 10.1088/1741-4326/ab71bc.

[140] T. R. Weber et al. "Impurity flow measurements at DIII-D using a coherence imaging spectrometer". en. In: *Journal of Nuclear Materials* 438 (July 2013), S1257–S1260. DOI: 10.1016/j.jnucmat.2013.01.279.

[141] S. A. Silburn et al. "Coherence imaging of scrape-off-layer and divertor impurity flows in the Mega Amp Spherical Tokamak (invited)". en. In: *Review of Scientific Instruments* 85.11 (Nov. 2014), p. 11D703. DOI: 10.1063/1.4891165.

[142] D. Gradic et al. "2D coherence imaging measurements of C^{2+} ion temperatures in the divertor of Wendelstein 7-X". en. In: *Nucl. Fusion* 61.10 (Oct. 2021), p. 106041. DOI: 10.1088/1741-4326/ac25bf.

[143] D. Gradic et al. "Impurity temperatures measured via line shape analysis in the island scrape-off-layer of Wendelstein 7-X". en. In: *Plasma Phys. Control. Fusion* 64.7 (July 2022). DOI: 10.1088/1361-6587/ac70fa.

[144] L. Wang et al. "Achievements of actively controlled divertor detachment compatible with sustained high confinement core in DIII-D and EAST". In: *Nucl. Fusion* 62.7 (July 2022), p. 076002. DOI: 10.1088/1741-4326/ac4774.

[145] T. Nakano et al. "Radiation process of carbon ions in JT-60U detached divertor plasmas". en. In: *Journal of Nuclear Materials* 390-391 (June 2009), pp. 255–258. DOI: 10.1016/j.jnucmat.2009.01.085.

[146] A. Kallenbach et al. "Impurity seeding for tokamak power exhaust: from present devices via ITER to DEMO". In: *Plasma Physics and Controlled Fusion* 55.12 (Nov. 2013), p. 124041. DOI: 10.1088/0741-3335/55/12/124041.

[147] S. Henderson et al. "Determination of volumetric plasma parameters from spectroscopic N II and N III line ratio measurements in the ASDEX Upgrade divertor". In: *Nuclear Fusion* 58.1 (Dec. 2017), p. 016047. DOI: 10.1088/1741-4326/aa96be.

[148] R. Janev, M. Harrison, and H. Drawin. "Atomic and molecular database for fusion plasma edge studies". In: *Nuclear Fusion* 29.1 (Jan. 1989), p. 109. DOI: 10.1088/0029-5515/29/1/015.

[149] R. K. Janev and D. Reiter. "Collision processes of CHy and CHy+ hydrocarbons with plasma electrons and protons". In: *Physics of Plasmas* 9.9 (Aug. 2002), pp. 4071–4081. DOI: 10.1063/1.1500735.

[150] A. McLean et al. "Electron pressure balance in the SOL through the transition to detachment". In: *Journal of Nuclear Materials* 463 (2015). PLASMA-SURFACE INTERACTIONS 21, pp. 533–536. DOI: https://doi.org/10.1016/j.jnucmat.2015.01.066.

[151] M. Wensing et al. "SOLPS-ITER simulations of the TCV divertor upgrade". In: *Plasma Physics and Controlled Fusion* 61.8 (July 2019), p. 085029. DOI: 10.1088/1361-6587/ab2b1f.

[152] G. Sun et al. "Performance assessment of a tightly baffled, long-legged divertor configuration in TCV with SOLPS-ITER". In: *Nuclear Fusion* 63.9 (Aug. 2023), p. 096011. DOI: 10.1088/1741-4326/ace45f.

Acknowledgements

I would like to start these acknowledgements by thanking my thesis directors, Basil Duval and Dmytry Mykytchuck. Under their supervision, I learned a lot, but I also had a fun time. They are very enthusiastic people, driven by endless curiosity towards big problems but also towards tiny little details. They gave me my fair share of responsibilities, but I always felt protected and never abandoned. They contributed significantly to my growth as a scientist and as a person during the last 5 years. I am grateful for the time we spent together. Also, thanks Basil, for considerably improving this and many other works at SPC with your valuable revisions.

I would like to further thank the members of my exam jury: Christine Stollberg, Ralph Dux and Kevin Verhaegh. Thanks for taking the time to carefully read this manuscript during the summer and to come to Lausanne to listen to what I had to present. I was lucky to have you as experts.

This thesis would not have been possible without the contribution of many other people, whom I would like to thank here. Thank you, Yanis Andrebe and Hammam Elaian, for your help and expertise in optical and mechanical systems. Your contribution to the DSS hardware upgrade was invaluable and laid the basis for all the work afterwards. I would also like to thank Artur Perek, Benjamin Vincent and Patrick Blanchard for providing me with MANTIS and TS data, without which the interpretation of DSS data would have been much harder, and the thesis would likely have been over after chapter 3. Thanks to Luke Simons, Claudia Colandrea, Martim Zurita and Sophie Gorno for all the complementary diagnostic data. Thanks to Massimo Carpita for the insightful conversations and for teaching me the 2PM. Thanks to Oliver Février, Christian Theiler, Holger Reimerdes and Marcelo Baquero for their valuable suggestions in preparation for the exam and throughout these years. And finally, thanks to Guillaume Lebars, who helped me daily, with endless patience, with computer stuff.

If I did not succumb while writing this work, it is only because I always have felt supported by the people around me. I have met many friends at SPC, and with some of them, I developed

Lorenzo Martinelli
Curriculum Vitae

Rue de Bassenges, 25, Ecublens
1024
CH
☐ *+41 779802881*
✉ *lorenzo.martinelli@epfl.ch*
in */martinelli-l/*
ⓘ *0000-0002-7618-1077*

Profile

- Doctoral assistant at EPFL, Physics department (Swiss Plasma Center - SPC)
- Acquired skills in plasma diagnostics hardware and software development
- Proficient data analysis skills and use of Matlab

Professional Experience

2018-2023
- Diagnostic responsible officer at the Tokamak à Configuration Variable (TCV - SPC)
  - Collaboration to optical spectroscopy diagnostic hardware upgrade design
  - Upgrade of diagnostic control system
  - Development of novel data analysis technique for plasma ion temperature measurements
  - Integration of complementary diagnostics data for a complete physical characterisation of divertor plasmas
- Collaboration within the EuroFusion scientific network (`https://euro-fusion.org`) for multiple international experimental campaigns and research topics performed at TCV-SPC
- Teaching and teaching assistant, focusing on problem-solving techniques; Master thesis co-supervisor;

2017-2018
- Development of a gamma-ray spectrometer for runaway electrons energy measurements, with a focus on hardware assembly and its characterisation, and development of analysis techniques for high energy spectra calibration with radioactive sources at the ISTP-CNR in Milano

---
Technical skills

2018-2023
- Hardware skills in optical spectroscopy instrumentation (e.g. spectrometers, CCD cameras, optical fibres...) - alignment, calibration and instrument characterisation;
- Improved and updated Matlab routines for data acquisition and analysis, implemented novel curve-fitting techniques of customised models on spectroscopy data;
- Codes maintenance using GitHub, GitLab and their documentation on Wiki pages.
- Scientific writing and presenting

2015-2018 Data analysis with C++, Python, ROOT (object-orient library developed at CERN)

Education

2018 - 2023 **PhD**, *EPFL - Swiss Plasma Center*, Lausanne
Physics - Nuclear Fusion

2015–2018 **MSc**, *Universitá degli Studi di Milano-Bicocca*, Milano, *110L/110*
Master degree in Physics - specialisation in Plasma Physics

2012–2015 **BSc**, *Universitá degli Studi di Milano-Bicocca*, Milano, *105/110*
Bachelor degree in Physics

PhD thesis

title Spectroscopic characterisation of TCV divertor towards a detached regime

description The thesis framework is that of power exhaust studies in nuclear fusion devices. The upgraded spectroscopic diagnostic I worked on allowed for novel time and space-resolved ion temperature measurements in the colder region of the plasma. My thesis was focused on describing the physical processes leading to the divertor plasma detachment from TCV walls for the safe operation of the forthcoming nuclear fusion power plants.

Languages

Italian Native

English C1 / C2   *Proficient*

Français B2   *Bonnes compétences orales*

Interests

Music Jazz - Student at EJMA's Jazz Atelier (bass guitar)

Sports Climbing, especially gym bouldering, skiing and snowboarding

Long trekkings Santiago de Compostela (ES), Trilho dos pescadores (PT), Via Francigena (IT)